CROSS-SHORE MIGRATION OF LUNATE MEGARIPPLES AND BEDLOAD SEDIMENT TRANSPORT MODELS

AMANI S. NGUSARU

INFORMATION TO USERS

This manuscript has been reproduced from the microfilm master. UMI films the text directly from the original or copy submitted. Thus, some thesis and dissertation copies are in typewriter face, while others may be from any type of computer printer.

The quality of this reproduction is dependent upon the quality of the copy submitted. Broken or indistinct print, colored or poor quality illustrations and photographs, print bleedthrough, substandard margins, and improper alignment can adversely affect reproduction.

In the unlikely event that the author did not send UMI a complete manuscript and there are missing pages, these will be noted. Also, if unauthorized copyright material had to be removed, a note will indicate the deletion.

Oversize materials (e.g., maps, drawings, charts) are reproduced by sectioning the original, beginning at the upper left-hand corner and continuing from left to right in equal sections with small overlaps.

Photographs included in the original manuscript have been reproduced xerographically in this copy. Higher quality 6" x 9" black and white photographic prints are available for any photographs or illustrations appearing in this copy for an additional charge. Contact UMI directly to order.

ProQuest Information and Learning
300 North Zeeb Road, Ann Arbor, MI 48106-1346 USA
800-521-0600

CROSS-SHORE MIGRATION OF LUNATE MEGARIPPLES AND BEDLOAD SEDIMENT TRANSPORT MODELS

By

©Amani S. Ngusaru

A Thesis Submitted to the
SCHOOL OF GRADUATE STUDIES
in Partial Fulfillment
of the Requirements for the Degree of
DOCTOR OF PHILOSOPHY
at
Earth Sciences
MEMORIAL UNIVERSITY OF NEWFOUNDLAND
ST. JOHN'S, NEWFOUNDLAND

MARCH 2000

Abstract

Rotary fan-beam and pencil-beam sonar images collected during the DUCK94 field experiment are used to determine the geometrical scales, orientations, and cross-shore migration velocities of cross-shore oriented lunate megaripples. The measurements show that these megaripples ranged from 0.05 to 0.5 m in height, 0.5 to 4.0 m in separation-length and 0.25 to 2.75 m in both span and spacing. There is a good correlation between both megaripple heights and separation-lengths, and megaripple span and spacings. The ratio of height to separation-length ranged from 0.12 to 0.13. Megaripple scales are somewhat correlated with both the flow energy and wave-orbital excursion. Megaripples in general migrated onshore at speeds of 10-40 cm/h. This onshore migration was opposite to the offshore-directed mean cross-shore velocity, U, for $|U| < 20$ cm/s. Megaripple migration stalled as U approached 20 cm/s in the offshore direction. Offshore migration appeared to occur for higher speed offshore mean flows. Wave-orbital velocity skewness and mean velocity are weakly correlated to migration velocity. The measured lunate megaripple "lee" face slopes are consistent with the angle of repose.

The observed migration velocities are reproduced reasonably well by stress-based bedload sediment transport models using the measured local waves and currents and best-fit values of the wave/current friction factor ratio. The model/data comparisons are not very sensitive to the stress exponent in the transport models. The values of the current friction factor f_c, and the wave/current friction factor ratio f_w/f_c, giving the best fit to the migration velocities ranged from $4.3\text{x}10^{-3}$ to $8.0\text{x}10^{-3}$, and 2 to 15, respectively. Infragravity waves are found to contribute mainly to the offshore transport, and treating infragravity velocities as waves gives about 10% better comparison compared to treating these motions as slowly varying currents. The megaripple orientations are better correlated with the direction of net sediment transport than that of the gross bedform-normal sediment transport.

Acknowledgements

I am indebted to Alex E. Hay, first for accepting me to be his student and second for providing exciting supervision, encouragement, support and vision. I am particularly grateful for having known and worked with Alex, whose dedication to science has been a source of inspiration for me. Alex has been the most important person, offering much helpful advice and clarifying discussions which greatly helped in expanding my knowledge of the field. Special thanks to the members of my dissertation committee for their helpful suggestions and insights: Richard N. Hiscott, William J. Scott and Ali E. Aksu. Appreciation is due for the effort expended by Richard Hiscott and William Scott in reading the contents of this thesis in such detail and giving me thoughtful suggestions. Many thanks are also due to the staff and students of Memorial University of Newfoundland: Len Zedel, Wes Paul, Douglas Wilson, Ian Clark and Anna Crawford, who worked long hours on the beach during the DUCK94 field experiment. The obtained high quality acoustic data formed the basis for my thesis. I also appreciate the contribution of the staff at the Federal Research Facility, U.S Army Corps of Engineers, during the DUCK94 experiment. I also wish to acknowledge Anthony J. Bowen for providing the hydrodynamics data.

Grateful acknowledgment is made to Memorial University of Newfoundland for giving me the privilege and opportunity to study in Canada. Colleen Clark and Anthony Dickinson provided constant encouragement and administrative assistance. I also want to thank the staff and students at the Department of Oceanography, Dalhousie University for their cooperation and for providing a good learning environment during the last two and half years of my research. Lastly, my family encouraged me throughout. The enthusiasm and support from my wife, Veronica, made it worthwhile.

The financial support during the first four years of the thesis was provided by CIDA/Marine Science Scholarship and during the last six months, by a Memorial University Graduate Fellowship.

Contents

Abstract ii

Acknowledgements iii

List of Tables vii

List of Figures viii

List of Symbols xv

1 Introduction 1

1.1 Background 2

1.2 Previous studies 4

1.3 Forcing for cross-shore lunate megaripple migration 7

1.4 Stress-based semi-empirical models 9

1.5 Objectives 14

2 Methods and data base 16

2.1 Study site 16

2.2 Instrumentation 20

2.3 DUCK94 Hydrodynamics 21

2.3.1 Days of interest 25

2.3.2 Velocity Spectra 25

2.4 Rotary sonar data 31

2.4.1 Fan-beam images 31
2.4.2 Pencil-beam images 32
2.4.3 Image processing 35
2.5 Reconstruction of bed profiles 35
2.6 Measurement of cross-shore migration velocities 36

3 Patterns and geometrical scales **40**
3.1 Lunate megaripple patterns during Storm1 41
3.2 Lunate megaripple patterns during Storm2 47
3.3 Persistence and timescales of change 49
3.4 Geometrical scales 52
3.4.1 Lunate megaripple heights and separation-lengths 53
3.4.2 Spans and spacings 59
3.4.3 Probability distributions 60
3.4.4 Comparison with total kinetic energy 66
3.4.5 Comparison with wave-orbital excursions 70
3.4.6 Comparison with other non-dimensional parameters 70
3.5 "Lee" face slopes 77

4 Cross-shore migration velocities **79**
4.1 Storm1 megaripples 79
4.2 Storm2 megaripples 82
4.3 Measured migration velocities 89

5 Modelling cross-shore migration velocities **95**
5.1 Bagnold's bedform migration model 95
5.2 Stress-based bedload transport models 97
5.2.1 Waves only 97
5.2.2 Combined waves and mean currents 98
5.2.3 Wave-orbital velocity amplitude 103
5.2.4 Friction Factor Ratio α 107

5.2.5 Model results 111
5.3 Bedload transport 124
5.4 Comparison between Sleath (1995) model and other semi-empirical model results 135

6 Lunate megaripple orientations and the direction of bedload sediment transport 142
6.1 Measured lunate megaripple orientations 143
6.2 Direction of incident waves, mean and total currents 149
6.3 Rule of maximum gross bedform-normal transport 153
6.4 Direction of resultant bedload sediment transport 161

7 Conclusions 167

Appendix 171

A 171
A.1 Marsh-McBirney electromagnetic current meters 171

B 174
B.1 Modelling the cross-shore migration velocities without including the longshore stresses 174

References 183

List of Tables

1.1 Previous measurements of cross-shore lunate megaripple migration velocities. 6

2.1 Marsh-McBirney electromagnetic current meters used during DUCK94 experiment 21

3.1 Summary of bedform persistence in hours as a function of bedform size. . . 52

3.2 Rayleigh distribution parameters for both Storm1 and Storm2. 66

5.1 Maximum correlation coefficients (R) for the comparison of measured megaripple migration velocities with $\overline{\chi_x}$ computed using various approaches of estimating wave-orbital velocity amplitudes. 110

5.2 The number of values in each averaging interval in Figures 4.15 and 4.16. . 120

5.3 Comparison between measured and computed megaripple migration velocities including longshore stresses. 127

B.1 Maximum correlation coefficients (R) for the comparison of measured megaripple migration velocities with $\overline{\chi_x''}$ computed using various approaches of estimating wave-orbital velocity amplitudes. 178

B.2 Comparison between measured and computed megaripple migration velocities without longshore stresses. 178

List of Figures

2.1 The study site. 17
2.2 Cross-shore bathymetric profile taken with the CRAB on Yearday 277. . . . 18
2.3 Plan view of the instrument frame, showing pencil-beam and fan-beam sonars (shaded). 19
2.4 Deep water incident wave conditions. 23
2.5 Time series of mean cross-shore current velocity, mean alongshore current velocity and rms wave-orbital velocity. 24
2.6 Hydrodynamic conditions at the frame location. 26
2.7 The average cross-shore velocity spectrum for Storm1 and Storm2. 27
2.8 3D wave power spectral density for gravity waves and infragravity waves during Storm1. 28
2.9 3D wave power spectral density for gravity waves and infragravity waves during Storm2. 29
2.10 Half hour averaged root-mean square of cross-shore infragravity wave velocities for Storm1 and Storm2. 30
2.11 Typical rotary fan-beam sidescan sonar image. 33
2.12 Typical rotary pencil-beam sonar image. 34
2.13 Lower portion of a pencil-beam image transformed into rectangular coordinates and the corresponding reconstructed bed profile. 37

3.1 Characteristic values of grain roughness Shields parameter for lunate megaripples observed during both Storm1 and Storm2. 42

3.2 Fan-beam images collected between 0019h to 1239h on Yearday 277 during Storm1. 43
3.3 Fan-beam images collected between 2259h on Yearday 277 and 0229h on Yearday 278 during Storm1. 44
3.4 Fan-beam images collected between 0459h to 1529h on Yearday 278 during Storm1. 46
3.5 Fan-beam images collected between 0634h to 1559h on Yearday 286 during Storm2. 48
3.6 Fan-beam images collected between 0019h to 0259h on Yearday 287 during Storm2. 50
3.7 Fan-beam images collected between 0739h to 1039h on Yearday 287 during Storm2. 51
3.8 Schematic diagram showing lunate megaripple geometrical parameters. . . 54
3.9 Time series of measured megaripple heights η and separation-lengths L statistic for Storm1. 55
3.10 Time series of measured megaripple heights η and separation-lengths L statistic for Storm2. 56
3.11 Scatter diagrams for the comparison between the measured statistic of megaripple heights and trough-to-trough separation-leghths for Storm1 and Storm2. 57
3.12 Histograms of measured megaripple heights and trough-to-trough separation-lengths for Storm1 and Storm2. 58
3.13 Example of an offshore fan-beam sub-image showing the digitized tips of megaripple horns and trough centers. 61
3.14 Time series of measured maximum (+), minimum (o) and mean (*) values of lunate megaripple spans and spacings for Storm1. 62
3.15 Time series of measured maximum (+), minimum (o) and mean (*) values of lunate megaripple spans and spacings for Storm2. 63
3.16 Histograms of the measured megaripple spans and spacings statistic for Storm1 and Storm2. 64

3.17 Scatter diagram for the comparison between lunate megaripple spacings with spans for Storm1 and Storm2. 65
3.18 Distribution of the probability density of normalized megaripple heights and chord-lengths for Storm1 and Storm2 compared with the Rayleigh distribution function. 67
3.19 Distribution of the probability density of normalized megaripple spans and spacings for Storm1 and Storm2 compared with the Rayleigh distribution function. 68
3.20 Scatter diagram for the comparison between total fluid kinetic energy and mean values of lunate megaripple spans and spacings for Storm1 and Storm2. 69
3.21 Comparison between the mean values of measured megaripple separation-lengths, spans, spacings and wave-orbital excursions. 71
3.22 Comparison between the mean values of measured megaripple separation-lengths and Shields parameter, Mobility number and Wave Reynolds number. 72
3.23 Comparison between the mean values of measured megaripple spans and Shields parameter, Mobility number and Wave Reynolds number. 73
3.24 Filtered and detrended bed profiles for Storm1 between +1 m and -4 m on either side of the pencil-beam transducer. 75
3.25 Histogram of measured lunate megaripple foreset slopes based on bed profiles for Storm1 between -2 m to +1 m in cross-shore distance. 76

4.1 A series of 1/2h separated, unfiltered pencil-beam bed profiles during Storm1. 80
4.2 A series of 20 minutes separated, unfiltered pencil-beam bed profiles for a 1.6-d interval during Storm2. 81
4.3 Fan-beam images of lunate megaripples during Storm1, on the offshore side of the frame. 83
4.4 Fan-beam images of lunate megaripples during the first stage of Storm2. . . 84
4.5 Fan-beam images of lunate megaripples during the second stage of Storm2. 85
4.6 Cross-shore profiles of the fan-beam signal amplitude during Storm1. . . . 86
4.7 Cross-shore profiles of the fan-beam signal amplitude during Storm2. . . . 87

4.8 Measured cross-shore lunate megaripple migration velocities (U_m). 88
4.9 Mean cross-shore and alongshore velocities and rms wave-orbital velocities for the days of interest during Storm1. 92
4.10 Comparison between the observed cross-shore lunate megaripple migration velocities and mean cross-shore velocity and wave-orbital velocity skewness. 94

5.1 Comparison between absolute values of cross-shore migration velocities and mean megaripple heights. 96
5.2 Schematic diagram showing the velocity components used to obtain U_c (and $\mathcal{U}_c$) when $U_{ifg}(t)$ and $V_{ifg}(t)$ are treated as waves (and slowly varying currents). 104
5.3 Schematic diagram showing the definition of wave-orbital velocity amplitude for a single wave. 105
5.4 Example of the method used to determine wave-orbital velocity amplitudes using the $0.5U_{pp}$ approach. 106
5.5 Correlation coefficients between measured migration velocities and $\overline{\chi_x}$ as a function of friction coefficient ratio. 109
5.6 Wave, infragravity and mean components of the calculated values of $\overline{\chi'_x}$ and $\overline{\chi}_x$ for Storm2. 113
5.7 Scatter plot of $\overline{\chi}_{IFG}$ versus $\overline{\chi'}_{IFG}$. (a) $\xi = 3/2$; (b) $\xi = 5/2$. 114
5.8 Comparison of modelled and field measured cross-shore megaripple migration velocities using the $0.5U_{pp}$ approach for Storm1. 116
5.9 Comparison of modelled and measured cross-shore megaripple migration velocities using the $0.5U_{pp}$ approach for Storm2. 117
5.10 Comparison of modelled and measured cross-shore megaripple migration velocities using the $2U_{rms}$ approach for Storm1. 118
5.11 Comparison of modelled and measured cross-shore megaripple migration velocities using the $2U_{rms}$ approach for Storm2. 119
5.12 Comparisons between the raw measured and computed cross-shore migration velocities using the $0.5U_{pp}$ approach. 122

5.13 Comparisons between the raw measured and computed cross-shore migration velocities sing the $2U_{rms}$ approach. 123
5.14 Comparisons between interval-averaged measured and computed cross-shore migration velocities using the $0.5U_{pp}$ approach. 125
5.15 Comparisons between interval-averaged measured and computed cross-shore migration velocities using the $2U_{rms}$ approach. 126
5.16 Measured volumetric cross-shore bedload sediment transport per unit width (Q_B) calculated using bedform migration model. 128
5.17 Plots of selected bathymetric profiles as measured using the CRAB, showing offshore bar migration during Yeardays 276-279. 129
5.18 Plots of selected bathymetric profiles as measured using the CRAB, showing offshore bar migration during Yeardays 285-287. 130
5.19 Plots of selected bathymetric profiles as measured using the CRAB, showing offshore bar migration during Yeardays 285-287. 131
5.20 Plots of Storm1 bathymetric profiles during Yeardays 277-279. 132
5.21 Plots of Storm2 bathymetric profiles during Yeardays 286-287. 133
5.22 The comparison between the cross-shore bedload sediment transport calculated using the Sleath (1995) model with results from other models. . . . 138
5.23 The comparison between the cross-shore bedload sediment transport calculated using the Sleath (1995) model with results from other models. . . . 140

6.1 Schematic diagram showing the measured lunate megaripple angles of orientation. 144
6.2 Measured mean megaripple orientations for Storm1 and Storm2. 146
6.3 Histograms of all the measured lunate megaripple orientations for Storm1 and Storm2. 147
6.4 Fitting of a probability density function to normalized megaripple orientations. 148

6.5 Time series of the measured mean lunate megaripple orientations, the calculated wave incident angles, direction of mean currents, and direction of total currents vector for Storm1. 150
6.6 Time series of the measured mean lunate megaripple orientations, the calculated wave incident angles, direction of mean currents, and direction of total currents vector for Storm2. 151
6.7 Scatter diagrams for the comparison between mean lunate megaripple orientations with calculated directions of wave incident angles, mean currents, and total currents vector for Storm1 and Storm2. 152
6.8 Schematic diagram showing the transport vectors and bedform orientation from Rubin and Hunter (1987). 154
6.9 Schematic diagram showing the orientations of lunate megaripples with respect to the directions of sediment transport vectors. 156
6.10 Normalized gross bedform-normal transport used in the estimation of megaripple orientations based on Rubin and Hunter hypothesis. 157
6.11 The difference between the maximum and minimum values of normalized gross bedform-normal transport compared with the mean cross-shore and along-shore velocities. 158
6.12 The time series of the measured lunate megaripple orientations compared to the calculated directions of maximum gross bedform-normal bedload transport for Storm1 and Storm2 using $\xi = 3/2$ model. 159
6.13 The time series of the measured lunate megaripple orientations compared to the calculated direction of the resultant bedload transport for Storm1 and Storm2. 162
6.14 The time series of the measured cross-shore and alongshore velocities for Storm1 and Storm2 during the days of interest. 163

6.15 Scatter diagrams for the comparison between lunate megaripple orientations, with calculated directions of maximum gross bedform-normal bedload transport, direction of the resultant bedload transport when using $\xi = 3/2$ and $\alpha = 6$. 164

6.16 Scatter diagrams for the comparison between lunate megaripple orientations, with calculated directions of maximum gross bedform-normal bedload transport, direction of the resultant bedload transport when using $\xi = 3/2$ and $\alpha = 1$. 165

A.1 Velocity measurements by all 4 flowmeters on the frame during calm days. . 172

B.1 Correlation coefficients between measured migration velocities and as a function of friction coefficient ratio, $\alpha'' = f''_w/f''_c$. 177

B.2 Comparisons between the raw measured and computed cross-shore migration velocities using $0.5U_{pp}$ approach, without longshore stresses. 179

B.3 Comparisons between the raw measured and computed cross-shore migration velocities using $2U_{rms}$ approach, without longshore stresses. 180

B.4 Comparisons between interval averaged measured and computed cross-shore migration velocities using $0.5U_{pp}$ approach, without longshore stresses. 181

B.5 Comparisons between interval averaged measured and computed cross-shore migration velocities using $2U_{rms}$ approach, without longshore stresses. 182

List of Symbols

English Letters

A	A constant in stress-based bedload sediment transport models
A_o	Wave-orbital semi-excursion
D	Median grain diameter
D_B	Dominant sediment transport vector
f_w	Wave friction coefficient
f_c	Current friction coefficient
f_{wc}	Combined wave and current friction coefficient
g	Acceleration due to gravity
G_B	Gross bedform-normal bedload sediment transport
Q_B	Volume bedload sediment transport rate per unit width
Q_{Bx}	Cross-shore volume bedload sediment transport rate per unit width
Q_{By}	Along-shore volume bedload sediment transport rate per unit width
H_o	Deep water significant wave height
H_s	Nearshore significant wave height
Hz	Frequency units
L	Lunate megaripple separation-length
M	Mobility number
P	Bottom pressure
Re_w	Wave Reynolds number
R	Correlation coefficient

s	Quartz grain specific density in sea water
S	Slope of the regression line
S_B	Subodinate sediment transport vector
T_p	Peak wave period
u	Total instantaneous cross-shore wave-orbital velocity
u_{rms}	Cross-shore root-mean square velocity
U_c	Total mean current velocity vector
U_m	Cross-shore lunate megaripple migration rate
U_{ifg}	Cross-shore infragravity wave velocity
U_{max}	Maximum cross-shore wave-orbital velocity
U_{wo}	Wave-orbital velocity amplitude
u_s	Significant wave-orbital velocity close to the bed
ũ	Wave component of the cross-shore wave-orbital velocity
U	Mean component of the cross-shore wave-orbital velocity
U_{ifg}	Infragravity component of the cross-shore wave-orbital velocity
u_w	Wave plus infragravity component of the cross-shore wave-orbital velocity
v	Total instantaneous along-shore wave-orbital velocity
ṽ	Wave component of the along-shore wave-orbital velocity
V	Mean component of the along-shore wave-orbital velocity
V_{ifg}	Infragravity component of the along-shore wave-orbital velocity
v_w	Wave plus infragravity component of the along-shore wave-orbital velocity
V_m	Along-shore lunate megaripple migration rate
v_{rms}	Along-shore root-mean square velocity
W	Grain settling velocity

Greek Letters

η	Lunate megaripple height
ρ	Water density
ρ_s	Sediment grain density
ψ	Shields parameter for waves
ψ_{cr}	Critical Shields parameter for initiation of sediment motion
Φ_B	Non-dimensional volume bedload transport rate
ω	Wave radian frequency
ν	Kinematic viscosity
τ_b	Bed shear stress
τ_{bx}	Cross-shore bed shear stress
τ_{by}	Along-shore bed shear stress
τ_c	Bed shear stress due to mean currents
τ_{cx}	Cross-shore bed shear stress due to mean currents
τ_{cy}	Along-shore bed shear stress due to mean currents
τ_w	Bed shear stress due to waves
τ_{wx}	Cross-shore bed shear stress due to waves
τ_{wy}	Along-shore bed shear stress due to waves
τ_{res}	Resultant bed shear stress due to waves and mean currents
ϵ	Sediment porosity
θ_o	Deep water wave incident angle [degrees]
α	Ratio of wave and current friction coefficients (f_w/f_c) including longshore currents
α'	Ratio of wave and current friction coefficients (f'_w/f'_c) without longshore currents
$\hat{\alpha}$	Angle between dominant sediment transport vectors and bedform orientation
γ	Divergence angle between dominant sediment transport vectors
β	Angle between G_B and cross-shore trend
χ_x	Cross-shore forcing for migration velocities including longshore stresses
χ_y	Along-shore forcing for migration velocities including longshore stresses
χ''_x	Cross-shore forcing for migration velocities without longshore stresses

ξ	Exponent used in bedload sediment transport models
Λ	A constant in Sleath(1995) bedload sediment transport model
ϕ_{wave}	Nearshore wave incident angle
ϕ_{mean}	Direction of mean current vector
ϕ_{total}	Direction of total current vector
ϕ_{Mrip}	Orientation of lunate megaripples
ϕ_{Migr}	Direction of lunate megaripple migration
ϕ_{NET}	Direction of resultant bedload sediment transport
ϕ_{RH}	Bedform orientation using Rubin and Hunter (1987) hypothesis

Chapter 1

Introduction

The sea bed in the nearshore zone tends to be flat or covered with bedforms. In general two main types of bedform are commonly observed: low amplitude ripples and relatively larger structures known as lunate megaripples. Both forms coexist outside the breakpoint under shoaling waves but in the surf-zone the smaller ripples can be destroyed by plunging breakers and high orbital current speeds (Vincent and Osborne, 1993).

Lunate megaripples and the other small scale features have been the subject of many geological and engineering studies. Vincent and Osborne (1993) concluded that lunate megaripples are a significant surf-zone feature. Other lunate megaripple observations in the nearshore zone have been reported; for example among many others, Clifton et al. (1971), Clifton (1976), Dingler (1974), Davidson-Arnott and Greenwood (1976), Hay and Bowen (1993), Hay and Wilson (1994), Hay and Bowen (1998), Gallagher et al. (1998).

There is a close similarity between marine lunate megaripples and desert dunes, and large ripples or sand waves. The latter have been the subject of many studies in fluvial, steady flows, intertidal environments, as well as in laboratory flumes; for example Bagnold (1946), Simons et al. (1964), Dalyrymple et al. (1978) and Southard et al. (1990).

This thesis is a study of cross-shore oriented lunate megaripples in the nearshore zone. The main focus is in studying their geometrical scales, orientations and cross-shore migration velocities. The measurements are then compared with the hydrodynamic forcing and used to test existing theories related to bedload sediment transport.

In the past, progress in studying nearshore bedforms was severely hampered by the lack of high quality measurements. Over the last few years, methods have improved considerably and our knowledge about these sedimentary features is rapidly improving. However, more field measurements and studies of marine bedforms are still needed especially under complex combined flows (Li et al., 1997). Information on dimensions, orientation and migration rate of the nearshore sedimentary structures is still very scarce. There is especially little information regarding lunate megaripple span and spacings, their persistence and timescale of change, all of which need to be carefully studied in order for these features to have any meaningful application in bedload transport models.

1.1 Background

The study of bedforms in marine environments has been of interest to marine geoscientists and oceanographers for many years. This continued interest is due to the fact that these seafloor features are strongly coupled to sediment transport processes. The bottom morphologic features are therefore central to nearshore sediment dynamics. Thus the understanding of sediment transport in the nearshore zone is normally associated, in part, with the understanding of bedform development. However, the complex relationship between bedforms, sediment transport and nearshore hydrodynamics is still poorly understood, especially for cases involving the combined action of waves and currents. The development and movement of bedforms also form an integral component of both the nearshore sediment transport problem, and the problem of interpreting the sedimentary record in terms of coastal sediment transport (e.g., Davidson-Arnott and Greenwood, 1974, 1976; Clifton et al., 1971; Clifton, 1976; Allen, 1979, 1984).

Understanding of marine sediment transport is also important for the solution of other problems of practical significance; for example, sediment mobility is of a major concern for ocean engineering projects (Gadd et al, 1978). An understanding of sediment response to fluid flow is also essential if seaside areas are to be protected from coastal erosion. Accurate sediment transport estimates are also desperately needed in calculating sediment

budgets, and for inclusion in numerical models for shoreline change. Information on sediment transport patterns is paramount for coastal planning, management of coastal resources and sensitive marine ecosystems. Proper understanding of sediment transport processes and bedform dynamics can therefore be considered as an essential component in coastal technology.

This research is related to the problem of measuring and predicting marine bedload sediment transport. The history of observations of sediment movement in streams and flumes dates as far back as Sorby (1859) and Gilbert (1914). Since then it has become common knowledge that bedform migration is an important vehicle for bedload sediment transport. Bedload transport in migrating bedforms has subsequently been studied in both the laboratory (e.g., Simons and Richardson, 1961) and in the field (e.g., McCave, 1971). On the other hand, although the problem of estimating sediment transport has been well researched, it is still not possible to predict with confidence the mass sediment transport (Dyer and Soulsby, 1988). No unified theory of sediment transport presently exists that is valid for all water depths and fluid motions in the nearshore zone (Larson and Kraus, 1995). It is especially difficult to model the cross-shore sediment transport because the net transport in the cross-shore direction occurs as an accumulation of small differences between the large values of onshore and offshore directed transport; each of these quantities must be evaluated correctly (Horikawa, 1988, pg. 167).

Previous investigators have used a variety of techniques to measure bedload transport with limited success. These techniques have included conventional sediment traps placed on the bottom, mechanical samplers, dyed sand, radioactive tracers, fluorescent sand tracers, bathymetric profiles and stake fields (e.g., Salsman et al., 1966; Komar and Inman, 1970; Aubrey, 1979; Heathershaw, 1981; Horn and Mason, 1994). Sediment traps are rendered unreliable when fine sands predominate since unknown amounts of suspended particles can also be trapped. Mechanical samplers are time-consuming, cannot respond to rapidly changing conditions and usually involve large mounting devices which can interfere significantly with the flow. The difficulty involved in monitoring small scale changes in the transport indicators limit tracer studies to short time scales and small areal coverage

only.

The lack of proper measurement schemes seems alarming especially because on-offshore sediment transport plays a vital role in the short-term beach adjustment such as severe beach erosion due to storm surges. These problems lead researchers to focus on indirect methods of measuring bedload transport using bedform migration, where the sediment transport involved in bedform migration is assumed to represent bedload transport. Analysis of flume experiments and some river data have indicated that a reasonable estimate of the bedload component of total sediment transport can be obtained using bedform migration velocities (Dyer and Soulsby, 1988). Some of the early attempts to measure bedload transport in the marine environment using bedform migration include Aubrey (1979), McLean (1983), Goud and Aubrey (1985), Dyer and Soulsby (1988) and Hay and Bowen (1993). Many studies have now suggested the usefulness of bedform geometrical scales and migration velocities in determining marine bedload sediment transport; for example Boyd et al. (1988).

1.2 Previous studies

Early nearshore geologic studies started to emerge in the 1960's. Initially, the nearshore sub-environments were defined by examining sediment texture, physical sedimentary structures, and biogenic features. Later, these initial ideas were developed further by relating nearshore sub-environments to the "oscillatory flow concept" (Clifton et al. 1971; Clifton, 1976; Davidson-Arnott and Greenwood, 1976). The conceptual model of Clifton (1976) is particularly useful for classifying nearshore bedform patterns and the cross-shore sequence of bedforms generated by shoaling waves.

Lunate megaripples were described by Clifton et al. (1971) as large scale, irregular half moon shaped sedimentary bedforms.They have typical horizontal length scales of the order 0.5-5 m, heights of the order 0.3-1m and rounded crests. Lunate megaripples tend to occur commonly in medium to coarse grained sand under conditions of intense asymmetric flow generated by long period waves (10-15 seconds). Other environmental conditions which

are associated with lunate megaripple development include water depths of 2-4 m, regular waves, maximum wave-orbital velocity of the order of 1 m/s and velocity asymmetry of at least 20-30 cm/s. Velocity asymmetry here refers to the average difference between maximum velocities in the onshore and offshore strokes. Lunate megaripples range from isolated lunate forms, sometimes arranged crudely en echelon, to laterally connected, or catenary forms. It is common for small ripples to coexist with lunate megaripples, their distribution depending on the prevailing wave conditions.

Clifton (1976) presented a conceptual model for the transition among bedform types as a function of distance offshore. The bedform progression, from deep water shorewards, starts with long-crested shore-parallel ripples with occasional crestline bifurcations, then irregular short-crested ripples, then cross-ripples, then lunate megaripples with crescent horns, and finally flat bed. This cross-shore progression was associated by Clifton with the progressive increase in the asymmetry of the oscillatory motion and bottom shear stress as a result of wave shoaling.

Early methods of nearshore bedform measurement used photographic or video techniques; for example, Kachel and Sternberg (1971), Boyd et al. (1988), Wright et al. (1991). This is fine when the water is clear; however during storms when visibility drops very rapidly, the optical methods are less useful. Observations of the temporal and spatial variation of lunate megaripple geometrical scales have therefore been carried out using scuba diving under low energy conditions; for example, Clifton et al. (1971) etc. As a result, there have been relatively few observations of these bedforms during high energy conditions when most of the bottom adjustments occur.

The development of high frequency acoustic altimetry techniques provided accurate measurement of bedforms on the sea bed and considerably improved the understanding of the shoreface morphodynamics; for example, Dingler et al. (1977) etc. This technique is successful mainly because it is relatively unaffected by suspended sediments compared to optical methods. In a more recent study, Hay and Wilson (1994) used rotary sidescan sonar to obtain 2-D plan view imagery of bedforms in the nearshore zone. This method proved to

Table 1.1: Previous measurements of cross-shore lunate megaripple migration velocities; U_m and the measured wave and current parameters; including peak wave period; T_p, rms wave-orbital velocity; u_{rms} and mean cross-shore velocity; U (negative offshore). Also shown are the median grain size; D, water depth; h and the method applied in megaripple observations. ABS= Acoustic Backscatter Sensors.

Author	Method	D (μm)	U_m (cm/h)	Migration Direction	h (m)	T_p (s)	U (cm/s)	u_{rms} (cm/s)
Clifton et al. (1971)	Divers		30	Onshore	3-5	8-12		15-25
Osborne and Vincent (1992)	ABS	212	132	Onshore	2.25	5-6	-5	75
Hay and Bowen (1993)	ABS	170	15-20	Offshore	2.2	6-8	-5	30-40
Hay and Bowen (1993)	ABS	170	24	Onshore	2.2	6-8	5	30-40
Vincent and Osborne (1993)	ABS	185	90	Onshore		5-8		
Vincent and Osborne (1993)	Divers	185	30	Onshore		5-8		
Hay and Wilson (1994)	Fan-beam	200	50	Onshore	1.5	4-5	-2	30-40
Gallagher et al. (1998b)	Sonar Altimeters	200	30	Onshore	2			

be very useful in making measurements of bedforms during storm events. The rotary sides-can fan-beam sonar together with rotary pencil-beam sonar are therefore simultaneously used in this thesis to study lunate megaripples in the nearshore zone.

Systematic measurements of cross-shore lunate megaripple migration velocities as a function of flow strength are surprisingly scarce in the literature. Some of the existing measurements includes Clifton et al., (1971); Osborne and Vincent, (1992); Hay and Bowen, (1993); Vincent and Osborne, (1993) and Hay and Wilson (1994). The summary of their results is given in Table 1.1. Water velocity measurement was not given in Vincent and Osborne (1993) due to a current meter problem during their experiment.

Hay and Bowen (1993) also compared the modeled and measured bedload transport using lunate megaripple migration velocities and showed that the models of Madsen and Grant (1977), Watanabe (1981) and Vincent et al. (1981) produced comparable results. Their study showed that lunate megaripples could reconcile the storm-averaged bedform transport rates with semi-empirical bedload transport models. Lunate megaripple dimensions and migration velocities are therefore particularly useful in testing various predictive models of bedload transport in the marine environment and determining coefficients relevant to each model when applied to irregular wave conditions (Hay and Bowen, 1993).

Despite its obvious importance, the information on lunate megaripple orientations with respect to changing nearshore flow dynamics is virtually non-existent. Lunate megaripple orientations may be quite useful indicators of sediment transport directions in both ancient and contemporary deposits. However there is a lack of agreement as to whether these features are oriented in the direction of net bedload transport, or megaripple crests are aligned such that the gross sediment transport normal to the megaripple crest is maximal as postulated by Rubin and Hunter (1987).

Lunate megaripples are studied in this thesis using the data set obtained during DUCK94 Nearshore Dynamics Experiment. Results shed light on many of the questions described above.

1.3 Forcing for cross-shore lunate megaripple migration

In order to understand the forcing for cross-shore lunate megaripple migration, it is helpful to examine the forcing for cross-shore bedload sediment transport based on existing theories. The cross-shore exchange of sand between the intertidal areas and the outer regions of the nearshore has been extensively described in coastal geological and engineering literature. The general situation is that sand migrates shorewards during fairweather to cause accretion and moves seaward under storm conditions to accumulate as surf-zone features such as bars.

Only recently, however, have the physical processes responsible for cross-shore transport in the surf-zone been examined in the field with any degree of rigor (Wright et al. 1991). Incident waves and infragravity waves have both been identified as significant contributors (Bowen, 1980; Holman and Bowen, 1982; Guza and Thornton, 1985a,b; Stive and Wind, 1986; Huntley and Hanes, 1987; Roelvink and Stive, 1989). There is general agreement that the incident waves are primarily responsible for mobilization of the sediment. Other suggested bedload sediment transport agents in the nearshore zone include the downslope component of gravity, incident wave non-linearity, steady (mean) currents, and undertow (Madsen and Grant, 1977).

Following Horikawa (1981), the incident waves propagating towards the shore develop non-linear characteristics, that is to say the wave profile is peaked at the crest and flattened at the trough. This reduced symmetry of the surface profile is also reflected in the near-bottom velocity which shows a larger forward velocity of shorter duration under the wave crest and a smaller backward velocity of longer duration under the troughs than predicted by small amplitude wave theory. Because of the asymmetrical characteristics of the velocity field, the on-offshore sediment transport due to wave action is not balanced over a wave period. Owing to the wave non-linearity, the net bedload transport and hence lunate megaripple migration would be expected to be in the onshore direction.

The role of steady currents and undertow or return flows is to enhance the asymmetry in wave-orbital motion which in turn produces net bedload sediment transport. Undertow is essentially a gravity driven current related to the phenomenon of wave setup. It occurs because the radiation stress gradient is not uniform over depth under breaking waves whereas the opposing pressure gradient from the wave setup is (nearly) uniform, and therefore dominates near the bed (Madsen and Grant, 1977). Steady (mean) currents are commonly observed even if the waves are purely sinusoidal. The action of these currents when combined with the wave motion will produce a net sediment transport. If the mean currents are weak, the wave motion may be considered as a stirring agent making the sediment available for transport by mean currents.

Gently sloping bottom gives rise to an asymmetry in the forces acting on a sediment

grain and hence may induce a net sediment transport. However, few experimental data are available on the influence of bottom slope on the rate of sediment transport in oscillatory flows (Madsen and Grant, 1977).

Infragravity waves are low frequency motions (surf-beat) in the period range greater than 20 seconds which may be in the form of edge waves. The importance of infragravity waves in nearshore processes was emphasized by Komar and Holman (1986). Early studies have shown that while incident waves may be responsible for onshore sediment transport, the interaction of incident waves with infragravity waves and with mean offshore flows can cause offshore sediment transport (e.g. Guza and Thornton, 1985b; Huntley and Hanes, 1987). Infragravity waves have also been associated with patterns of erosion and deposition in the swash zone (e.g. Sallenger and Richmond, 1984; Holman and Bowen, 1982; Howd and Holman, 1984).

1.4 Stress-based semi-empirical models

The normal approach to modelling bedload sediment transport is to invoke semi-empirical formulae, where the frictional force that the fluid exerts upon the bed is related to the mass of sediment moved. The momentum fluxes are controlled by the bed shear stress, and in turn the shear stresses within the bottom boundary layer influence morphodynamics by determining the near-bottom velocity profiles and skin friction applied to sediment particles. Fluid motion in the nearshore zone is, however, very complicated and varies with the incoming waves and wave-induced currents. Sediment movement therefore takes place in accordance with such complicated fluid motion.

Because of the importance of bedload sediment transport, there have been numerous formula suggested for use in unidirectional flows (Yalin, 1977). Most of the original semi-empirical sediment transport models were developed by engineers based on steady-flow concepts appropriate to rivers. Under the effect of waves, there is an additional net transport due to wave non-linearity. Thus, in order to apply existing formulae in marine environments, the original unidirectional formulae have to be modified.

There have been many attempts to apply the unidirectional formulae in marine environments. Most of the original unidirectional formulae performed very well with the data for which they were validated. However, this is not the case when the formulae are tested in oceanic environments. Seymour and King (1982) compared various cross-shore bedload transport models with site measurements in California and concluded that none of the models were entirely successful. The problem with semi-empirical models is that their empirical coefficients are usually based on laboratory data; extrapolation to variable field conditions can be risky (Sleath, 1984 pg. 299).

Other early attempts to evaluate the applicability of semi-empirical models in marine conditions include Kachel and Sternberg (1971), Gadd et al. (1978), Heathershaw and Hammond (1979a), Heathershaw (1981) and Pattiaratchi and Collins (1985). Most of these studies also concluded that there is a wide difference in predicted sediment transport for similar flow speeds, flow depth, particle sizes and sea-bed roughness lengths.

The variations between the theoretical estimates emphasized the need for more field experiments in marine environments in order to constrain the models. Numerous attempts followed with the aim of developing reliable formulae for coastal sediment transport. Early suggested models for marine environments involved the effect of waves alone; however, it was realised early on that waves alone could not explain the observed bedload transport. The combined effects of waves and currents has to be considered for any optimal bedload transport models in the nearshore zone. The following sections give a summary of the stress-based bedload sediment transport formulae that are commonly applied in the nearshore zone.

Meyer-Peter and Müller (1948)

Meyer-Peter and Müller (1948) used extensive flume data to develop a bedload transport formula based on excess bottom shear stress. The original formula was modified by Wilson (1966) in order to explicitly include the Shields parameter. The volume of bedload sediment transport per unit time per unit width (Q_B) is given by

$$Q_B = 8\left[D\sqrt{(\frac{\rho_s}{\rho} - 1)\rho g D}\right](\psi - \psi_{cr})^{3/2}. \tag{1.1}$$

where ψ is the Shields parameter for waves and ψ_{cr} is the critical Shields parameter at which sand motion is just initiated, D is the median grain size, ρ is the fluid density, ρ_s is the sediment grain density and g is the acceleration due to gravity. This formula was also applied by Goud and Aubrey (1985) in estimating bedload sediment transport in the nearshore zone. [Based on the grain size at Duck94 (D=0.02 cm), the critical Shields parameter for initiation of movement is taken to be 0.07 following Horikawa (1988, pg. 180).] Shields parameter for waves is given by

$$\psi = \frac{\tau}{(\rho_s - \rho)gD} = \frac{0.5\rho f_w {u_s}^2}{(\rho_s - \rho)gD}, \tag{1.2}$$

where τ is the bed shear stress and f_w is Jonsson's (1966) wave friction factor and u_s is the significant wave orbital velocity close to the bed given by

$$u_s = 2\sqrt{{u_{rms}}^2 + {v_{rms}}^2}. \tag{1.3}$$

Madsen and Grant (1977)

Madsen and Grant (1977), using laboratory data collected using traps in oscillating trays by Kalkanis (1964) and Abou-Seida (1965), modified the Einstein-Brown equation for uni-directional flow (Brown, 1950) and utilized a friction factor (Jonsson, 1966) allowing the bottom shear stress to vary with the instantaneous wave-orbital velocity. They developed a bedload sediment transport formula of the form

$$\Phi_B = 12.5\psi^3, \qquad (\psi > \psi_{rc}) \tag{1.4}$$

where Φ_B is the non-dimensional volume bedload transport rate given by

$$\Phi_B = \frac{Q_B}{WD}, \tag{1.5}$$

W is the fall velocity and D is the median grain size.

Sleath (1978)

Sleath (1978) used a different method to non-dimensionalize Q_B in Equation (1.5) for waves of radian frequency ω such that

$$\Phi_B = \frac{Q_B}{\omega D^2}, \tag{1.6}$$

therefore obtaining a formula for the laboratory data of Kalkanis (1964) and Abou-Seida (1965) given by

$$Q_B = 4\tilde{\tau}\omega D^2[\psi - \psi_{cr}]^{3/2}. \tag{1.7}$$

Vincent et al. (1981)

Madsen and Grant (1977) interpreted the material collected in the trays of Kalkanis (1964) and Abou-Seida (1965) as a measure of bedload sediment transport. However, Vincent et al. (1981) interpreted the sand deposited in these trays as a measure of the concentration of sand in suspension. They then re-analyzed the laboratory data together with that of Madsen and Grant (1977) and suggested a modified formula of the form

$$Q_B(t) = 0.09[\psi' - \psi_{cr}](U + u_w), \tag{1.8}$$

where ψ' is as given by

$$\psi' = \frac{0.5\rho f_{cw}(U + u_w)|U + u_w|}{(\rho_s - \rho)gD}, \tag{1.9}$$

f_{cw} is a combined wave-current friction factor where they applied a value of $f_{cw} = 0.01$, U is the mean current vector and u_w is the oscillatory wave-orbital velocity.

Watanabe, Riho and Horikawa (1980)

Watanabe, Riho and Horikawa (1980) used bedload transport data measured in a 2-D wave flume with sand grains of 0.2 mm diameter and suggested a formula of form

$$Q_B = AWD(\psi - \psi_{cr}). \tag{1.10}$$

The coefficient A in the Watanabe et al. (1980) model ranges from A=1-5 depending on grain size and position inside or outside the breaker zone.

Watanabe (1982)

Later Watanabe (1982) re-analysed Watanabe et al. (1980) data and suggested a modified form of Equation (1.10) to obtain

$$Q_B = 7WD(\psi - \psi_{cr})\psi^{1/2}. \tag{1.11}$$

Watanabe (1982) showed that Equation (1.11) described the full range of Watanabe et al. (1980) flume data.

Kajima et al. (1982a)

In another study, Kajima et al. (1982a) used data from a prototype wave flume and suggested a bedload transport rate formula of the form

$$Q_B = 3WD(\psi - \psi_{cr})\psi^{1/2}. \tag{1.12}$$

Sleath (1995)

Sleath (1995) derived a formula for cross-shore bedload sediment transport by waves and currents from first principles by considering the situation where the steady current exerts a bed shear stress τ_c and the waves exerts a shear stress τ_w. He used the cosine rule and

obtained the resultant shear stress for colinear wave and current shear stress at any instant to be given by

$$\vec{\tau}_{res} = [\vec{\tau}_c + \vec{\tau}_w]. \tag{1.13}$$

After assuming that bedload transport is proportional to $(\tau_{res})^{5/2}$, Sleath (1995) obtained a formula given by

$$\frac{Q_B}{(\frac{\rho_s - \rho}{\rho_s} g D^3)^{1/2}} = \Lambda \tau_c \frac{(\tau_c{}^2 + 0.46\tau_w{}^2)^{3/4}}{[(\rho_s - \rho)gD]^{5/2}}, \tag{1.14}$$

where Λ is an empirical constant.

1.5 Objectives

The principal objective of this thesis is to study the characteristics of shoreward migrating lunate megaripples in a natural nearshore zone, and relate them to existing bedload sediment transport theories. Specific research objectives are:

1. To use the rotary fan-beam sidescan sonar images to study the patterns of nearshore lunate megaripples during storms, measure their geometric scales and test the avalanche model of megaripple migration.

2. To use both the rotary fan-beam sidescan sonar images and the rotary pencil-beam sonar images to measure the cross-shore lunate megaripple migration velocities. Then to use the existing hydrodynamic theories related to bedload sediment transport to model the observed cross-shore lunate megaripple migration velocities.

3. To use the rotary fan-beam sidescan sonar images to measure the orientation of lunate megaripples in the natural nearshore zone, and to compare the results with the direction of incident waves, net bedload sediment transport direction and the hypothesis suggested by Rubin and Hunter (1987).

4. To estimate bedload sediment transport using lunate megaripple migration velocities and compare the results with the transport obtained from commonly applied stress-based semi-empirical models in the nearshore zone.

The methods and data base used in this thesis are presented first in Chapter 2. The days of interest during the Duck94 experiment and a brief description of the fan-beam and pencil-beam acoustic images are also given in Chapter 2. The cross-shore lunate megaripple patterns, geometrical scales and characteristic slopes are discussed in Chapter 3, giving the nature of the bedforms studied in this thesis. Chapter 4 deals with the measured cross-shore lunate megaripple migration velocities using both fan-beam and pencil-beam data. Chapter 5 deals with modelling the observed migration velocities using a shear-stress based model similar to that suggested by Sleath (1995). The application of the Bagnold (1946) bedform migration model is also tested for relating bedload transport with megaripple migration velocities. Chapter 5 also gives the comparison between the measured cross-shore bedload sediment transport using lunate megaripple migration and the results obtained using some of the commonly applied semi-empirical models in the nearshore zone. Chapter 6 compares the measured lunate megaripple orientations with the directions of incident waves, mean currents, total currents, net bedload sediment transport and the gross bedform-normal bedload transport suggested by Rubin and Hunter (1987). Finally Chapter 7 gives a summary and conclusions derived from this thesis.

Chapter 2

Methods and data base

This Chapter describes the data used in this thesis and the methods used in obtaining the measurements of lunate megaripple patterns, geometrical scales and their cross-shore migration velocities.

2.1 Study site

The data set used in this thesis was collected as part of DUCK94 Nearshore Dynamics Experiment, from the nearshore zone seaward of the U.S. Army Corps of Engineers Field Research Facility (FRF) at Duck, North Carolina. The study area is located approximately half way between Cape Hatteras in the south and the entrance to Chesapeake Bay in the north (Figure 2.1). Detailed description of the site is given by Birkemeier et al. (1981). The field experiment was conducted between October 2 and 25, 1994.

Duck is a very exposed beach, facing the open North Atlantic Ocean. The bottom sediments are mostly comprised of cohesionless well sorted sand with median grain size of 0.02 cm. Bathymetric profiles were obtained from a series of surveys carried out daily by FRF staff using the CRAB, a 3-wheeled amphibious vehicle (Birkemeier et al., 1985).

Figure 2.2 shows a shore-normal bathymetric profile taken on Yearday 277 at 15 m north of the location of the instrument frame. The bottom profile was dominated by a nearshore trough and bar system. The instrument frame was deployed in the trough inside

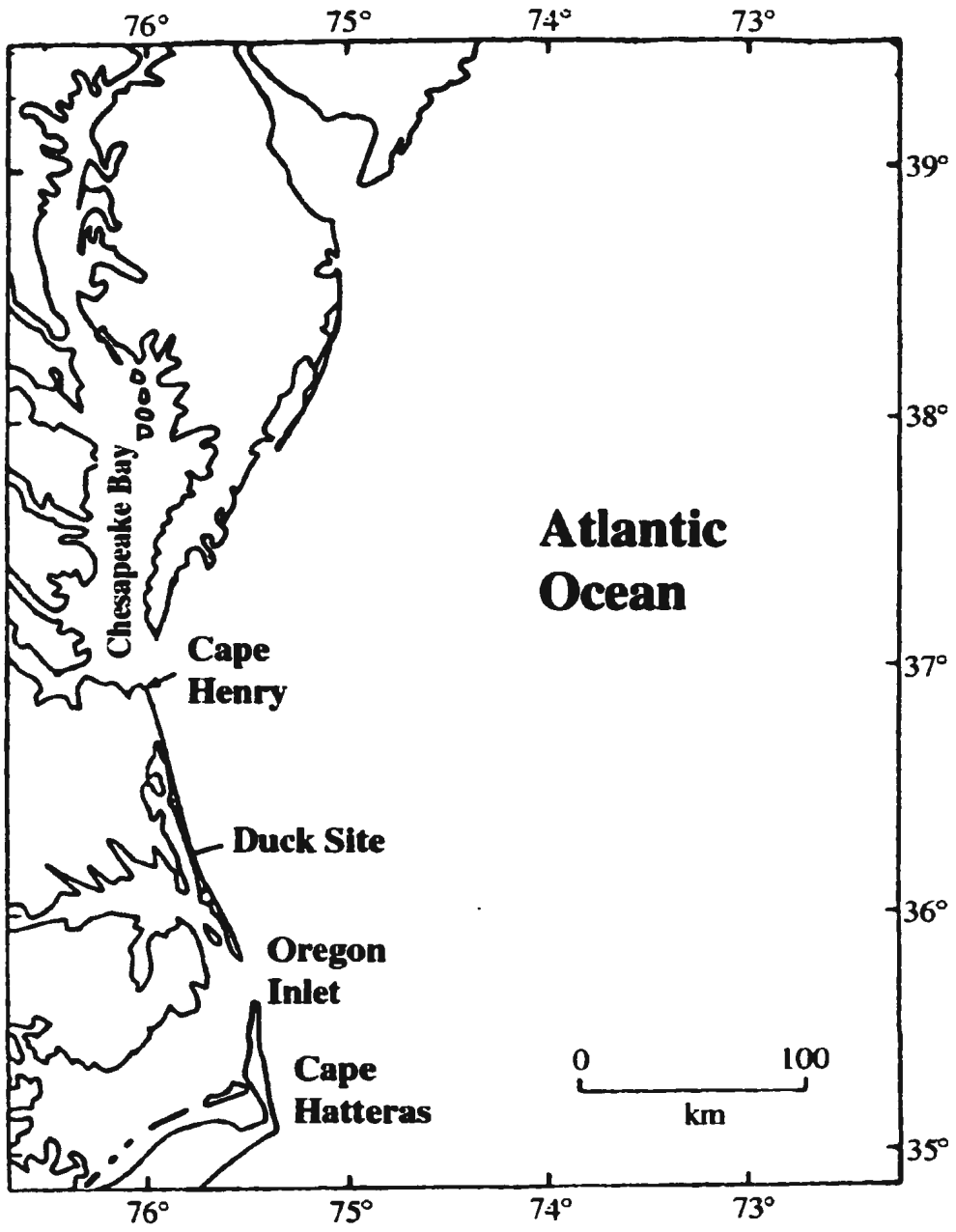

Figure 2.1: The study site.

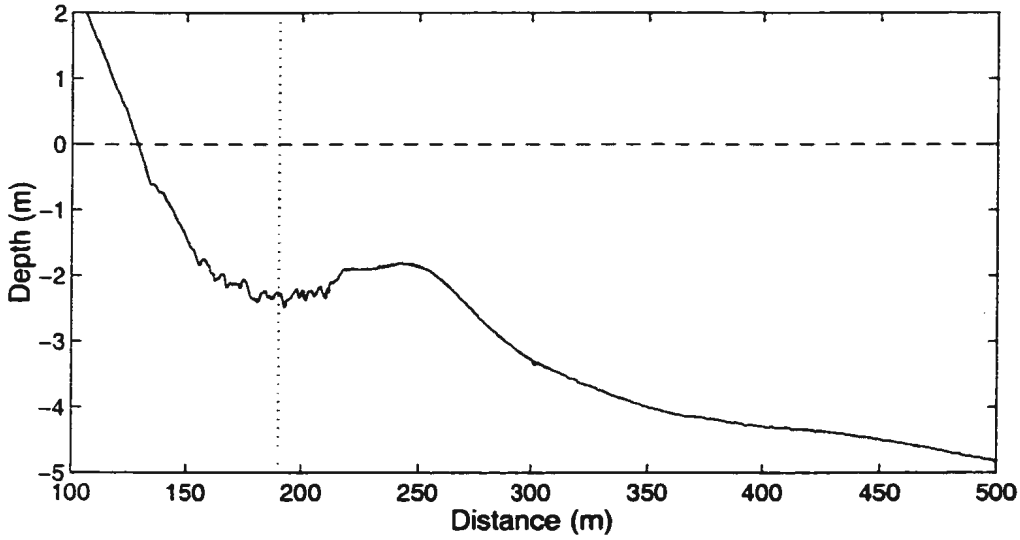

Figure 2.2: Cross-shore bathymetric profile taken with the CRAB on Yearday 277. The instrument frame (dotted line) was deployed near the center of the trough at 190 m in the cross-shore FRF coordinate, about 60 m from the shoreline. Note the O(10 cm) bed elevation variation in the trough: these are due to megaripples.

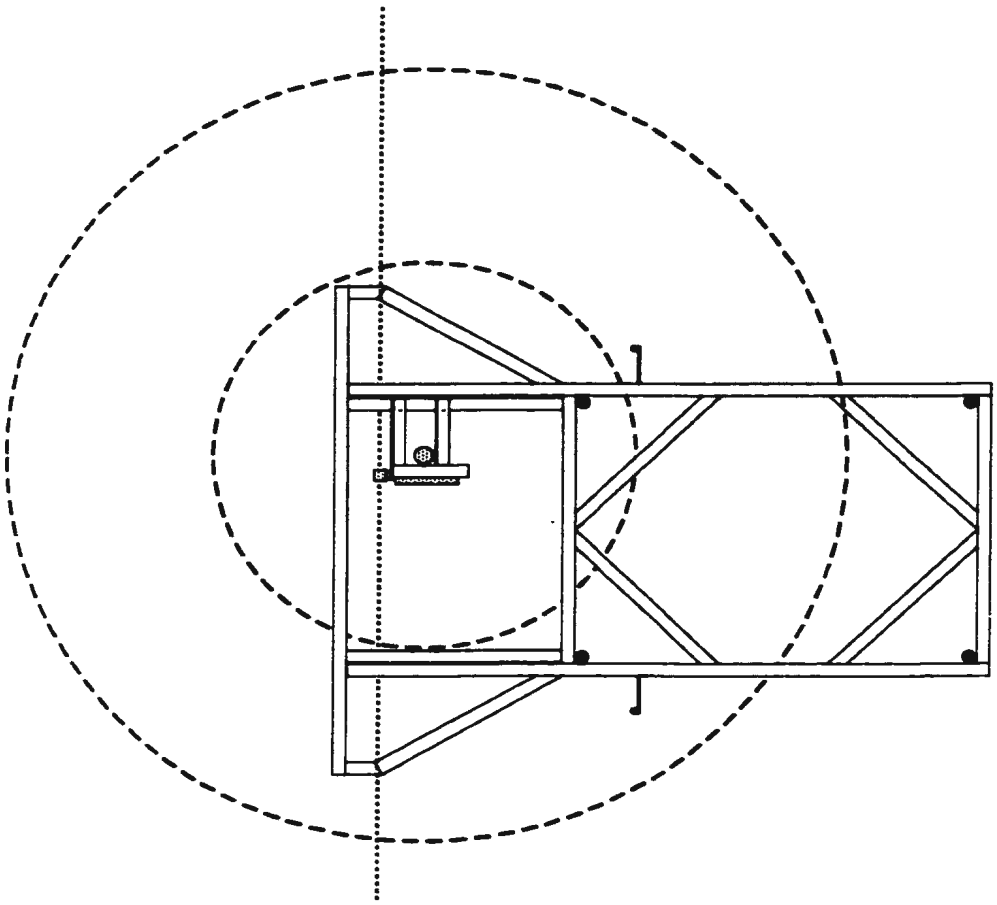

Figure 2.3: Plan view of the instrument frame, showing pencil-beam and fan-beam sonars (shaded). The dashed circles are at 1 m radius intervals centered on the fan-beam. Dotted line is the intersection of the pencil-beam with the bottom.

the primary bar, in roughly 2 m mean water depth about 60 m from the shoreline. The tidal range at the site was typically 1 m maximum during the experiment; thus, the instruments and the bed were not exposed at low tide, therefore permitting continuous observation of seabed response throughout the tidal cycle.

2.2 Instrumentation

The sensors were mounted on a frame supported by four 5 cm diameter, 6 m long posts jetted approximately 4.5 m into the sand. A schematic diagram showing the plan view of the frame and the location of the acoustic sensors is shown in Figure 2.3. The frame was a cantilever design so as to reduce any frame-induced disturbance of the bed immediately beneath the sensors. The cantilevered instrument support faced in the upstream direction for the anticipated southward flow of the longshore current produced by northeast winds during October storms.

Marsh-McBirney electromagnetic current meters (EM) were used to measure both the cross-shore and longshore components of the fluid velocity. Bottom pressure sensors were used to measure the tidal fluctuations and incident wave heights.

Four EM's and one bottom pressure transducer were mounted on the cantilevered support on both the seaward and shoreward sides of the frame to measure the waves and currents. The four flowmeters, their locations on the frame and deployment depths above the bottom are shown in Table 2.1. The pressure case housing the electronics for supplying power, sampling the point sensors and transmitting data to the shore over hard wired cable links was mounted on the main part of the frame between the four posts.

Two types of acoustic sounders were used to image the bedforms on the seabed, namely the rotary fan-beam sidescan sonar and the rotary pencil-beam sonar. Both acoustic sounders were operated at 2.25 MHz. Each was equipped with a rotary transducer mount driven by a step motor (0.225 degree step increments). The acoustic images from both imaging methods were acquired digitally on a PC based system, and were sampled at 250 KHz. Fan-beam and pencil-beam data runs were typically collected at half hour intervals.

Table 2.1: Marsh-McBirney electromagnetic current meters used during DUCK94 experiment. Also listed are the flowmeter locations on the frame, deployment height above the bottom and an example of averaged cross-shore rms velocity as measured by the four flowmeters.

Flowmeter	Location	Height (cm)	u_{rms} (cm/s)
EM849	Bottom Landward	35	32.9
EM1320	Top Landward	60	22.9
EM1301	Top Seaward	60	23.0
EM884	Bottom Seaward	35	27.2

The range resolution of the image data was close to 1 cm, corresponding to a 10 μs transmitted pulse length, and 3-sample block average of the raw data before storage. The backscatter returns from 4 consecutive transmissions (pings) were also averaged in order to reduce noise levels. The azimuthal resolution of the stored images was 0.9 degrees. The time to acquire a single image was 37 seconds, and the typical sampling protocol was to acquire 5 consecutive images every 20 or 30 minutes.

2.3 DUCK94 Hydrodynamics

The deep-water incident wave conditions were measured by an FRF-operated instrument array located in 8 m water depth. Figure 2.4 shows the deep water significant wave heights (H_o), wave incident angles (θ_o) and peak periods of incident waves (T_p). Two storms occurred during the period of the DUCK94 experiment, the first storm between Yeardays 276-279 during which up to 2.5 m significant wave heights were produced, while the second storm started on Yearday 283, producing up to 3.5 m wave heights.

Routine collection of the rotary sonar and EM data commenced on Yearday 276 and continued until Yearday 289. Figure 2.5 shows the 30-minute averaged cross-shore mean velocity (U), positive onshore, alongshore mean velocity (V), positive southward, and shore normal rms wave-orbital velocity (u_{rms}), as measured by all four flowmeters on the frame and sampled at 10 Hz.

The measured velocities show strong semi-diurnal modulation. Mean cross-shore velocity was mostly directed offshore throughout the duration of DUCK94 experiment as shown in Figure 2.5. It is important to note here that the offshore directed mean cross-shore velocity was consistently recorded by all four current meters on the frame. In general the mean cross-shore velocities were relatively weaker between Yeardays 277-283 (5 to 10 cm/s) compared to Yeardays 283-288 when the currents became considerably stronger. Two stages can be distinguished during the second storm. The first stage is during the onset of the second storm between Yearday 283 and the first half of Yearday 287 when a mean cross-shore flow of about 5 to 20 cm/s offshore corresponding to 2 m significant wave height was measured. The second stage starts when the second storm intensified between the second half of Yearday 287 and Yearday 288, reaching a significant wave height of 3 m and mean cross-shore velocity of 20 to 30 cm/s offshore. As will be shown later, this brief increase in mean cross-shore velocity had an interesting effect on the migration of lunate megaripples.

Mean longshore current velocity was weak (0 to 20 cm/s) and directed southwards between Yearday 278-283. The direction of mean longshore current during this period was consistent with the NE angles of incidence of deep water waves. During the onset of the second storm (Yearday 283) the mean longshore velocity increased sharply from 0-20 cm/s up to 50 cm/s southwards, then decreased slowly, changing direction to northwards between Yeardays 287 and 288.

The rms wave-orbital velocities were in general much stronger than the measured mean cross-shore velocities, for example u_{rms} ranged from 15 to 40 cm/s between Yeardays 277-283 and from 20 to 50 cm/s between Yeardays 283-288. The averaged u_{rms} values as measured by the 4 flowmeters for the duration of Duck94 experiment are shown in Table 2.1. Comparison between the velocity measurements by each flowmeter as shown by Figure A.1 in Appendix shows that 3 of the flowmeters, EM1320, EM849 and EM1301, had gain problems. EM 1320 and 1301 had longer time constant electronics resulting in reduced variance (or gain). EM 849 had a different offset from the other 3 EM's. The bottom seaward flowmeter (EM884), positioned at a nominal height of 35 cm above the

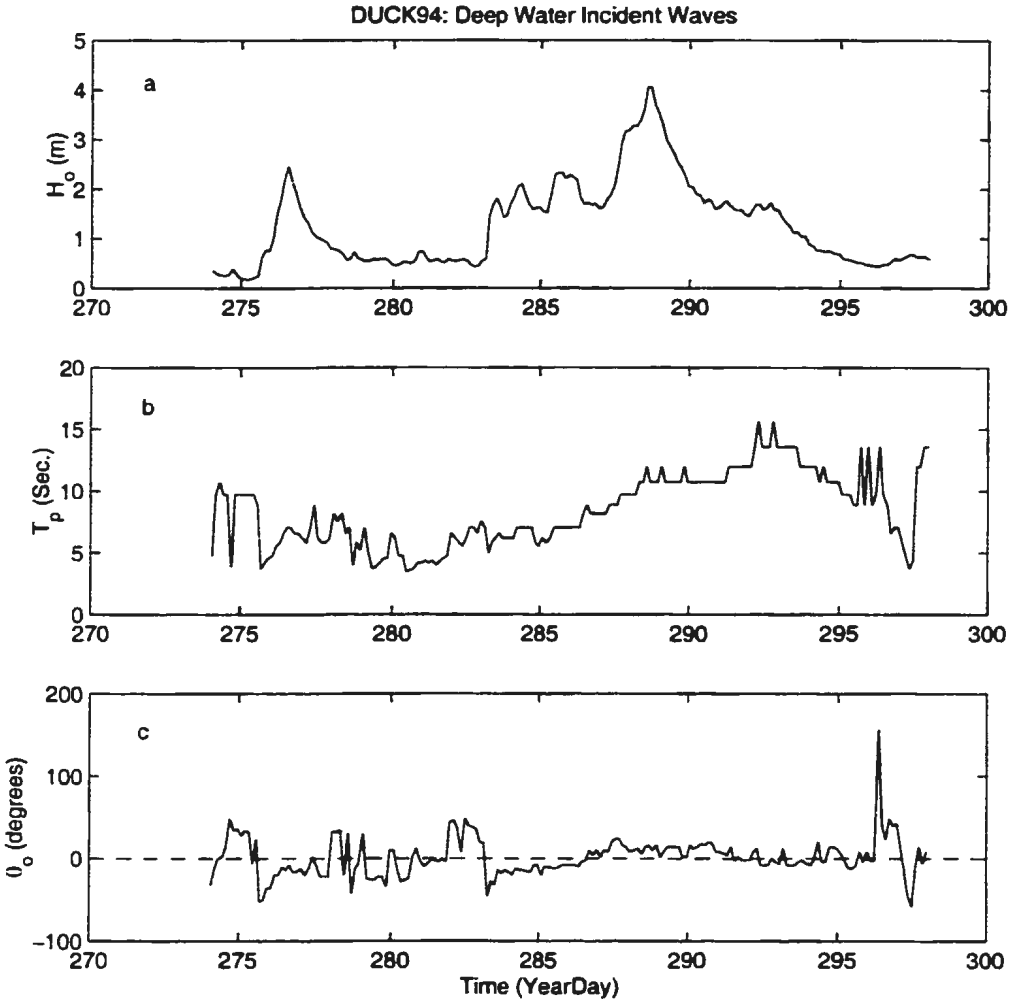

Figure 2.4: Deep water incident wave conditions including (a) the significant wave heights H_o, (b) peak periods of incident waves T_p and (c) deep water wave angles of incidence θ_o as measured by the FRF at 8 m array, where 0° is shore-normal while positive and negative angles refers to Northeast and Southeast incident wave angles respectively.

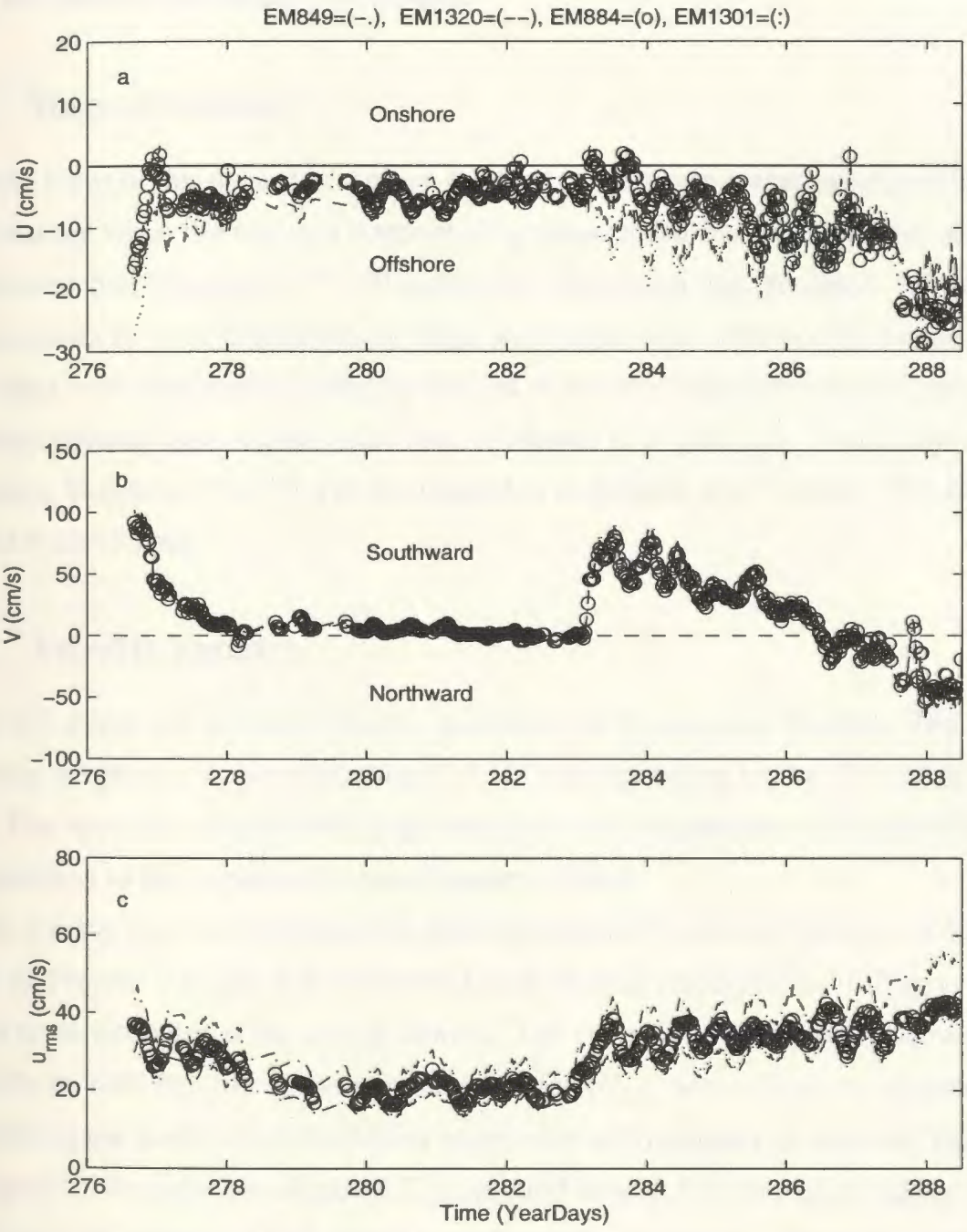

Figure 2.5: Time series of mean cross-shore current velocity (a), mean alongshore current velocity (b) and rms wave-orbital velocity (c) as measured by all the current meters on the frame during the whole period of DUCK94 experiment.

bottom, seems to have been less affected. EM884 velocity data were therefore used for the rest of the analysis presented in this thesis.

2.3.1 Days of interest

The main focus of this thesis is the cross-shore oriented lunate megaripples, and the periods of interest are when the bed was dominated by these bedforms. Examination of fan-beam data showed that Yeardays 277-279 during the first storm and Yeardays 286-288 during the second storm were dominated by large scale cross-shore oriented lunate megaripples. These days were also characterized by periods of weaker longshore currents and moderate rms shore normal wave-orbital velocities, as shown in Figure 2.6. From here onward in this thesis, Yeardays 277-279 will be referred to as Storm1 and Yeardays 286-288 will be referred to as Storm2.

2.3.2 Velocity Spectra

Figure 2.7 shows the average velocity spectrum for Storm1 and Storm2. The dominant frequency of gravity waves was about 0.1 Hz corresponding to the 10 s peak wave periods. The spectrum also showed high energy in low frequencies of about 0.02-0.03 Hz corresponding to the infragravity wave frequency band.

The gravity wave and infragravity wave power spectra for all the days of interest are shown in Figures 2.8 and 2.9 for Storm1 and Storm2 respectively. Infragravity waves seemed to be strongest at the end of Storm2. The typical frequency of infragravity waves seemed to be 0.02 Hz. Infragravity wave velocities (U_{ifg}) were therefore separated by low pass filtering the wave-orbital velocities using a cut-off frequency of 0.01 Hz. Figure 2.10a and Figure 2.10b show the obtained U_{ifg}, plotted here as the root-mean square departure from 30 minutes mean for both Storm1 and Storm2 respectively. The magnitude of cross-shore infragravity wave velocity ranged from 5-20 cm/s.

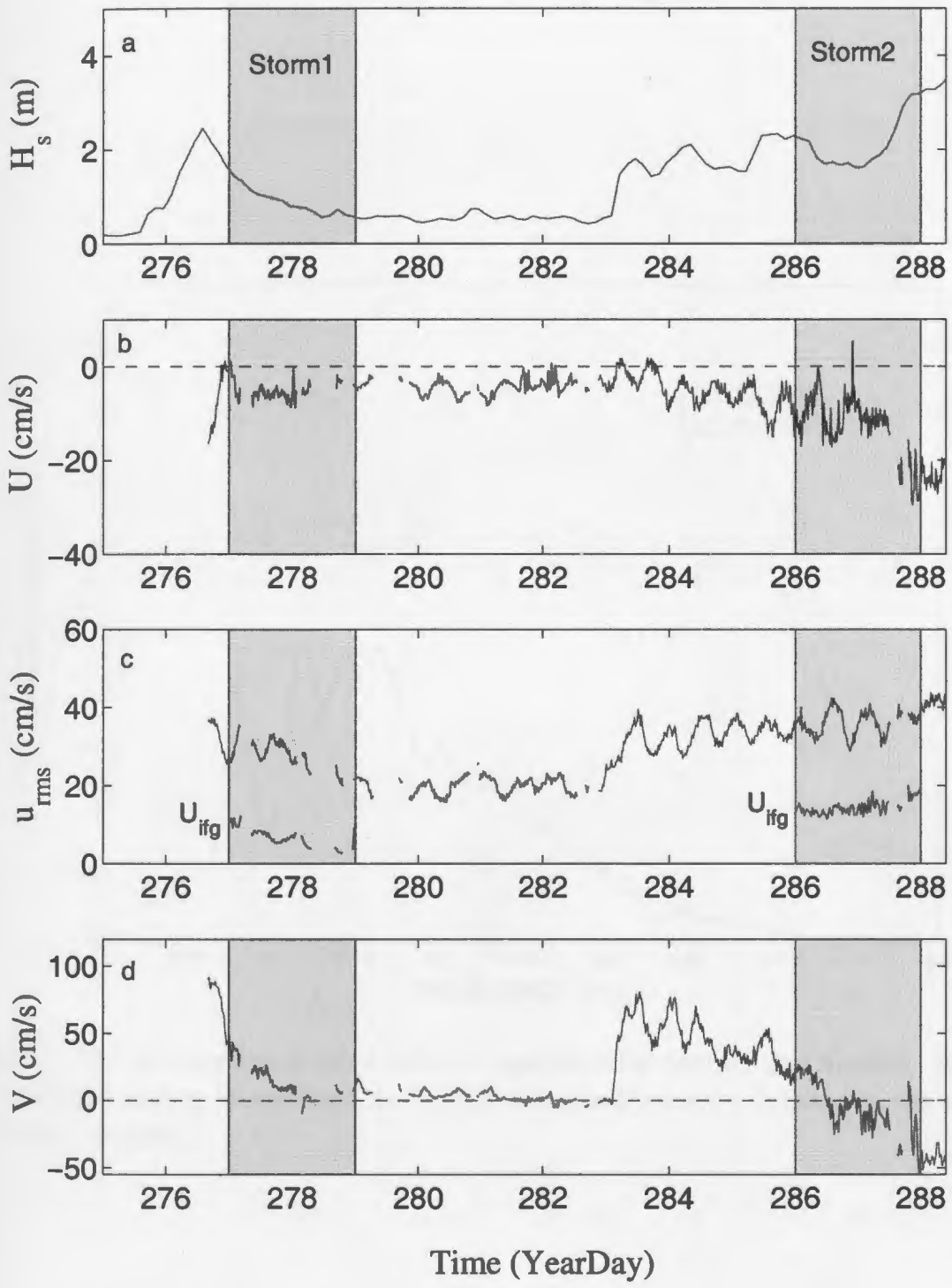

Figure 2.6: Hydrodynamic conditions at the frame location: significant wave height, H_s (a), mean cross-shore velocity, U (b), rms wave-orbital velocity, u_{rms} (c) and mean longshore velocity, V (d). U is positive onshore; V positive southward. The days dominated by cross-shore oriented lunate megaripples during Storm1 and Storm2 are shaded.

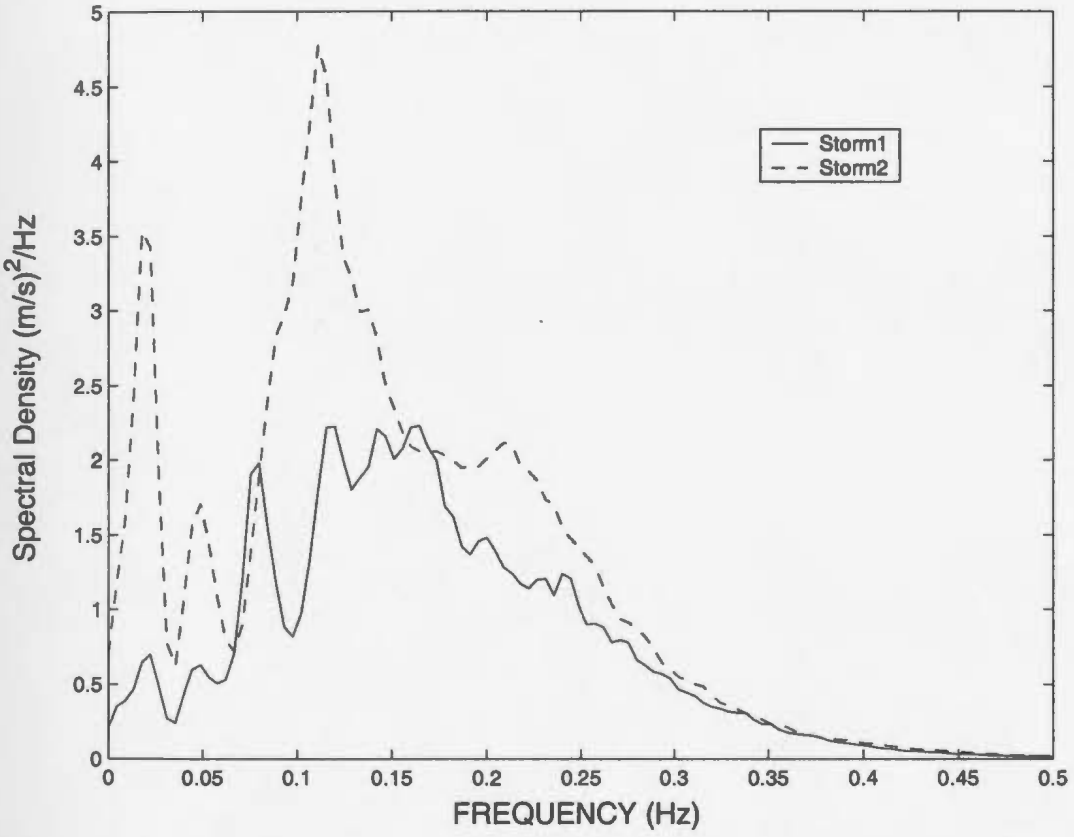

Figure 2.7: The average cross-shore velocity spectrum for Storm1 and Storm2. Note the higher energies during Storm2,and the higher infragravity energy, relative to the incident band, during Storm2.

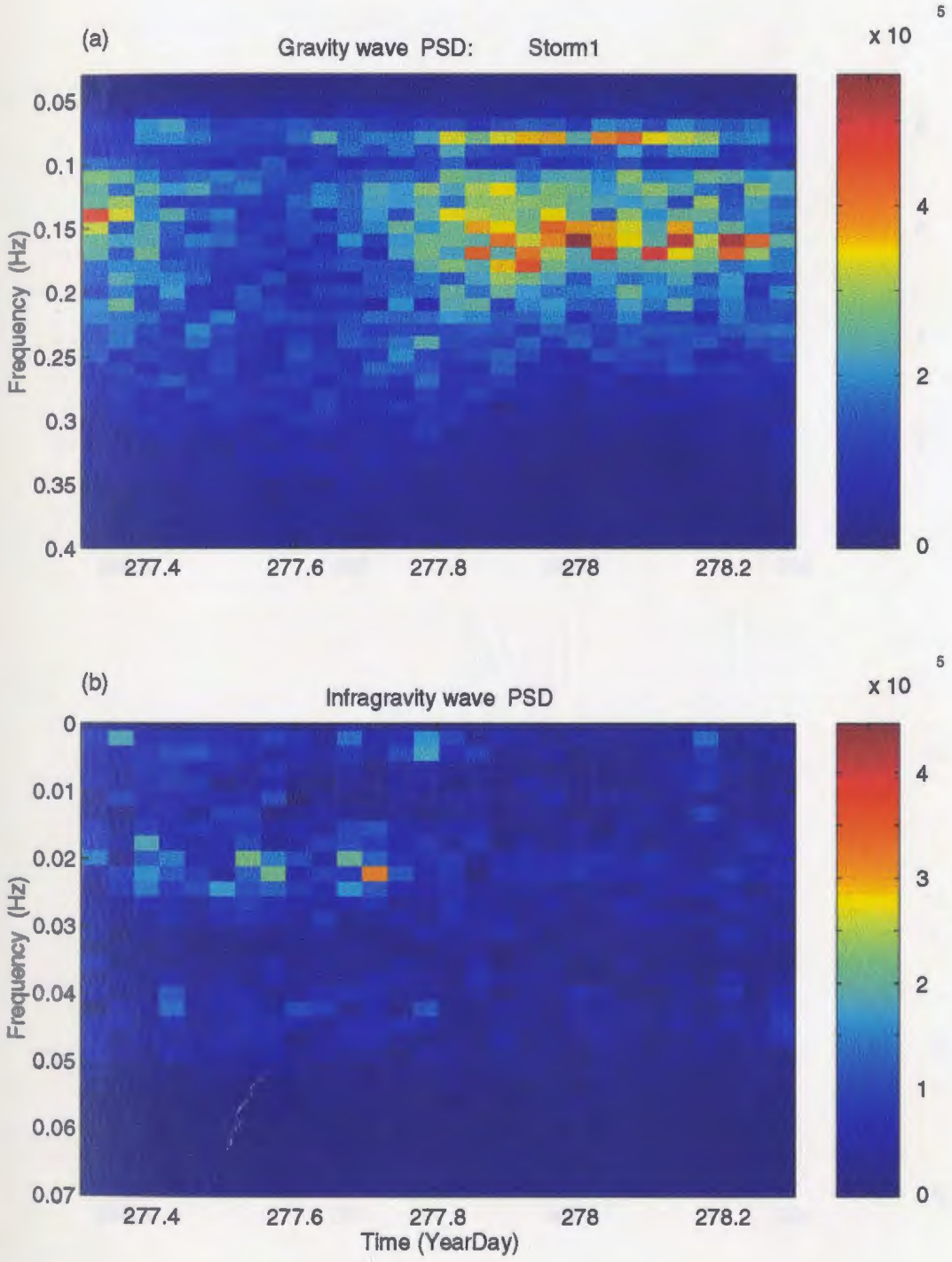

Figure 2.8: 3D wave power spectral density for gravity waves (a) and infragravity waves (b) during Storm1.

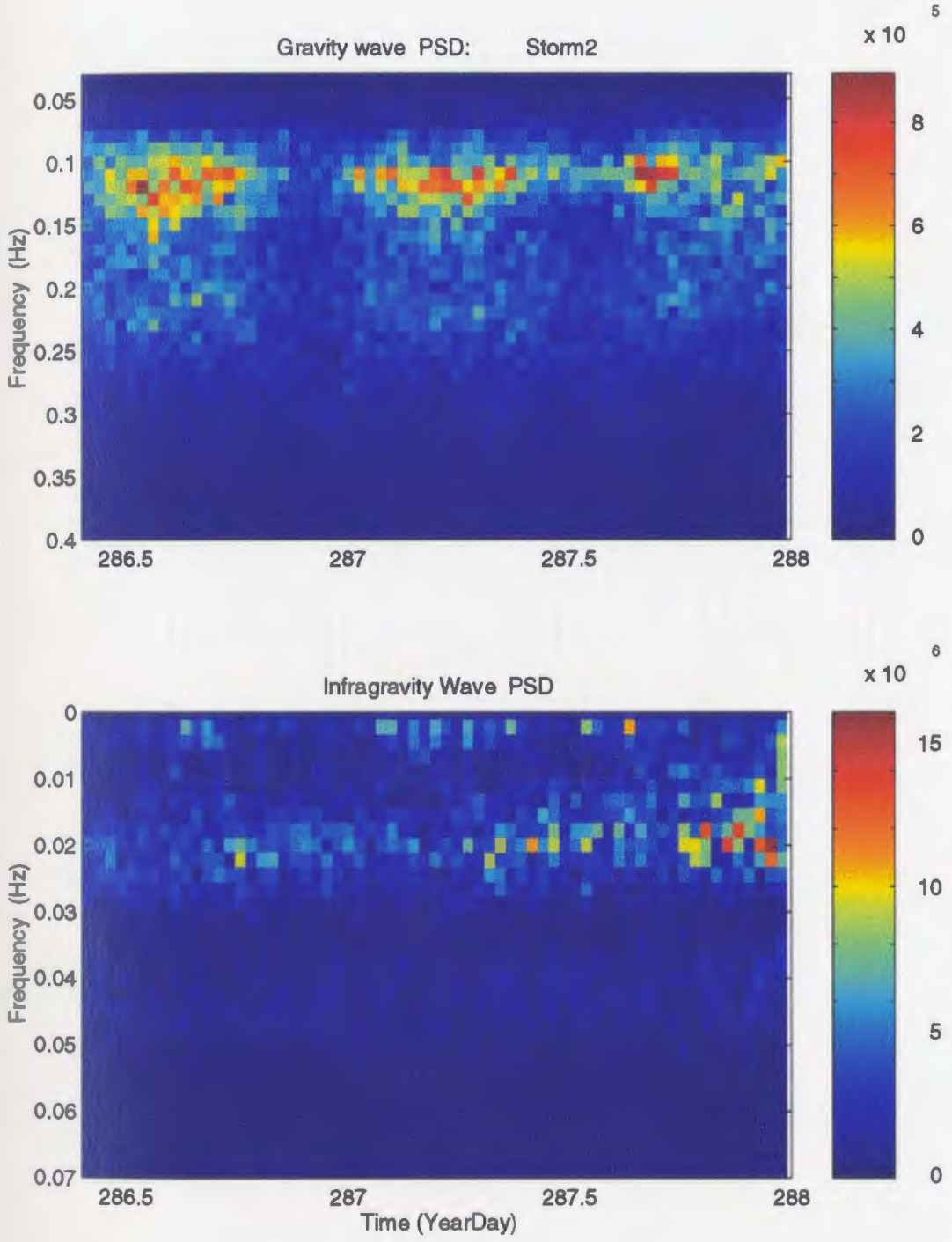

Figure 2.9: 3D wave power spectral density for gravity waves (a) and infragravity waves (b) during Storm2.

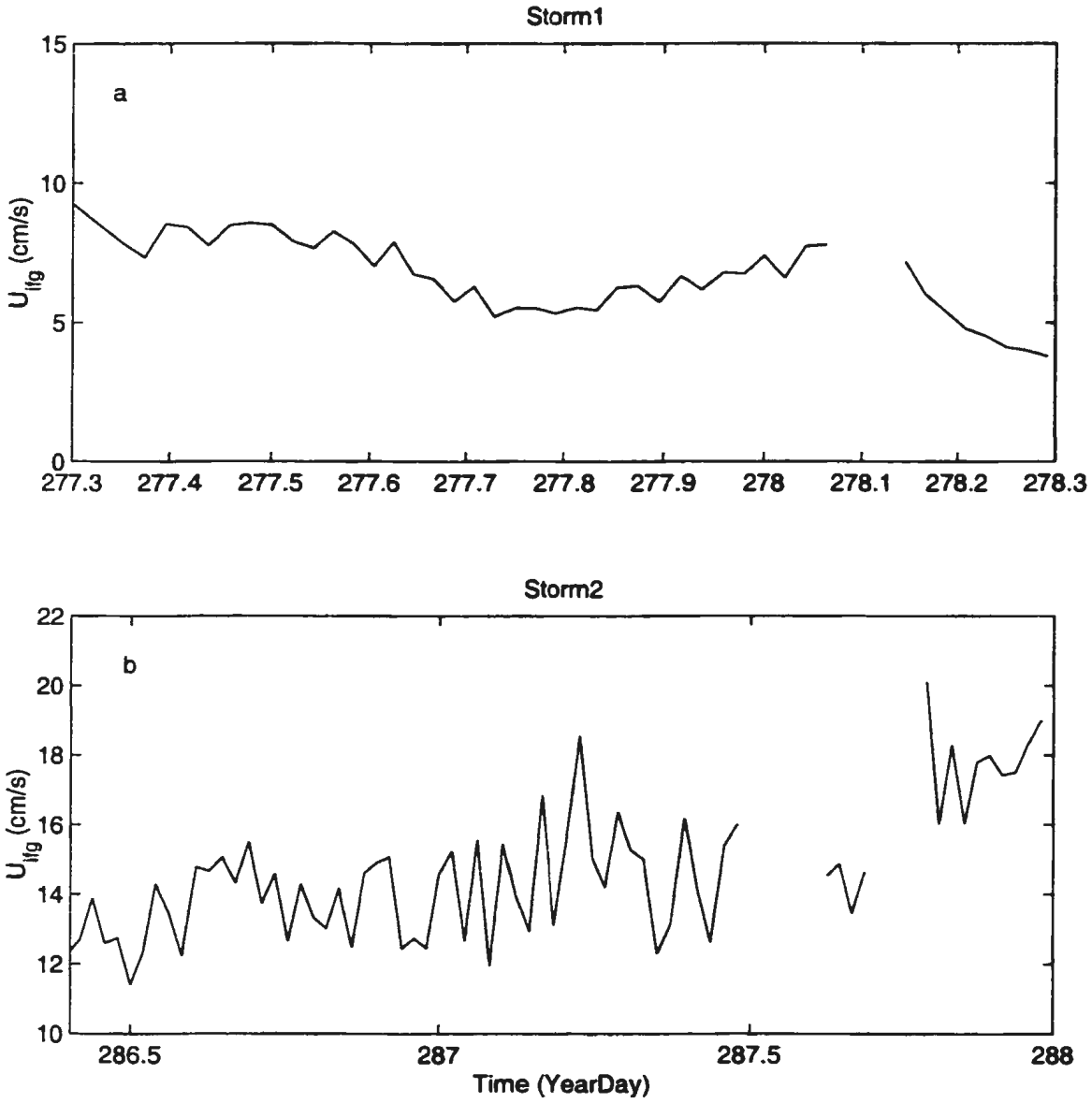

Figure 2.10: Half hour averaged root-mean square of cross-shore infragravity wave velocities for Storm1 (a) and Storm2 (b).

2.4 Rotary sonar data

2.4.1 Fan-beam images

The fan-beam rotated about a vertical axis and used a fan shaped beam to scan the bottom. The fan-beam width in the far field was nominally 0.9 degrees in the horizontal, and 30 degrees in the vertical. The echo, which takes some period of time to return as the fan-beam interacts with the bottom, was then mapped onto a video display. The echo return strength was represented by a grey color and the time (or slant range) of a particular return was represented as a position along a radial line on the display.

As the fan-beam rotates, the lines of varying signal level are plotted radially on the display. The result is a sonar image of a particular area, providing a 2-D plan-view picture of the bed with recognizable sizes, shapes and surface reflecting characteristics of the bedforms. Figure 2.11 shows a typical rotary fan-beam sidescan sonar image, clearly showing 2-D patterns of cross-shore oriented lunate megaripples.

The rotary fan-beam sidescan sonar was positioned about 1 m above the bottom. This height varied slightly with time depending on the bedform migration and the general erosion and accretion processes below the transducer. The transducer head was oriented in such a way that up to a 10-m-diameter image was produced. Because of the angle of inclination of the transducer head with respect to the horizontal, and the general distribution pattern of the transmitted sound lobes, features within the 1 m radius ring were not imaged (white central area in Figure 2.11.

All fan-beam images were plotted in such a way that the offshore is always at the top while the onshore direction is at the bottom of the images. The darker shades of grey in fan-beam images represent higher amplitudes of the acoustic signal. Figure 2.11 shows an example of cross-shore oriented lunate megaripples with a size of about 1 m, measured from horn-to-horn. The dark grey concave-shoreward features seaward of the sensor are the crests and the avalanche faces of megaripples while the white and light grey zones containing smaller scale ripples, are the megaripple troughs. In contrast, the crescentic patches onshore are areas of acoustic shadow cast by the avalanche faces over the troughs

while the grey zones are the stoss sides.

Also seen on the right hand side of some images is a thin shadow trending on-offshore. This is produced by the electrical cables. The cables are not visible in all images, as they were eventually buried. Variations in background grey tone are present intermittently in fan-beam images; these are produced by attenuation and/or scattering from bubble clouds produced by breaking waves, and by suspension events associated with individual waves. Because the acquisition time of the images was roughly 6 wave periods, the contamination from disturbances produced by individual waves typically occupies a sector of 60° or less on these 360° images.

2.4.2 Pencil-beam images

The second type of sonar was a profiling pencil-beam sonar characterized by a narrow pencil shaped beam. Its beam width in the far field was nominally 2°. The profiling sonar rotated about a horizontal axis parallel to the shoreline, providing a 2-D shore-normal bed profile across the image area of the fan-beam transducer. There was a 5 minute time difference between the acquisition of pairs of pencil-beam and fan-beam images.

The pencil-beam transducer was positioned about 1 m above the bottom. The transducer head was also located about 22 cm below and 30 cm to the left of the fan-beam transducer head, and 15 cm closer to the shore (Figure 2.3). A typical averaged pencil-beam image is shown in Figure 2.12; megaripple relief is clearly resolved. The images are plotted relative to the plane of the frame with the seaward direction always to the left. The bed is shown in the pencil-beam images as a solid black echo, except when shadowed by a bedform crest, which created gaps in the bottom profiles. Pencil-beam images gave about 10-m-long cross-shore bed profiles. At about 2 m radius from the center and beyond, the bottom profile is jagged because of the 0.9° angular resolution.

The increasing width of the bottom echo with range is due to the increase in the projected area of the beam intersecting the bottom as the angle of incidence increases with range. Comparing the bed profiles to the corresponding fan-beam images in the regions beyond 1 m distance from the center, one can clearly see a one-to-one correspondence

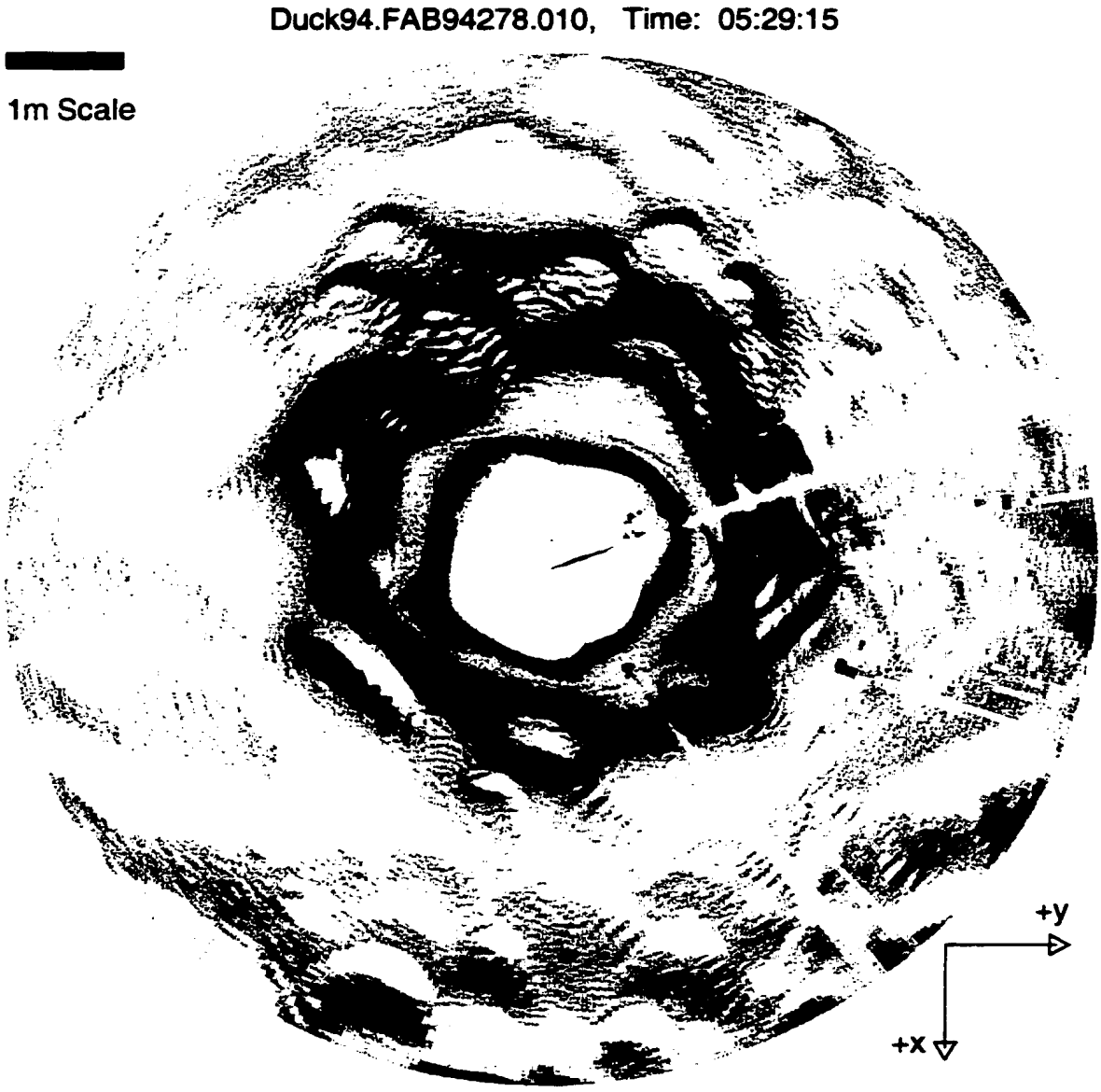

Figure 2.11: Typical rotary fan-beam sidescan sonar image showing the patterns of cross-shore oriented lunate megaripples where positive x is onshore and positive y is southward, shore-parallel. The white, and light grey zones are areas of acoustic shadow. The orientation of the steep faces of the megaripples and crescentic shapes indicate inshore migration. The acoustically bright structures seen to the right of the image are from the 4 posts supporting the frame, and from the flowmeter heads and their cantilever supports. The two closely-spaced dark spots on the extreme right are anchor posts for the cable line.

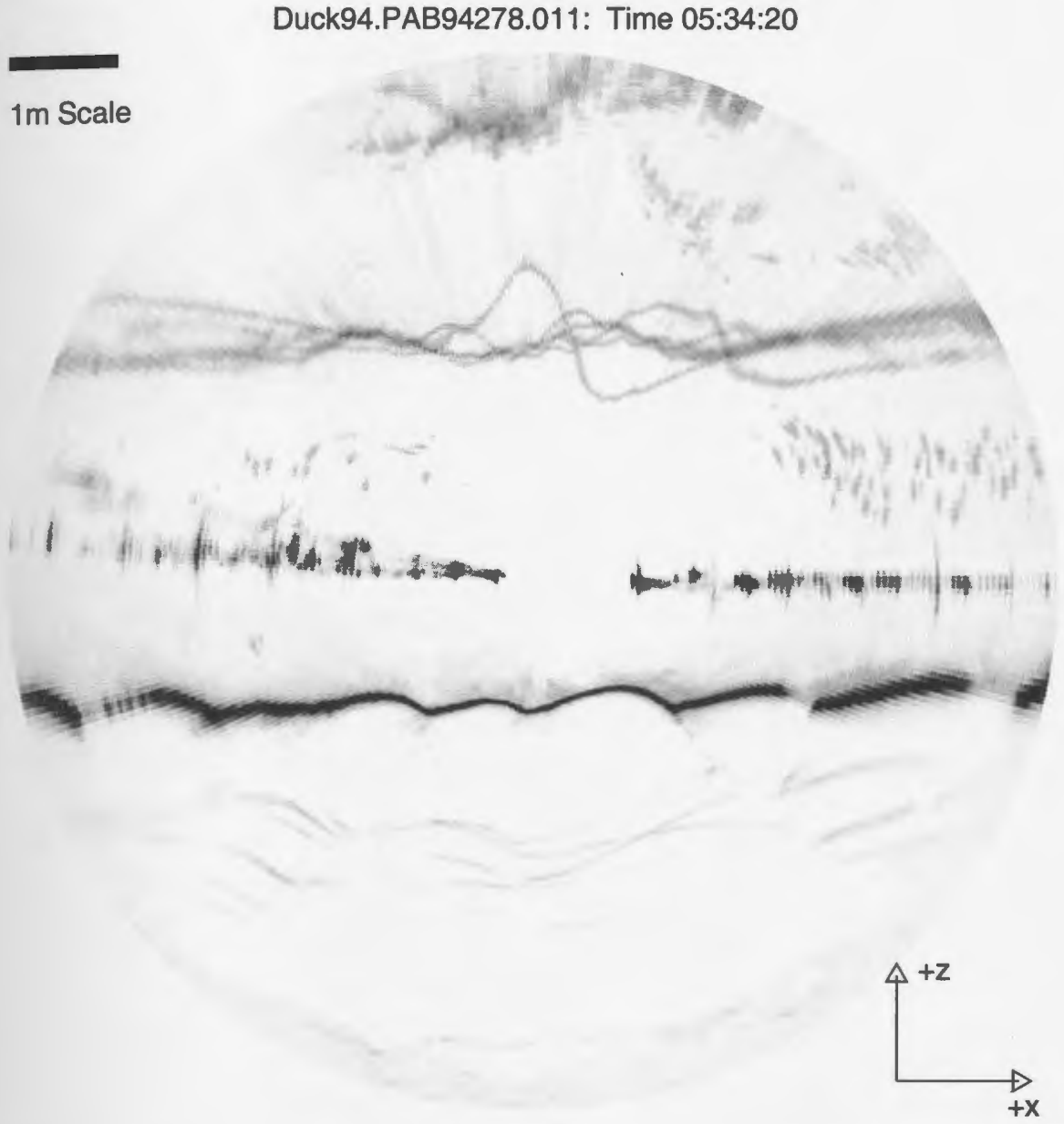

Figure 2.12: Typical rotary pencil-beam sonar image showing the cross-shore bed profile where positive x is onshore and positive z is vertical elevation. The bed is the solid echo, except where shadowed by megaripple crests which create gaps on the bottom profile. The structures below and above the solid echo are due to multiple reflections and reflections from frame posts, respectively. Waves propagating at the sea surface can also be seen at the top. At about 2 m radius distance from the center and beyond, the bottom profile is jagged because of the 0.9^{o} angular resolution at longer ranges.

between megaripple features in the planform (fan-beam) and in the vertical slice (pencil-beam) images.

2.4.3 Image processing

Both fan-beam and pencil-beam images were typically acquired in a radial coordinate system. In order to facilitate calculations, the radial images were converted into rectangular coordinates consisting of pixels of equal size. Various image processing techniques were also applied to the raw fan-beam and pencil-beam images before computing the migration velocities or obtaining the geometrical characteristics of the bedforms.

In order to reduce noise in these images a number of successively collected images was averaged. Thus, in addition to the 4-ping and 3-sample block averaging mentioned earlier, 5 consecutive images acquired at 37 second intervals were averaged to further reduce noise. This both reinforced the bottom echo and filtered out the random contributions from bubbles, sediment plumes and any other transient objects.

1-D and 2-D digital filters were applied to filter the bed profiles and fan-beam images respectively, before computing migration velocities. This was done to facilitate comparison of the estimated migration velocities using bed profiles and fan-beam methods at the same spatial frequencies. Similar filter characteristics were applied to the bed profiles and fan-beam images. The basic idea was to remove the high frequency structures, while retaining sufficient resolution of some small-scale bedforms (3 to 5 cycles per meter in bed profiles).

The filtered fan-beam images were also corrected for slant-range assuming a horizontal bed, in order to remove the geometric distortion caused by the elevation of the fan-beam transducer.

2.5 Reconstruction of bed profiles

The method used for reconstructing bed profiles from the rotary pencil-beam images was to determine the bottom positions by locating the position of maximum backscatter in the pencil-beam images. The maximum backscatter method was not only simple to use but

also robust, as it improved the resolution of the profiles at locations far away from the transducer.

Figure 2.13 shows the bed profile obtained from a typical pencil-beam image using the maximum backscatter method, and the bottom echo on the pencil-beam image. Increased noise is evident at distances beyond 2 m radius. Bed profiles were therefore filtered to remove these noise and any other high frequency structures as shown in Figure 2.13b.

2.6 Measurement of cross-shore migration velocities

Both fan-beam and pencil-beam images were typically acquired each half-hour. Using the series of time-separated fan-beam images and bed profiles, the migration of large scale features like lunate megaripples could be observed. Two independent methods were used to measure quantitatively the migration velocities. The first method used the fan-beam images and the second method used the pencil-beam bed profiles.

The first method used 2-D cross-correlation of pairs of averaged and filtered fan-beam sub-images typically separated by one hour. These fan-beam sub-images contained the selected individual megaripples within rectangular sub-images centered at the same position and entirely contained within the outer or inner boundaries of the fan-beam images. The size of the rectangular grids was small enough to analyse only the migration velocities of individual megaripples. Furthermore, in order to be able to compare the migration velocities estimated from bed profiles and those obtained from fan-beam images, the fan-beam rectangular grids were selected along the line where the pencil-beam intersected the fan-beam images. This cross-shore line was located 30 cm to the left of the center of fan-beam images, since the pencil-beam transducer head was located 30 cm to the left of the fan-beam transducer head.

The size of the rectangular grid in the second (1-hour separated set) image of each pair was made larger by twice the number of lags (distance) used, for both rows and columns, in order to minimize edge effects. The rectangular grids were also selected from the offshore sides of fan-beam images only, because the megaripple slip faces used in determining

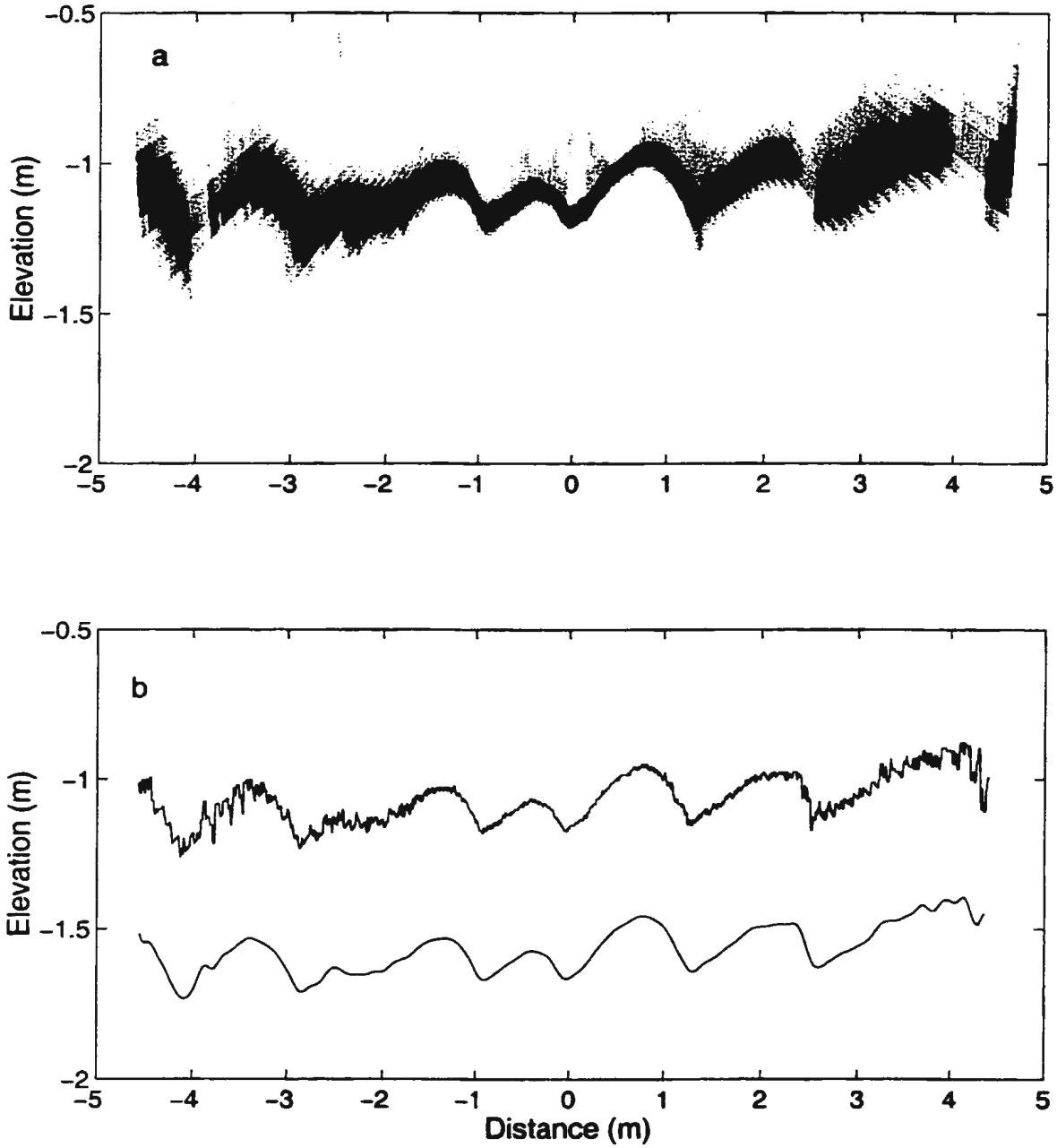

Figure 2.13: Lower portion of a pencil-beam image transformed into rectangular coordinates (a) and the corresponding reconstructed bed profile (b) based on the maximum backscatter method (solid line). Also shown in (b) is the low-pass filtered bed profile, offset by -0.5 m.

the migration velocities were most clearly imaged offshore rather than onshore of the transducer. This is due to the fact that the slip faces of the megaripples faced onshore, producing stronger acoustic returns than the slip faces of more landward bedforms that were in the shadow zone.

The 2-D cross-correlation analysis was performed on a rectangular domain where fan-beam images consisted of rectangular pixels of equal size. The migration velocities were evaluated at the peak of the 2-D cross-correlation function. The advantage of this method is that it provides both cross-shore and alongshore migration velocities simultaneously.

The second method used an ordinary 1-D cross-correlation analysis of pairs of bed profiles separated by one hour. Due to the fact that only the cross-shore bed profiles were measured during the Duck94 experiment, only the cross-shore megaripple migration velocities could be obtained using this method. The lagged cross-correlation of filtered and detrended bed profile pairs was then computed. The results were then recast as megaripple migration velocities.

Due to the nature of the pencil-beam sonar imaging technique, some parts of the bed profiles located in shadow zones of the acoustic beam could not be imaged. These gaps were not included in the calculation of migration velocities using this method. Because of this, although up to 10 m of bed profiles were produced by pencil-beam images, only parts of each profile (up to 7 m) could actually be used in the cross-correlation analysis for estimating the migration velocities.

Hay and Bowen (1998) explained in detail the resolution limits associated with the estimated migration velocities using the above methods. The minimum possible resolution in the measured migration velocities is due to the resolution limit of the pencil-beam and fan-beam images, which is fixed. In the case of pencil-beam images, the range resolution was close to 1 cm, corresponding to a $10\mu s$ transmitted pulse length and 3-sample block averaging of the raw data before storage. Bed profiles separated by one hour were used to obtain the migration velocities. Thus, the resolution limit for pencil-beam estimated migration velocities due to the range resolution of pencil-beam images alone is 0.01 m/h.

In the case of fan-beam images, the slant-range-corrected fan-beam images were constructed of pixels 1.8 cm on a side. Fan-beam images separated by one hour were also used in estimating the migration velocities. Thus, the resolution limit for fan-beam estimated migration velocities due to the resolution of fan-beam images alone is roughly 0.02 m/h. The resolution limit for fan-beam estimated migration velocities is therefore twice that of pencil-beam estimates.

Another source of error for the estimated migration velocities is noise generated by signal intensity fluctuations and sediment plumes at the bed. This error is reduced by averaging; however, migration rate estimates at higher energies are likely to have a larger error because of this type of noise.

Chapter 3

Patterns and geometrical scales

This chapter summarizes the cross-shore lunate megaripple patterns and their evolution during DUCK94 experiment, lunate megaripple geometrical scales and the characteristic slopes of the avalanche faces. The sea-bed images obtained by rotary fan-beam sidescan sonar provided plan view images which clearly showed the bedform patterns and their evolution. The geometrical scales were estimated from both fan-beam images and bed profiles, while the megaripple slopes were estimated from the bed profiles.

The properties of wave-generated bedforms depend upon the magnitude of the Shields bottom stress parameter (Nielsen, 1981), which is a dimensionless bed shear stress given by the ratio of the bed shear stress to the product of the specific weight (immersed weight) of the grain and its diameter. An increase in Shields bottom stress parameter indicates either an increase in flow velocity and shear stress or a decrease in grain size or density. The lunate megaripples during Storm1 were observed to occur at values of grain roughness Shields parameter ranging between 0.5 and 0.8 (Figure 3.1a). The lunate megaripples for Yeardays 286-288 were mainly observed to occur at values of Shields parameter ranging between 0.75 and 1.4 (Figure 3.1b). As explained earlier, Storm2 Yeardays 286 and 287 were chosen for analysis because they were dominated by cross-shore oriented lunate megaripples. These Yeardays also represented the middle period of the storm, whereas the Storm1 data represent the waning stage of that event.

3.1 Lunate megaripple patterns during Storm1

The fan-beam images collected between 0019h and 1239h on Yearday 277 during the waning stage of Storm1 are shown in Figure 3.2. At 0019h, the field of view consisted of 1-2 m-scale megaripples (marked A) which were arranged en-echelon in the offshore half of the image in Figure 3.2a. The field of view was also dominated by isolated 3-m scale lunate megaripples with horns directed alongshore as shown by the feature marked B in the left quadrant of Figure 3.2a; these structures were migrating southward towards the instrument frame. The longshore current at this time was 45-50 cm/s southwards. (Note that the horn-to-horn span is here taken to be the characteristic measure of the horizontal scale of the megaripples).

The image collected at 1019h on Yearday 277, about 10 hours later, shows that the 3 m-scale features observed earlier were no longer present (Figure 3.2b); the longshore current at this time had diminished to 25-30 cm/s. The 1-2 m-scale megaripples were still present, marked A in Figure 3.2b, now showing a pronounced concave-shoreward orientation. The megaripples at this time seem to have been asymmetrical, with their southward horns being slightly longer than the other horns, indicating the effect of the longshore currents.

The image collected at 1239h on Yearday 277 shows that major changes had occured in terms of the megaripple size, shape and position. A number of meter and sub-meter scale features had developed and dominated the field as shown by features marked C in the offshore half of Figure 3.2c. The 1-2 m-scale cross-shore-oriented feature was still visible (marked A). The sub-meter scale ripple structures seem to be mostly located in the megaripple troughs, with their crests oriented in a shore normal direction, perpendicular to the troughs.

The offshore halves of images in Figure 3.3a-c show a 4-5 m-long shore-parallel but sinuous megaripple (marked A: not the same feature as A in Figure 3.1) with 1-2 m-scale undulations, migrating onshore. Figure 5.3c shows that at 0229h the 1-2 m-scale sinuous megaripple was starting to break up into smaller meter-scale features. The mean longshore current during this time was about 10-15 cm/s.

Another type of bedform was also visible at 2259h on Yearday 277 (Figure 3.3a). These

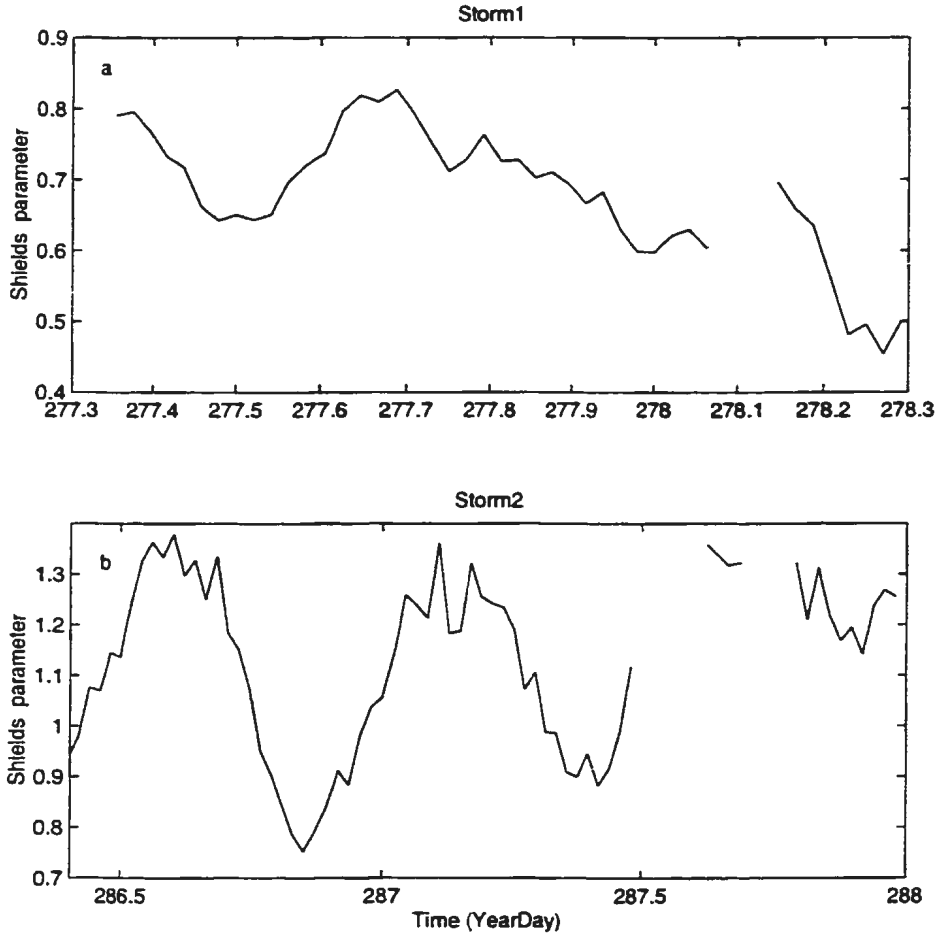

Figure 3.1: Characteristic values of grain roughness Shields parameter for lunate megaripples observed during both Storm1 (a) and Storm2 (b).

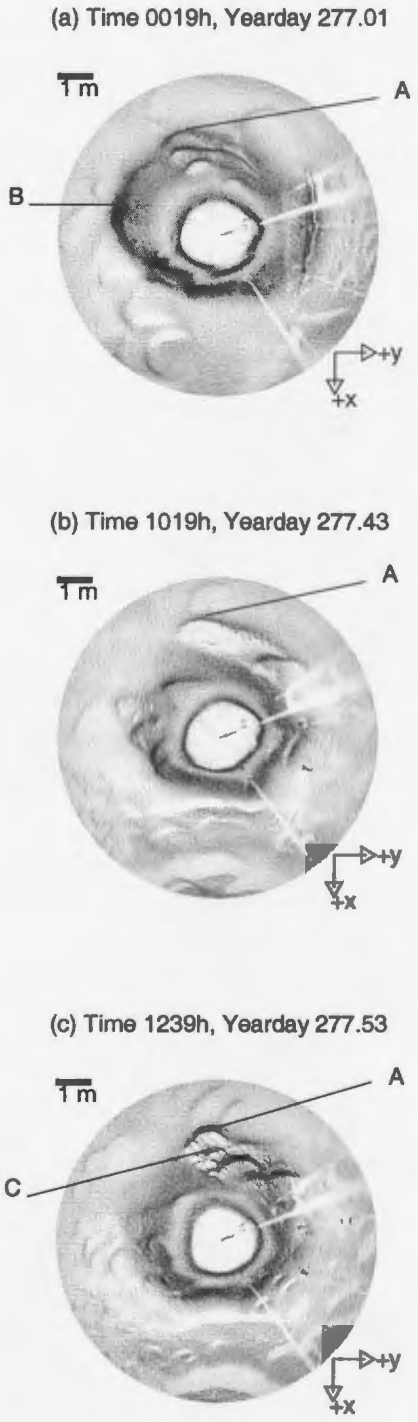

Figure 3.2: Fan-beam images collected between 0019h to 1239h on Yearday 277 during Storm1. Positive x indicate onshore and positive y indicate southward directions.

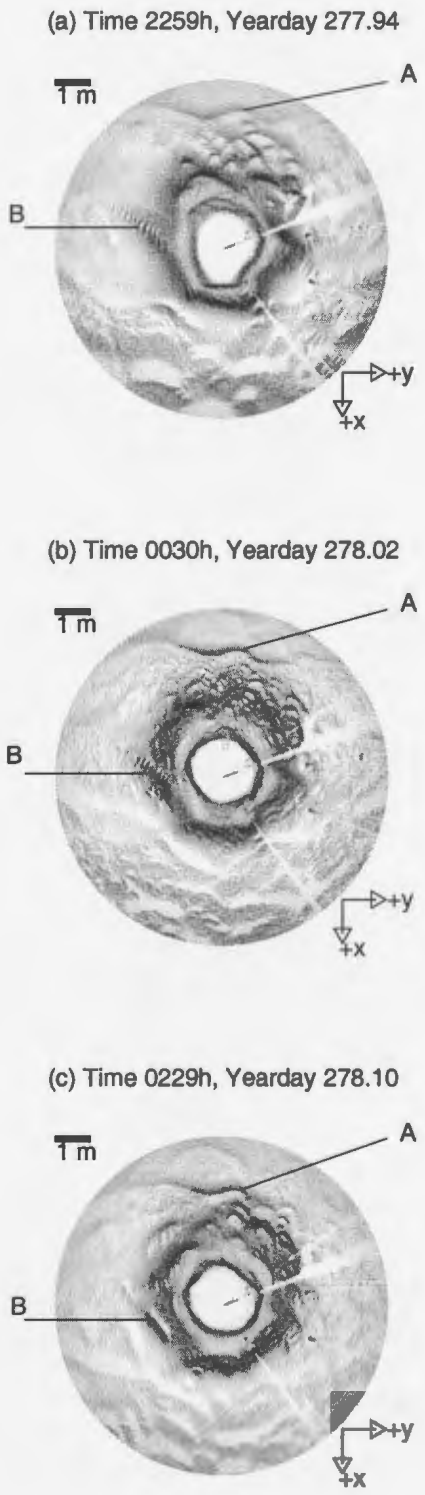

Figure 3.3: Fan-beam images collected between 2259h on Yearday 277 and 0229h on Yearday 278 during Storm1. Positive x indicates onshore and positive y indicates southward directions.

consisted of a narrow train of 20 cm-wavelength ripples which were oriented oblique to the shoreline as shown by feature marked B on the left quadrant of Figure 3.3a. Remnants of the narrow 20 cm-wavelength ripple train were still visible in Figure 3.3b&c A and seems to have migrated onshore while maintaining its form and orientation.

Figure 3.3a-c also show numerous sub-meter-scale lunate features throughout the field. The characteristic scale of these features changed significantly over 0.5-2 hour timescales.

A new group of 1 m-scale megaripples seems to have dominated the field of view in Yearday 278 as shown by features marked A in Figure 3.4a. These megaripples were also migrating onshore. All the sub-meter-scale structures which were observed previously had by now changed into these 1 m-scale megaripples. These megaripples were clearly oriented with their horns directed shoreward. Small scale ripples, marked B in Figure 3.4a, were also superimposed on megaripple troughs. The 1 m-scale megaripple and the superimposed A was still recognisable at 1059h in Figure 3.4b, and had migrated shoreward.

The small scale ripples oriented oblique to the shore were by this time dominant. Some of these ripples had relatively short wavelength as shown by features marked C in Figure 3.4b; others had longer wavelength as shown by features marked D in Figure 3.4b. Many of these ripple trains appear to have issued from megaripple troughs; with the axis of the train roughly perpendicular to the trough and horns.

Images collected at about 1100h onwards on Yearday 278 showed a continued collapse to smaller scales. Larger scale features remained up to 1200h on Yearday 278. However, by 1529h (Figure 3.4c), the dominant form had become sets of narrow trains of oblique, short crested ripples. One set of these ripples is marked C while the other is marked D in Figure 3.4c. The pattern developed by intersection of sets of these ripples is commonly referred to as cross-ripples. The cross-rippled bed state persisted throughout the night of Yearday 278 then gradually became less pronounced until the morning of Yearday 279, nearly 10 to 11 hours later, when all traces of cross-ripples had disappeared, and short-crested, 3-D, irregular ripples became the main type of bedform present. The irregular ripples persisted for the next four days until very early in Yearday 283, immediately preceding Storm2.

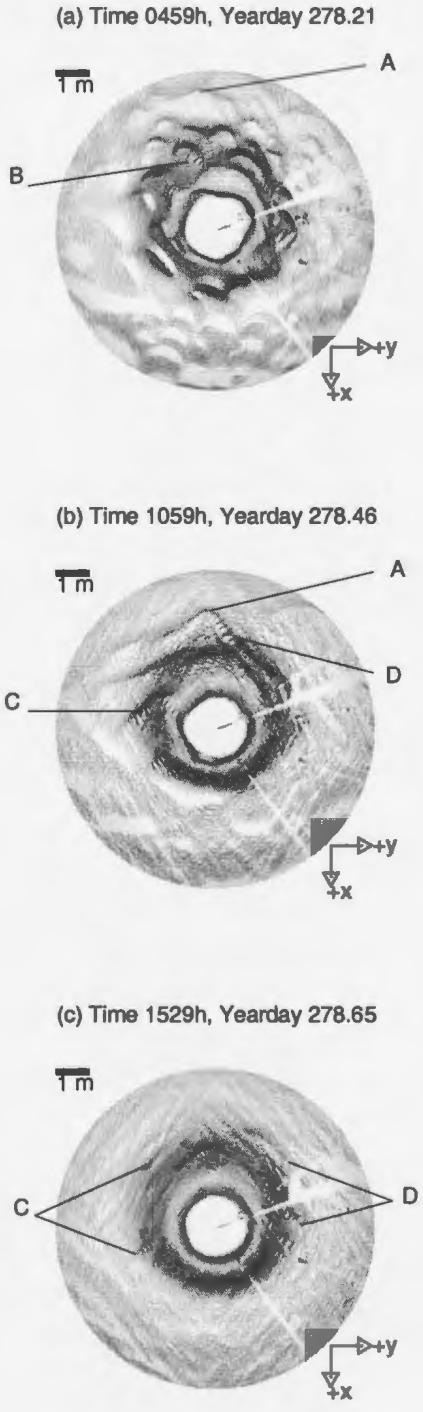

Figure 3.4: Fan-beam images collected between 0459h to 1529h on Yearday 278 during Storm1. Positive x indicates onshore and positive y indicates southward directions.

3.2 Lunate megaripple patterns during Storm2

The quality of some of the fan-beam images collected during this period was affected by strong suspended sediment plumes. As in the waning stage of Storm1, the horns of the lunate megaripples during the onset of Storm2 were mainly facing onshore which was also the direction of megaripple migration.

Figure 3.5a shows the sinuous feature (marked A), partly visible at the top of the image. Another 2-3 m linear feature can be seen at the bottom of Figure 3.5a (marked B).These features were migrating onshore and represent the type of bedform that dominated during Storm2. This period was also characterized by isolated alongshore oriented lunate megaripples remnants of which can still be recognised; for example the ripple train marked C in Figure 3.5a.

Figure 3.5b shows the image collected at 1019h about 4 hours later. Both the sinuous and the linear features (marked A and B respectively) were still present and have migrated onshore. At this time, another group of 1-2 m-scale sinuous features can also be seen onshore of the larger 2-3 m-scale sinuous feature. The ripple train marked C was still present at 1019h (Figure 3.5b).

The group of 2-3 and 1-2 m-scale sinuous features shown in Figure 5.5b seem to have been short lived; they subsequently tended to reorganise into smaller scale features. The image collected on Yearday 286 at 1559h (Figure 3.5c) shows that the group of megaripples in Figure 3.5b had reorganised into 1 m-scale megaripples as shown by a feature marked D in Figure 3.5c.

In summary, the first half of Yearday 287 was dominated by onshore-migrating, cross-shore-oriented lunate megaripples. The bedform state shown in Figure 3.5c persisted until mid-night of Yearday 286 when a new group of onshore-migrating megaripples appeared (Figure 3.6b) as shown by a system of features marked A.

Figure 3.7a-c show another group of 1-2 m-scale megaripples at the top of the image (marked A). These features appeared first at 0739h on Yearday 287. The field of view was also characterized by 3-4 m long sinuous feature (marked B) near the bottom of the images in Figure 3.7a-c. The megaripples marked A and B were all migrating onshore as shown

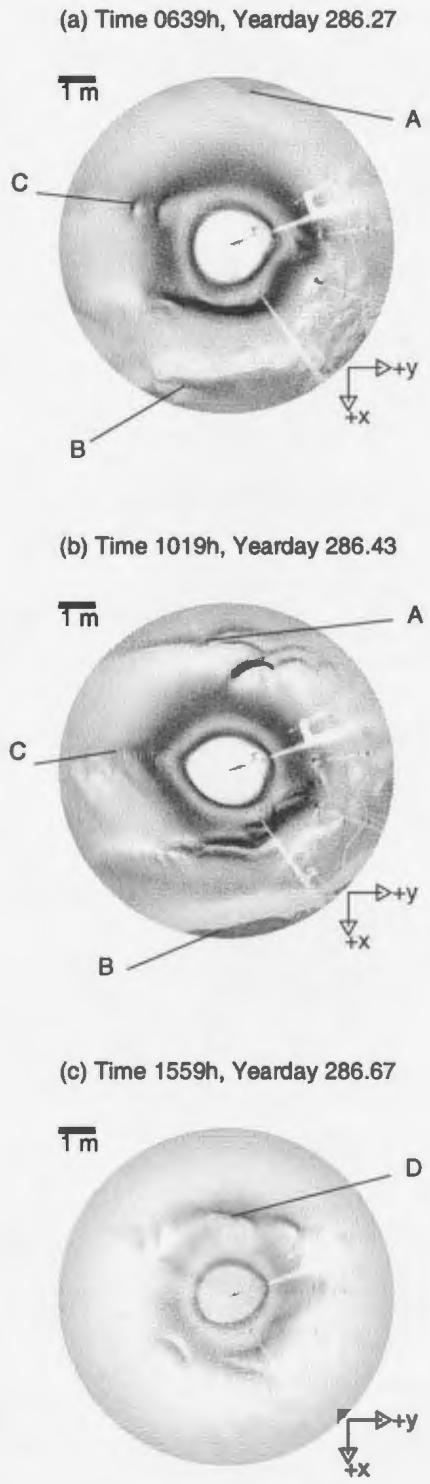

Figure 3.5: Fan-beam images collected between 0634h to 1559h on Yearday 286 during Storm2. Positive x indicates onshore and positive y indicates southward directions.

by their positions in subsequent images in Figure 3.7a-c. Northward longshore flow during Storm2 especially during the second half of Storm2 became increasingly strong, reaching 50 cm/s by 1900h on Yearday 287. Lunate megaripples, during the second half of Storm2 on Yearday 287, were therefore characterized by northward pointing horns.

3.3 Persistence and timescales of change

Lunate megaripples and other bedforms in the nearshore zone do not live forever. They tend to come into existence, migrate for some distance and then either disappear or change into different forms. The evolution of bedforms in general represents a response to the changing fluid forcing. However, in order to understand the complex relationship between the fluid forcing and these responses it may also be important to investigate the timescales of these seabed adjustments.

DUCK94 data show that a range of bedform sizes evolved under different timescales over the period of the two investigated storms. This section gives a summary of the observed timescales of changes for various bedform sizes in the data segment studied for this thesis.

During Storm1, the 1-2 m-scale cross-shore-oriented lunate megaripple with slightly longer right limb (marked A) in the upper half of Figure 3.2b persisted for about 3 hours, before it started to reorganize into 1 m-scale bedforms. The large 3 m-scale alongshore-oriented lunate megaripple (marked B) on the left of Figure 3.2a was first observed at 2040h on Yearday 276, and it persisted until 0140h on Yearday 277. About 5 hours later, it disappeared.

The 4-5 m-long shore-parallel but sinuous feature with 1-2 m-scale undulations (marked A) at the offshore side of the images in Figure 3.3a persisted for about 3 hours before changing into small ripples.

The 2-3 m-scale sinuous features at the offshore half of Figure 3.5b (marked A) seem to have first appeared at 0604h, on Yearday 286. Then they progressively migrated onshore while maintaining their size and form up to 1159h, about 6 hours later, before reorganising

(a) Time 0019h, Yearday 287.01

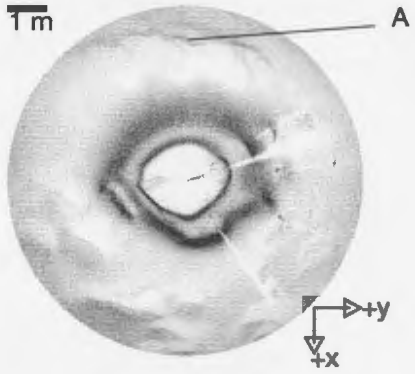

(b) Time 0139h, Yearday 287.07

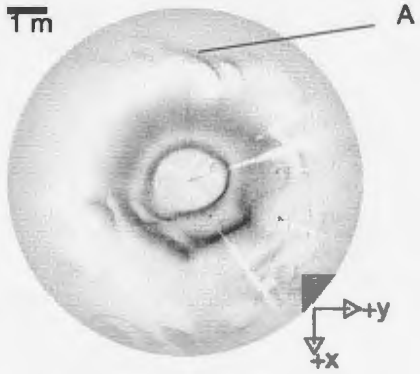

(c) Time 0259h, Yearday 287.12

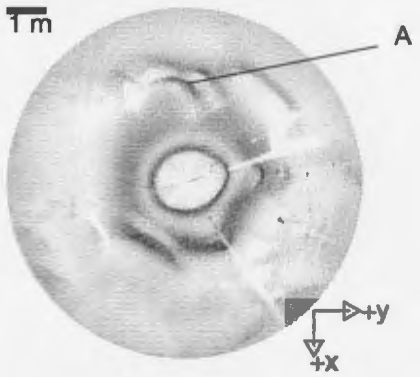

Figure 3.6: Fan-beam images collected between 0019h to 0259h on Yearday 287 during Storm2. Positive x indicates onshore and positive y indicates southward directions.

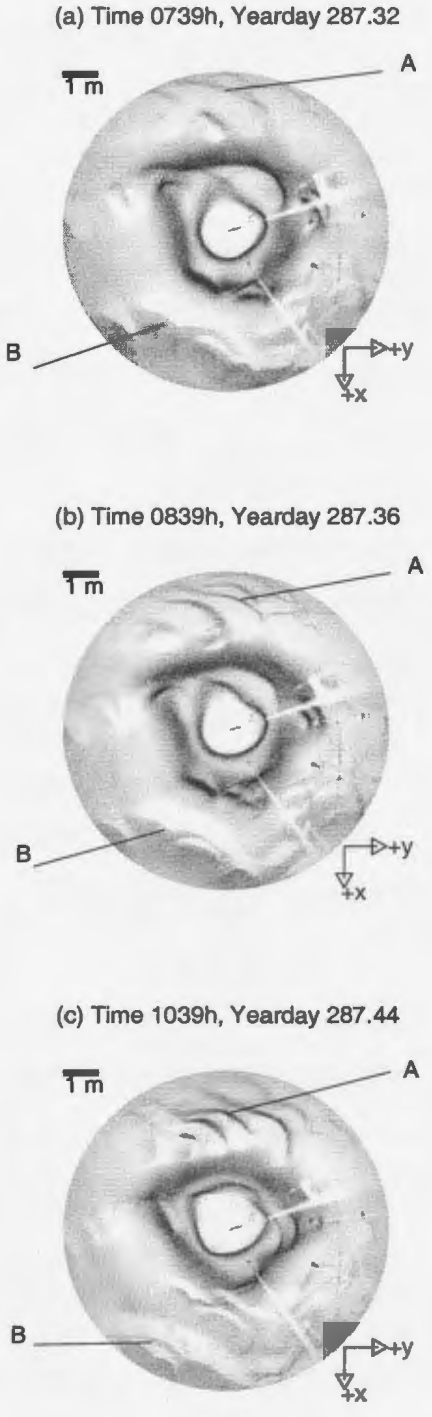

Figure 3.7: Fan-beam images collected between 0739h to 1039h on Yearday 287 during Storm2. Positive x indicates onshore and positive y indicates southward directions.

Table 3.1: Summary of bedform persistence in hours as a function of bedform size.

Bedform scale (m)	3	1-2	2-3	1-2	1	1-2	1-2	0.2
Persistence (hours)	5	3	6	5	3	5	5	8

into sub-meter-scale megaripples. The 1-2 m-scale isolated cross-shore-oriented lunate megaripples at the offshore half of Figure 3.5c (marked D) seem to have first appeared at 1559h on Yearday 286 and progressively migrated northward up to 2059h, about 5 hours later, before they changed to small ripples.

The group of meter to sub-meter-scale cross-shore-oriented lunate megaripples at the upper half of Figure 3.6a (marked A) seems to have first appeared at 2219h Yearday 286 and persisted up to 0139h Yearday 287 (Figure 3.6b), more than 3 hours later, before coalescing into larger 1 m-scale megaripples. The 1-2 m-scale obliquely oriented megaripple at the upper half of Figure 3.6c (marked A) migrated northward for up to 5 hours.

The 1-2 m-scale obliquely oriented megaripples at the upper half of Figure 3.7a (marked A) seem to have appeared first at 0559h on Yearday 287 and persisted for 5 hours up to 1119h on Yearday 287. During all this time they migrated onshore while maintaining their size and form.

On the other hand, the narrow train of 20 cm-wavelength ripples observed in Figure 3.3a seems to have first appeared at 1729h on Yearday 277 and persisted for 8 hours up to 0100h on Yearday 278. During all this time, it progressively migrated onshore.

3.4 Geometrical scales

Measurements of nearshore lunate megaripple geometrical scales are rare in the literature. However, such information is very important in many problems related to bedload sediment transport. As described earlier, this has been a direct result of the difficulties involved in making these measurements. Lunate megaripples were clearly imaged by the pencil-beam and fan-beam sonars in DUCK94 data set. This offered a good opportunity to study the

scales of these structures and their variability during storms.

Lunate megaripples are 3-D structures and can exist as solitary features or in laterally connected forms. To avoid ambiguities, only the scales of solitary features were measured in this thesis. Figure 3.8 shows the definition sketch of the geometrical scales, which included lunate megaripple spans, heights and chord-lengths; these terms are as defined by Allen (1968) and Clifton et al. (1971). The spans were taken as the horn-to-horn distances for individual megaripples and were measured from fan-beam images. The heights (η) were measured as the vertical distances between megaripple crests and troughs using the pencil-beam profiles. Also measured was the trough-to-trough separation-length (L) using the pencil-beam profiles and megaripple spacing which represents the nearest horizontal separation between common points on megaripples as measured from fan-beam images. The spans and heights give an idea about the size of the measured structures, while spacings and trough-to-trough separation-lengths give an idea about the density of the measured megaripples.

3.4.1 Lunate megaripple heights and separation-lengths

A zero-crossing method is used for obtaining the megaripple heights and separation-lengths. In order to apply this approach, the interpolated and filtered bed profiles were detrended, and dissected by a zero-crossing method into a series of individual megaripples.

Zero-crossing of the first derivative of bed profiles gave the corresponding positions of individual megaripple crests and troughs. Local humps and hollows were simply discarded if they did not cross the zero line. The trough-to-trough separation-lengths were obtained as the horizontal distance between two successive zero-upcrossing points on the first derivative of bed profiles. Typically the heights were obtained as the vertical distance between the highest and lowest elevations between two successive trough positions on the bed elevation profiles.

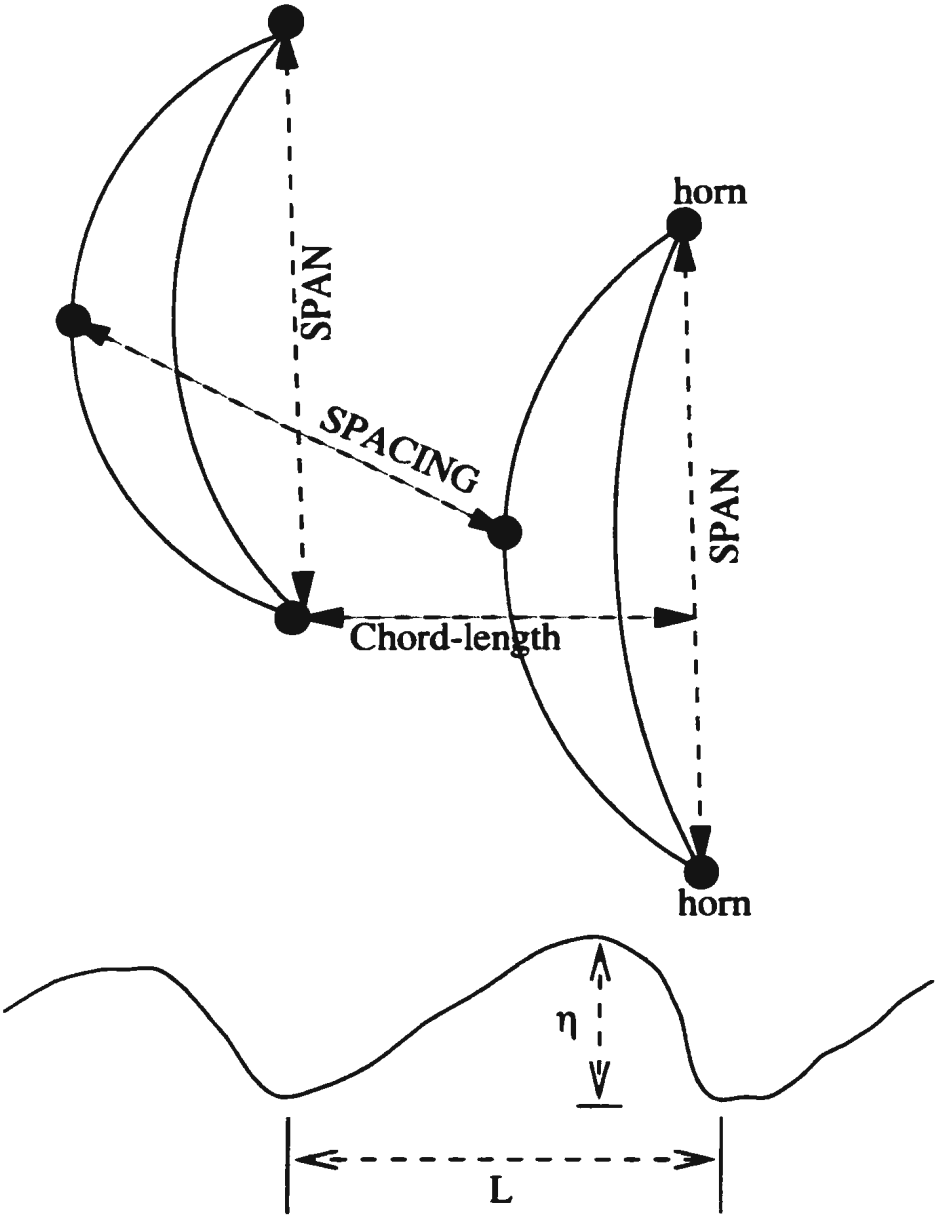

Figure 3.8: Schematic diagram showing lunate megaripple geometrical parameters such as span, spacing, megaripple height (η), chord-length and trough-to-trough separation-length (L).

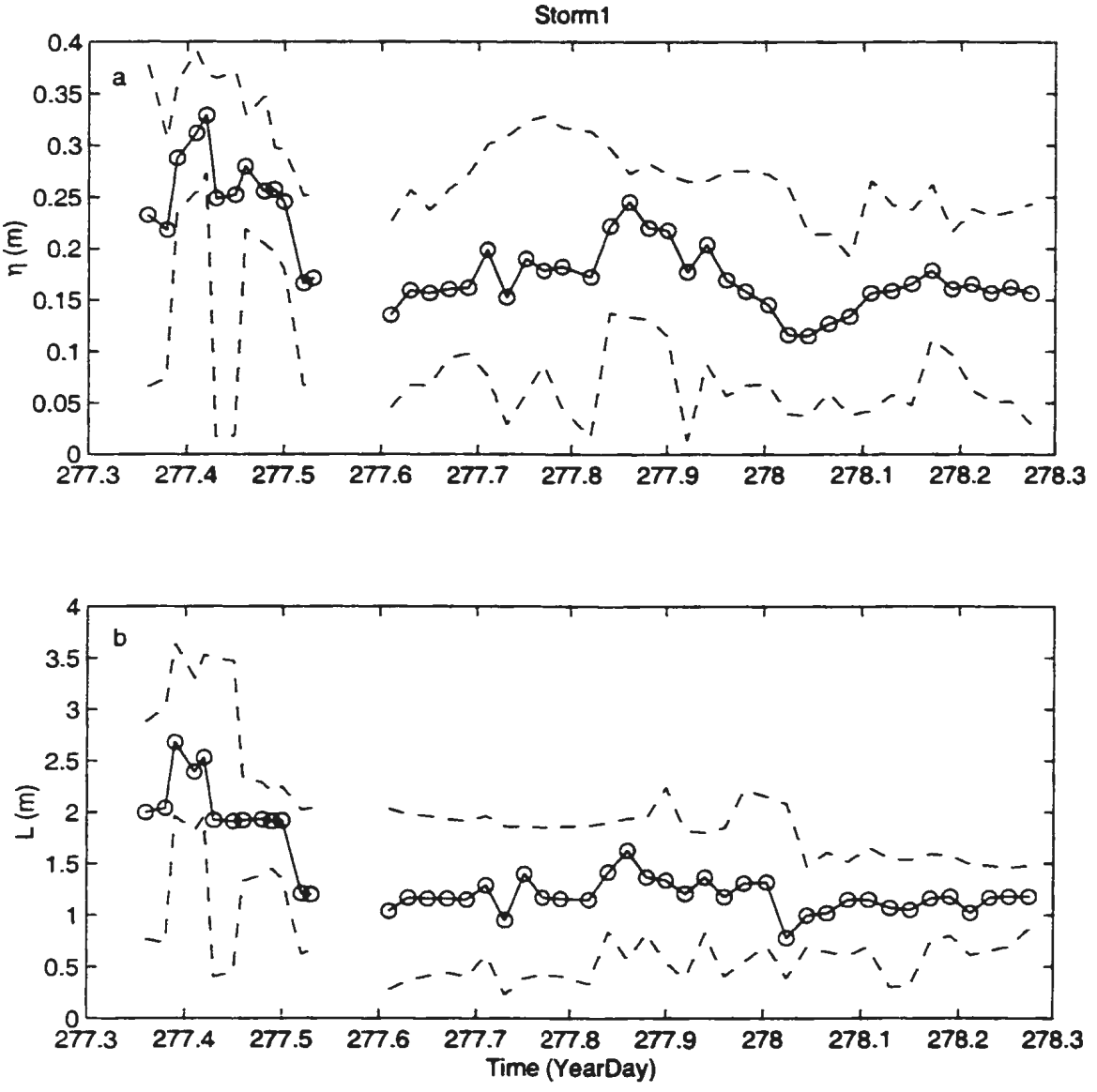

Figure 3.9: Time series of measured megaripple heights η (a) and separation-lengths L (b) statistic as obtained from the half-hour bed profiles for Storm1, where (o) indicates the mean and (- -) indicates the maximum and minimum values.

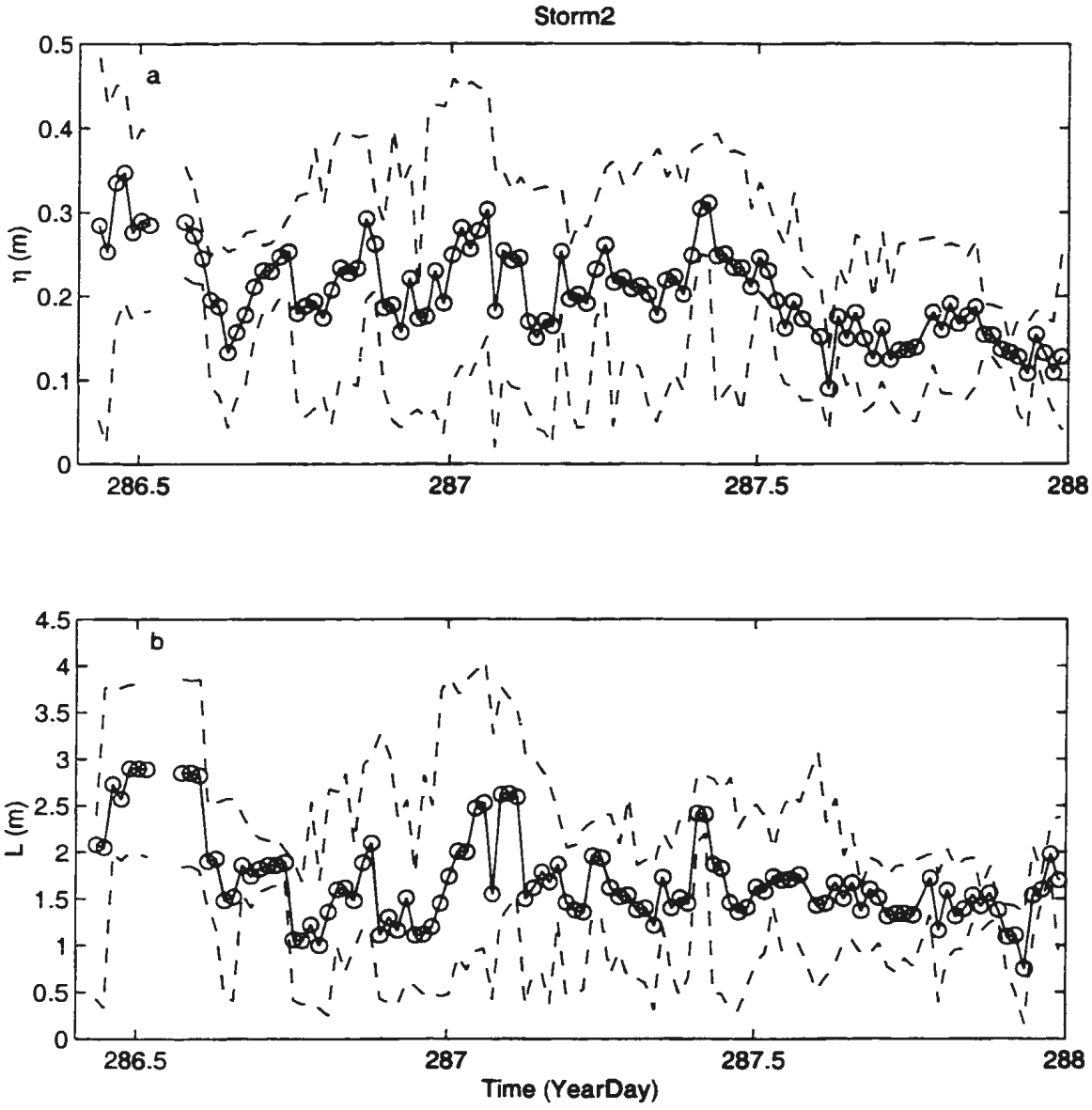

Figure 3.10: Time series of measured megaripple heights η (a) and separation-lengths L (b) statistic as obtained from the half-hour bed profiles for Storm2, where (o) indicates the mean and (- -) indicates the maximum and minimum values.

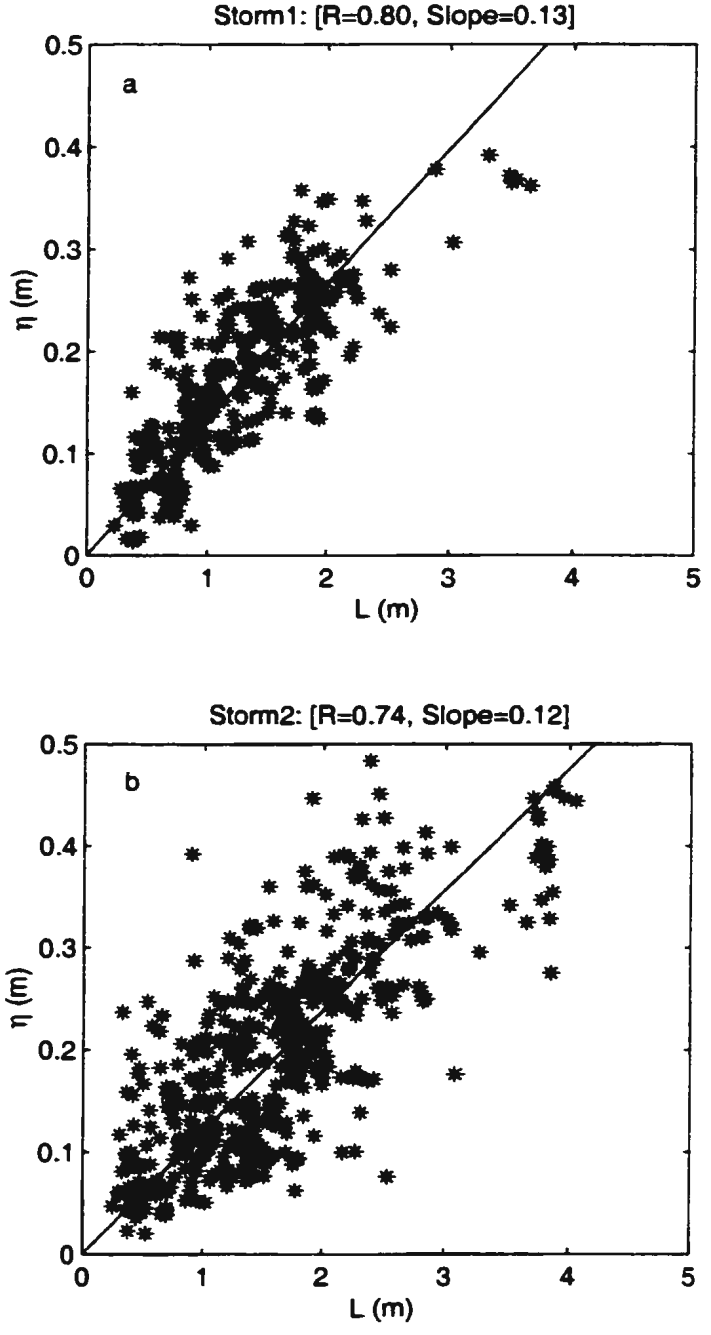

Figure 3.11: Scatter diagrams for the comparison between the measured statistic of megaripple heights (η) and trough-to-trough separation-leghths (L) for Storm1 (a) and Storm2 (b).

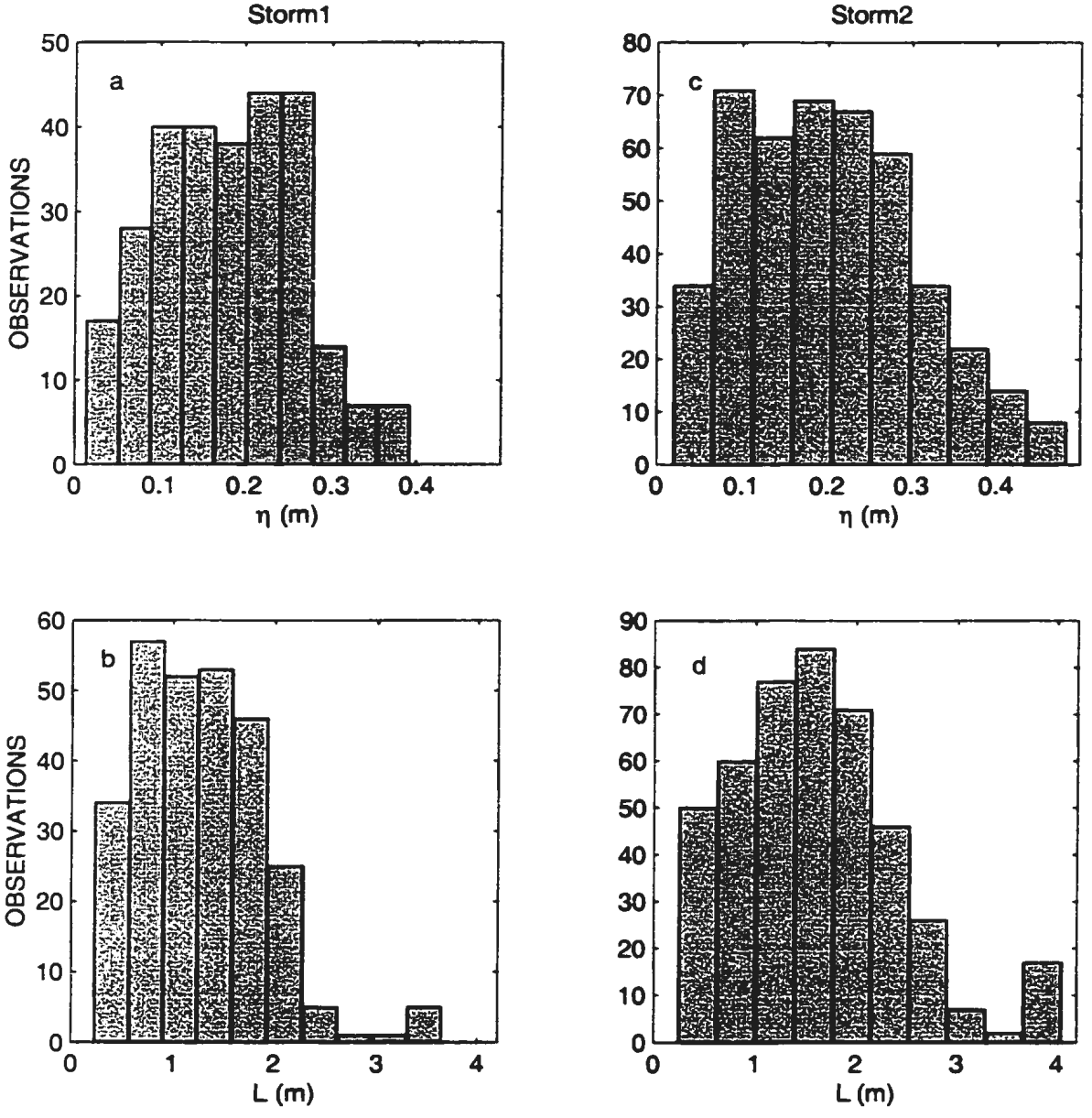

Figure 3.12: Histograms of measured megaripple heights (η) and trough-to-trough separation-lengths (L) for Storm1 (a and b) and Storm2 (c and d).

The obtained megaripple heights and separation-lengths are shown as time series in Figure 3.9 for Storm1 and Figure 3.10 for Storm2. Figure 3.12 shows the histograms of measured megaripple height and trough-to-trough separation length. The measured megaripple heights ranged from 0.05-0.5 m while the separation-lengths ranged from 0.5-4 m, consistent with Clifton et al. (1971) observations using divers. Megaripple heights and separation-lengths were generally larger during the early part of Storm1 between Yeardays 277.3 and 277.5; the measured η and L later diminished and remained constant between Yeardays 277.6 and 278.3 (Figure 3.9). On the other hand, there was little change in both both megaripple heights and separation-lengths throughout Storm2 (Figure 3.10).

There is good correlation between megaripple heights and separation-lengths for both storms as shown in Figure 3.11. The correlation coefficient for Storm1 is 0.80 and 0.74 for Storm2. The slopes (η/L) of the regression lines in Figure 3.11 were 0.13 for Storm1 and 0.12 for Storm2. These η/L ratios can be compared with other data like Ripple Steepness (η/λ) which is an equivalent parameter for other ripples types, where λ is the ripple wavelength. Orbital ripples have a typical ripple steepness of $\eta/\lambda = 0.15$ (Dingler and Inman, 1977; Clifton and Dingler, 1984). Wiberg and Harris (1994) obtained the values of maximum ripple steepness in the range of $\eta/\lambda = 0.12$ for anorbital ripples and $\eta/\lambda = 0.17$ for orbital ripples. Hay and Bowen (1993) obtained η_{rms}/λ=0.13, 0.18 and 0.30 for ripples that occured in three different storms during their investigation. The values obtained for Duck94 megaripples are therefore generally comparable to the previously obtained values for wave-generated ripples.

3.4.2 Spans and spacings

Lunate megaripple spans and spacings were measured from fan-beam images, based on a rectangular sub-image of 12.8 m^2 area selected on both offshore and onshore sides of the images. The size of each frame was determined such that it covered as large a part of the images as possible without intersecting the edges or the central parts that were not imaged. All the megaripples observed within this frame were then digitized, as illustrated in Figure 3.13.

Three points on the megaripple slip faces were digitized. The first two points were the horn tips giving the megaripple spans. The third point was at the center of the megaripple trough for offshore sub-images and at the center of crests for onshore sub-images. Because the megaripples were mostly facing onshore during the periods under investigation, the trough areas of the megaripple slip faces which directly faced the fan-beam in the offshore frames were quite clearly defined. On the other hand the megaripple slip faces in onshore frames were in shadow zones of the fan-beam; in these cases the crests were more sharply defined.

The digitized arrays for all the megaripples in individual images were then analysed to obtain the megaripple spans and spacings, and are presented as time series for Storm1 and Storm2 in Figure 3.14 and Figure 3.15 respectively. Although there is considerable scatter in these measurements, the Storm2 data tend to suggest temporally coherent variations in both size and spatial density of the megaripples on timescales of approximately 3-5 hours. These timescales are consistent with the 3-6 hours obtained qualitatively from raw fan-beam images (Table 3.1, for lunate megaripples of over 1 m-scale).

Figure 3.16 shows histograms of measured spans and spacings for both Storm1 and Storm2. Both spans and spacings ranged up to slightly less than 3 m. The histograms for Storm1 have a mode at about 0.5 m while those for Storm2 have a mode at about 0.75m. This shows that in general lunate megaripples were larger during Storm2 than during Storm1. The comparison between megaripple spans and spacings showed a good correlation (Figure 3.17). The ratio of spacing/span for these megaripples is 1 for both storms.

3.4.3 Probability distributions

Wave heights tend to be Rayleigh distributed (Horikawa, 1988 pg.68). Assuming that there may be an analogy between random wave fields and irregular 3-D bedforms, the distributions of the measured megaripple geometrical scales can be compared to the Rayleigh distribution

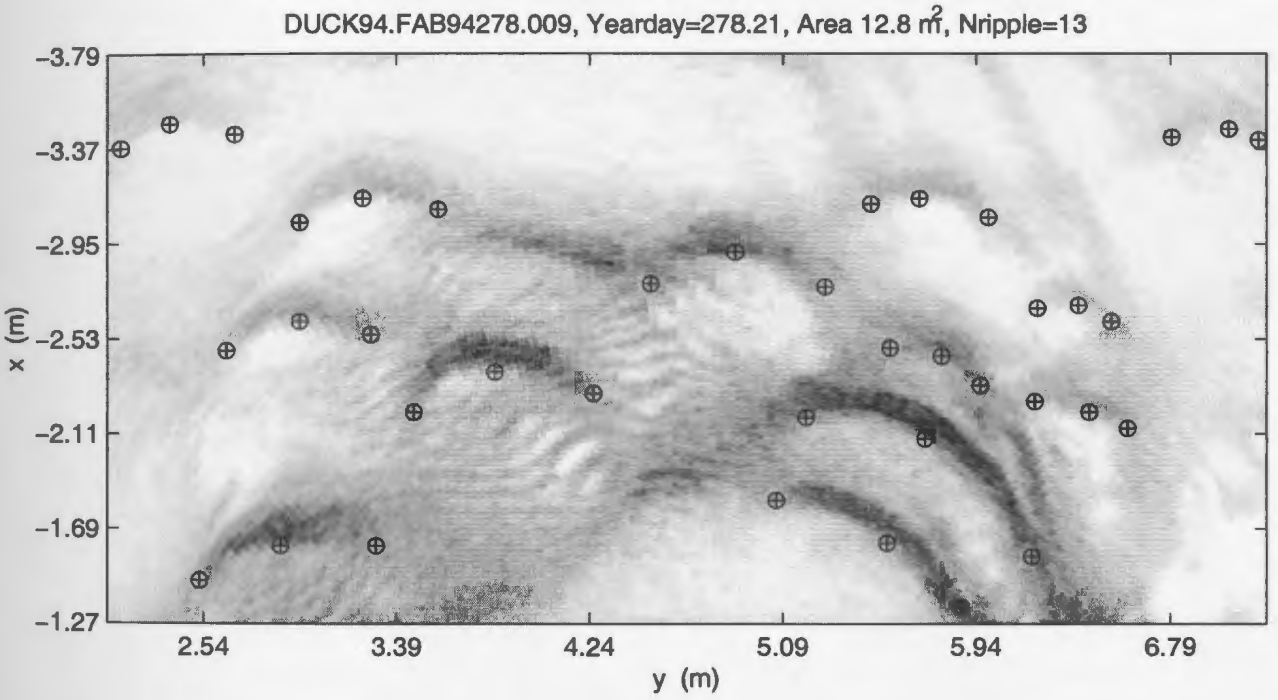

Figure 3.13: Example of an offshore fan-beam sub-image showing the digitized tips of megaripple horns and trough centers as used in estimating megaripple spans and spacings. The cross-shore distance is indicated by x (negative offshore), while y indicate the horizontal distance parallel to the shoreline.

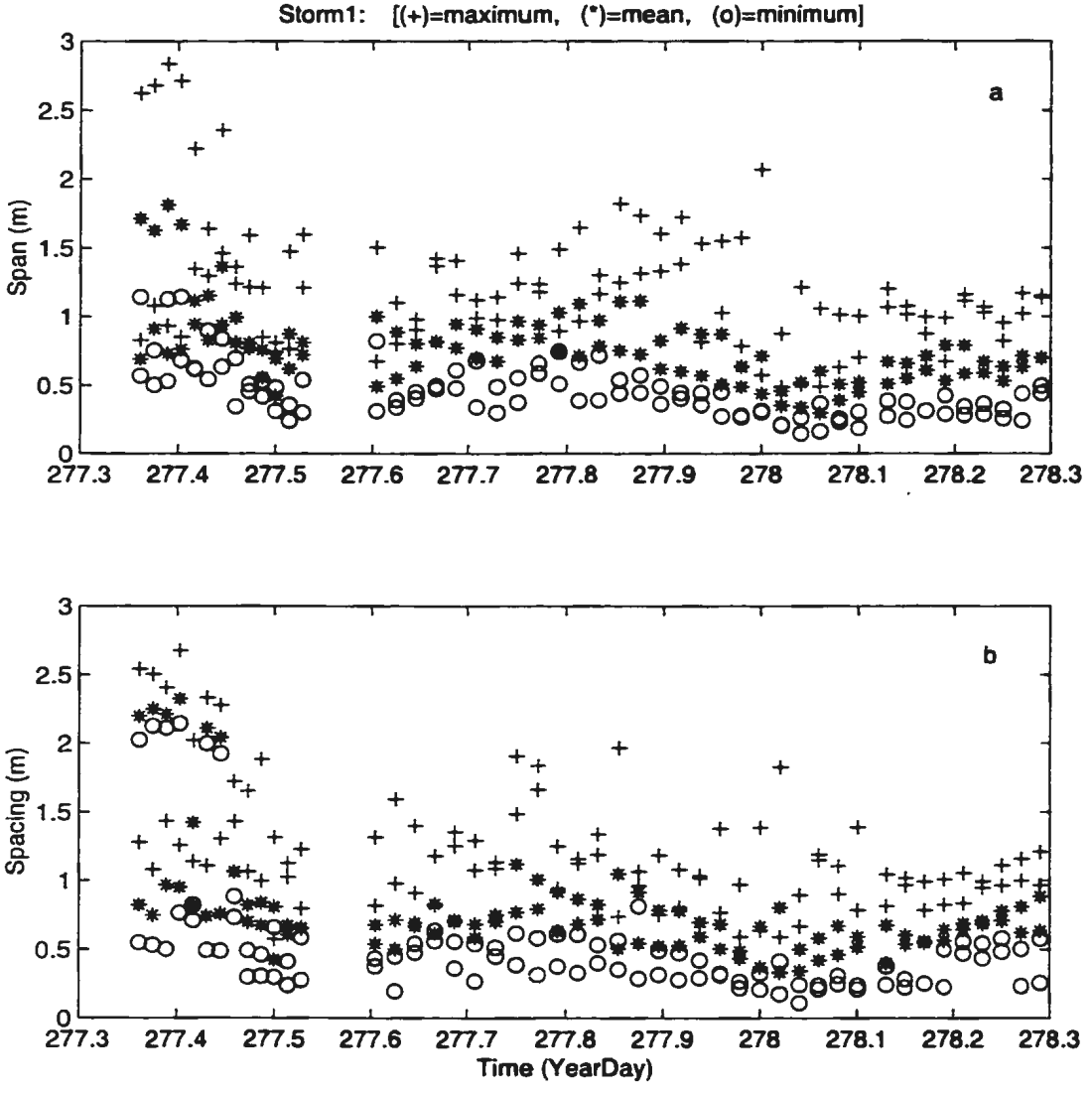

Figure 3.14: Time series of measured maximum (+), minimum (o) and mean (*) values of lunate megaripple spans (a) and spacings (b) for Storm1.

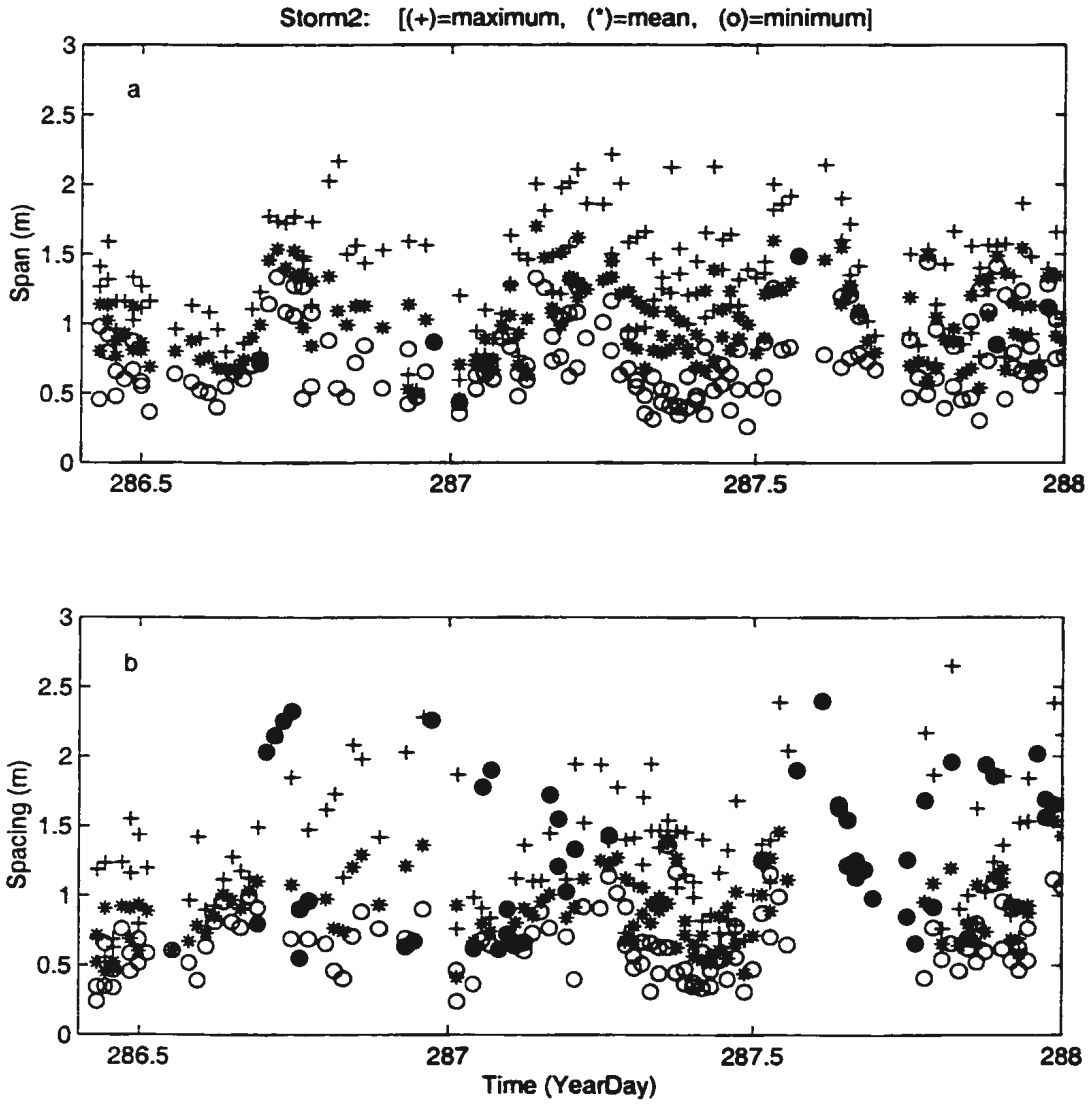

Figure 3.15: Time series of measured maximum (+), minimum (o) and mean (*) values of lunate megaripple spans (a) and spacings (b) for Storm2.

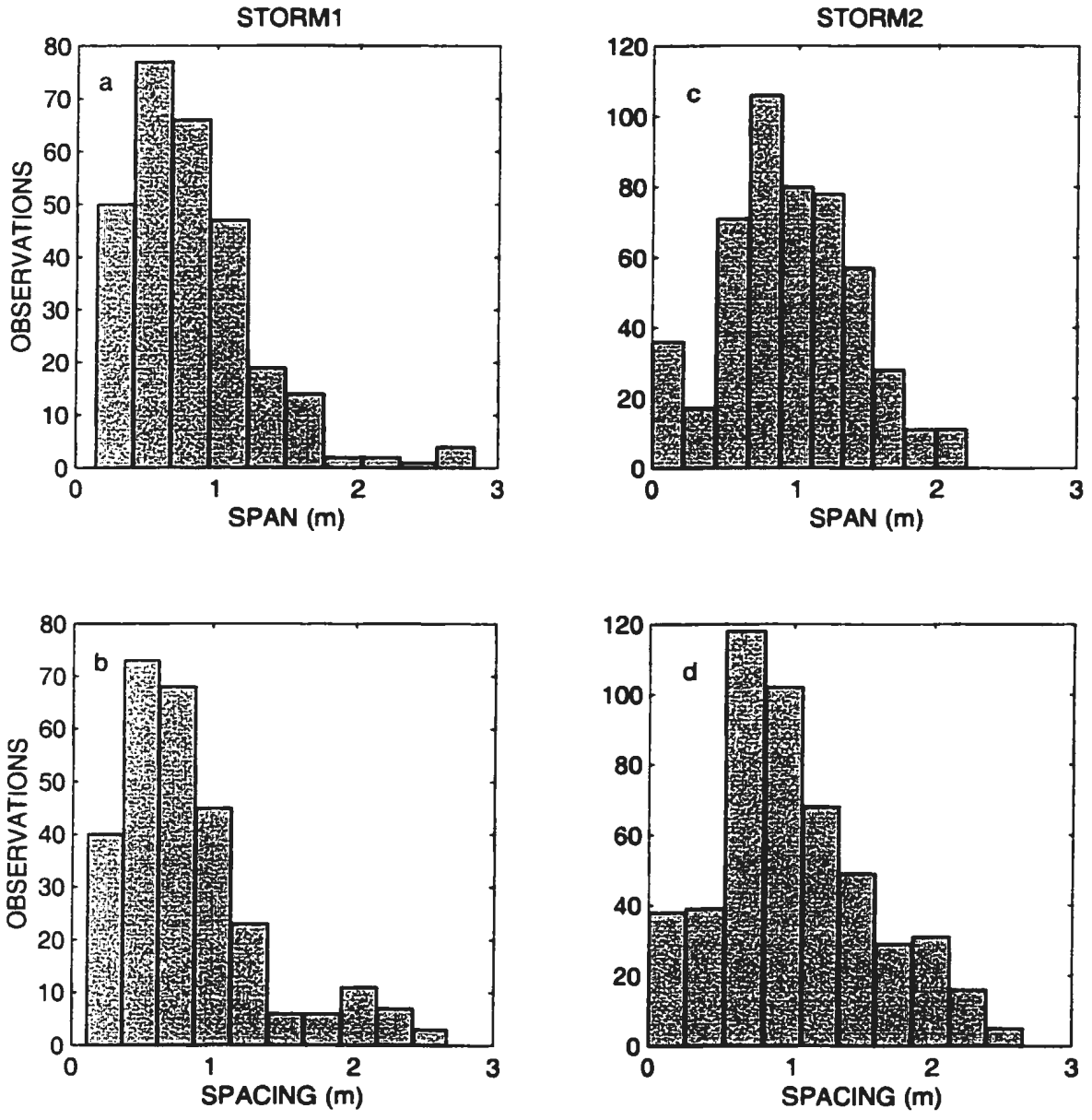

Figure 3.16: Histograms of the measured megaripple spans and spacings statistic for Storm1 (a and b) and Storm2 (c and d).

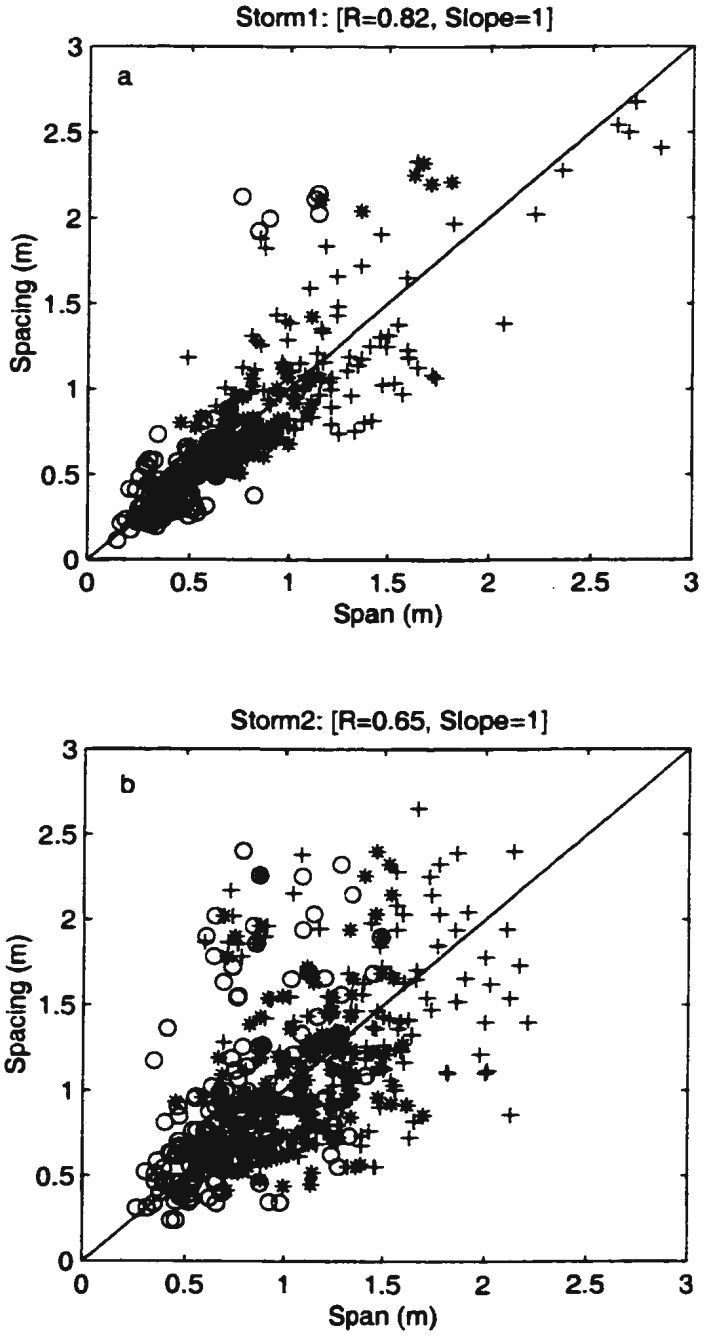

Figure 3.17: Scatter diagram for the comparison between lunate megaripple spacings with spans for Storm1 (a) and Storm2 (b), where (+)=maximum, (o)=minimum and (*)=mean values.

Table 3.2: Rayleigh distribution parameters for both Storm1 and Storm2.

	σ_η (m)	σ_L (m)	σ_{Spans} (m)	$\sigma_{Spacings}$ (m)
Storm1	0.08	0.63	0.46	0.52
Storm2	0.10	0.81	0.47	0.56

$$P_r = \frac{x}{\sigma^2} e^{-\frac{x^2}{2\sigma^2}} \tag{3.1}$$

where P_r is the probability density, x represents the observed quantity and σ is the standard deviation of the observations. The measured megaripple heights, separation-lengths, spans and spacings were therefore normalized by $\sigma\sqrt{2}$. The computed histogram frequencies were then converted into probability densities to obtain the probability density functions for both storms. The distribution of the probability densities for megaripple heights (η) and separation-lengths (L) for both Storm1 and Storm2 as compared to the Rayleigh distribution are shown in Figure 3.18, where the solid line indicates the Rayleigh distribution function. Figure 3.19 shows a similar comparison for megaripple spans and spacings. The Rayleigh distribution parameters for both storms are given in Table 3.2.

These results indicate that the measured megaripple heights, separation-lengths, spans and spacings are approximately Rayleigh distributed.

3.4.4 Comparison with total kinetic energy

The second storm was generally dominated by relatively higher energy conditions than the first storm, and the measured megaripple spans and spacings seem to have been larger than during Storm1. Figure 3.20 shows the relationship between the measured total kinetic energy as given by $[{u_w}^2 + {v_w}^2 + U^2 + V^2]$ and the mean spans and spacings for both storms. Although there is considerable scatter, giving low correlation coefficients of 0.41 and 0.48 for the comparison with spans and spacings respectively; lunate megaripple spans and spacings seem to be generally increasing with the increase in total kinetic energy.

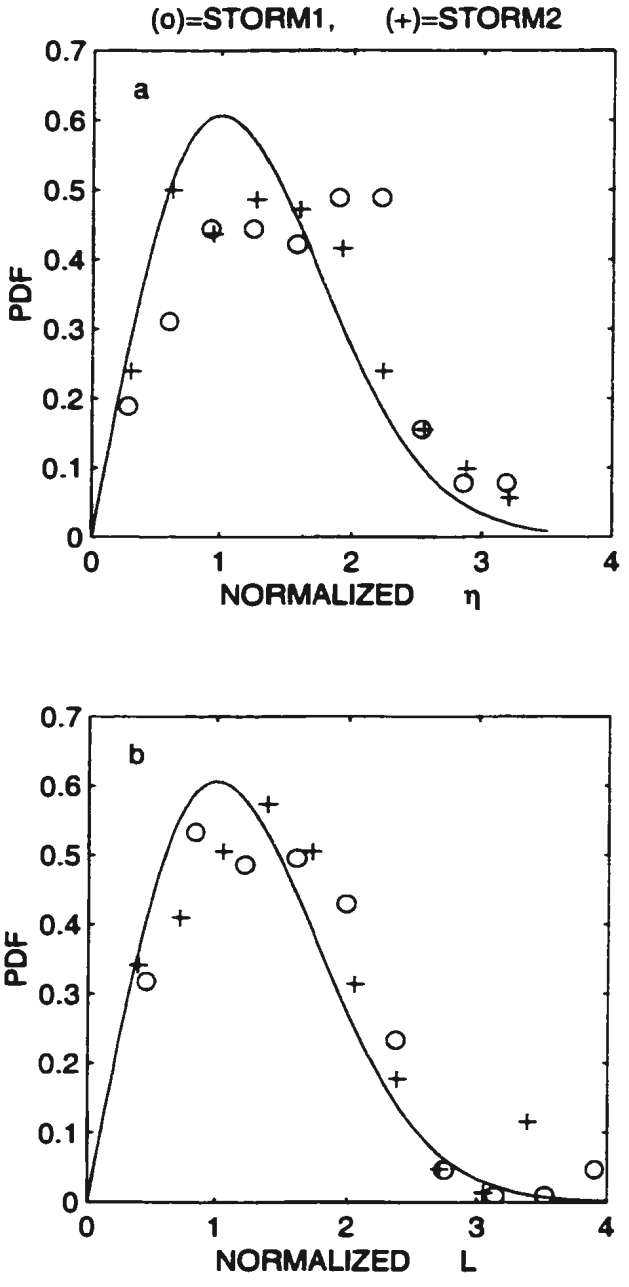

Figure 3.18: Distribution of the probability density of normalized megaripple heights (η) and chord-lengths (L) for Storm1 (o) and Storm2 (+) compared with the Rayleigh distribution function (solid line).

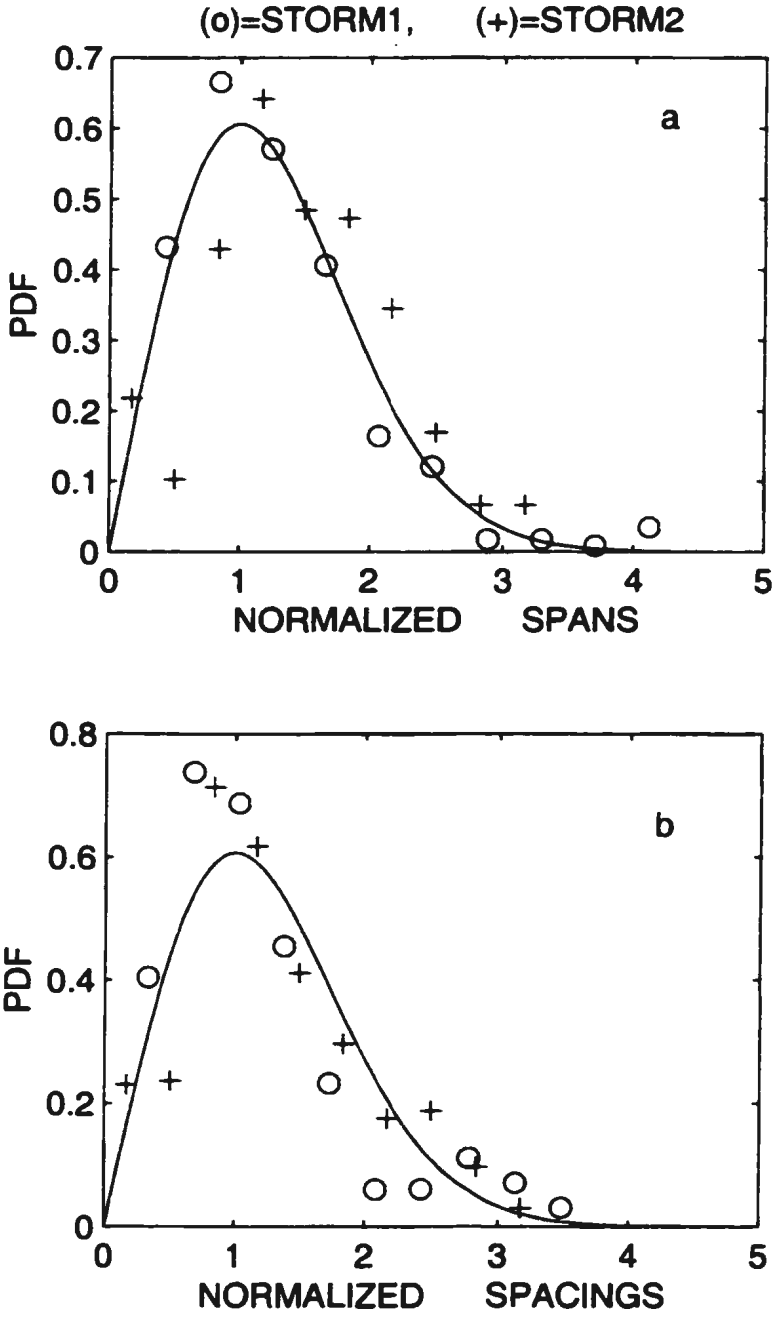

Figure 3.19: Distribution of the probability density of normalized megaripple spans and spacings for Storm1 (o) and Storm2 (+) compared with the Rayleigh distribution function (solid line).

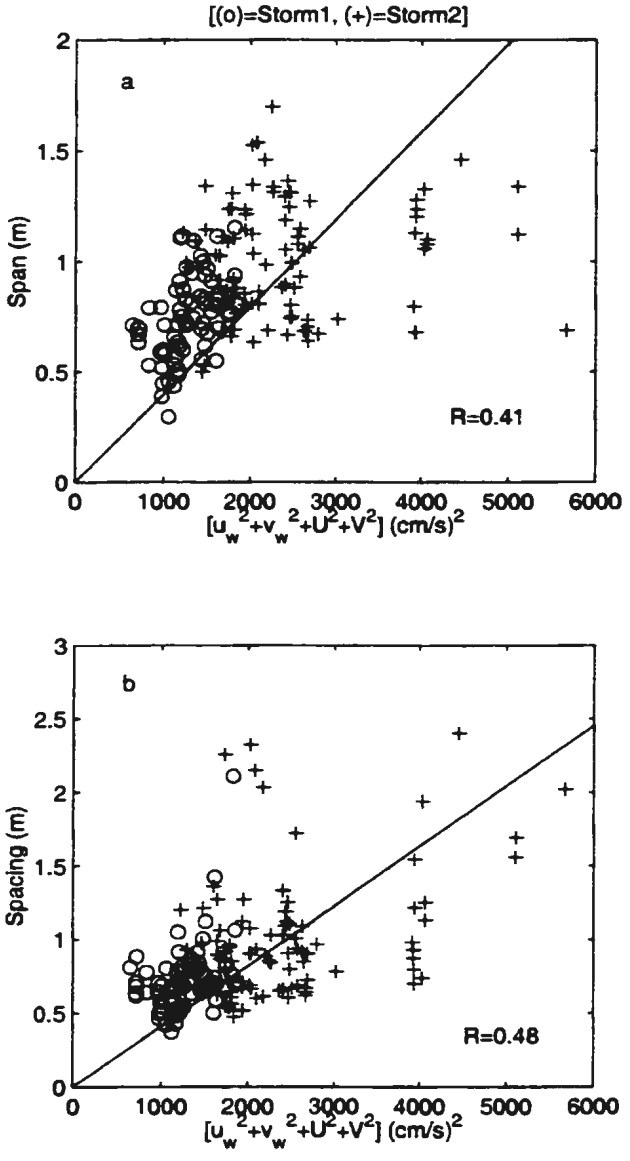

Figure 3.20: Scatter diagram for the comparison between total fluid kinetic energy and mean values of lunate megaripple spans and spacings for Storm1 (o) and Storm2 (+).

3.4.5 Comparison with wave-orbital excursions

It is also interesting to compare the measured megaripple scale with the wave-orbital excursions, $2A_o = (u_s T_p)/\pi$. Vincent and Osborne (1993) found no significant relationship between the wavelength of small ripples and A_o. However, they found a significant correlation between the wavelength of larger bedforms and A_o. The comparisons made using DUCK94 measurements shown a considerable scatter, giving low correlation coefficients of 0.34, 0.40 and 0.30 for the comparison between L, spans and spacings with $2A_o$ (Figure 3.21a-c) respectively. However, there is a pattern that tends to suggest a relationship between these geometrical scales and the wave-orbital excursions. In general, the measured megaripple separation-lengths (L), spans and spacings were all increasing with the increase in wave-orbital excursions.

3.4.6 Comparison with other non-dimensional parameters

Dimensionless parameters which are normally used as predictors of bedform wave-lengths and migration velocities were also looked at. These parameters included (a) Wave Reynolds number Re_w (b) Shields parameter ψ and (c) Mobility number M. These numbers are defined in the usual way (Vincent and Osborne, 1993) as follows

$$Re_w = \frac{U_{max} A_o}{\nu}, \tag{3.2}$$

$$\psi = \frac{0.5 f_w {u_s}^2}{(s-1)gD}, \tag{3.3}$$

$$M = \frac{(A_o \omega)^2}{(s-1)gD}, \tag{3.4}$$

where ν is the kinematic viscosity (0.014 cm^2/s), s is the specific density of sediment

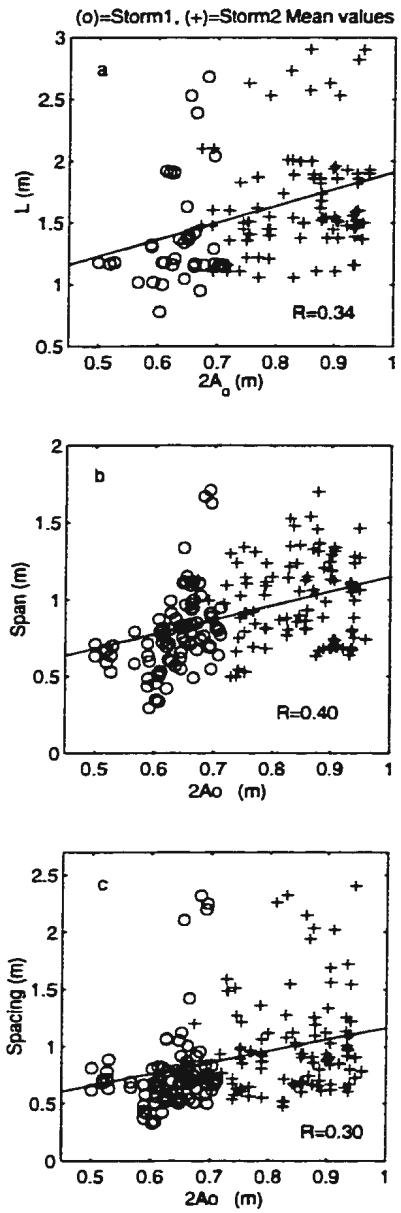

Figure 3.21: Comparison between the mean values of measured megaripple separation-lengths (a), spans (b), spacings (c) and wave-orbital excursions ($2A_o$). The symbols (o) and (+) indicate comparisons using Storm1 and Storm2 values respectively.

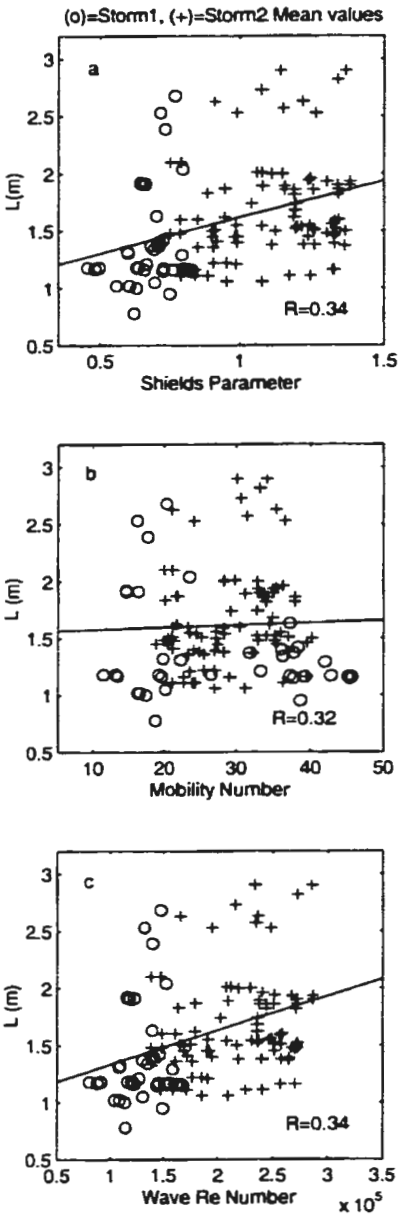

Figure 3.22: Comparison between the mean values of measured megaripple separation-lengths and Shields parameter (a), Mobility number (b) and Wave Reynolds number (c). The symbols (o) and (+) indicate comparisons using Storm1 and Storm2 values respectively.

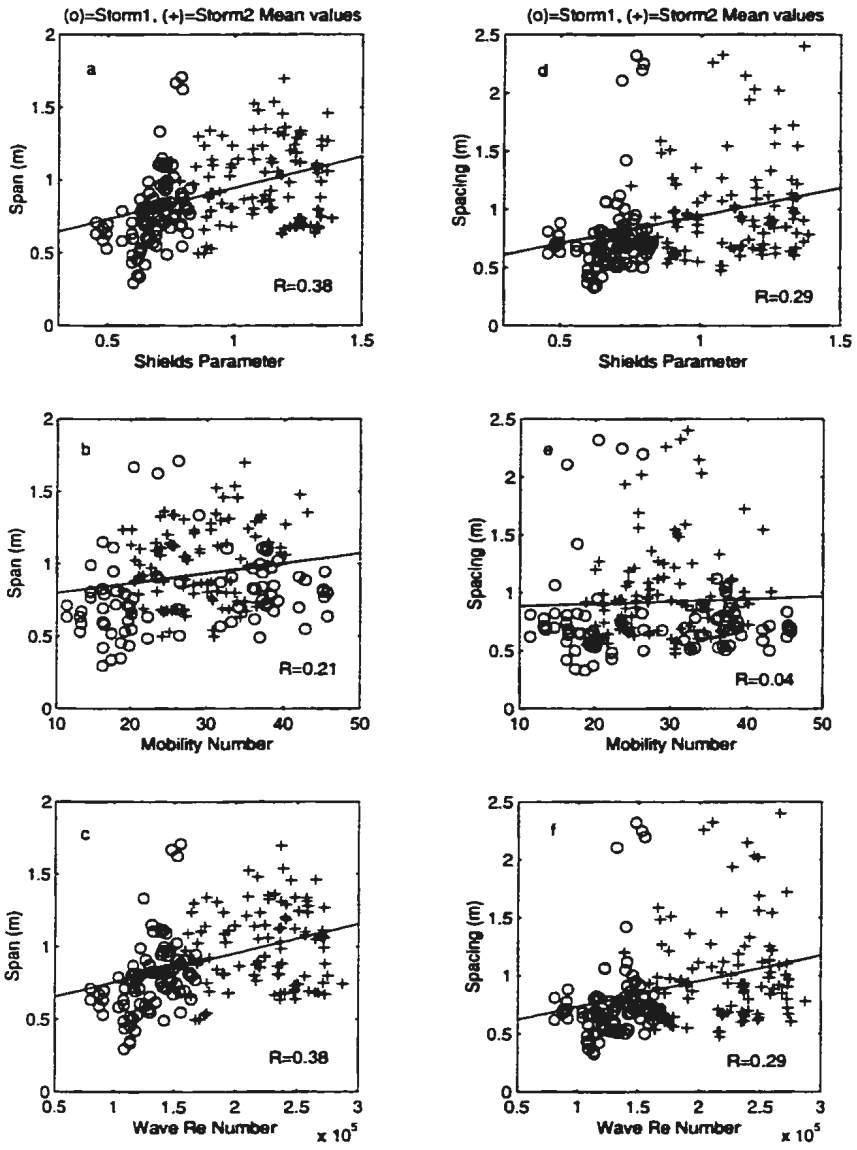

Figure 3.23: Comparison between the mean values of measured megaripple spans and Shields parameter (a), Mobility number (b) and Wave Reynolds number (c). The symbols (o) and (+) indicate comparisons using Storm1 and Storm2 values respectively. Also shown is the comparison between the mean values of measured megaripple spacings and Shields parameter (a), Mobility number (b) and Wave Reynolds number (c).

grains (s=2.7), D is the median grain size (D = 0.02 cm at Duck), g is the acceleration due to gravity, the wave angular frequency is given by $\omega = 2\pi/T$, A_o is the wave-orbital semi-excursion, f_w is the wave friction factor as defined by Jonsson (1966), and u_s is the significant wave-orbital velocity ($u_s = 2\sqrt{u^2_{rms} + v^2_{rms}}$).

The comparison between megaripple separation-lengths (L) with the Shields parameter, Wave Reynolds number and Mobility number show a considerable scatter giving low correlation coefficients (Figure 3.22). However, there is a pattern that tends to suggest a relationship between megaripple separation-lengths (L) with both Shields parameter and Wave Reynolds number (Figure 3.22a&c) respectively. The measured megaripple separation-lengths (L) appears to be generally increasing with the increase in Shields parameter and Wave Reynolds number.

Similarly, the comparison between megaripple spans and spacings with the Shields parameter, Wave Reynolds number and Mobility number show a considerable scatter for both storms giving low correlation coefficients (Figure 3.23). However, there is a pattern that tends to suggest a relationship between megaripple span and spacings with both Shields parameter and Wave Reynolds number for both Storm1 (Figure 5.23a&c) and Storm2 (Figure 5.23d&f) respectively. The measured megaripple spans and spacings seems to be generally increasing with the increase in Shields parameter and Wave Reynolds number.

In summary, correlation coefficients of $R \sim 0.4$ are obtained for the comparison of lunate megaripple spans with computed values of wave-orbital excursions, Shields parameter, Wave Reynolds number and total kinetic energy. Best correlation ($R \sim 0.5$) is obtained for the comparison of lunate megaripple spacings with total kinetic energy. The flow parameters Re_w, M, $2A_o$, ψ all depend on wave variables, and are somewhat related. Total kinetic energy is the only parameter which depends on the mean flow as well as waves. It is interesting therefore that total kinetic energy gives the highest correlation. In general, these results seem to suggest that the scales lunate megaripples tend to be correlated with the flow energy and wave-orbital excursions.

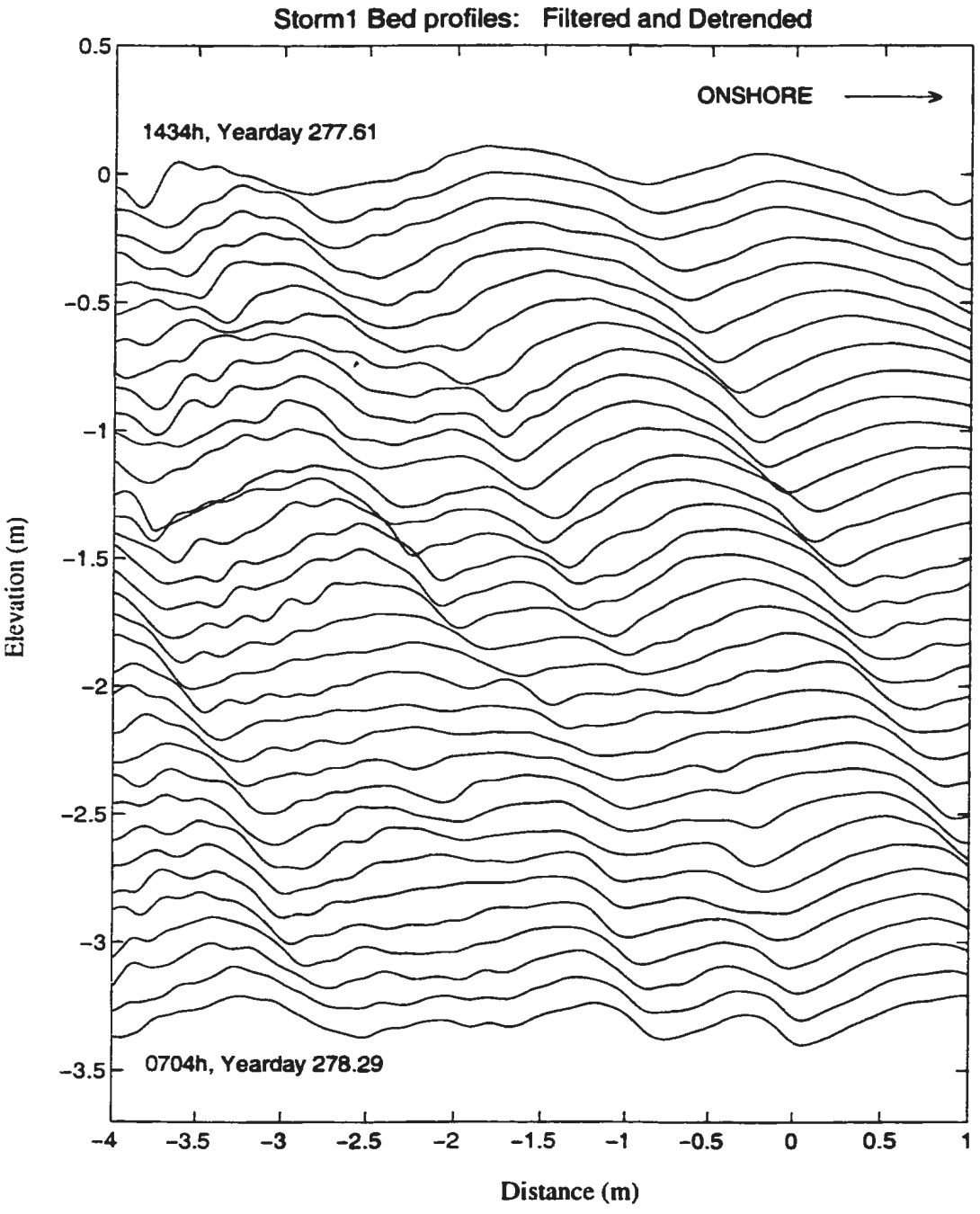

Figure 3.24: Filtered and detrended bed profiles for Storm1 between +1 m and -4 m on either side of the pencil-beam transducer, clearly showing the lunate megaripple relief and their onshore migration. Time increases from top to bottom. The time for the first and last profiles are shown. Successive profiles are offset by -0.1 m.

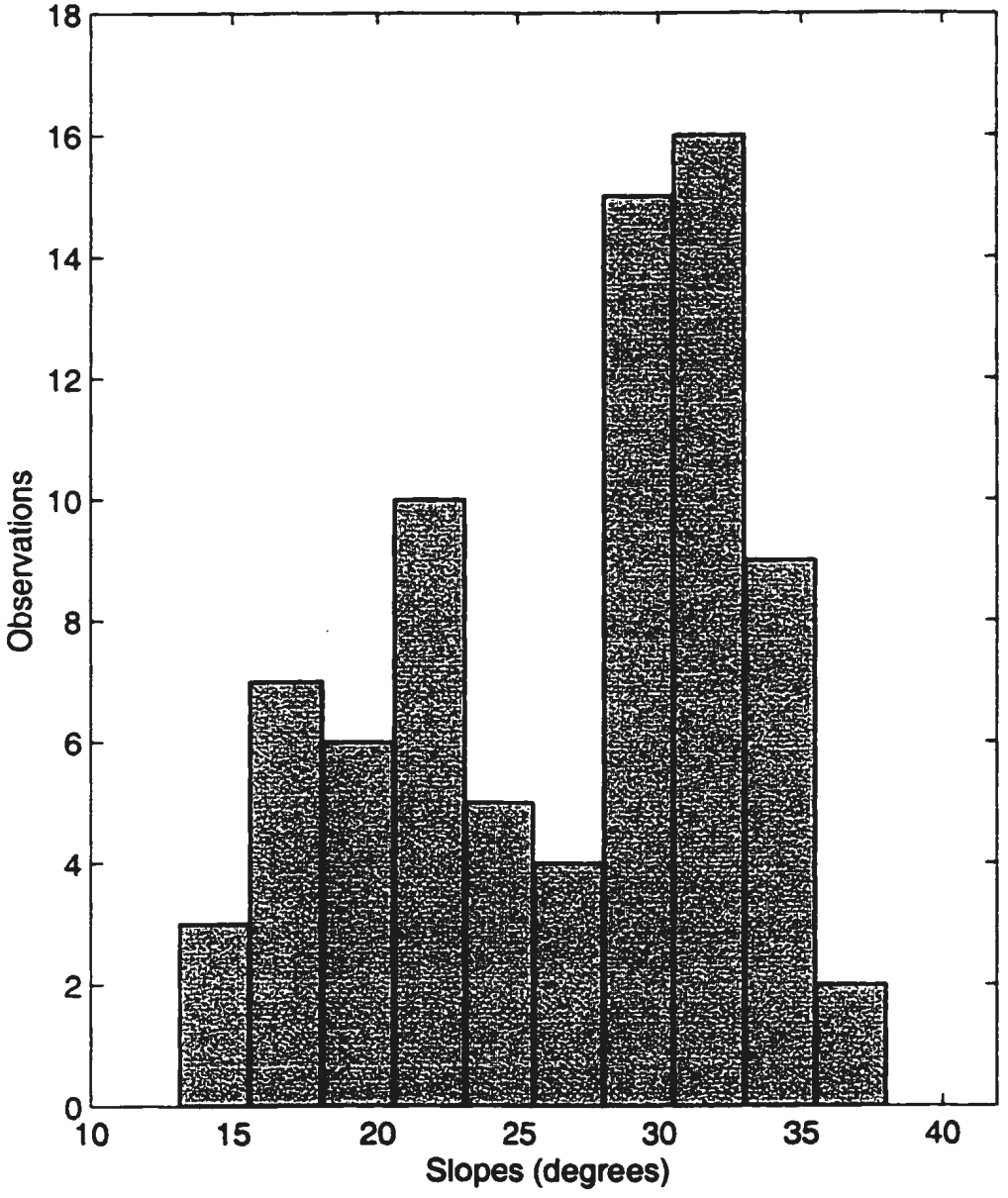

Figure 3.25: Histogram of measured lunate megaripple foreset slopes based on Storm1 bed profiles between -2 m to +1 m in cross-shore distance.

3.5 "Lee" face slopes

According to the avalanche model of dune migration, sediments are transported over the stoss sides, deposited on the crests and eventually slip naturally under gravity down the "lee" faces. An expectation of the avalanche model is that the lee face would be close to the angle of repose. "Lee" face for oscillatory flow is ambiguous. The face sheltered during the onshore stroke is here chosen to be the "lee" face.

Following Sleath (1984), known angles of repose depend on sediment grain size and porosity. Cornforth (1973) suggests values of angles of repose for natural sediments ranging from about 28 up to 36° when porosity is maximum and from about 45 up to 53° at minimum porosity.

The bed profiles for Storm1 given in Figure 3.24 were quite suitable for testing the avalanche model. This segment of the data was particularly chosen because the megaripple relief in these profiles was clearly resolved and megaripples were unambiguously migrating onshore, in the direction of the avalanche faces. Individual megaripples and the avalanche faces were therefore easily identified in the filtered and detrended profiles using the zero-crossing method. The selected megaripples were then analysed individually for the maximum angles of the avalanche faces.

Due to acoustic shadowing of the "lee" faces for horizontal distances greater than 1 m on the shoreward side of the pencil-beam profiles, the bed profiles beyond 1 m to the right of the transducer could not be used in this analysis. Also, the resolution of bed profiles decreased away from the transducer location. Slopes were therefore estimated using profiles ranging from +1 m to -2 m only. Figure 3.25 shows the histogram of the measured slopes with a peak at 33°. This result is consistent with the angle of repose suggested by Cornforth (1973) for sediments with maximum porosity. The "lee" slopes presented here, together with the other observation that megaripples during Storm1 were migrating onshore in the direction of the slip faces support the avalanche model for these bedforms.

Summary

In summary, the megaripples presented here occured at values of Shields bottom stress parameter ranging from 0.5-1.4. Lunate megaripple fields were complex and involved multiplicity of scales. The persistence of the large scale lunate megaripples (over 1 m-scale) seems to be in the order of 3-6 hours (Table 3.1). The transition from 3 m-scale megaripples to mainly 1-2 m-scale megaripples took only 2-3 h. The transition from megaripples to cross-ripples took 5-6 h, while the transition from cross-ripples to irregular ripples took 10-11 h. The measured megaripple heights (η) ranged from 0.05-0.5 m and the horozontal separation-lengths (L) ranged from 0.5-4 m. There is a very good correlation between megaripple heights and the horizontal separation-lengths, with the ratio $\eta/L \sim 1.2$ which is comparable to the value for 2-D ripples. Megaripple spans and spacings ranged from 0.25-2.75 m. There is a very good correlation between the spans and spacings with the ratio spans/spacings=1. The comparison between spans and spacings with the flow kinetic energy produced a better correlation (r$\sim$4) than with the other examined flow variables. The "lee" slopes of megaripples ($\sim$33°) are consistent with the avalanche model of bedform migration.

Chapter 4

Cross-shore migration velocities

In this Chapter, cross-shore megaripple migration velocities are determined by two independent methods, from the measured fan-beam images and from the bed profiles, for the days of interest. The results are then compared with hydrodynamic forcing parameters.

4.1 Storm1 megaripples

Qualitatively the series of pencil-beam bed profiles for Storm1 (Figure 4.1) shows clearly that megaripples were migrating onshore for Yeardays 277-278 during Storm1. The fan-beam images in Figure 4.3 show the megaripple patterns corresponding to the bed profiles shown in Figure 4.1. These images collected during the 3-hour interval on Yearday 278 show onshore migrating lunate megaripples (to the bottom of the images), with their horns facing in the direction of migration.

Figure 4.6 shows the series of low pass filtered backscatter intensity profiles for Storm1 obtained from fan-beam images along the location where the pencil-beam profiles shown in Figure 4.1 were taken. The middle part of these profiles indicate a data gap where the bottom was not imaged by the fan-beam transducer at about 1 m radius from the center of fan-beam images. This fan-beam data also shows that the large scale features were clearly migrating onshore during Storm1, especially in the offshore side of the transducer where the fan-beam was directly illuminating the megaripple slip faces.

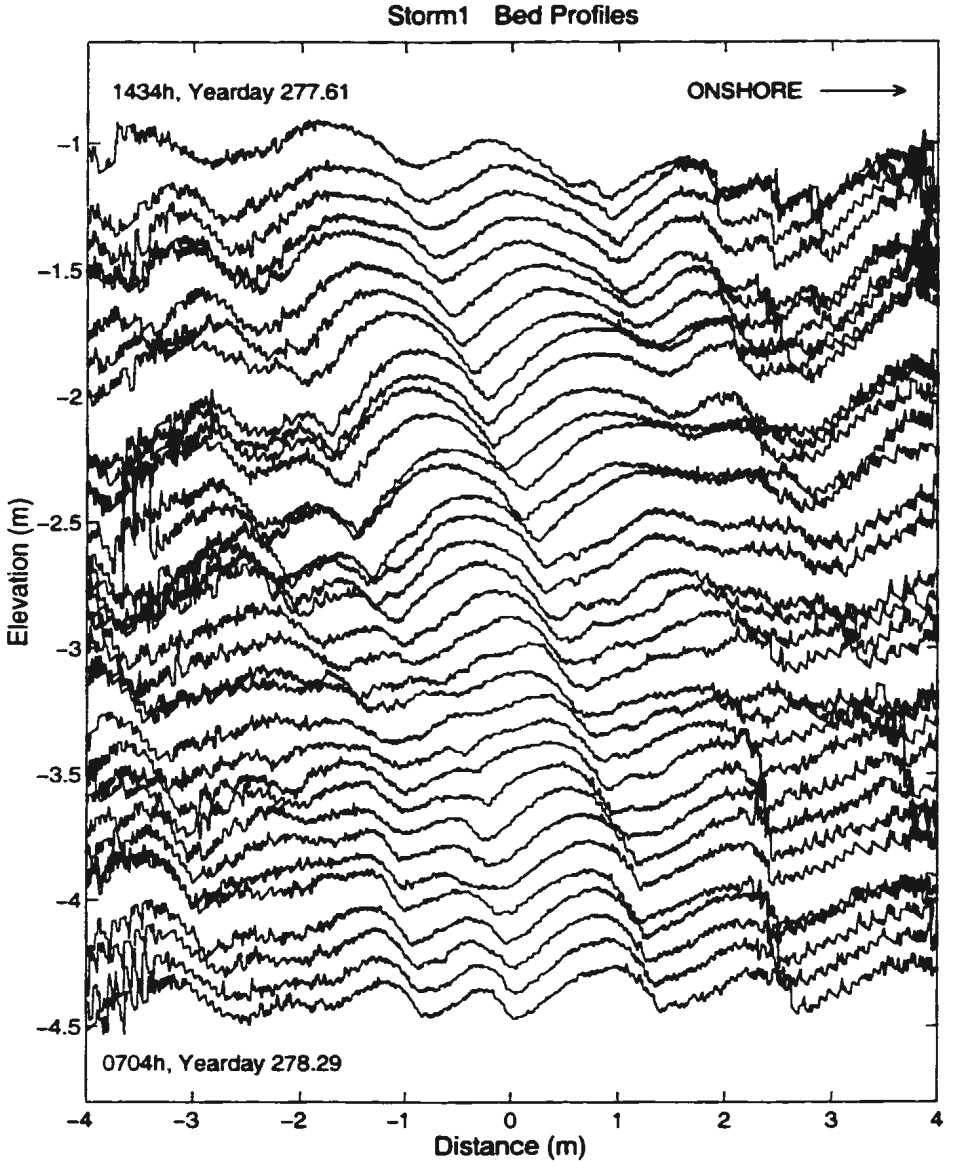

Figure 4.1: A series of 1/2h separated, unfiltered pencil-beam bed profiles during Storm1. Time increases from top to bottom. The times for the first and last profile are shown. Successive profiles are offset by -0.2t meters, where t is the time in hours after the first profile. Note the shoreward migrating bedforms with 15-30 cm heights, O(1 m) horizontal scale, shoreward asymmetry, and persistence in some cases for the full 0.7-d shown.

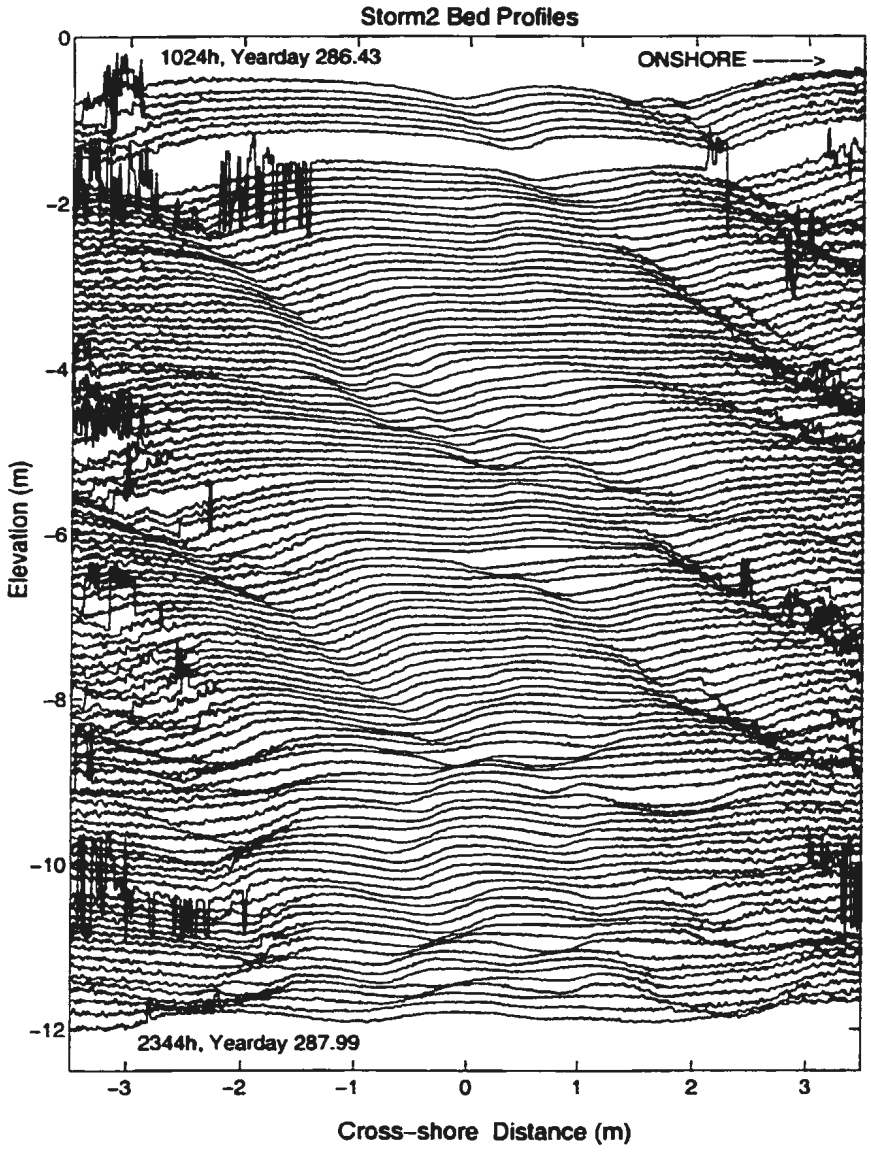

Figure 4.2: A series of 20 minutes separated, unfiltered pencil-beam bed profiles for a 1.6-d interval during Storm2. Time increases from top to bottom. The times for the first and last profile are shown. Successive profiles are offset by -0.2t meters, where t is the time in hours after the first profile. Note the onshore migration early in the interval, and the more confused pattern later, with indication at times of offshore migration and offshore asymmetry.

4.2 Storm2 megaripples

The series of bed profiles for Storm2 (Figure 4.2) shows that megaripples were migrating onshore (to the right of the profiles) during Yearday 286 and through the first half of Yearday 287 during the first stage of Storm2. However, as Storm2 intensified the megaripples started to stall and some megaripples seem to be migrating offshore near the end of Yearday 287, during the second stage of Storm2.

The fan-beam images in Figure 4.4 show the megaripple patterns corresponding to the bed profiles shown in Figure 4.2. These images collected during a 2-hour period on day 287 during the first stage of Storm2, show onshore migrating (to the bottom of the images) lunate megaripples; for example, the group of megaripples at the top of the images seem to be progressively migrating onshore. Some megaripples between 0819h and 0939h show horns which are northward pointing due to strong longshore currents during this period.

Due to strong plumes of suspended sediments towards the end of Storm2, the fan-beam images were relatively poor during this period. However, careful examination of images collected during a 40 minutes interval on yearday 287 during the second stage of Storm2 (Figure 4.5) shows evidence for offshore megaripple migration; for example, the system of megaripples at the upper half of the images between 2319h to 2359h seem to be migrating offshore. However, their horns were northward pointing due to strong longshore currents during this period and there was also a noticiable northward migration.

Figure 4.7 shows the series of low pass filtered backscatter intensity profiles for Storm2 obtained from fan-beam images along the location where the pencil-beam profiles shown in Figure 4.2 were taken. This fan-beam data also show that the large scale features were clearly migrating onshore during the first half of Storm2 and that megaripples stalled and occassionally migrated offshore near the end of Storm2.

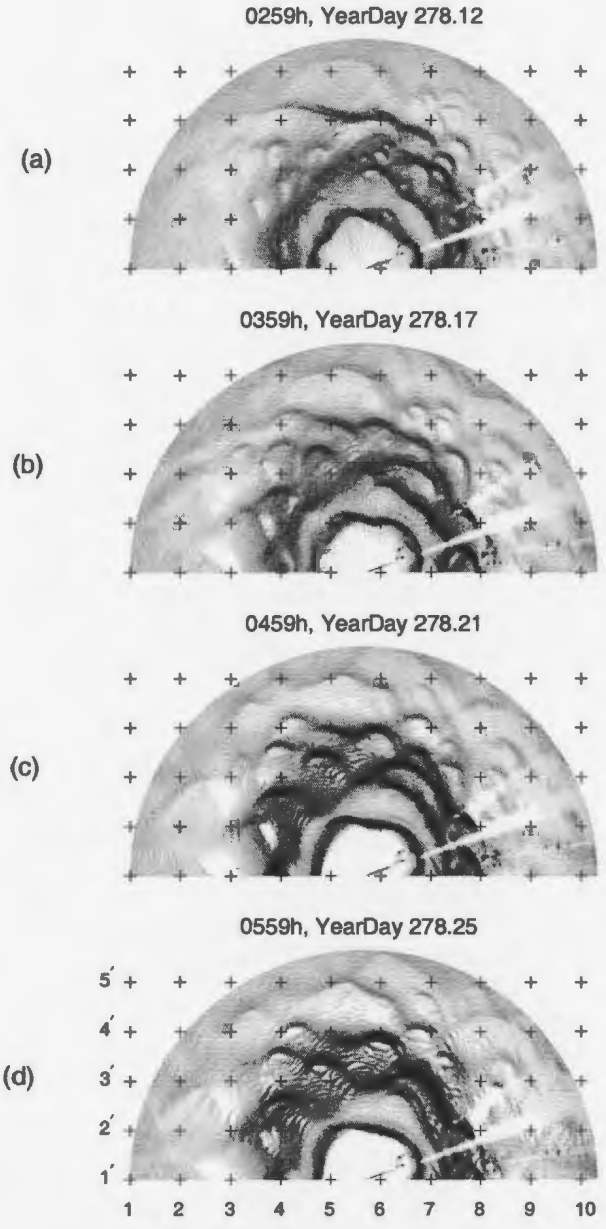

Figure 4.3: Fan-beam images of lunate megaripples during Storm1, on the offshore side of the frame. The crosses are spaced 1 m apart. Note the onshore-oriented lunate forms, 0.5-1 m in horizontal scale. Individual lunate features can be seen to migrate shoreward, near grid point 5,5′ for example (see also Figure 4.1).

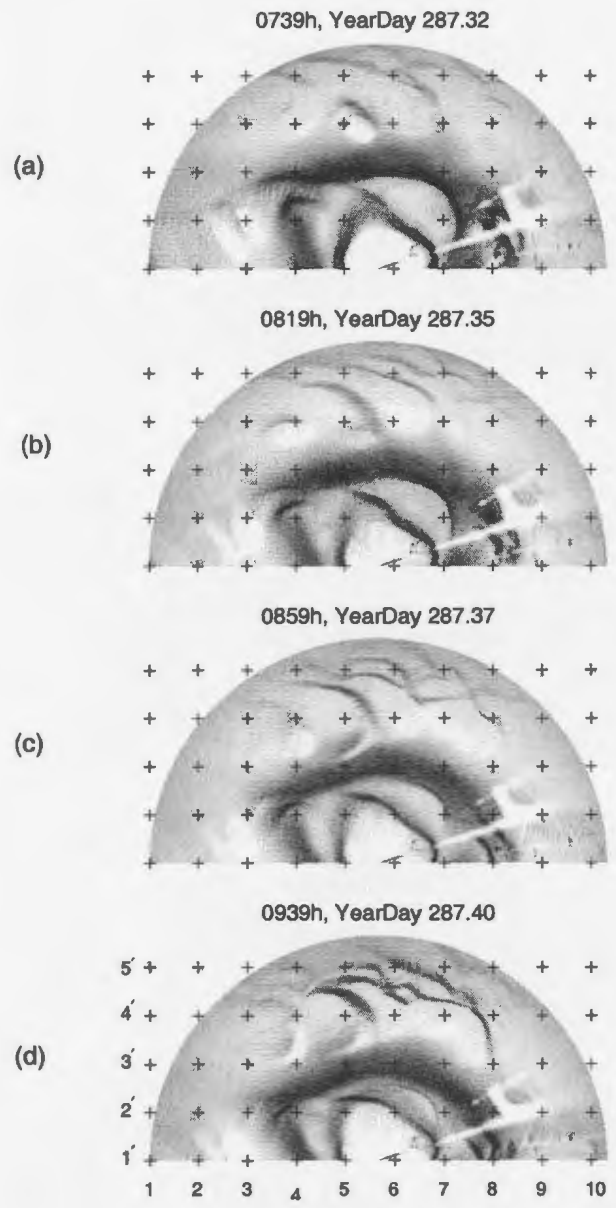

Figure 4.4: Fan-beam images of lunate megaripples during the first stage of Storm2, on the offshore side of the frame. Note the development of longshore (northward) oriented, nearly stationary lunate features (near grid point 5,4′ for example). Features farther offshore were migrating mainly onshore (e.g. near grid point 6,5′).

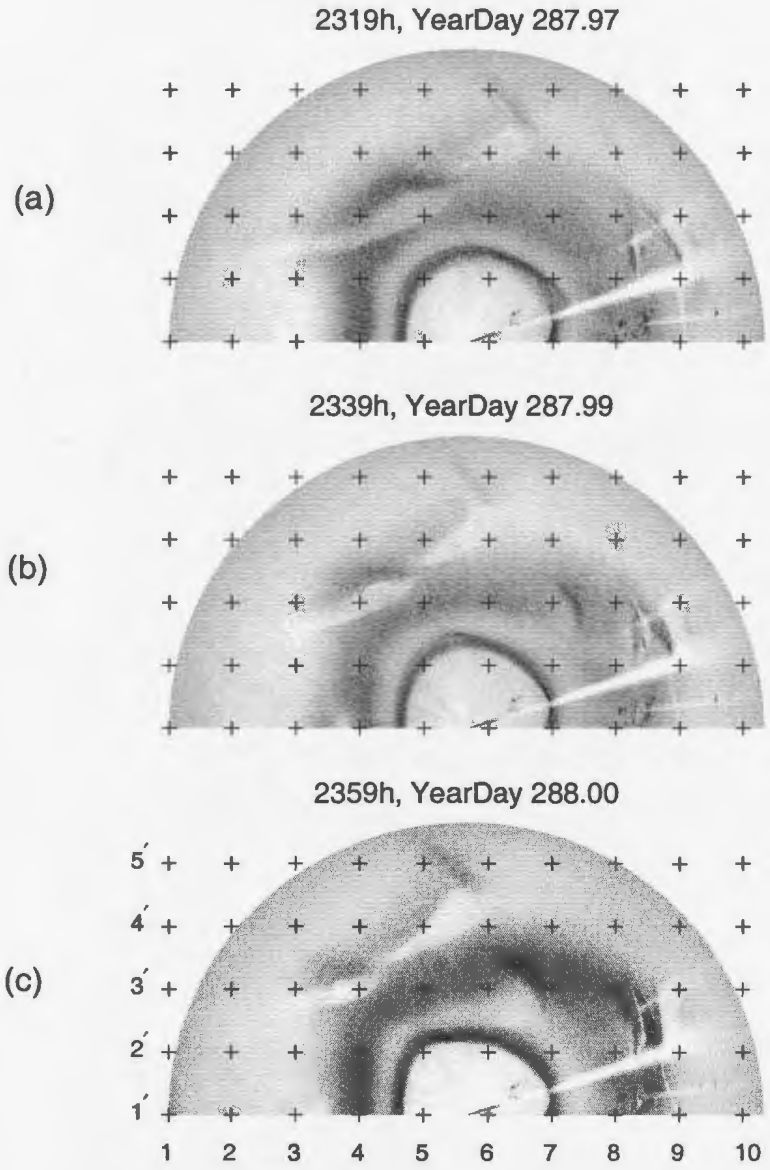

Figure 4.5: Fan-beam images of lunate megaripples during the second stage of Storm2, on the offshore side of the frame. Note the longshore-oriented, northward migrating lunate features (near grid points 6,4′ and 7,3′).

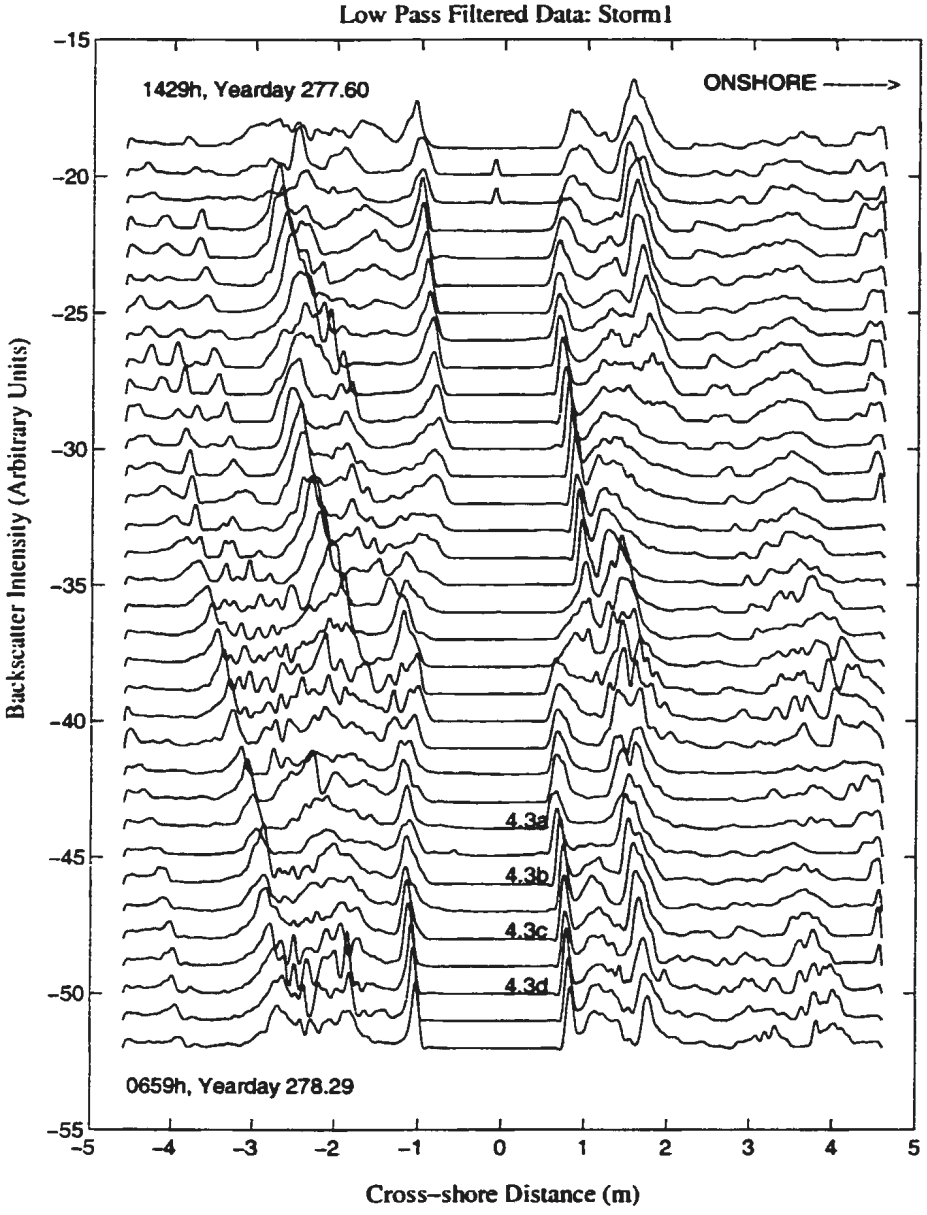

Figure 4.6: Cross-shore profiles of the fan-beam signal amplitude during Storm1 at the times of the pencil-beam bed profiles in Figure 4.1. Time increases from top to bottom. The times for the first and last profiles are shown. Profiles corresponding to images in Figure 4.3 are indicated. Note the onshore migration of individual features.

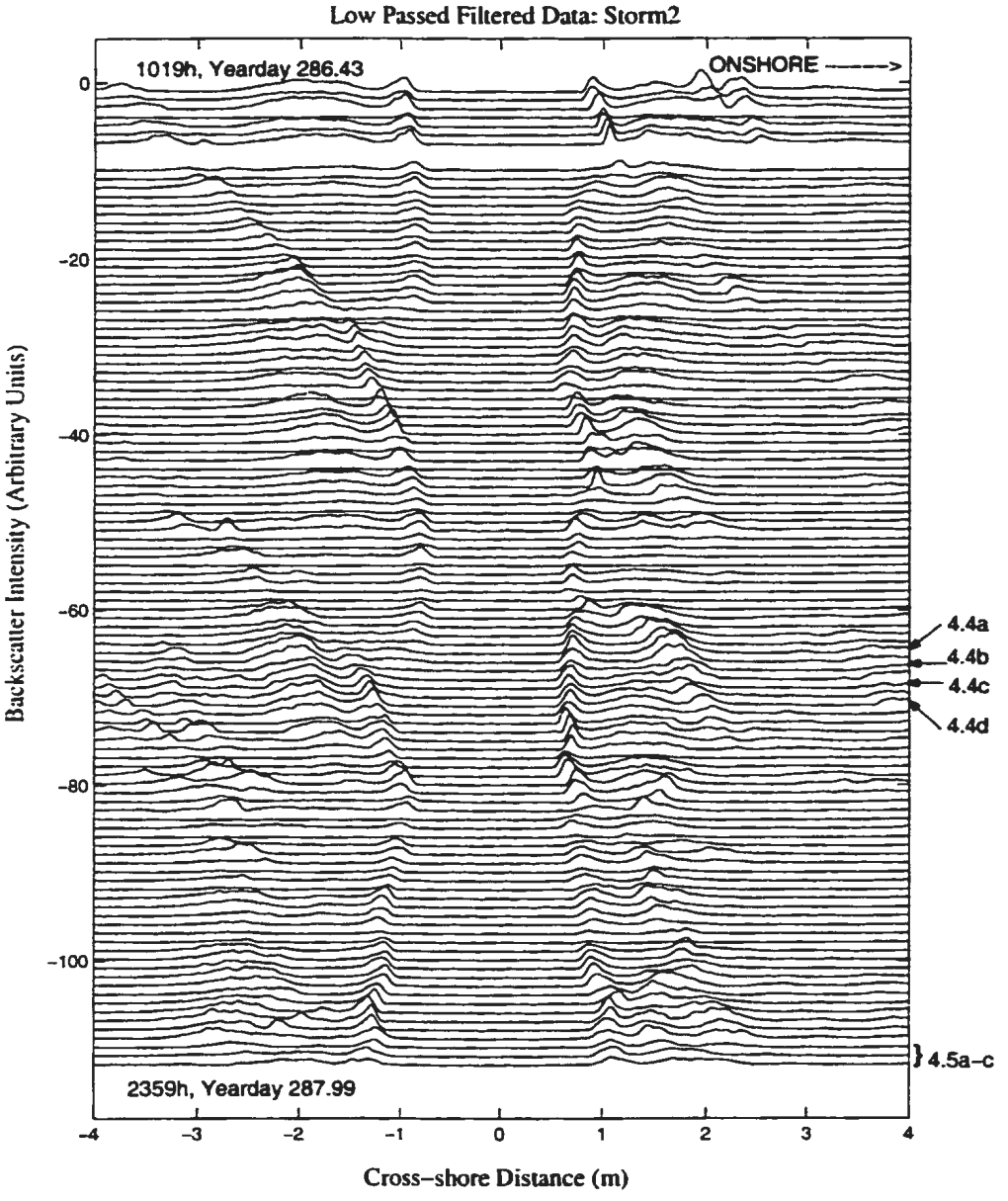

Figure 4.7: Cross-shore profiles of the fan-beam signal amplitude during Storm2 at the times of the pencil-beam bed profiles in Figure 4.2. Time increases from top to bottom. The times for the first and last profiles are shown. Profiles corresponding to the images in Figure 4.4 and Figure 4.5 are indicated. Note general onshore migration except late in the interval, when some individual features appear to migrate offshore.

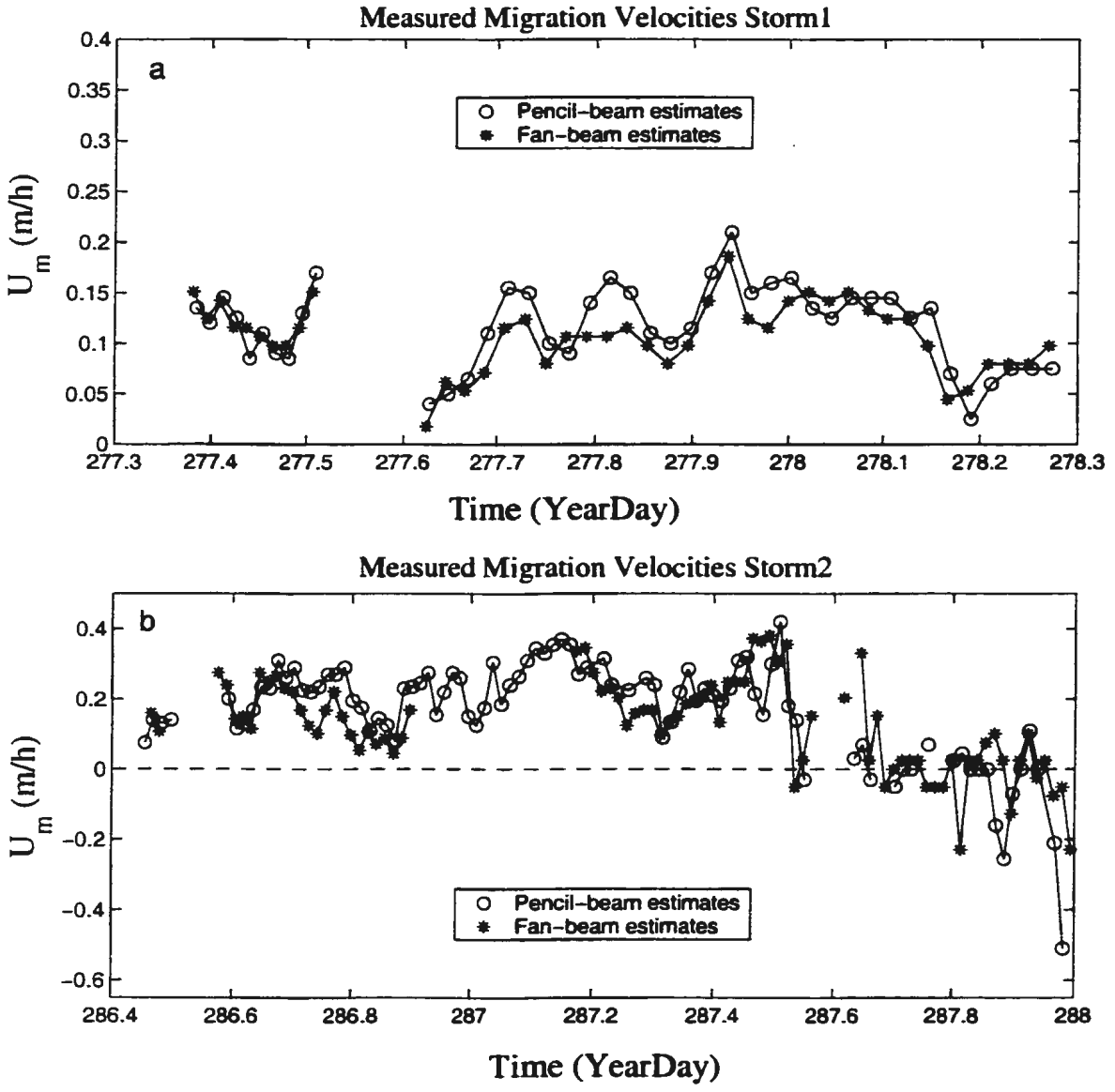

Figure 4.8: Measured cross-shore lunate megaripple migration velocities (U_m) using both pencil-beam and fan-beam data for Storm1 (a) and Storm2 (b). Note general onshore migration, except late in the Storm2 interval. Positive values indicate onshore and negative values indicate offshore migration velocities.

4.3 Measured migration velocities

The measured cross-shore megaripple migration velocities were quantitatively estimated using both cross-correlation of bed profiles and 2-D cross-correlation of fan-beam sub-images. The results are shown in Figure 4.8 for Storm1 and Storm2. The measurements obtained using the two independent cross-correlation methods show a good agreement. Differences are attributed to the fact that fan-beam estimates involved the migration of individual megaripples, and in most cases the largest and most clearly imaged megaripples along the cross-shore line where the pencil-beam was taken. In contrast, the pencil-beam estimates involved bed profiles spanning up to 7 m, therefore covering several megaripples of variable sizes along the profile. Because smaller megaripples are expected to migrate faster than larger ones, pencil-beam estimates that include large and small bedforms give higher average migration velocities. This difference is minimal when megaripples of comparable sizes occupy the field of view. The cross-correlation results are also consistent with the qualitative observations of bed profiles and fan-beam images shown earlier in Figure 4.1 to 4.7.

In summary, the cross-correlation results suggest that lunate megaripples were migrating at 10-20 cm/h onshore during Storm1, 10-40 cm/h onshore during the first stage of Storm2 and 0-50 cm/h offshore during the second stage of Storm2. Megaripples were therefore migrating in the opposite direction of the mean cross-shore current during Storm1 and the first stage of Storm2 (Figure 4.9a and c). The only exception was during the second stage of Storm2 on Yearday 287 when both mean cross-shore water flow and megaripple migration were in the same offshore direction.

The observation of possible offshore megaripple migration is particularly interesting because it could illuminate the flow characteristics that lead to either onshore or offshore megaripple migration. It is also interesting to note that some of the corresponding fan-beam images showed megaripples with their horns consistently oriented shoreward. This observation can also shed light on the direction of megaripple migration with respect to bedform orientation.

Figures 4.10a shows that for weak mean cross-shore flow ($| U |$ less than 15 cm/s),

there is poor correlation between megaripple migration velocities and mean cross-shore water velocities. However, stronger mean cross-shore flow tend to be correlated with the offshore megaripple migration velocities, suggesting that strong offshore mean cross-shore water velocities may have been partly responsible for the observed offshore megaripple migration velocities.

On the other hand, positive values of wave-orbital velocity skewness show a positive correlation with onshore megaripple migration velocities (Figure 4.10b). However, the skewness was always positive. This indicates that wave-orbital velocity skewness may have been primarily responsible for onshore megaripple migration, but cannot by itself explain the observed offshore migration. Positive values of skewness are consistent with non-linear wave theories, where wave-orbital velocities are skewed in the direction of wave propagation. Velocity skewness is calculated from the cross-shore wave-orbital velocity (u_w) using the relation that skewness=$\overline{(u_w)^3}/[\overline{(u_w)^2}]^{3/2}$

Figure 4.9a also shows that the mean longshore flow was directed southward (positive values) at 0-20 cm/s during Storm1. Similarly, for the early stage of Storm2, the mean longshore current was also flowing southward at 0-20 cm/s (Figure 4.9c). However, there were periods of strong northward longshore currents reaching 20-50 cm/s during the second stage of Storm2. This suggests that the cross-shore components of the bed shear stress due to longshore currents may be important for modelling the cross-shore lunate megaripple migration velocities discussed in this thesis.

In general, there appears to be a tendency for megaripples to exhibit long periods of onshore migration during the period when mean cross-shore water flow is less than 20 cm/s offshore, under the dominant influence of wave-orbital velocity skewness. The periods of zero migration or occasional offshore migration seem to occur during the more intense parts of a storm when mean cross-shore water flow exceeds 20 cm/s offshore. During this period, megaripples appear to migrate offshore under the dominant influence of the undertow (mean cross-shore water flow). The strong mean cross-shore water velocities at the end of Storm2 seem to have been chiefly responsible for the observed offshore megaripple migration. However, it is important to mention that some of the apparent offshore migration

may have been associated with development of alongshore migrating lunate forms. These results tend to suggest that both waves and mean currents are likely to be important to any meaningful explanation for the observed on-offshore megaripple migration velocities. in Chapter 4.

The present results for megaripple migration rate with respect to the mean cross-shore water velocity can be compared with previous measurements in the literature; for example, Osborne and Vincent (1992), Hay and Bowen (1993), Vincent and Osborne (1993), Hay and Wilson (1994). These other workers showed that cross-shore lunate megaripples migrate in the opposite direction to the mean cross-shore flow. However, the magnitude of mean cross-shore velocity was rather small for all of these observations. For example, 10 cm/s in Osborne and Vincent (1992), 1.3 cm/s in Hay and Wilson (1994), and in the data reported in this thesis 10-20 cm/s during onshore migration and 25-30 cm/s during offshore megaripple migration.

Vincent and Osborne (1993) compared lunate megaripple migration velocities with non-dimensional wave parameters including Shields parameter for waves, Wave Reynolds number and Mobility number. Their results showed no significant correlation between cross-shore megaripple migration velocities and these parameters. Results obtained using Duck94 data are consistent with Vincent and Osborne's observations. There is no correlation between migration velocities and Mobility number (Figure 4.11c). The comparison between the migration velocities and Shields parameter and Wave Reynolds number also showed a considerable scatter (Figure 4.11a and b). There is therefore no significant correlation between these parameters and the observed megaripple migration velocities. Other wave parameters like u_{rms} also showed weak relationship with the observed migration velocities (Figures 4.9b and d), however none of them could explain the observed offshore migration velocities.

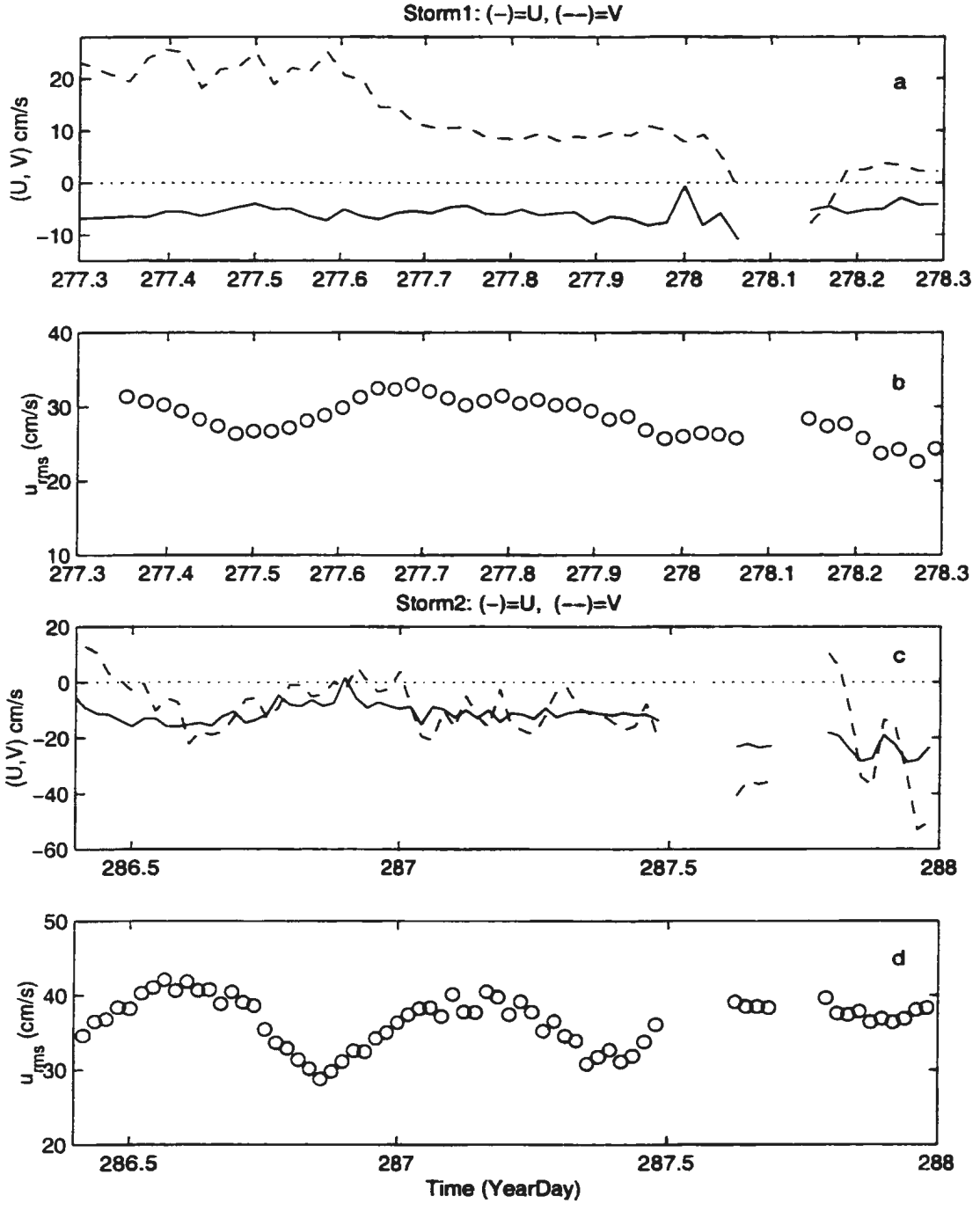

Figure 4.9: Mean cross-shore and alongshore velocities (a) and rms wave-orbital velocities (b) for the days of interest during Storm1. (c and d) show similar measurements for Storm2.

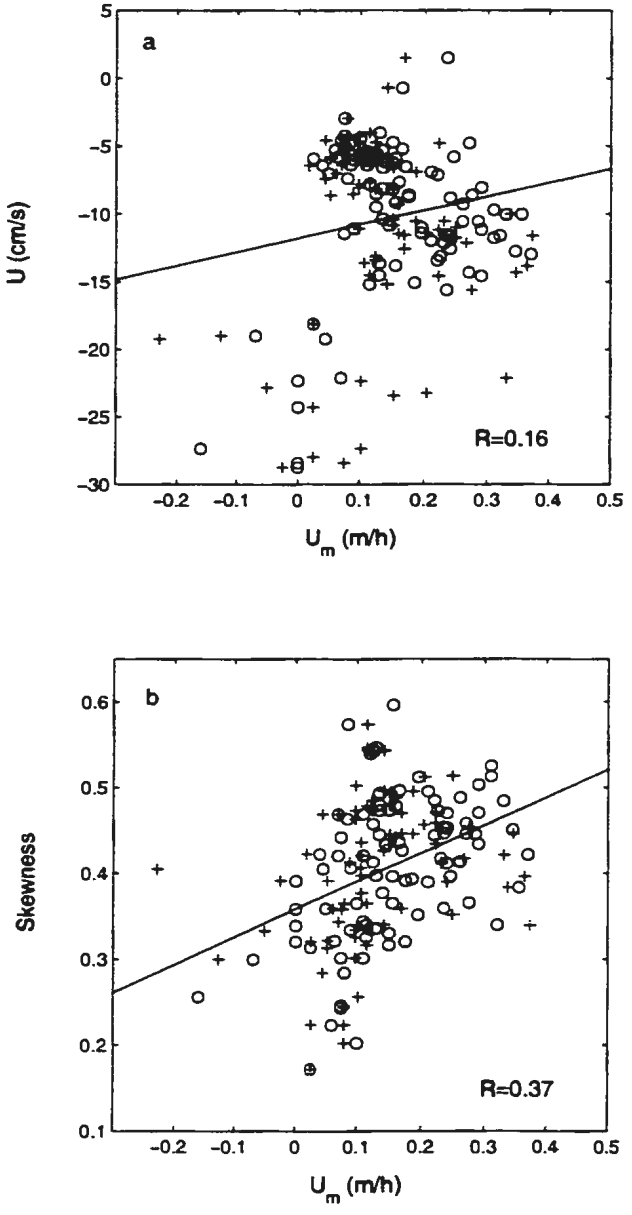

Figure 4.10: Comparison between the observed cross-shore lunate megaripple migration velocities and mean cross-shore velocity (a) and wave-orbital velocity skewness (b) for both Storm1 and Storm2. Fan-beam and pencil-beam estimated migration velocities are represented by plus signs and open circles respectively. The relationships between migration velocity and both skewness and mean cross-shore current are weak.

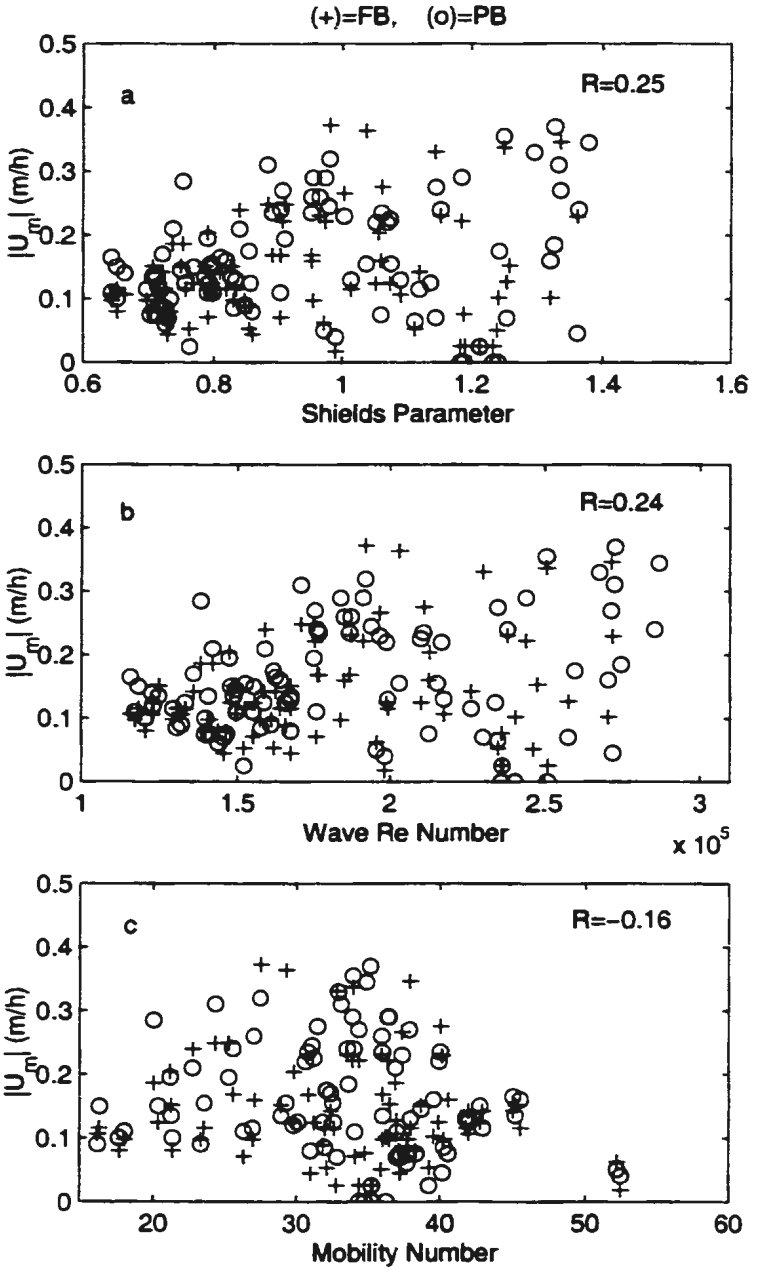

Figure 4.11: Cross-shore lunate megaripple migration velocities compared to the Wave Shields parameter (a), Wave Reynolds number (b) and Mobility number (c) for Storm1 and Storm2. The comparisons using fan-beam estimated migration velocities are shown by (+) and pencil-beam estimates are shown by (o).

Chapter 5

Modelling cross-shore migration velocities

5.1 Bagnold's bedform migration model

Bagnold (1946), while studying the physics of desert dunes, suggested a bedform migration model where the relationship between dune migration velocities (U_m), volumetric bedload sediment transport per unit width (Q_B) and dune height (η) is given by

$$U_m = \frac{Q_B}{[\eta(1-\epsilon)]}, \tag{5.1}$$

where ϵ is the sediment porosity. This model was first applied to unidirectional flows by Bagnold (1946); it is also quoted elsewhere, for example Middleton and Southard (1984, pg. 279); Fredsoe and Deigaard (1992, pg. 266). Recently, this model was applied successfully by Hay and Bowen (1999) in relating longshore lunate megaripple migration with bedload transport under combined flows.

Hay and Bowen (1999) argued that barchans have plan-view shapes roughly similar to those of lunate megaripples but on a much larger scale. Therefore, the suggested bedform migration model in Equation (5.1) may also be applicable to lunate megaripples in marine environments. In this thesis, the Bagnold (1946) model is tested in relating the cross-shore

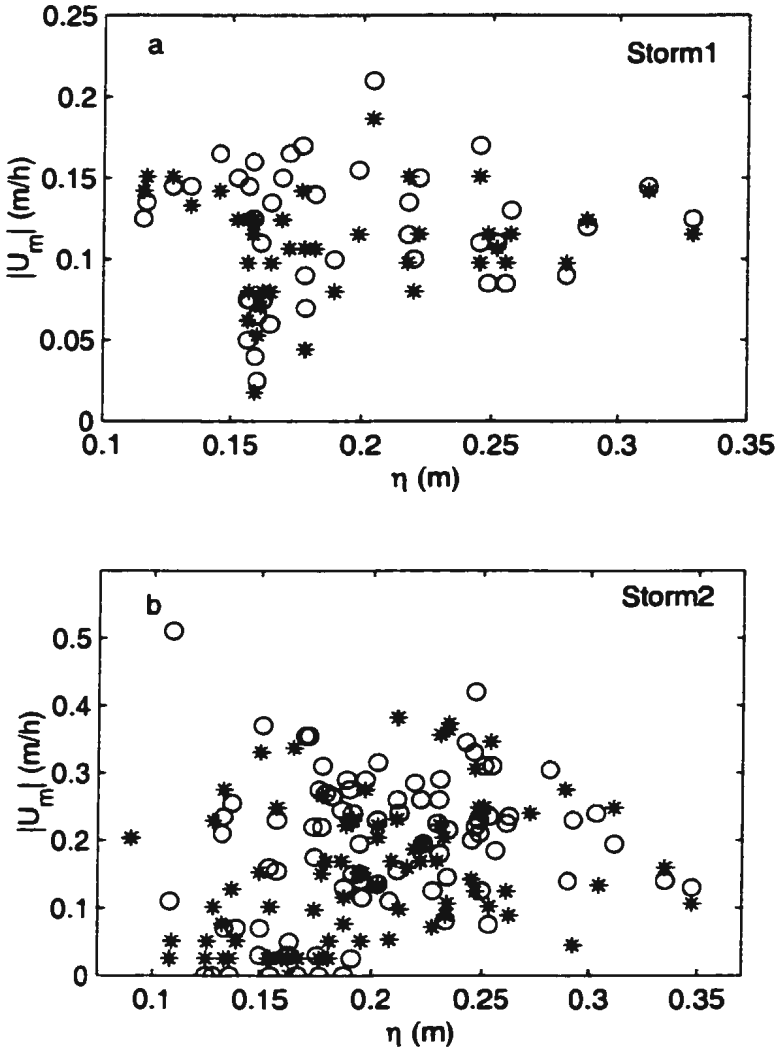

Figure 5.1: Comparison between absolute values of cross-shore migration velocities and mean megaripple heights for Storm1 (a) and Storm2 (b), where (o) and (*) represents comparisons using pencil-beam and fan-beam estimated migration velocities respectively.

lunate megaripple migration velocities with bedload sediment transport under combined flows.

Equation (5.1) suggests that the megaripple migration rate is inversely proportional to megaripple heights provided that the bedload sediment transport remains constant. Similarly, the megaripple migration rate is directly proportional to the bedload sediment transport provided that megaripple height variability remains small. For constant bedload sediment transport, megaripples with smaller heights should migrate faster than larger megaripples.

Comparison of absolute values of measured megaripple migration velocities with measured mean megaripple heights (Figure 5.1) indicates that there is no strong dependence of megaripple migration rate on megaripple height. Megaripple heights were rather constant during the two storms, as shown in Figures 3.9 & 3.10. This in part explains why there is no strong correlation between absolute values of megaripple migration velocities and mean megaripple heights. However, the other explanation which is more relevant here is that bedload sediment transport (Q_B) were not constant. Thus the variability in the measured megaripple migration velocities is mainly due to variations in Q_B, and hence the dependence of megaripple migration velocities on Q_B can be investigated.

5.2 Stress-based bedload transport models

5.2.1 Waves only

One of the objectives of this thesis is to model the measured migration velocities. A good place to start is therefore to compare the migration velocities with the measured waves and currents. However, before that is done, the existing theoretical links between bedform migration and hydrodynamic forcing are examined. Such relationships can be obtained from the previously presented bedload sediment transport formulae.

One commonly applied theory is based on bed shear stress, where bedload sediment transport is normally related to the excess bottom shear stress due to waves and currents. Most shear stress-based models take the general form

$$Q_B = \hat{A}(\tau_b - \tau_{cr})^{\xi}. \qquad (\tau_b > \tau_{cr}) \qquad (5.2)$$

where $\hat{A}$ is a constant normally determined empirically. In many formulae, ξ is some experimentally or theoretically determined exponent, usually 3/2 or 5/2 , τ_b is the bed shear stress, and τ_{cr} is the critical bed shear stress above which bottom sediment starts to move. For unidirectional flows, τ_b can be written as a quadratic function of the mean velocity at some height above the bed. However, in combined flows the contributions of waves and mean currents to the total bed shear stress are interdependent.

For simplicity and because the peak stress during a wave cycle far exceeds the threshold stress, it is assumed that $\tau_b \gg \tau_{cr}$. Initially, the effect of longshore forcing is neglected. Because bed shear stress is proportional to the square of the near bed velocity, the cross-shore component of the time-averaged equation for bedload sediment transport due to waves alone can be written as

$$\overline{Q_{Bx}} = \hat{A}\rho\frac{f_w}{2}\overline{u_w{}^{2\xi}}, \qquad (5.3)$$

where the over bar represents averaging over many wave cycles. If Q_{Bx} is directly proportional to the cross-shore megaripple migration velocities as suggested by Bagnold (1946), then Equation (5.3) forms the basis for the comparison of the measured migration velocities with $\overline{u_w{}^3}$ (for ξ=3/2), which represents wave-orbital velocity skewness, since when this term is normalized by the variance it gives the usual definition of skewness.

5.2.2 Combined waves and mean currents

One of the problems that makes the cross-shore bedload transport particularly difficult to model in the nearshore zone is the fact that the net transport in the cross-shore direction occurs as an accumulation of small differences between the large values of onshore and offshore directed transports; each of these individual quantities must be evaluated correctly (Horikawa, 1988, pg. 167).

The approach taken here is to model the observed migration velocities using simple stress-based models under the combined effect of waves and currents. The formulation of the required cross-shore forcing should therefore start with the correct expression for the resultant bottom shear stress for collinear waves and currents. Some examples of stress-based bedload transport models commonly applied in nearshore environments include Meyer-Peter and Müller (1948), Madsen and Grant (1977), Sleath (1978), Watanabe et al. (1980), Watanabe (1982), Vincent et al. (1981) and recently Sleath (1995).

Following Christoffersen and Jonsson (1985) and Sleath (1995), the resultant bed shear stress for waves and currents is given by a vector sum of the wave and current shear stresses,

$$\tau_b = [{\tau_c}^2 + {\tau_w}^2 + 2(\tau_{cx}\tau_{wx} + \tau_{cy}\tau_{wy})]^{1/2}, \tag{5.4}$$

where τ_c and τ_w are the magnitudes of the bed shear stress felt by the mean current and the waves respectively. That is,

$${\tau_c}^2 = {\tau_{cx}}^2 + {\tau_{cy}}^2, \tag{5.5}$$

and

$${\tau_w}^2 = {\tau_{wx}}^2 + {\tau_{wy}}^2. \tag{5.6}$$

where the subscript x and y denote the (x, y) components. The components of the mean current bed shear stress are

$$\tau_{cx} = \rho\frac{1}{2}f_c U_c U. \tag{5.7}$$

and

$$\tau_{cy} = \rho\frac{1}{2}f_c U_c V, \tag{5.8}$$

where (U, V) are the mean cross-shore and alongshore velocities respectively and $U_c^2 = U^2 + V^2$.

The components of the wave bed shear stress are

$$\tau_{wx} = \rho \frac{1}{2} f_w U_{wo} u_w, \tag{5.9}$$

and

$$\tau_{wy} = \rho \frac{1}{2} f_w U_{wo} v_w. \tag{5.10}$$

where (u_w, v_w) are the x-y components of wave-orbital velocity outside the wave boundary layer, U_{wo} is the wave-orbital velocity amplitude, defined later.

The equations for bed shear stress for waves and currents given in above were developed for a mean current in the presence of monocromatic waves, and in general the values of the friction factors f_c and f_w differ from the current-only and wave-only cases. In nearshore field conditions, however, the waves are generally irregular and distributed over a range of frequencies in the sea and swell band, and significant energy is often present in the infragravity frequency band between zero frequency mean current and the (sea and swell) incident wave band.

In order to investigate the relative importance of the different transport components by waves, mean currents and infragravity components, the instantaneous cross-shore (u) and alongshore (v) velocities are separated into three frequency bands such that

$$u(t) = \tilde{u}(t) + U_{ifg}(t) + U \tag{5.11}$$

$$v(t) = \tilde{v}(t) + V_{ifg}(t) + V \tag{5.12}$$

where $(\tilde{u}, \tilde{v})$, (U_{ifg}, V_{ifg}) and (U, V)represent the wave, infragravity and mean cross-shore and alongshore velocity components respectively, and t is the time during each data run of

1/2h duration. The relative contribution of the different bands to the stress is not so straight forward, however, due in part to the question of how best to specify a friction factor for the infragravity band. Here, the calculations were performed for two cases, when $U_{ifg}(t)$ and $V_{ifg}(t)$ are treated either as waves or as currents.

When $U_{ifg}(t)$ and $V_{ifg}(t)$ are treated as waves, the xy-components of the wave velocity $\vec{u}_w$ are

$$[u_w(t), v_w(t)] = [\bar{u}(t) + U_{ifg}(t), \quad \bar{v}(t) + V_{ifg}(t)], \tag{5.13}$$

and the current velocity is

$$\vec{U}_c = [U, V]. \tag{5.14}$$

as shown in Figure 5.2

When the infragravity band is treated as currents, the wave velocity is

$$\vec{u}_w = (\bar{u}, \bar{v}) \tag{5.15}$$

and the current velocities are

$$[\mathcal{U}(t), \mathcal{V}(t)] = [U_{ifg}(t) + U, \quad V_{ifg}(t) + V]. \tag{5.16}$$

as shown in Figure 5.2.

Following Hay and Bowen (1999), the cross-shore component of the time-averaged bedload transport is given by

$$\overline{Q}_{Bx} = \hat{A}\overline{|\tau_b|^{\xi-1}\tau_{bx}} \tag{5.17}$$

where

$$\tau_{bx} = \tau_{cx} + \tau_{wx}. \tag{5.18}$$

Thus,

$$Q_{Bx} = [\hat{A}(\rho\sqrt{f_c f_w})^{\xi-1}(\rho f_c)]\chi_x(t). \tag{5.19}$$

When the infragravity band is treated as waves, $\overline{\chi_x(t)}$ in Equation (5.19) is given by

$$\overline{\chi_x(t)} = \overline{|Z(t,t_s)|^{\xi-1}\left[\frac{U_c}{2}U + \frac{\alpha}{2}U_{wo}(t_s)U_{ifg}(t) + \frac{\alpha}{2}U_{wo}(t_s)u_w(t)\right]}, \tag{5.20}$$

where $Z(t,t_s)$ is given by

$$Z(t,t_s) = \left\{\frac{U_c^4}{4\alpha} + \frac{\alpha U_{wo}(t_s)^2[u_w(t)^2 + v_w(t)^2]}{4} + \frac{U_c U_{wo}(t_s)}{2}[Uu_w(t) + Vv_w(t)]\right\}^{1/2} \tag{5.21}$$

and $\alpha = f_w/f_c$ is the wave and current friction factor ration, and t_s is a slow time scale defined below.

When the infragravity waves are treated as slowly varying currents, $\overline{\chi_x(t)}$ is given by

$$\overline{\chi_x'(t)} = \overline{|\mathcal{Z}(t,t_s)|^{\xi-1}\left[\frac{\mathcal{U}_c(t)}{2}U + \frac{\mathcal{U}_c(t)}{2}U_{ifg}(t) + \frac{\alpha}{2}\mathcal{U}_{wo}(t_s)\tilde{u}(t)\right]}, \tag{5.22}$$

where $\mathcal{Z}(t,t_s)$ is given by

$$\mathcal{Z}(t,t_s) = \left\{\frac{\mathcal{U}_c(t)^4}{4\alpha} + \frac{\alpha\mathcal{U}_{wo}(t_s)^2[\tilde{u}(t)^2 + \tilde{v}(t)^2]}{4} + \frac{\mathcal{U}_c(t)\mathcal{U}_{wo}(t_s)}{2}[\mathcal{U}(t)\tilde{u}(t) + \mathcal{V}(t)\tilde{v}(t)]\right\}^{1/2} \tag{5.23}$$

Similarly, Q_{By} is given by Equation (5.19) with χ_x replaced by χ_y, where

$$\overline{\chi_y(t)} = \overline{|Z(t,t_s)|^{\xi-1}\left[\frac{U_c}{2}V + \frac{\alpha}{2}U_{wo}(t_s)V_{ifg}(t) + \frac{\alpha}{2}U_{wo}(t_s)v_w(t)\right]}, \tag{5.24}$$

and

$$\overline{\chi'_y(t)} = \overline{|\mathcal{Z}(t,t_s)|^{\xi-1}\left[\frac{\mathcal{U}_c(t)}{2}V + \frac{\mathcal{U}_c(t)}{2}V_{ifg}(t) + \frac{\alpha}{2}\mathcal{U}_{wo}(t_s)\bar{v}(t)\right]}. \tag{5.25}$$

In Equation (5.20) and (5.22) the first term inside the square brackets represents the transport associated directly with the mean current, and the second and third terms represent the infragravity band and wave band transports respectively.

In order to calculate $\overline{\chi_x(t)}$ in Equation (5.20) and $\overline{\chi'_x(t)}$ in Equation (5.22), the values of α and wave-orbital velocity amplitude (U_{wo}) need to be estimated, all the other parameters are readily obtained from the measured velocities. As will be discussed in the next section, the values of α were obtained by model fitting with the measured migration velocities. However, the approach used to estimate U_{wo} can influence in the fitted α values. Two approaches were therefore used in estimating U_{wo} and their results compared.

5.2.3 Wave-orbital velocity amplitude

The significant wave-orbital velocity may be estimated from the longshore and cross-shore velocities such that $U_{wo} = 2\sqrt{{u_{rms}}^2 + {v_{rms}}^2}$ (Thornton and Guza, 1983). Wave-orbital velocity amplitude estimated using this approach is here referred to as $2U_{rms}$. In this case U_{wo} is a constant for each 1/2-h data run.

Another approach is to calculate the orbital velocity amplitude for individual waves from the peak amplitudes for each half-wave cycle as shown in Figure 5.3. This estimate is given by

$$U_{wo}(t_s) = \frac{A_1(t_s) + A_2(t_s)}{2}. \tag{5.26}$$

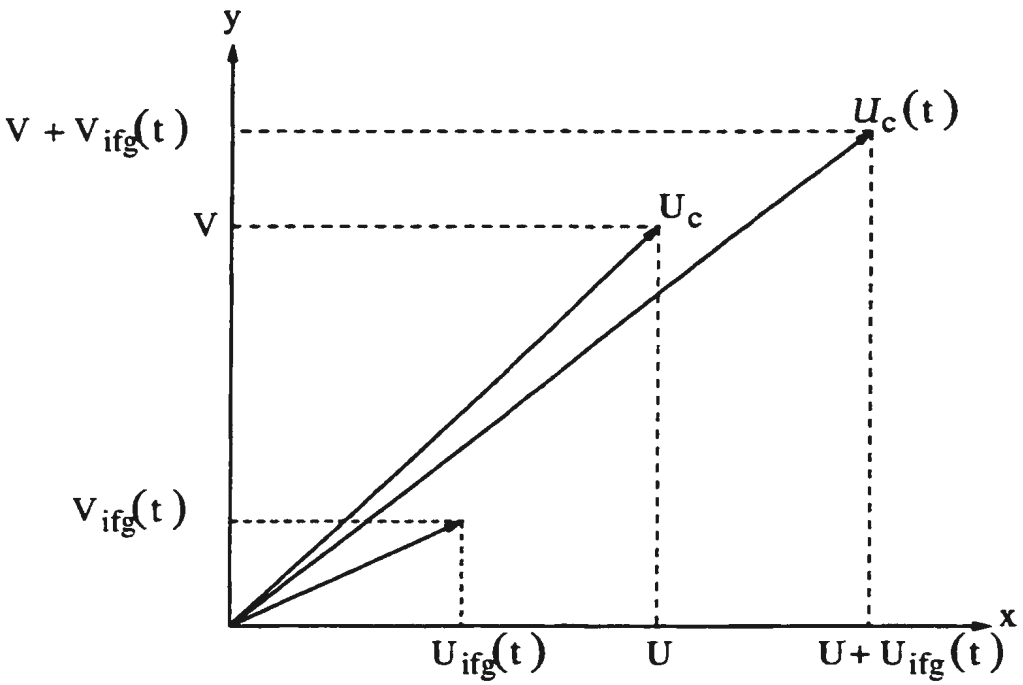

Figure 5.2: Schematic diagram showing the velocity components used to obtain U_c (and $\mathcal{U}_c$) when $U_{ifg}(t)$ and $V_{ifg}(t)$ are treated as waves (and slowly varying currents).

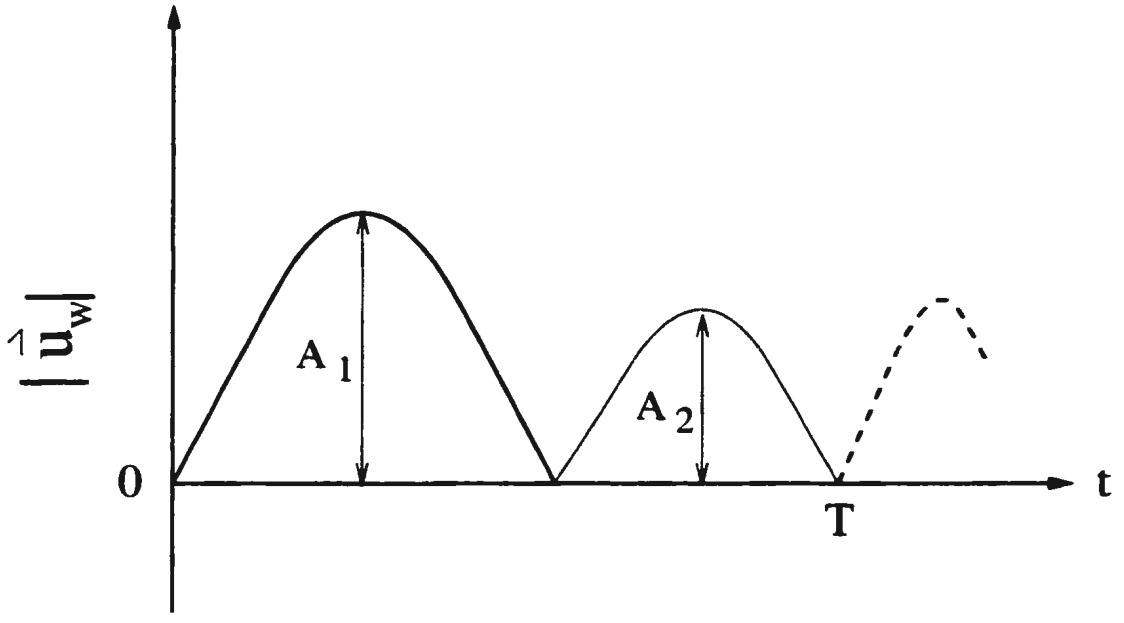

Figure 5.3: Schematic diagram showing the definition of wave-orbital velocity amplitude for a single wave used in Equation (5.26), where T is the wave period. The dashed line represents the continuation of the time series.

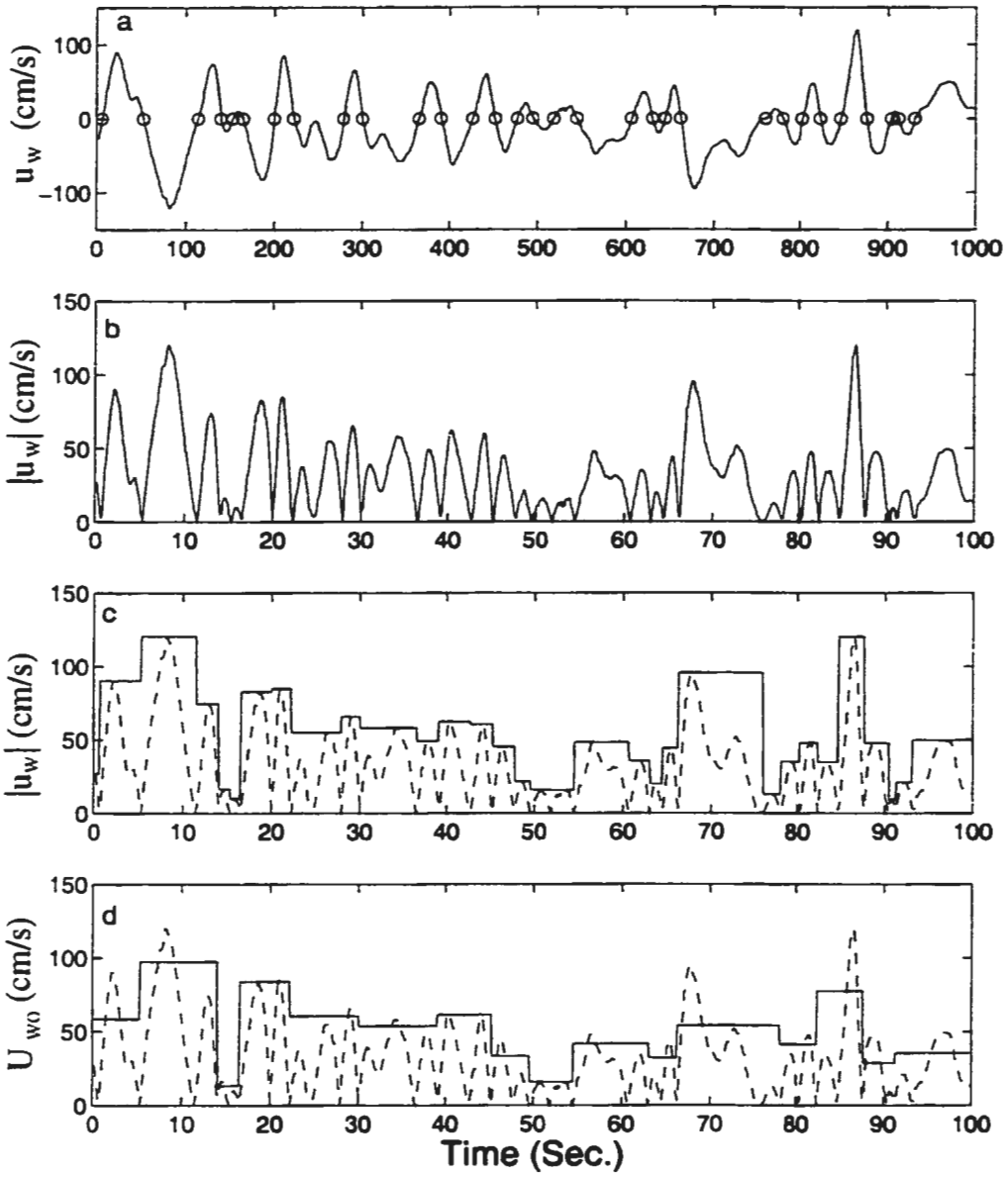

Figure 5.4: Example of the method used to determine wave-orbital velocity amplitudes using the $0.5U_{pp}$ approach. (a) shows the wave-orbital velocity record where the zero crossings are shown by (o) which marks the half wave cycles, (b) shows the magnitude of wave-orbital velocities for each half wave cycle, (c) shows the steps which indicate the peak velocity amplitudes for each half wave cycle, and (d) shows the wave-orbital velocity amplitude obtained by averaging the peak amplitudes of successive half wave cycles.

where $A_1(t_s)$ and $A_2(t_s)$ represent the peak amplitudes during successive half cycles of a given wave.These amplitudes vary from wave to wave, and therefore on a slow time scale t_s defined as

$$t_s = \sum_{n=0}^{N}(n-1)T_n \tag{5.27}$$

where T is the wave period and N the number of points for a single data run. Equation (5.26) is equivalent to a half the peak-to-peak height and thus is designated the $0.5U_{pp}$ approach. When the infragravity band is treated as waves, A_1 and A_2 are obtained from $\sqrt{u_w(t)^2 + v_w(t)^2}$. When the infragravity band is treated as currents, A_1 and A_2 are obtained from $\sqrt{\bar{u}(t)^2 + \bar{v}(t)^2}$ and the wave-orbital velocity amplitude is designated by $U_{wo}(t_s)$.

The $0.5U_{pp}$ approach accounts for every wave, while the total wave-orbital velocity amplitude estimated using the $2U_{rms}$ approach represents all waves by a single statistic. The wave-orbital velocity amplitude is mathematically given by the average of the two peak velocities for the forward and backward strokes over the wave period, which is exactly the basis for the $0.5U_{pp}$ approach. Both $2U_{rms}$ and $0.5U_{pp}$ approaches were investigated for modelling the measured migration velocities.

Figure 5.4 shows an example of the $0.5U_{pp}$ approach used in estimating the wave-orbital velocity amplitude. The amplitudes of velocities in forward and backward strokes for each wave cycle were averaged to obtain the wave-orbital velocity amplitude given in Figure 4.3d.

5.2.4 Friction Factor Ratio α

The problem of estimating wave and current friction factors in combined flows has been reviewed by Nielsen (1992, p.147). Following Nielsen (1992), the flat-bed wave friction factor without currents and for fixed sand grain roughness can be computed using

$$\hat{f}_w = exp\left(5.213\left(\frac{K_N}{A_{ws}}\right)^{0.194} - 5.977\right). \tag{5.28}$$

where the 'hat' here denotes fixed roughness, A_{ws} is the significant wave orbital semi-excursion, and K_N is the Nikuradse sand roughness, which is equal to 2.5 times the median grain diameter (Jonsson, 1966; Nielsen, 1992, p.105). Using DUCK94 data values for significant wave-orbital velocity of 65-90 cm/s, 6-8 s wave periods, and 0.02 cm median grain diameter, Equation (5.28) gives $\hat{f}_w$ in the range of $8\text{x}10^{-3}$ to $9.5\text{x}10^{-3}$.

Similarly, the flat-bed current friction factor without waves for immobile beds can be estimated from the grain diameter using the Manning-Strickler formula (Sleath, 1984 p.220)

$$\hat{f}_c = \frac{0.122}{4}\left(\frac{K_N}{h}\right)^{1/3}, \tag{5.29}$$

where 'hat' again denotes fixed roughness, h is the water depth, and K_N is taken to be 2.5 times median grain diameter. For 3 m water depth, Equation (5.29) gives $\hat{f}_c$=$1.7\text{x}10^{-3}$.

Thus the fixed grain roughness values of α estimated from waves-only and currents-only values would be O(10). However, for combined flows the friction coefficients are different, and in particular f_c is expected to increase (Hay and Bowen, 1999). Therefore, one might expect on this basis that α should be O(10) or less.

The values of wave and current friction factors were not measured during DUCK94 experiment, therefore the ratio f_w/f_c here referred to as α were estimated by fitting with the measured migration velocities. Figure 5.5 shows the correlation coefficients between $\overline{\chi}_x$ and the measured migration velocities as a function of α. Peak-to-peak and rms approaches were used in determining the wave-orbital velocity amplitudes with infragravity velocities treated as either currents or waves. Two stress exponents, $\xi = 5/2$ and $\xi = 3/2$, were investigated.

The peak correlation coefficient for $0.5U_{pp}$ approach and $\xi = 5/2$ corresponds to $\alpha = 2$, while the peak correlation coefficient for $2U_{rms}$ approach and $\xi = 5/2$ corresponds $\alpha = 4$ (Figure 5.5a). Likewise, the peak correlation coefficient for $0.5U_{pp}$ approach and $\xi = 3/2$

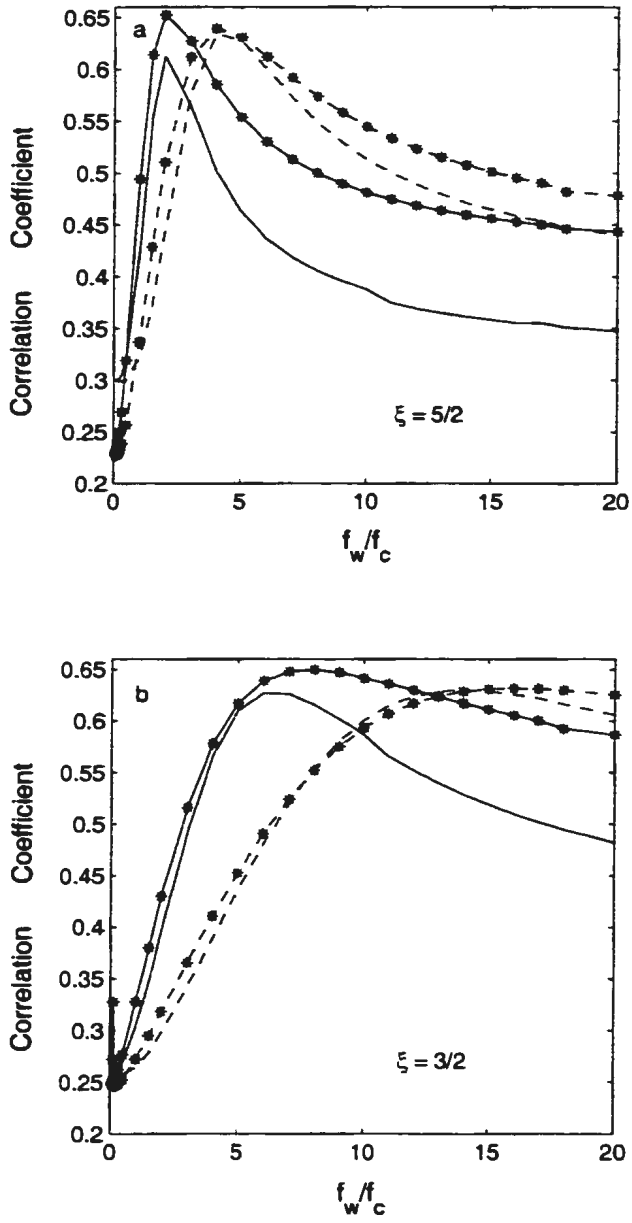

Figure 5.5: Correlation coefficients between measured migration velocities and $\overline{\gamma_x}$ as a function of friction coefficient ratio, $\alpha = f_w/f_c$. The solid lines are the results for $U_{wo}(t_s) = 0.5U_{pp}(t)$; the dashed lines for $U_{wo} = 2U_{rms}$. The symbol (*) is for the case with infragravity velocities treated as waves; lines with no symbols are for infragravity velocities treated as currents.

Table 5.1: Maximum correlation coefficients (R) for the comparison of measured megaripple migration velocities with $\overline{\chi_x}$ computed using various approaches of estimating wave-orbital velocity amplitudes, ξ values and $\alpha = f_w/f_c$ ratios.

U_{wo} Approach	ξ	α	R
$0.5U_{pp}$ & U_{ifg}, V_{ifg} as waves	3/2	8	0.65
$0.5U_{pp}$ & U_{ifg}, V_{ifg} as currents	3/2	6	0.63
$0.5U_{pp}$ & U_{ifg}, V_{ifg} as waves	5/2	2	0.65
$0.5U_{pp}$ & U_{ifg}, V_{ifg} as currents	5/2	2	0.61
$2U_{rms}$ & U_{ifg}, V_{ifg} as waves	3/2	16	0.63
$2U_{rms}$ & U_{ifg}, V_{ifg} as currents	3/2	14	0.63
$2U_{rms}$ & U_{ifg}, V_{ifg} as waves	5/2	4	0.64
$2U_{rms}$ & U_{ifg}, V_{ifg} as currents	5/2	4	0.63

is consistent with $\alpha = 6$, while the peak correlation coefficient for $2U_{rms}$ using $\xi = 3/2$ is consistent $\alpha = 15$ (Figure 5.5b). Note the differences in breadth of the correlation functions. The summary of the peak correlation coefficients (R) for the comparison between $\overline{\chi}_x$ and the measured migration velocities is also given in Table 5.1. The values of R ranged from 0.61-0.65 for all the considered cases.

The results show that there is not a big change in R when $\xi = 3/2$ and $\xi = 5/2$ are used for either $0.5U_{pp}$ or $2U_{rms}$ approaches, with infragravity wave velocities treated as either waves or currents. The values of α seem to be mainly dependent on the magnitude of ξ: consistently a factor of 3-4 larger for $\xi = 3/2$ compared to $\xi = 5/2$. The values of α seem to be reasonably comparable to the estimated value of $\hat{\alpha}$ for $0.5U_{pp}$ and $\xi = 3/2$, or for $2U_{rms}$ and $\xi = 5/2$. The values of α were a factor of 2 smaller for $0.5U_{pp}$ approach and $\xi = 5/2$ compared to estimated values of $\hat{\alpha}$. On the other hand the values of α were a factor of 3 larger for $2U_{rms}$ approach and $\xi = 3/2$ compared to $\hat{\alpha}$. The α values shown in Table 5.1 were used in modelling the megaripple migration velocities.

In summary, treating infragravity velocities as waves consistently improved the comparison of and $\overline{\chi}_x$ with the measured migration. The results for the case without longshore stresses are presented in Appendix B, where the values R ranged from 0.57-0.63: about

10% less than the values shown in Table 5.1.

5.2.5 Model results

Most of the existing stress-based sediment transport models are written in non-dimensional form. Therefore as in Sleath (1995), the time-averaged bedload transport rate in Equation (5.17) is non-dimensionalized by $[(s-1)gD^3]^{1/2}$, where s is the specific gravity of sediments. Similarly the bed shear stresses are non-dimensionalized by $[\rho(s-1)gD]$. Thus the non-dimensional cross-shore time-averaged bedload transport rate in Equation (5.19) can be written as

$$\Phi_{Bx} = \frac{\overline{Q_{Bx}}}{[(s-1)gD^3]^{1/2}} = \frac{A(\sqrt{f_c f_w})^{\xi-1}(\rho f_c)}{[\rho(s-1)gD]^{\xi}}\overline{\chi_x(t)}.$$

Therefore

$$\overline{Q_{Bx}} = \frac{A(\sqrt{f_c f_w})^{\xi-1} D f_c}{[(s-1)gD]^{\xi-1/2}}\overline{\chi_x(t)}. \tag{5.30}$$

Equation (5.1) and Equation (5.30) are then combined to obtain

$$U_m = A\left[\frac{(\sqrt{f_c f_w})^{\xi-1} f_c D/\eta}{(1-\epsilon)[(s-1)gD]^{\xi-1/2}}\right]\overline{\chi_x(t)}. \tag{5.31}$$

which is the model estimate of cross-shore migration velocity. The values of current friction factor (f_c) in Equation (5.31) needed to be specified. Once f_c is known, the values of wave friction factor, f_w, were directly obtained using estimated values of α. The procedure used here was to select the most reasonable f_c values that produced theoretical migration velocities that agreed well with the measurements. Other parameters in the model are: relative density of sediments (s=2.7), median diameter of sediments at Duck (D=0.02 cm)

and porosity ($\epsilon = 0.4$). The value of the empirical constant $A = 0.4$ for $\xi = 5/2$ is used following Sleath (1995) for rough beds. Similarly, for ξ =3/2, the value of $A = 8$ is applied following Meyer-Peter and Müller (1948). Both $0.5U_{pp}$ and $2U_{rms}$ approaches with U_{ifg} and V_{ifg} treated as either waves or slowly varying currents were tried.

The cross-shore migration velocities were therefore computed from Equation (5.31) using α values given in Table 5.1 and $\chi_x(t)$ and $\chi'_x(t)$ for the cases when $U_{ifg}(t)$ and $V_{ifg}(t)$ are treated either as waves or as slowly varying currents respectively. Figure 20 shows example of the results from the contribution by the wave band, infragravity band and mean components in the calculated $\overline{\chi_x}$ and $\overline{\chi'_x}$ using $\xi = 3/2$ model for Storm2. The results for Storm1 and $\xi = 5/2$ model were similar and are not shown. These results shows that the calculated contribution by the wave band was consistently positive (onshore) when $U_{ifg}(t)$ and $V_{ifg}(t)$ are treated as either currents (Figure 5.6a) or as waves (Figure 5.6b). In the contrary, the calculated contribution by both infragravity band and mean components were consistently negative (offshore) for both cases. This shows that depending on the choice of the friction coefficients, the infragravity band contribution can be made to be dominant compared to the contribution by mean currents.

Treating $U_{ifg}(t)$ and $V_{ifg}(t)$ as waves also in general tend to increase the noise in the sum of calculated contribution due to the three components. Although the contribution by both infragravity band and mean components were both in the offshore direction, the magnitudes were much larger for the mean component compared to the infragravity band near the end of Storm2. This is the period when megaripples occasionally migrated offshore. Therefore, it gives another indication that the strong mean cross-shore velocities observed near the end of Storm2 were primarily responsible for the observed offshore lunate megaripple migration. Figure 5.7 shows the plot of infragravity band contribution in the calculation of $\chi_x(t)$ againt the contribution in the calculation of $\chi'_x(t)$. The contribution by the infragravity band was rather small in the case when $U_{ifg}(t)$ and $V_{ifg}(t)$ are treated as currents ($\chi'_x(t)$) compared to when they are treated as waves ($\chi_x(t)$).

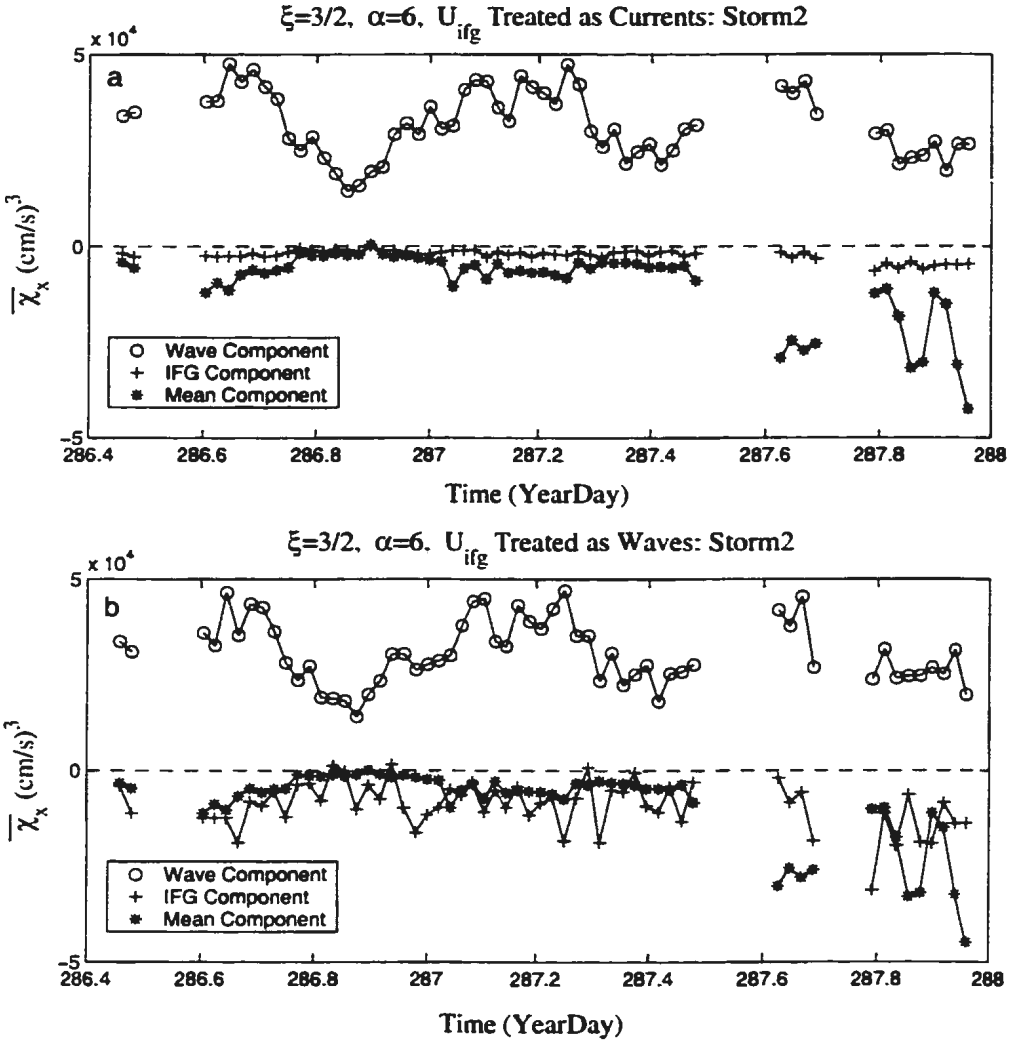

Figure 5.6: Wave, infragravity and mean components of the calculated values of $\overline{\chi'_x}$ (a) and $\overline{\chi}_x$ (b) for Storm2, as obtained using $\xi = 3/2$. Note the increased offshore transport in the infragravity band when this band is treated as waves (b).

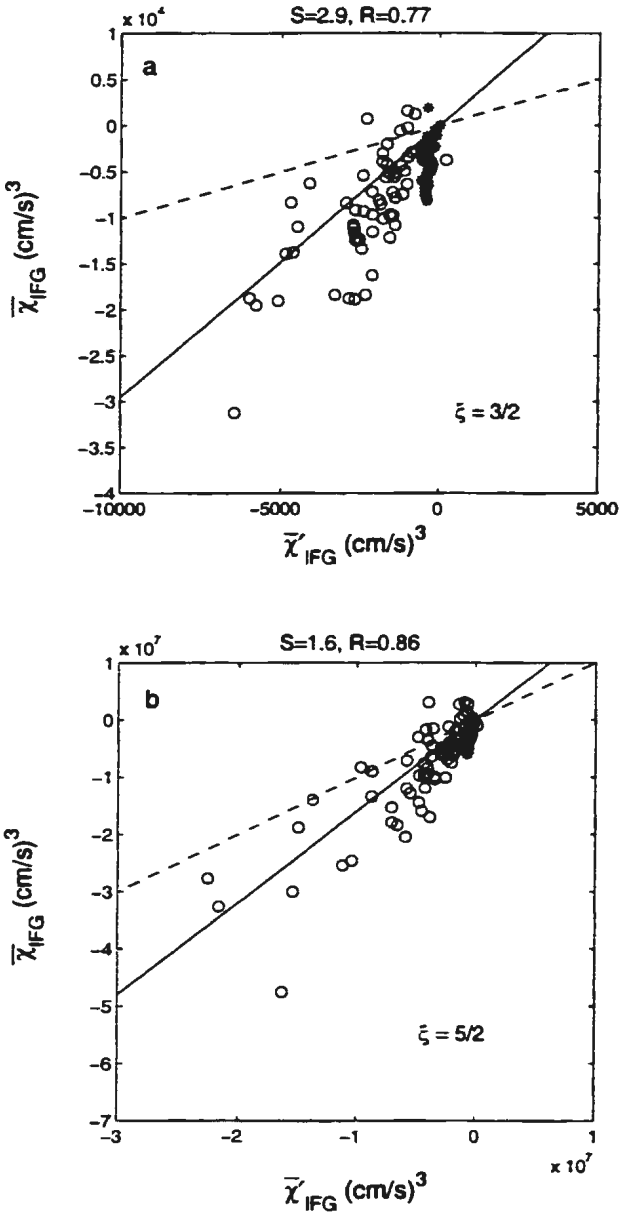

Figure 5.7: Scatter plot of $\overline{\chi}_{IFG}$ (the contribution of the infragravity band to the bedload transport with the infragravity band treated as waves) versus $\overline{\chi'}_{IFG}$ (the infragravity band treated as currents). (a) $\xi = 3/2$; (b) $\xi = 5/2$. The solid line is the regression line and the dashed line is the 1:1 line, S is the slope of the regression line, R is the correlation coefficent, * is Storm1 values and o is Storm2 values. Note that S>1 in both cases, showing that transports are larger (especially offshore transport) when infragravity band is treated as waves.

The results show a reasonable agreement between the measured and modelled migration velocities. Figure 5.8 and Figure 5.9 show the example of comparison between modelled and measured cross-shore migration velocities using the $0.5U_{pp}$ approach for Storm1 and Storm2 respectively. Both the directions and magnitudes of measured megaripple migration velocities agree reasonably well with those predicted by the model. Figures 5.10 and 5.11 show the comparison of modelled and measured cross-shore migration velocities using the $2U_{rms}$ approach for Storm1 and Storm2 respectively. Likewise, the directions and magnitudes of measured megaripple migration velocities in general agreed reasonably well with those predicted by the model. It is also encouraging to note that the event where megaripples stalled and showed offshore migration at the end of Storm2 is quite well reproduced by the model. There is in general more variability in the modelled than in the measured migration velocities.

In order to quantify the relationship between the model results and the measurements, scatter diagrams of calculated and measured data were plotted. The slopes of the regression lines were calculated to show the difference between the modelled values compared to the 1:1 predictions. These parameters were also useful in determining the role of infragravity velocities and in the investigation as to which exponent, $\xi = 3/2$ or $\xi = 5/2$, is better for modelling the cross-shore megaripple migration velocities.

Figures 5.12 and 5.13 show the scatter diagrams for the comparisons between measured and modelled cross-shore migration velocities using raw data. The solid lines are regression lines for 95% confidence interval while R and S are the correlation coefficient and slope of the regression lines, respectively.

There is considerable scatter in these comparisons using raw data, consequently producing low correlation coefficients. The highest correlation coefficient of 0.59 was obtained where infragravity velocities were treated as waves. Both $0.5U_{pp}$ and $2U_{rms}$ approaches for estimating wave-orbital velocity amplitude produced similar results.

Table 5.3 summarizes the correlation coefficients (R) for raw data, model-fitted current friction factors, α values and the slopes of regression lines (S) for both $0.5U_{pp}$ and $2U_{rms}$ approaches. It appears that higher correlation coefficients were obtained with the

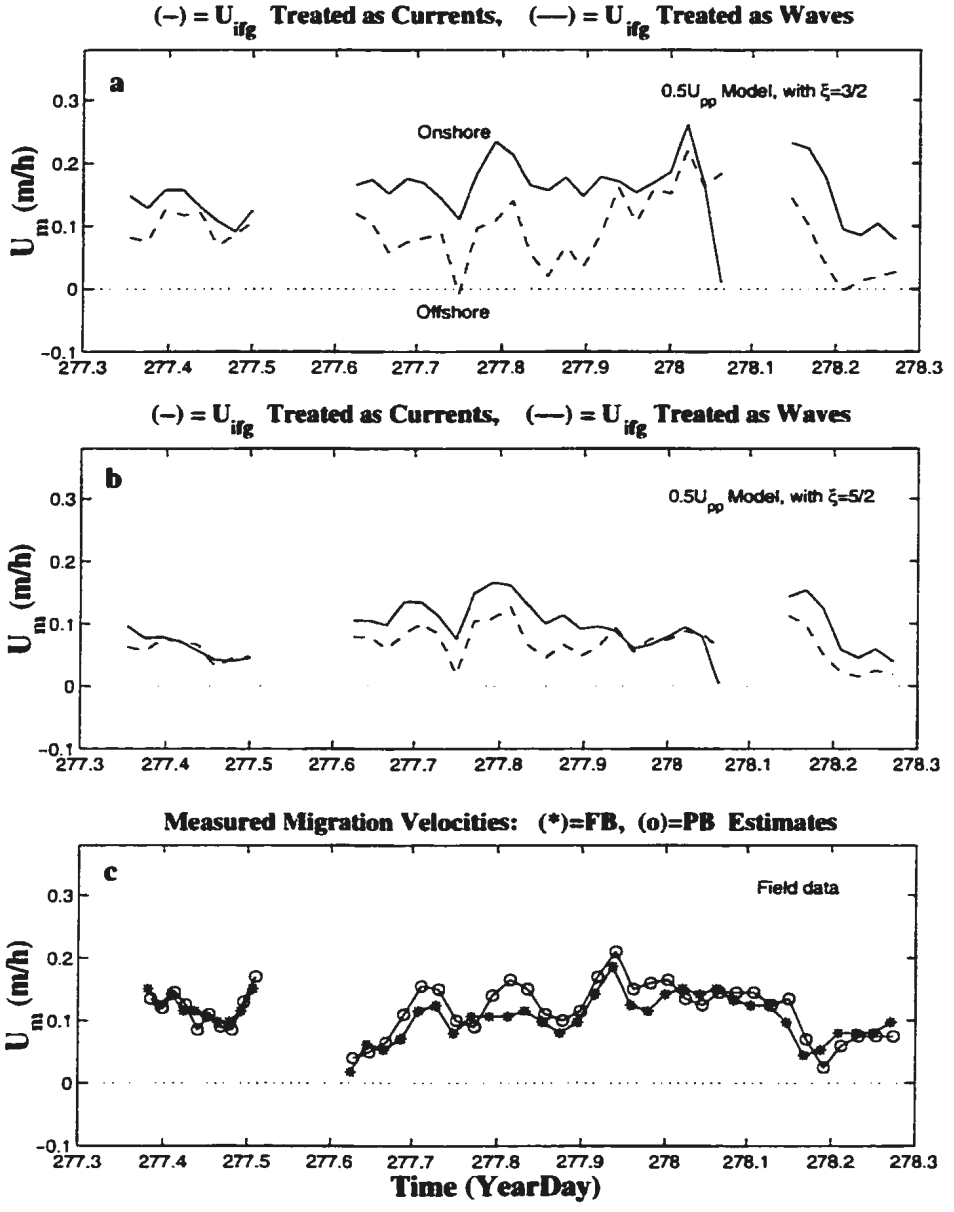

Figure 5.8: Comparison of modelled and field measured cross-shore megaripple migration velocities using the $0.5U_{pp}$ approach including longshore stresses for Storm1. Both the directions and magnitudes of measured migration velocities agree reasonably well with the model results using either $\xi = 3/2$ or $\xi = 5/2$. The symbols * and o refer to fan-beam and pencil-beam estimated migration velocities respectively. The dashed and solid lines are for $U_{ifg}(t)$ and $V_{ifg}(t)$ treated as either waves or currentls respectively. Note that predicted and measured migration velocities are all onshore, and similar magnitude.

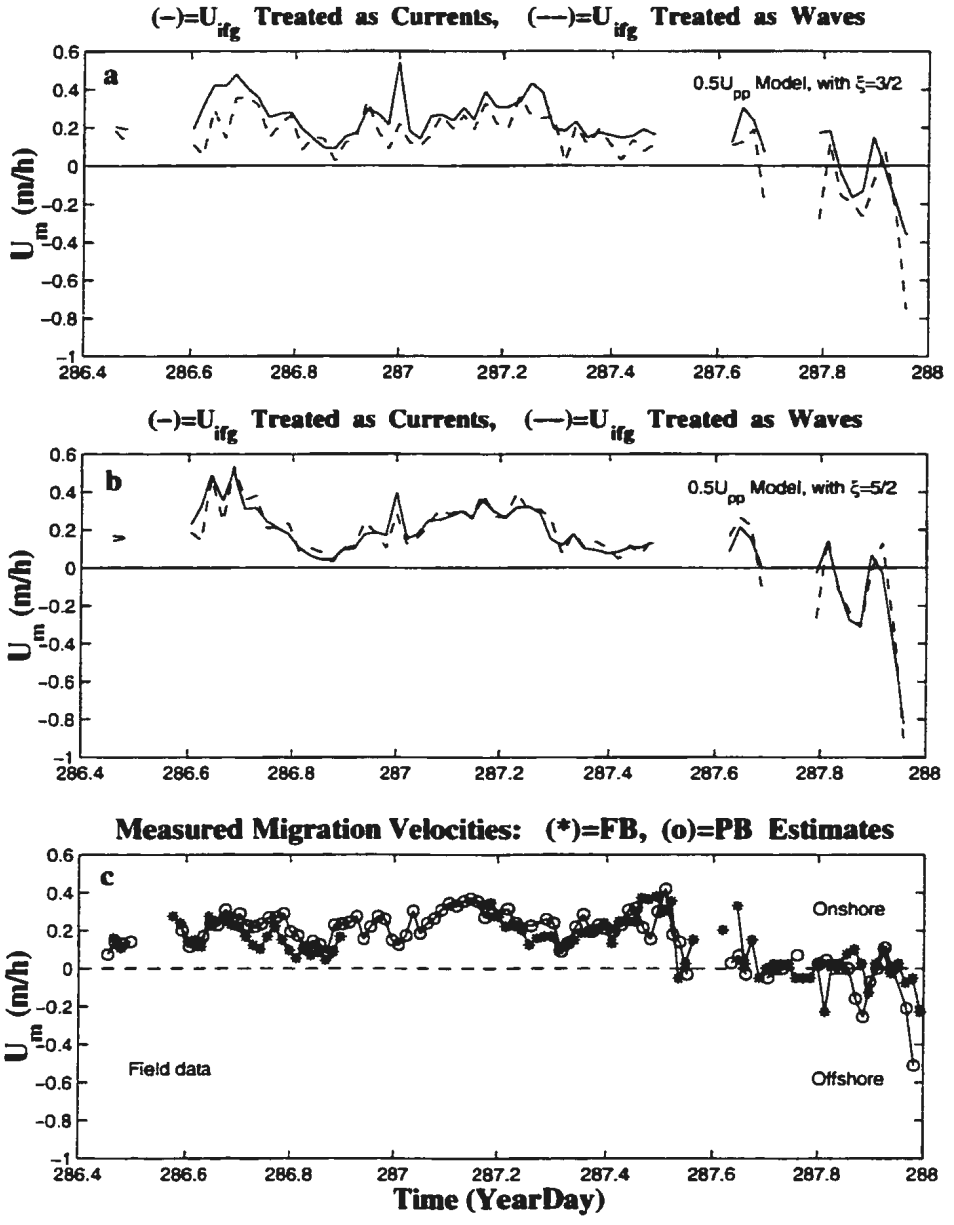

Figure 5.9: Comparison of modelled and measured cross-shore megaripple migration velocities using the $0.5U_{pp}$ approach including longshore stresses for Storm2. Both the directions and magnitudes of measured migration velocities agree reasonably well with the model results using either $\xi = 3/2$ or $\xi = 5/2$. The symbols * and o refer to fan-beam and pencil-beam estimated migration velocities respectively. The dashed and solid lines are for $U_{ifg}(t)$ and $V_{ifg}(t)$ treated as either waves or currentls respectively. Note the period of nearly zero or offshore migration velocities late on day 287, both measured and predicted.

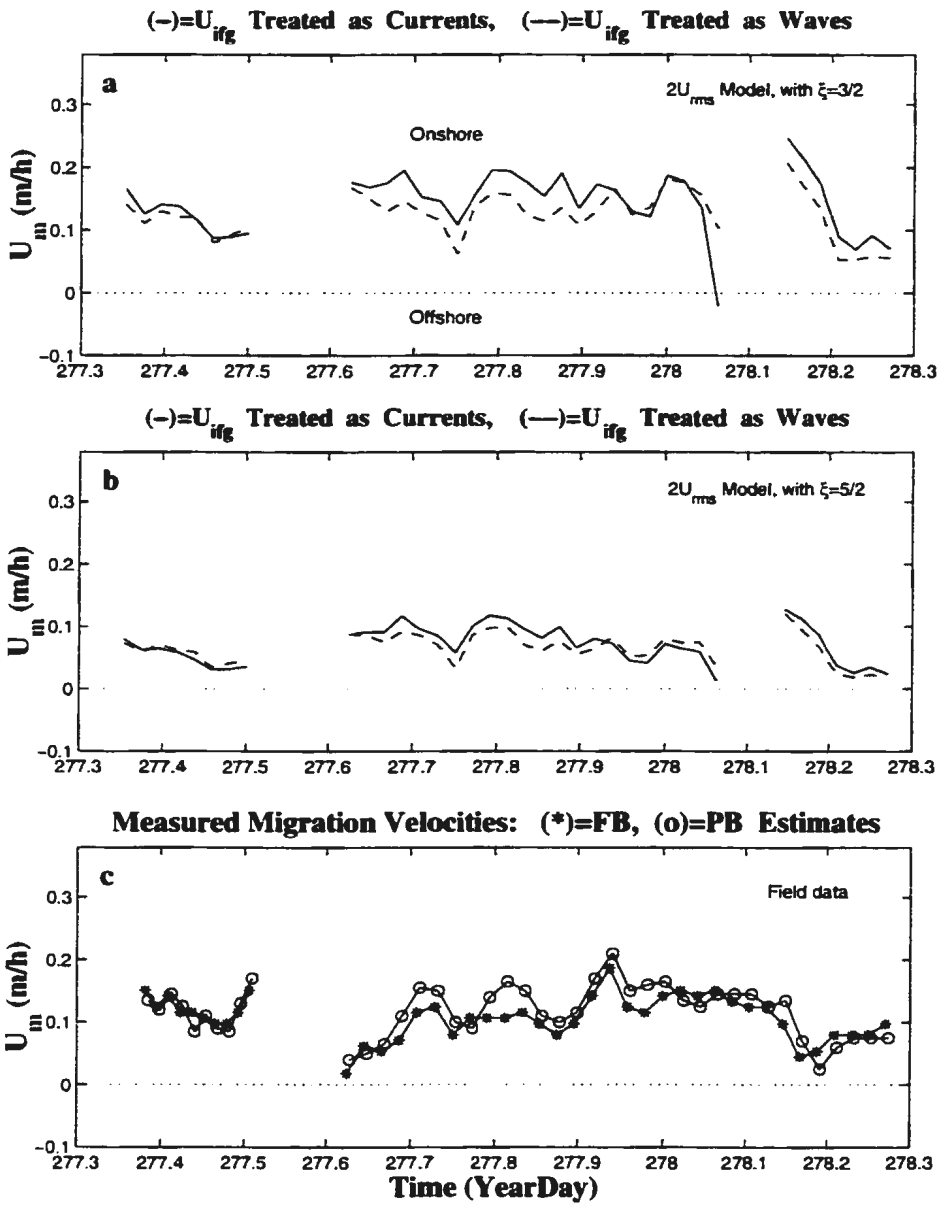

Figure 5.10: Comparison of modelled and measured cross-shore megaripple migration velocities using the $2U_{rms}$ approach including longshore stresses for Storm1. Both the directions and magnitudes of measured migration velocities agree reasonably well with the model results using either $\xi = 3/2$ or $\xi = 5/2$. The symbols * and o refer to fan-beam and pencil-beam estimated migration velocities respectively. The dashed and solid lines are for $U_{ifg}(t)$ and $V_{ifg}(t)$ treated as either waves or currentls respectively. Note that predicted and measured migration velocities are all onshore, and similar magnitude.

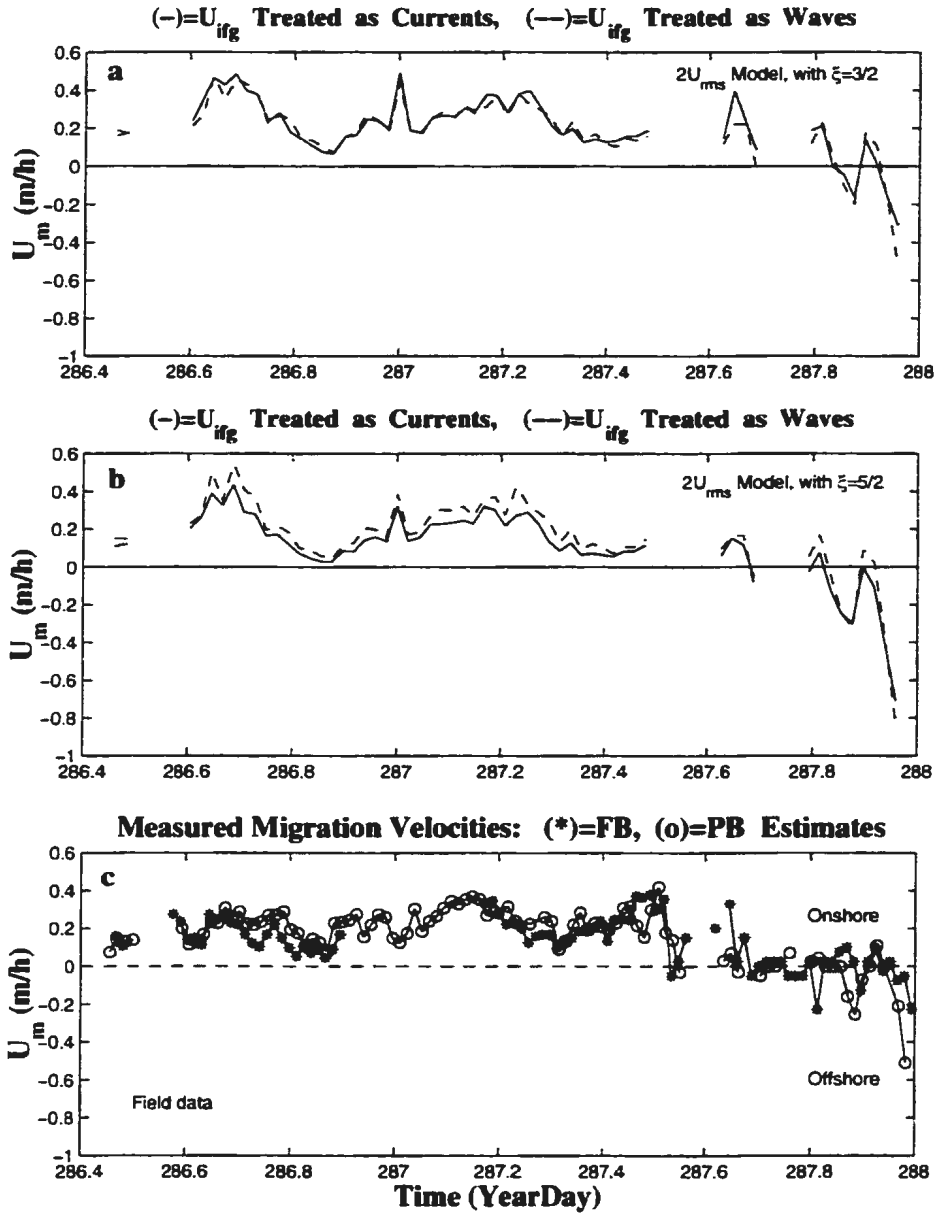

Figure 5.11: Comparison of modelled and measured cross-shore megaripple migration velocities using the $2U_{rms}$ approach including longshore stresses for Storm2. Both the directions and magnitudes of measured migration velocities agree reasonably well with the model results using either $\xi = 3/2$ or $\xi = 5/2$. The symbols * and o refer to fan-beam and pencil-beam estimated migration velocities respectively. The dashed and solid lines are for $U_{ifg}(t)$ and $V_{ifg}(t)$ treated as either waves or currentls respectively. Note the period of nearly zero or offshore migration velocities late on day 287, both measured and predicted.

Table 5.2: The number of values in each averaging interval in Figures 4.15 and 4.16.

U_m intervals (m/h)	Number of values
-0.23 to -0.13	2
-0.13 to -0.03	3
-0.03 to 0.07	26
0.07 to 0.17	88
0.17 to 0.27	35
0.27 to 0.37	18

$0.5U_{pp}$ approach when longshore stresses was included. The use of exponent $\xi = 5/2$ produced consistently higher correlation coefficients than $\xi = 3/2$ for both $0.5U_{pp}$ and $2U_{rms}$ approaches.

In order to reduce the amount of scatter in the raw data, and in order to determine whether or not there is a linear relationship between the modelled and field measured migration velocities, the raw data were divided into six equal intervals and averaged. Table 5.2 show the number of averaged values in each interval considered.

Figures 5.14 and 5.15 show scatter diagrams for the comparison between modelled and measured migration velocities using the interval-averaged data. The results show a good linear relationship between the computed and measured migration velocities. The dashed lines indicate the 1:1 prediction and R_I and S_I indicate the correlation coefficient and slope of the regression line for the interval-averaged data. Higher correlation coefficients R_I were obtained compared with the correlation coefficients obtained using the raw data. Table 5.3 also summarizes the correlation coefficients (R_I) and slopes of regression lines (S_I) for all the considered interval-averaged cases.

In the case of unaveraged migration velocity data, the regression seem to give more weight to the near-zero values than an eye would; for example in Figure 5.12d. By shifting to the values averaged over time intervals, the correlations improve, suggesting that averaging over time intervals gives more weight to the numerically larger values of migration

velocity. Also in going to the values averaged over the fixed intervals, the same weight is given to each interval, whether there are few or many values in that interval. Consequently, the regression for the interval-averaged data depends more on the higher-velocity intervals.

Comparing Table 5.3 and Table B.2 (Appendix B), it can be seen that when the cross-shore stresses alone were considered, the correlation coefficients (R) for the raw data ranged from 0.48-0.58; however, when both cross-shore and alongshore stresses were included, R ranged from 0.53-0.59. The inclusion of longshore stresses improved the correlation coefficients by 3-6% in the case of the $0.5U_{pp}$ approach. Similarly, the slopes of the regression lines for the comparison of raw data when cross-shore stresses only are considered ranged from S=0.49-0.81 which was farther from 1 than for the case when longshore stresses were included (S=0.67-0.98). The inclusion of longshore stresses moved the slopes of the regression lines 20-38% closer to 1 in the case of the $0.5U_{pp}$ approach. This indicates that longshore stresses are important in modelling the cross-shore migration velocities. The same conclusion is arrived at by considering the interval-averaged data for the $0.5U_{pp}$ approach, where both the correlation coefficients R_I and slopes of best-fit lines S_I improved with the inclusion of longshore stresses.

The results shown in Table 5.3 were looked at more closely for specific interpretations. The slopes of regression lines for both raw and interval-averaged data when both $0.5U_{pp}$ and $2U_{rms}$ approaches were applied shows that this analysis provides a reasonable prediction of the measured cross-shore megaripple migration velocities. For the $0.5U_{pp}$ approach, the slope of regression lines ranged from S=0.69-0.84 and S_I=0.48-0.68 for $\xi = 3/2$, and from S=0.86-0.98 and S_I=0.62-0.70 for $\xi = 5/2$. This suggests that the slopes improved (relative to a 1:1 slope) by 14-17% and 2-14% for the raw data and interval-averaged data, respectively, when $\xi = 5/2$ was applied. Similarly, for the $2U_{rms}$ approach, the slope of regression lines ranged from S=0.67-0.68 and S_I=0.47-0.48 for $\xi = 3/2$, and from S=0.82-0.94 and S_I=0.63-0.65 for $\xi = 5/2$. This suggests that the slopes improved by 15-26% and 16-17% for the raw data and interval-averaged data, respectively, when $\xi = 5/2$ was applied. Therefore, the results seem to suggest that the use of $\xi = 5/2$ improved the correlation between model results and the measured migration velocities compared to the

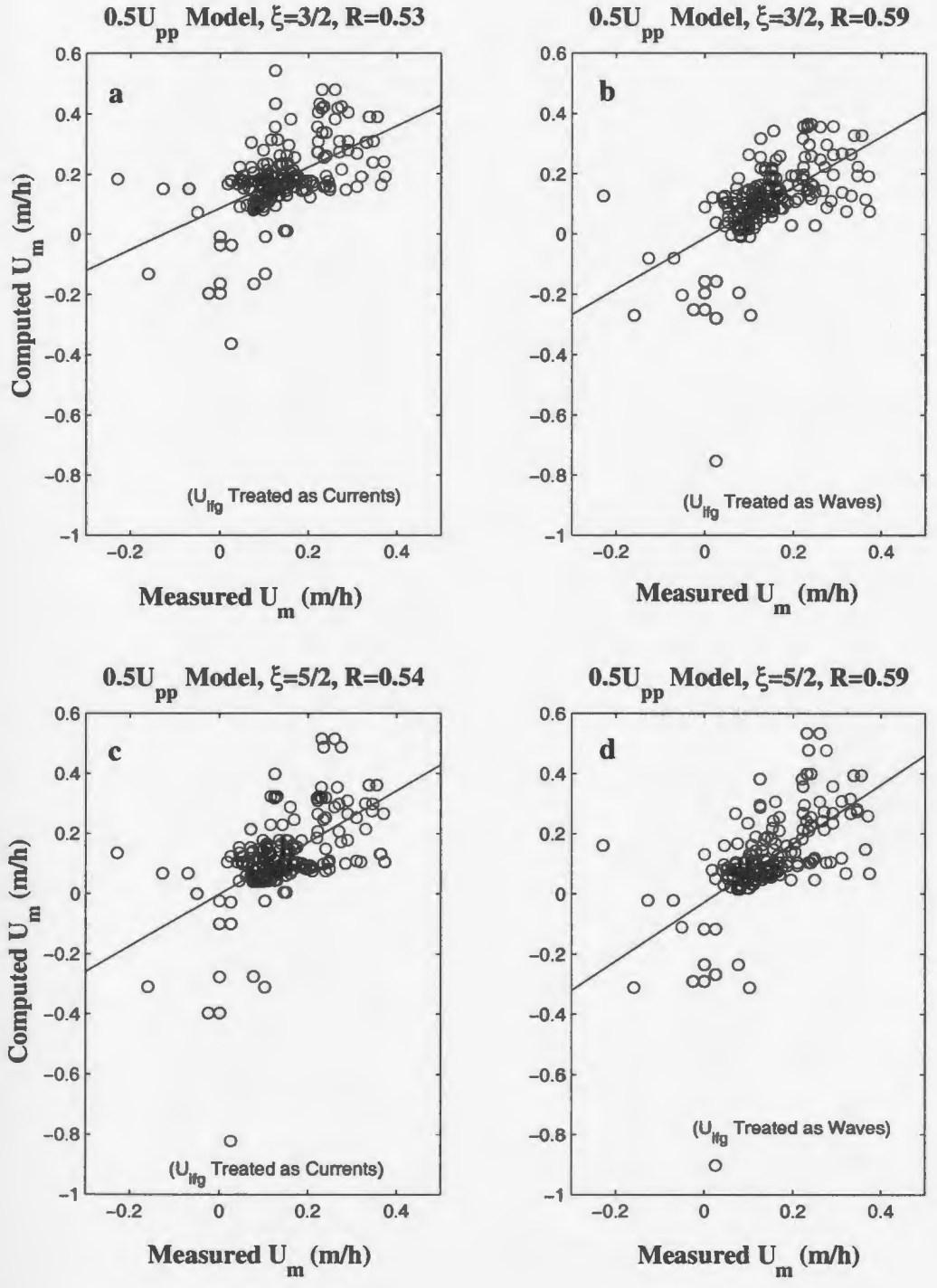

Figure 5.12: Comparisons between the raw measured and computed cross-shore migration velocities using the $0.5U_{pp}$ approach and including longshore stresses, with $U_{ifg}(t)$ and $V_{ifg}(t)$ treated as currents and $\xi = 3/2$ (a), with $U_{ifg}(t)$ and $V_{ifg}(t)$ treated as waves and $\xi = 3/2$ (b), with $U_{ifg}(t)$ and $V_{ifg}(t)$ treated as currents and $\xi = 5/2$ (c), with $U_{ifg}(t)$ and $V_{ifg}(t)$ treated as waves and $\xi = 5/2$ (d). The solid lines are linear regression lines; R is the correlation coefficient.

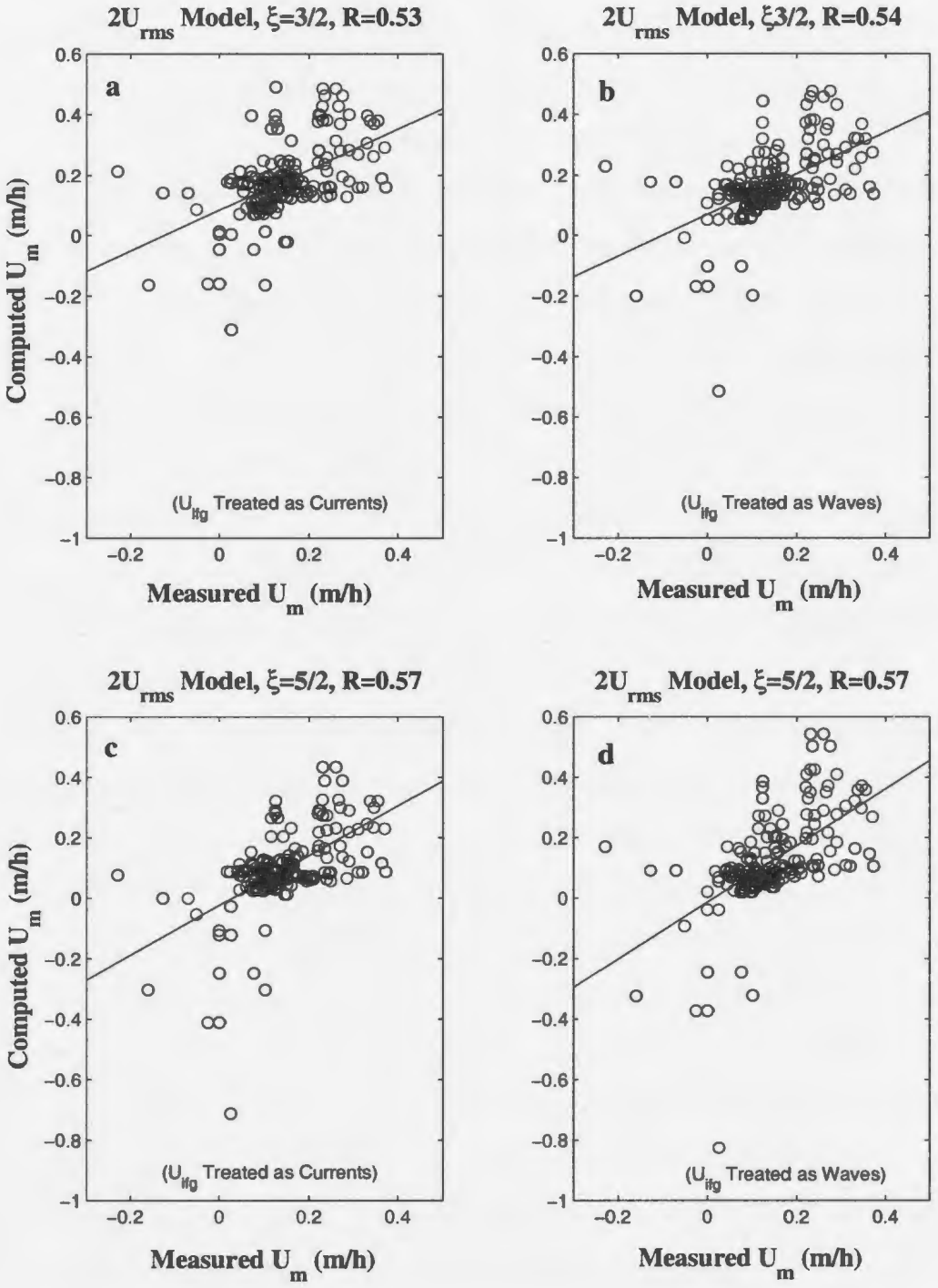

Figure 5.13: Comparisons between the raw measured and computed cross-shore migration velocities using the $2U_{rms}$ approach and including longshore stresses, with $U_{ifg}(t)$ and $V_{ifg}(t)$ treated as currents and $\xi = 3/2$ (a), with $U_{ifg}(t)$ and $V_{ifg}(t)$ treated as waves and $\xi = 3/2$ (b), with $U_{ifg}(t)$ and $V_{ifg}(t)$ treated as currents and $\xi = 5/2$ (c), with $U_{ifg}(t)$ and $V_{ifg}(t)$ treated as waves and $\xi = 5/2$ (d). The solid lines are linear regression lines; R is the correlation coefficient.

use of $\xi = 3/2$.

The role of infragravity velocities is also clarified by Table 5.3. For example, for the $0.5U_{pp}$ approach, the slopes of regression lines for raw data improved by 15% and 12% for $\xi = 3/2$ and $\xi = 5/2$, respectively, when infragravity velocities were treated as waves. The slope of regression lines for interval-averaged data also improved by 20% and 8% for $\xi = 3/2$ and $\xi = 5/2$, respectively, when infragravity velocities were treated as waves. Similarly, for the $2U_{rms}$ approach, the slopes of regression lines for raw data improved by 1% and 12% for $\xi = 3/2$ and $\xi = 5/2$, respectively, when infragravity velocities were treated as waves. The slope of regression lines for interval-averaged data, however, decreased by 1% and improved by 2% for $\xi = 3/2$ and $\xi = 5/2$, respectively, when infragravity velocities were treated as waves. Therefore, it seems that treating infragravity velocities as waves in calculation of the bottom stresses is generally important for modelling the cross-shore megaripple migration velocities, leading to improved agreement between model results and field data.

In summary, there is reasonably good quantitative agreement between the modelled and measured cross-shore migration velocities. This agreement depends upon the choice of friction factors. The applied values of f_c ranged from $4.3\text{x}10^{-3}$ to $8.0\text{x}10^{-3}$, which is a factor of 2-5 larger than the estimated flat-bed, fixed roughness, mean currents only, values ($\hat{f}_c$) computed for DUCK94 data. This is reasonable because in the presence of migrating bedforms and under the combined effects of waves and currents the values of f_c are expected to be larger than those suggested for flat-bed, fixed roughness case. Similarly, the applied values of α seem to be reasonably comparable to the estimated value of $\hat{\alpha}$ for $0.5U_{pp}$ with $\xi = 3/2$ and $2U_{rms}$ with $5/2$ models. The applied values of α were however a factor of 3 larger and a factor of 2 smaller compared to estimated $\hat{\alpha}$ values when $2U_{rms}$ with $\xi = 3/2$ and $0.5U_{pp}$ with $\xi = 5/2$ were applied respectively.

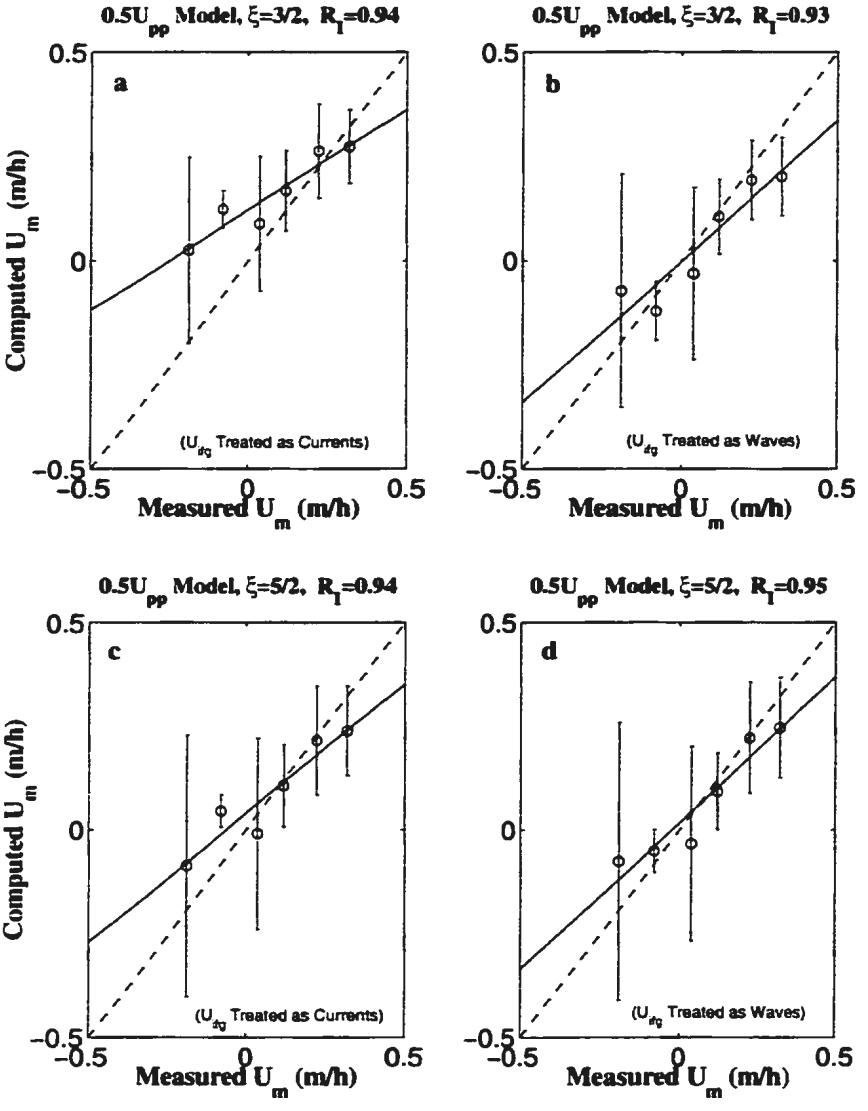

Figure 5.14: Comparisons between interval-averaged measured and computed cross-shore migration velocities using the $0.5U_{pp}$ approach and including longshore stresses, with $U_{ifg}(t)$ and $V_{ifg}(t)$ treated as currents and $\xi = 3/2$ (a), with $U_{ifg}(t)$ and $V_{ifg}(t)$ treated as waves and $\xi = 3/2$ (b), with $U_{ifg}(t)$ and $V_{ifg}(t)$ treated as currents and $\xi = 5/2$ (c), with $U_{ifg}(t)$ and $V_{ifg}(t)$ treated as waves and $\xi = 5/2$ (d). The solid lines are the linear regression lines; The dashed lines are for a 1:1 fit and R_I is the correlation coefficient. The vertical bars at each data point represent standard deviations of the computed values within the averaged interval.

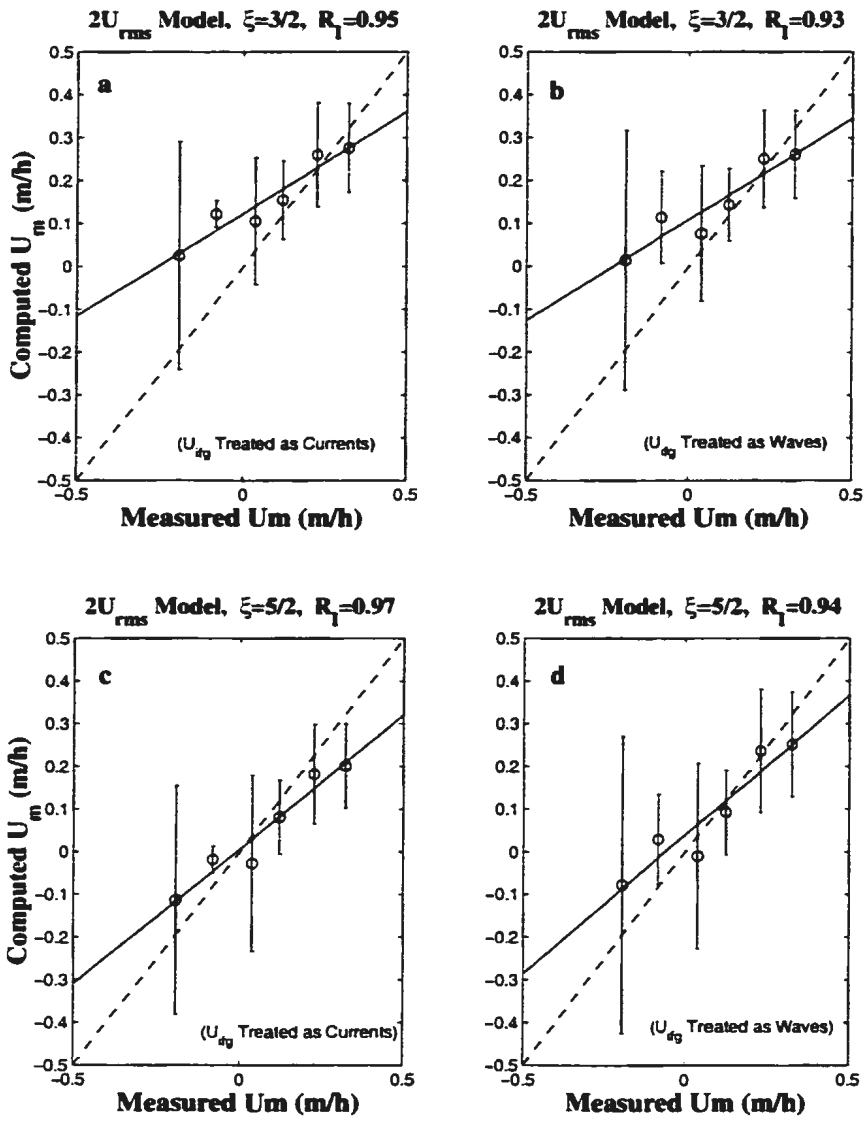

Figure 5.15: Comparisons between interval-averaged measured and computed cross-shore migration velocities using the $2U_{rms}$ approach and including longshore stresses, with $U_{ifg}(t)$ and $V_{ifg}(t)$ treated as currents and $\xi = 3/2$ (a), with $U_{ifg}(t)$ and $V_{ifg}(t)$ treated as waves and $\xi = 3/2$ (b), with $U_{ifg}(t)$ and $V_{ifg}(t)$ treated as currents and $\xi = 5/2$ (c), with $U_{ifg}(t)$ and $V_{ifg}(t)$ treated as waves and $\xi = 5/2$ (d). The solid lines are linear regression lines; The dashed lines are for a 1:1 fit and R_l is the correlation coefficient. The vertical bars at each data point represent standard deviations of the computed values within the averaged interval.

Table 5.3: Comparison between measured and computed megaripple migration velocities including longshore stresses where R and S are the correlation coefficients and slopes of linear regression lines using raw data,R_I and S_I are the correlation coefficients and slopes of linear regression lines using interval-averaged data, $\alpha = f_w/f_c$ and f_c are the constants used in the model.

U_{wo} Approach	ξ	α	f_c	R	S	R_I	S_I
$0.5U_{pp}$ & U_{ifg}, V_{ifg} as waves	3/2	6	$8.0\text{x}10^{-3}$	0.59	0.84	0.93	0.68
$0.5U_{pp}$ & U_{ifg}, V_{ifg} as currents	3/2	6	$8.0\text{x}10^{-3}$	0.53	0.69	0.94	0.43
$0.5U_{pp}$ & U_{ifg}, V_{ifg} as waves	5/2	2	$4.5\text{x}10^{-3}$	0.59	0.98	0.95	0.68
$0.5U_{pp}$ & U_{ifg}, V_{ifg} as currents	5/2	2	$4.5\text{x}10^{-3}$	0.54	0.86	0.94	0.56
$2U_{rms}$ & U_{ifg}, V_{ifg} as waves	3/2	15	$6.0\text{x}10^{-3}$	0.54	0.68	0.93	0.47
$2U_{rms}$ & U_{ifg}, V_{ifg} as currents	3/2	15	$6.0\text{x}10^{-3}$	0.53	0.67	0.95	0.48
$2U_{rms}$ & U_{ifg}, V_{ifg} as waves	5/2	4	$4.3\text{x}10^{-3}$	0.57	0.94	0.94	0.65
$2U_{rms}$ & U_{ifg}, V_{ifg} as currents	5/2	4	$4.3\text{x}10^{-3}$	0.57	0.82	0.97	0.63

5.3 Bedload transport

Cross-shore lunate megaripple migration velocities (U_m) and maximum megaripple heights (η_{max}) were used to calculate the average volumetric bedload sediment transport per unit width (Q_B) based on the bedform migration model represented by Equation (4.1). Rearranging this equation, Q_B is given by

$$Q_B = U_m[\eta_{max}(1-\epsilon)].$$

where sediment porosity, ϵ, is taken to be 0.4. The cross-shore volumetric bedload sediment transport per unit width for Storm1 and Storm2 is shown in Figure 5.16. The measured cross-shore bedload transport using lunate megaripple migration ranged from 0.03-0.08 cm^2/s onshore during Storm1, 0.05-0.22 cm^2/s onshore during the first stage of Storm2 and 0-0.14 cm^2/s offshore during the second stage of Storm2.

It is interesting to compare the observed megaripple migration with the migration of the bar. Figure (4.18) shows bathymetric profiles to the north and south of the frame during Storm1 while Figures (4.19) and (4.20) show the profiles for Storm2. Survey lines 235,

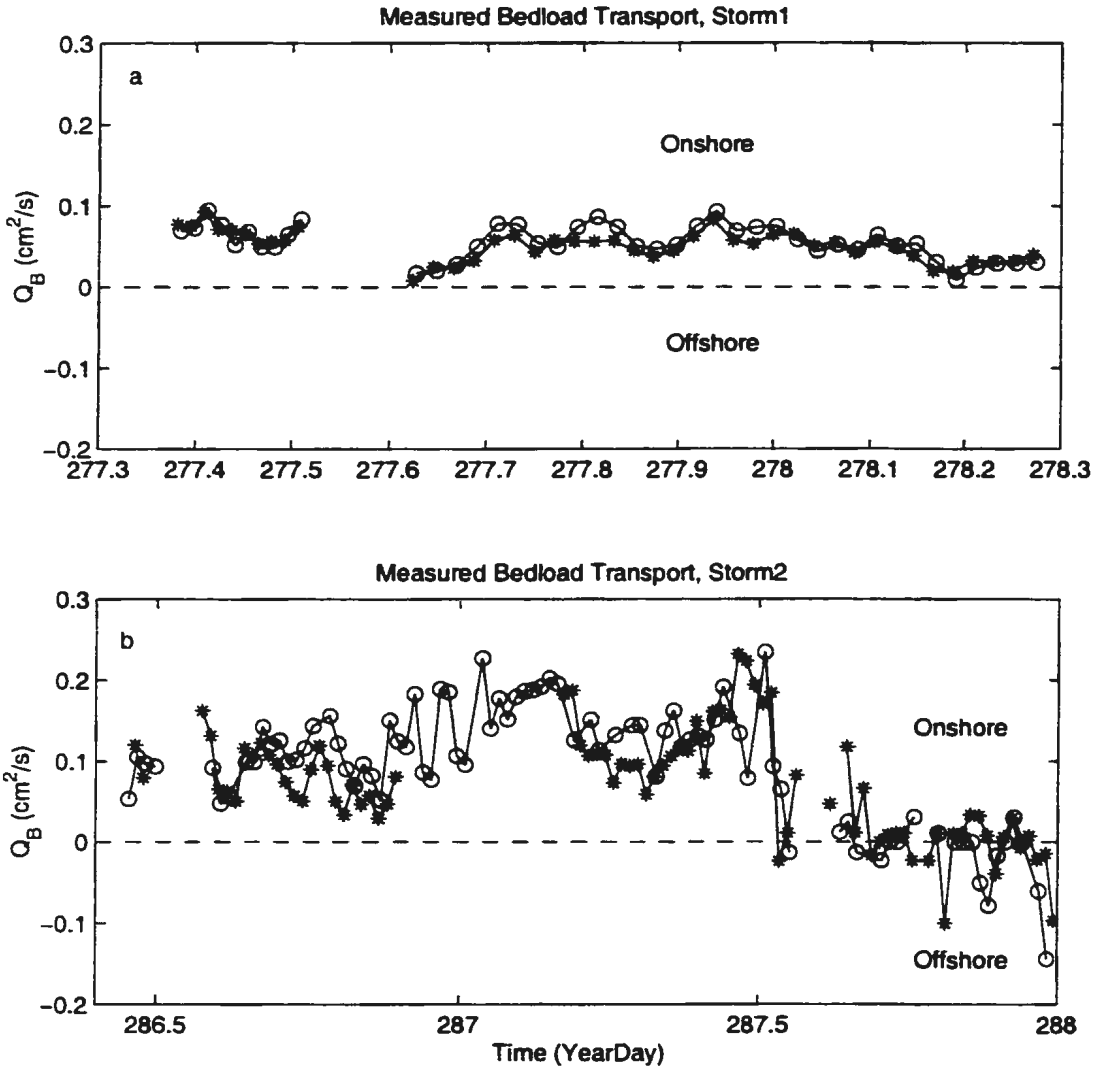

Figure 5.16: Measured volumetric cross-shore bedload sediment transport per unit width (Q_B) calculated using bedform migration model; where (o) represent Q_B obtained using pencil-beam estimated migration velocities and (*) represent Q_B obtained using fan-beam estimated migration velocities. (a) is Storm1, (b) is Storm2.

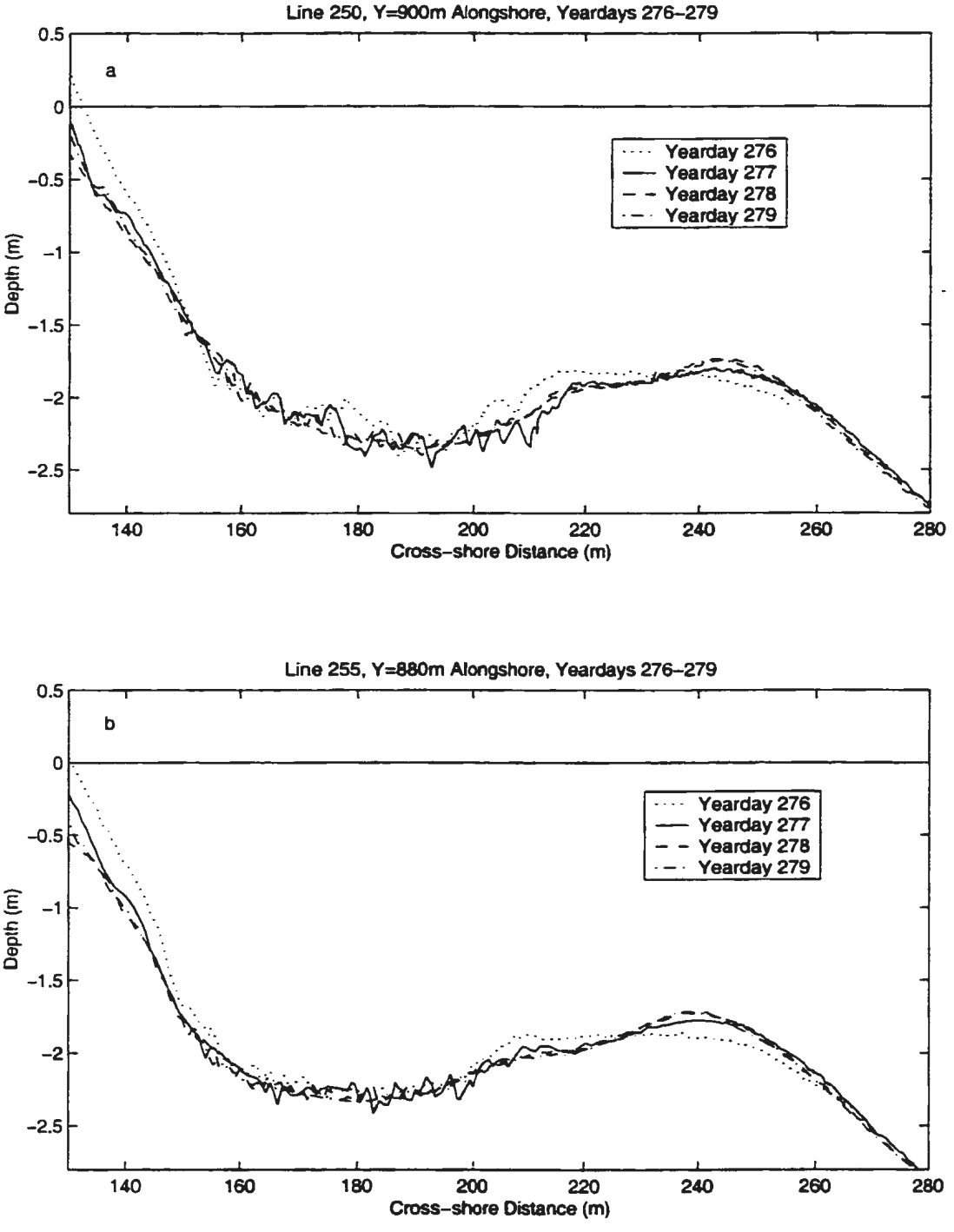

Figure 5.17: Plots of selected bathymetric profiles as measured using the CRAB, showing offshore bar migration during Yeardays 276-279 at line 250 (a) and at line 255 (b).

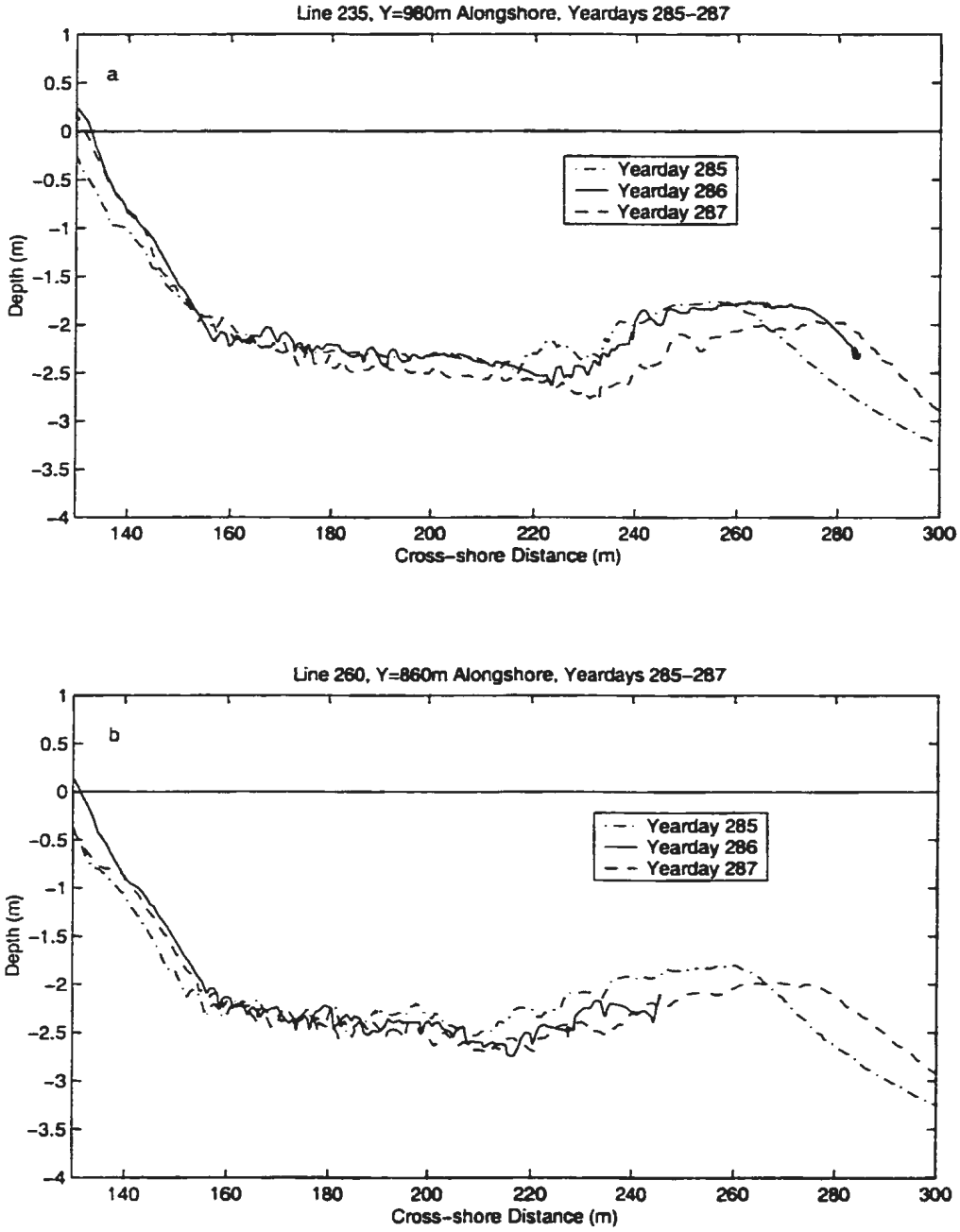

Figure 5.18: Plots of selected bathymetric profiles as measured using the CRAB, showing offshore bar migration during Yeardays 285-287 at line 235 (a) and at line 260 (b).

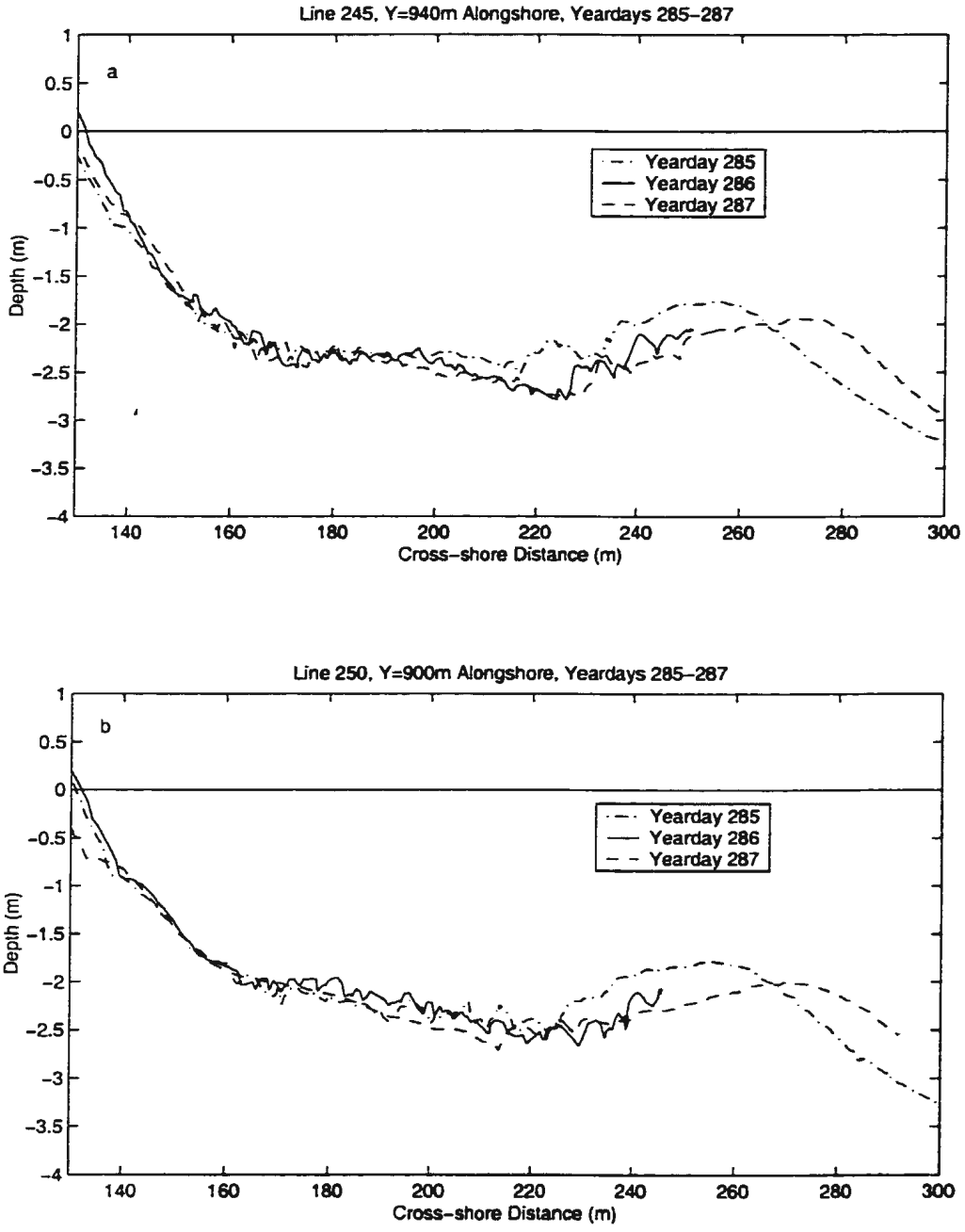

Figure 5.19: Plots of selected bathymetric profiles as measured using the CRAB, showing offshore bar migration during Yeardays 285-287 at line 245 (a) and at line 250 (b).

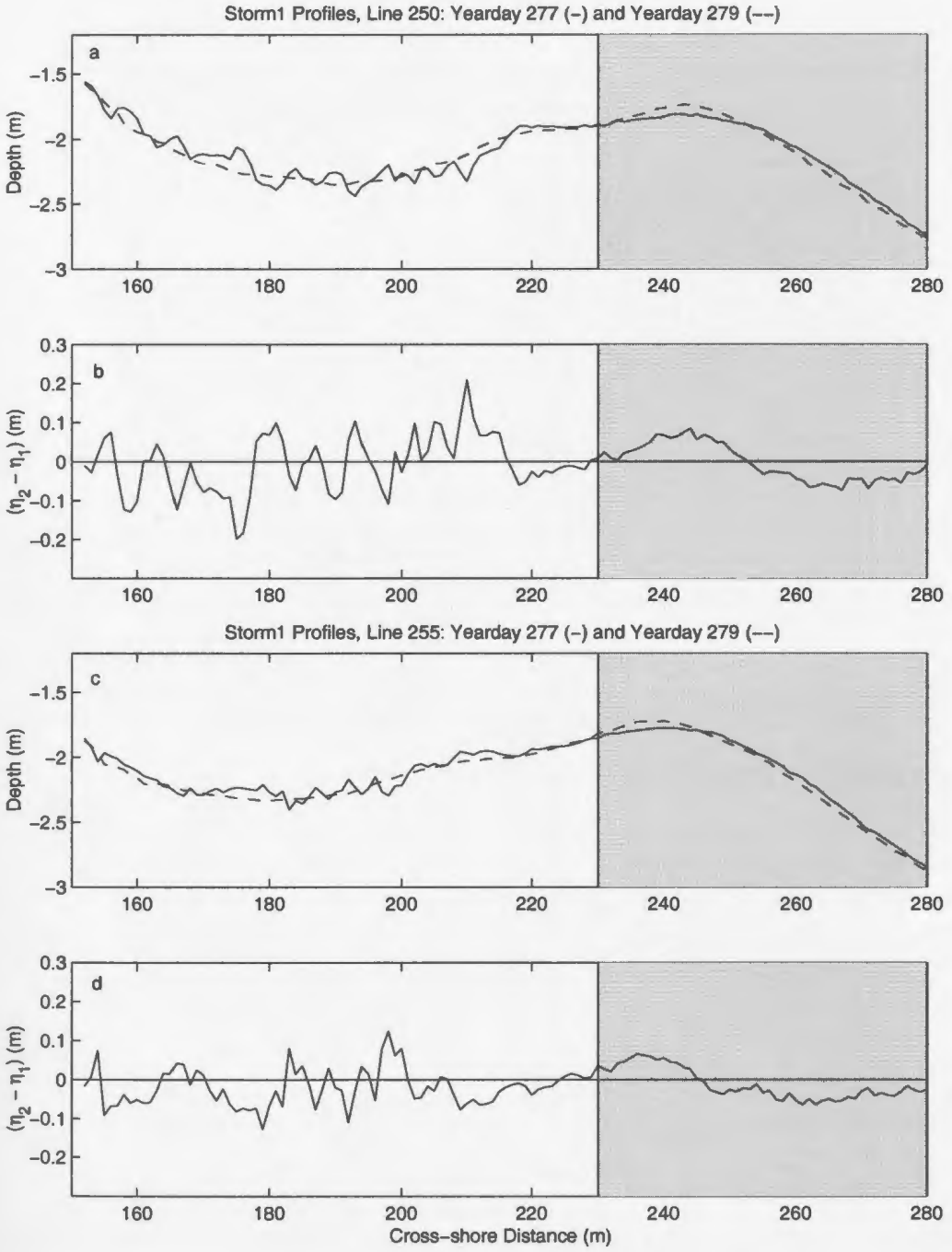

Figure 5.20: Plots of Storm1 bathymetric profiles during Yeardays 277-279 at line 250 (a) and Line 255 (c). The difference between the bar elevations ($\eta_2 - \eta_1 = \Delta\eta$) within the 2 days interval are shown for Line 250 (b) and Line 255 (d). η_2 and η_1 are the bar elevations for Yeardays 286 and 287 respectively. The shaded parts represent the areas over which sediment movement associated with bar migration seem to have taken place.

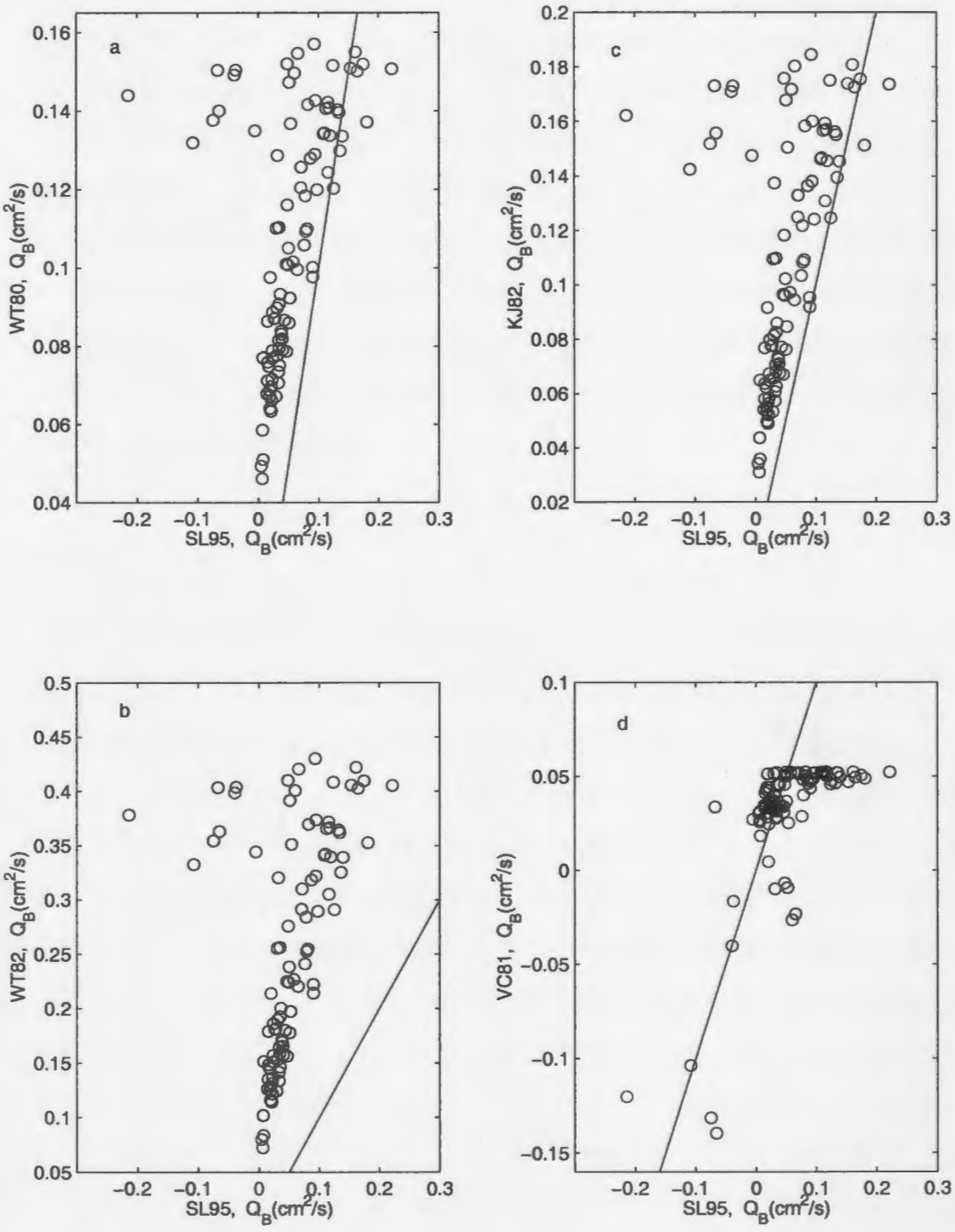

Figure 5.23: The comparison between the cross-shore bedload sediment transport calculated using the Sleath (1995) model with results from the Watanabe et al. (1980) model (a), Watanabe (1982) model (b), Kajima et al. (1982) model (c) and Vincent et al. (1981) model (d). The solid line indicates a one-to-one relationship between the Sleath (1995) model and other models.

245 and 250 were made at about 90 m, 50 m and 10 m north of the instrument frame respectively. Similarly, survey lines 255 and 260 were made at about 10 m and 30 m south of the instrument frame respectively. These CRAB profiles during Duck94 experiment show that the changes in bar position were similar at different longshore locations.

During Storm1 the sand bar was migrating offshore between Yeardays 276-277 (Figure 5.17). However, the bar seems to have migrated onshore between Yeardays 277-279 and 278-279. Unfortunately, most of the surveys during Storm2 did not extend seaward much beyond the bar crest (Figures 4.19 and 4.20). However, it can be seen that the bar migrated offshore between Yeardays 286 and 287 during Storm2 (Figure 4.19a). The bar was also migrating offshore between Yeardays 285 and 287 (Figure 5.18b and Figure 5.19a&b). It is not possible to determine the direction of the bar migration between Yeardays 287 and 288 due to gaps in CRAB data. The wave and current conditions during the first half of Yearday 287 were however comparable to those observed during Yearday 286. Furthermore, the second half of Yearday 287 was characterized by energetic waves and strong near-bottom offshore directed mean current; these conditions tend to favor offshore bar motion (Gallagher et al., 1998). An array of sonar altimeters deployed during Duck94 experiment showed that the sand bar wassteadly migrating offshore between Yeardays 283-293 (Gallagher et al., 1998).

Megaripples were therefore generally migrating in the same direction as that of the bar during Storm1. However, the observed onshore megaripple migration during the first stage of Storm2 is opposite to the direction of the bar migration during that time.

The average value of volumetric sediment transport due to bar migration can be estimated using

$$Q = \frac{\Delta\eta}{\Delta t}\Delta x(1-\epsilon), \tag{5.32}$$

where $\Delta\eta$ is the change in bar elevation and Δx represents the horizontal distance over which sediment erosion or deposition associated with the bar migration occured. The factor $(1-\epsilon)$ is for the porosity correction and Δt is the time interval between surveys showing the bar elevation change.

The estimated values $\Delta\eta$ and Δx for Storm1 are obtained from Figures 4.21b&d for the two considered profile lines. The estimates were taken at cross-shore distances between 230-280 m within which the bar movement seems to have taken place (shaded areas Figure 5.20). Both profile lines show that $\Delta\eta$ ranged from 5-10 cm while Δx ranged from 20-25 m (Shaded area in Figure 5.20b&d). Using these values, the obtained Storm1 value of Q for Δt= 2 days ranged from Q=0.03-0.09 cm^2/s. The estimated bedload transport using megaripple migration velocities for Storm1 (Q_B=0.03-0.08 cm^2/s) is therefore remarkably similar in magnitude and in the same direction as the computed sediment transport using the bar migration.

Similarly, the bar elevation change between Yeardays 286 and 287 ranged from $\Delta\eta$=30-50 cm (shaded are in Figure 5.21b). However, the CRAB data were not available beyond 285 m distance offshore. It was therefore difficult to get good estimates of Δx values during Storm2. Thus the magnitude of sediment transport using the bar migration during this period could not be calculated. It was clear however that the bar was migrating offshore, opposite to the direction of megaripple migration on days 286 and 287 during Storm2.

5.4 Comparison between Sleath (1995) model and other semi-empirical model results

The modelled lunate megaripple migration velocities in section 4.4 were obtained using the Sleath (1995) stress-based model. It is interesting to compare the results obtained using other commonly applied stress-based models of Meyer-Peter and Müller (1948), Madsen and Grant (1977), Sleath (1978), Watanabe et al. (1980), Vincent et al. (1981), Watanabe (1982) and Kajima et al. (1982a). These models were described in Chapter 1. Most formulas are deterministic and relatively straightforward to apply. The values of Shields parameter in these models were calculated each 30 minutes based on half-hour average of time series measurements of u_s, then the half-hour averaged bedload transport is obtained and a rate per hour is calculated.

The Sleath (1995) model (here referred to as SL95), as given by Equation (1.18) in

Chapter 1, was applied using the constant Λ=0.4 for rough beds. The cross-shore bedload transport modelled with SL95 ranged from 0-0.1 cm^2/s onshore during Storm1, 0.05-0.22 cm^2/s onshore during the first stage of Storm2 and 0-0.14 cm^2/s offshore during the second stage of Storm2. These results are consistent with the bedload sediment transport measurements obtained using lunate megaripple migration velocities. Both the magnitudes and directions of measured bedload transport are quite reasonably reproduced by the Sleath (1995) model; good agreement was obtained even near the end of Storm2 where offshore transport was suggested by the measurements.

The Meyer-Peter and Müller (1948) (here referred to as MP48) formula is given by Equation (1.1) in Chapter 1. The bedload transport rate in the MP48 model is proportional to the square of the fluid velocity. This model was originally developed for sediments with grain size D $\geq$ 2mm (Yalin, 1977 pg. 114). The typical grain size during DUCK94 was D = 0.2mm, which is less than the limit recommended for MP48 application. Nevertheless, this formula is examined here to check its predictive ability for DUCK94 conditions. The critical Shields parameter $\psi_{cr} = 0.07$ is used following Horikawa (1988, pg. 180) and Shields parameter for waves as given by Madsen and Grant (1977) is also applied.

The comparison between SL95 and MP48 model results is shown in Figure 5.22a. Both SL95 and MP48 computed values show similar trends during Storm1 and the first stage of Storm2 when sediments were being moved onshore. However, there are inconsistencies during the second stage of Storm2 where measurements suggested offshore transport while the MP48 model suggests onshore transport. The magnitudes of Q_B computed with MP48 were also inconsistent with SL95 values. MP48 values for Q_B during Storm1 ranged from 0.28-0.69 cm^2/s onshore, which is an order of magnitude larger than SL95 values. The same variations were observed during Storm2 where MP48 values ranged from 0.55-1.39 cm^2/s onshore, which is also an order of magnitude higher than SL95 values.

Madsen and Grant (1977) modified the original Einstein-Brown transport equation for unidirectional flow (Brown, 1950) and compared the modified form with experimental data to obtained the formula given by Equation (1.6) in Chapter 1 (referred to here as MG77

model). It is important to note that Madsen and Grant (1977) did not compare their calculated sediment transport with experimental measurements for combined waves and currents conditions. It is therefore interesting to test this model with DUCK94 data that is obtained in oscillatory flow conditions. The bedload transport rate in MG77 is proportional to the sixth power of the fluid velocity. The value of the fall velocity (W) in MG77 model is calculated using Gibbs et al. (1971) expression.

The comparison between SL95 and MG77 model results is shown in Figure 5.22b. The values of constants used in the MG77 model includes acceleration due to gravity (g), specific gravity of grains (s=2.7), viscosity (ν=0.014 cm^2/s), median grain size (D=0.02 cm) and sediment settling velocity for DUCK94 (W=2 cm/s). The results of bedload sediment transport obtained by MG77 ranged from 0.07-0.35 cm^2/s onshore during Storm1 and 0.28-1.25 cm^2/s onshore during Storm2. Besides the slight variations in the magnitudes of Q_B, there seem to be no significant differences between the results obtained by the MG77 and MP48 models.

Sleath (1978), here referred to as SL78, non-dimensionalized the transport in MG77 formula using wave frequency and square of the median grain size, then used the data of Kalkanis (1964) and Abou-Seida (1965) to obtain the transport formula given by Equation (1.8) in Chapter 1. The comparison between SL95 and SL78 model results are shown in Figure 5.22c. The results of bedload transport obtained by the SL78 model ranged from 0.03-0.06 cm^2/s onshore during Storm1 and 0.03-0.05 cm^2/s onshore during Storm2. The results of the SL78 model are of the same order of magnitude as both the measurements and SL95 model results. However, like the previous models, the SL78 model could not predict the offshore transport at the end of Storm2, as suggested by both field measurements and the SL95 model.

Watanabe et al. (1980), here referred to as WT80, used flume experiments to suggest a formula given by Equation (1.14) in Chapter 1, where bedload sediment transport is proportional to the square of the fluid velocity. The Shields parameter for this model is similar to that suggested by MG77. A critical Shields parameter $\psi_{cr} = 0.07$ and the model coefficient $A = 3$ was used. The comparison between SL95 and WT80 model results

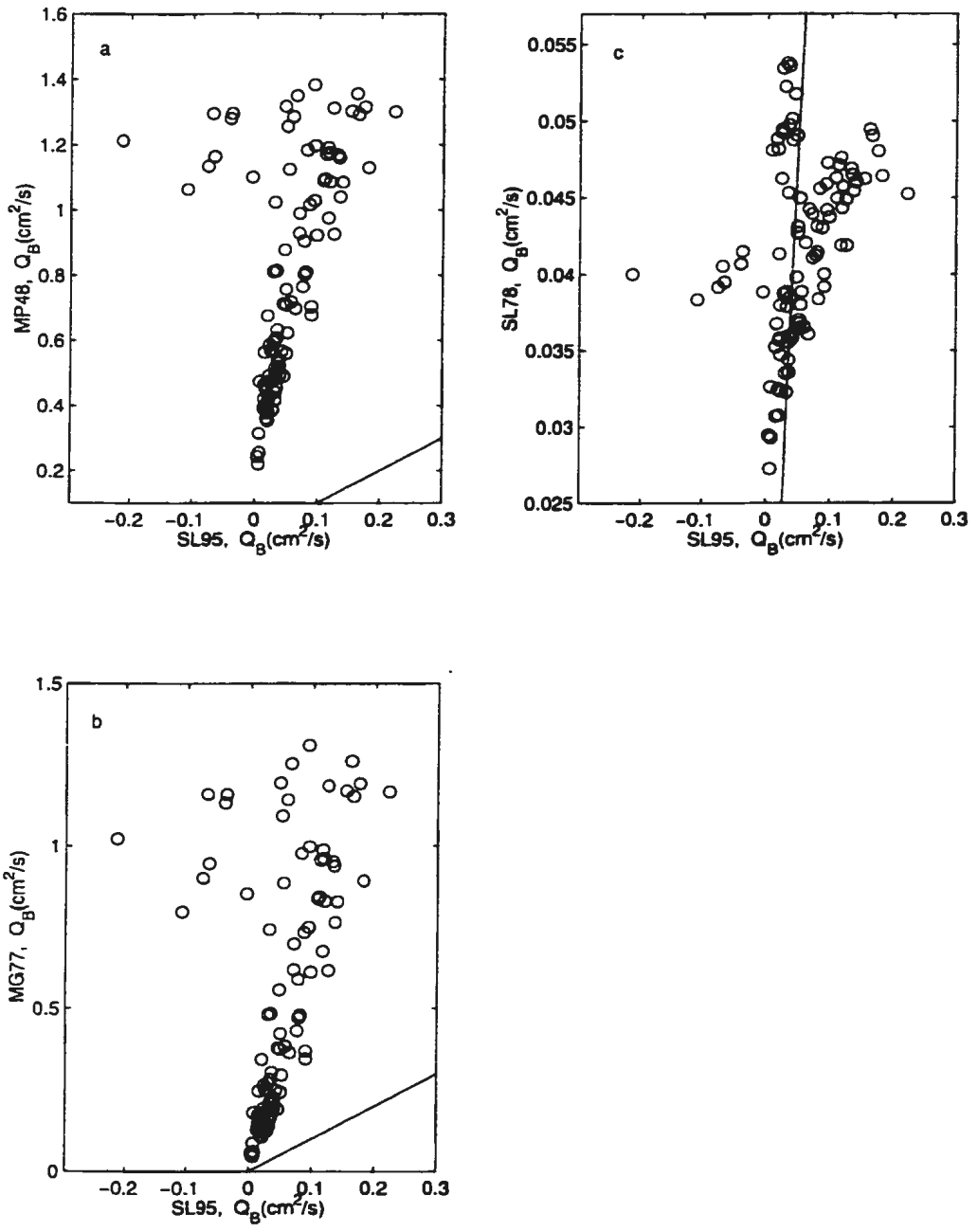

Figure 5.22: The comparison between the cross-shore bedload sediment transport calculated using the Sleath (1995) model with results from the Meyer-Peter and Müller (1948) model (a), Madsen and Grant (1977) model (b), and Sleath (1978) model (c). The solid line indicates a one-to-one relationship between the Sleath (1995) model and other models.

is shown in Figure 5.23a. The results of bedload transport obtained by the WT80 model ranged from 0.03-0.08 cm^2/s onshore during Storm1 and 0.06-0.16 cm^2/s onshore during Storm2. Similar to the SL78 model, the results of WT80 model are of the same order of magnitude as both the measurements and the SL95 model, but could not predict the offshore bedload transport at the end of Storm2.

Watanabe (1982), here referred to as WT82, re-analysed the data of Watanabe et al. (1980) and suggested a slightly modified form given by Equation (1.15) in Chapter 1. The bedload sediment transport using the WT82 model is proportional to the cube of the fluid velocity. The comparison between the SL95 and WT82 model results is shown in Figure 4.24b. Using the model coefficient $A = 7$ as suggested by Watanabe (1982), the results of bedload sediment transport obtained by the WT82 model ranged from 0.06-0.22 cm^2/s onshore during Storm1 and 0.14-0.42 cm^2/s onshore during Storm2. The results of the WT82 model were of the same order of magnitude but generally higher than both field measurements and the SL95 model results. Also the WT82 model could not predict the offshore transport at the end of Storm2.

Kajima et al. (1982a), here referred to as KJ82, used experimental data from a prototype wave flume and suggested a bedload sediment transport model given by Equation (1.16) in Chapter 1, which differs from the WT82 model by having a model coefficient of 3 instead of 7. The comparison between the SL95 and WT82 model results is shown in Figure 5.23c. The results of bedload sediment transport obtained by the KJ82 model ranged from 0.03-0.08 cm^2/s onshore during Storm1 and 0.06-0.17 cm^2/s onshore during Storm2. These results were of the same order of magnitude as both field measurements and the SL95 model results. The KJ82 model is able to reproduce quite reasonably the measured values of onshore bedload sediment transport; however, it could not predict the offshore transport at the end of Storm2.

The Vincent et al. (1981) bedload transport model, here referred to as the VC81 model, is given by Equation (1.13) in Chapter 1. This model is based on the MG77 approach and was obtained after reinterpreting the original data. Bedload sediment transport in the VC81 model is proportional to the cube of the fluid velocity. Vincent et al. (1981) also

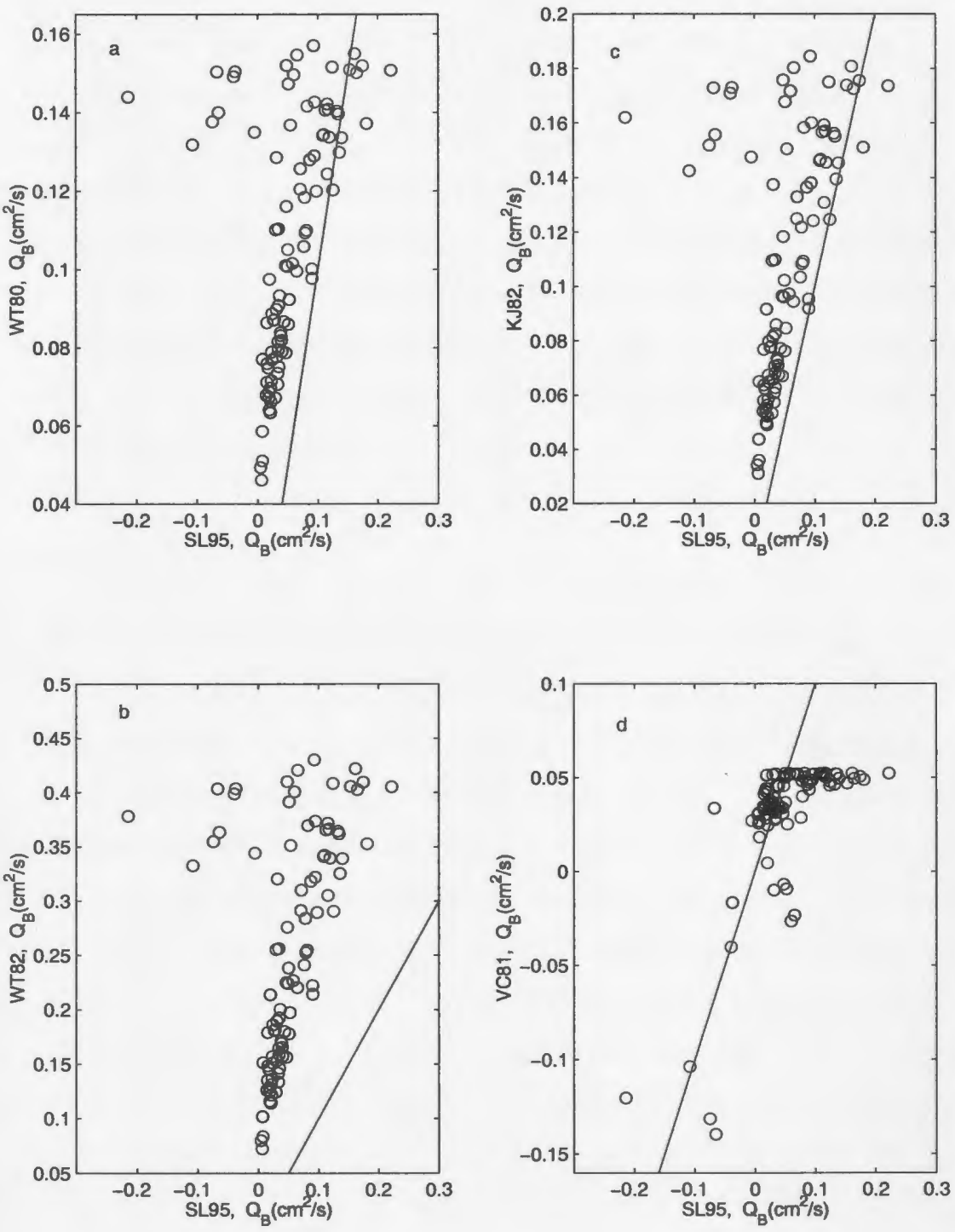

Figure 5.23: The comparison between the cross-shore bedload sediment transport calculated using the Sleath (1995) model with results from the Watanabe et al. (1980) model (a), Watanabe (1982) model (b), Kajima et al. (1982) model (c) and Vincent et al. (1981) model (d). The solid line indicates a one-to-one relationship between the Sleath (1995) model and other models.

applied a value of f_{cw}=0.01 in their model, the same value used in this thesis. The comparison between the SL95 and VC81 model results is shown in Figure 5.23d. The results of bedload sediment transport obtained by the VC81 model ranged from 0.01-0.04 cm^2/s onshore during Storm1, 0-0.06 cm^2/s onshore during the first stage of Storm2 and 0-0.14 cm^2/s offshore during the second stage of Storm2. These results are interesting because the VC81 model reproduced at least the correct directions of measured bedload sediment transport. The magnitude of the offshore bedload transport predicted by the VC81 model is reasonably similar to that suggested by both the field measurements and the SL95 model. However, the VC81 model predict values for onshore transport slightly lower than both the measurements and the SL95 model.

Summary

In summary, the cross-shore lunate megaripple migration velocities were well modelled using the stress-based models. Sleath (1995) model produced results that are consistent with the present measurements of cross-shore migration velocities. Sleath (1995) model seem to have better predictive skills of cross-shore megaripple migration velocities compared to all the other stress-based models that were examined in this thesis. Bagnold (1946) model was successful in relating the measured migration velocities and heights with bedload transport computed using a stress-based model. Therefore provided megaripple heights remains constant, these results suggest that cross-shore bedload transport is directly proportional to lunate megaripple migration velocities. The results also show that longshore stresses are important in modelling the cross-shore migration velocities. Better comparison between measured and modelled migration velocities are also obtained when treating the infragravity velocities as waves as opposed to currents. There is not much difference between the use of $\xi = 3/2$ or $\xi = 5/2$ exponents in the models provided the appropriate coefficients are applied. Both $0.5U_{pp}$ and $2U_{rms}$ approaches of obtaining the wave-orbital velocity amplitude produce similar results.

Chapter 6

Lunate megaripple orientations and the direction of bedload sediment transport

The problem of bedform orientation with respect to the flow field has been puzzling geomorphologists for a long time. For example Frere (1870) wondered why some bedforms are oriented roughly transverse to the flow, whereas others are parallel or oblique to the flow. Since then, the problem of bedform alignment has been the subject of considerable field observation and speculation (Rubin and Ikeda, 1990). Another problem related to bedform alignment concerns the direction of net bedload sediment transport. Today we at least know that storm processes are the dominant factor in marine sediment transport. However the magnitude and direction of net bedload sediment transport are still not well known. The net sediment transport direction is of particular interest when determining the sediment transport pathways in sediment depositional basins.

The difficulty of relating bedform trends to various flow directional parameters is more apparent for flows that vary in direction, such as wave-generated oscillatory flows with or without mean current. This is because the different directional parameters can diverge. It is in these types of flow that there is no general agreement on which parameters are responsible for controlling the bedform trends (Rubin and Hunter, 1987).

Rubin and Hunter (1987) performed an experiment where a large sand-covered table was rotated periodically in steady winds. The study of the generated wind ripples supported

the hypothesis that bedforms are not oriented in the direction of the resultant sediment transport vector, but instead in such a way that the total bedform-normal sediment transport is maximized. Later Rubin and Ikeda (1990) examined the same problem using subaqueous dunes generated on a 3.6 m diameter sand-covered turntable on the floor of a 4 m wide flume. The results supported the same conclusions obtained in the earlier experiment of Rubin and Hunter (1987).

Although wind ripples and subaqueous dunes investigated in the laboratory had trends that yielded maximum gross bedform-normal sediment transport, there have been extremely few reports on field measurements of nearshore lunate megaripple orientations and their comparison with these existing theories. Recently, Gallagher et al. (1998) used an array of downward-looking altimeters to measure megaripple migration directions from the alongshore and cross-shore migration velocity components during the DUCK94 experiment. The migration velocities were determined from cross-correlating 48-hour records of bottom elevation time series. They then computed the predicted migration directions based on the relation suggested by Rubin and Hunter (1987) using sediment transport calculated as proportional to the instantaneous velocity cubed. Their results showed that megaripples in the surf-zone did not migrate in the direction of the vector sum of currents, but were aligned such that sediment transport normal to the bedform is maximized as hypothesized by Rubin and Hunter (1987).

Gallagher et al. could not measure megaripple orientations. It is therefore interesting to compare measured orientations (determined at 0.5-hour intervals) with fluid forcing directions (wave incident angles, and mean and total current directions) and with the computed resultant bedload transport direction and maximum normal transport direction proposed by Rubin and Hunter (1987).

6.1 Measured lunate megaripple orientations

Lunate megaripple orientations (ϕ_{Mrip}) were measured from the half-hourly fan-beam images using the same data base as the measurements of lunate megaripple spans and spacings

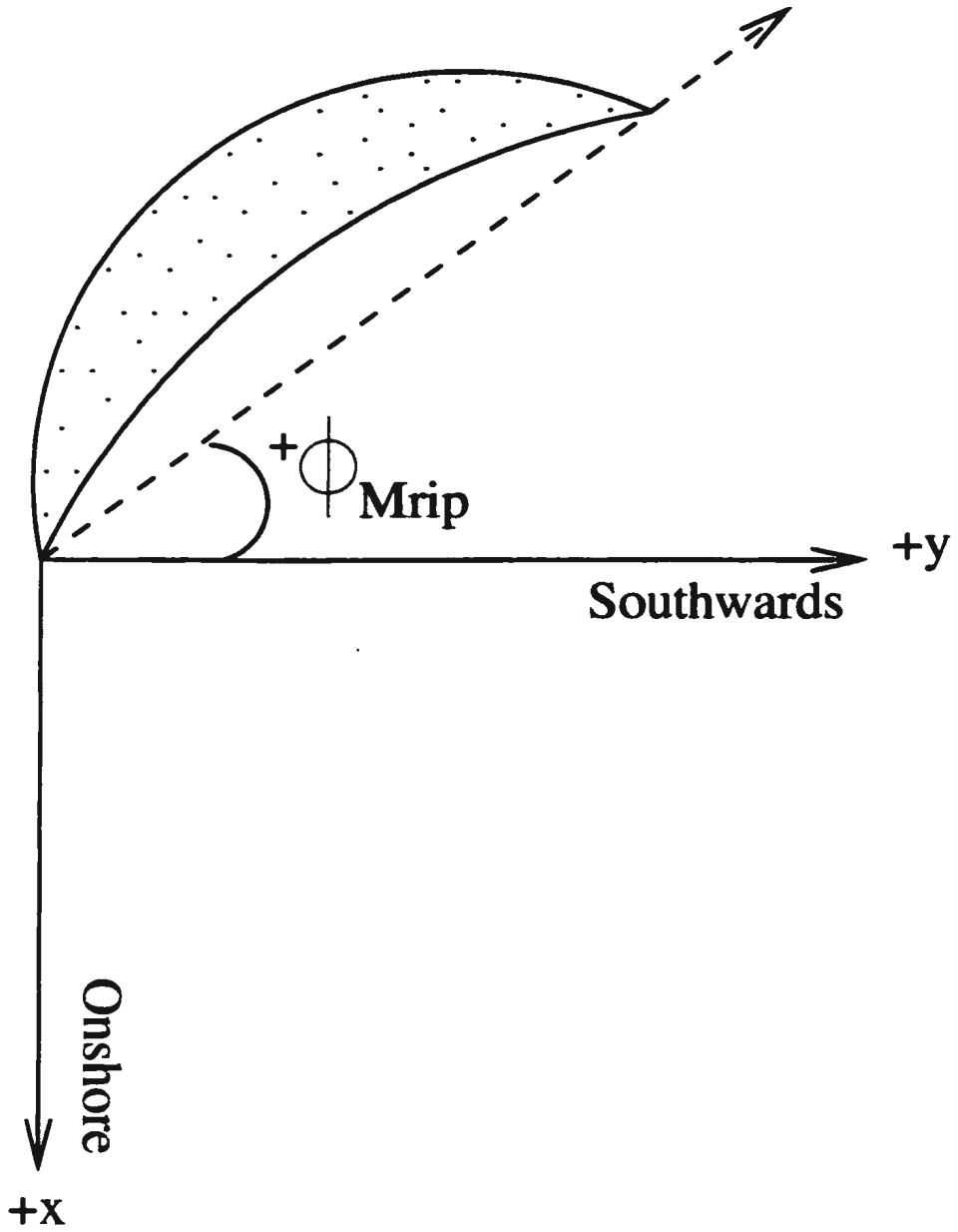

Figure 6.1: Schematic diagram showing the measured lunate megaripple angles of orientation (ϕ_{Mrip}) with respect to the along-shore (y) and cross-shore directions (x).

discussed in Chapter 5. The orientations were defined as the angle between the horn-to-horn trend and the horizontal axis parallel to the shoreline as shown in Figure 6.1. Since all the megaripples considered here were essentially cross-shore oriented, with their horns pointing roughly shoreward, the estimated orientations were either positive for megaripples pointed southward or negative for megaripples pointed northward as shown in Figure 6.1. It should also be mentioned here that only the orientations of solitary, clearly defined megaripples were measured. This created a few gaps where some images could not be analysed for orientations.

Figure 6.2 shows time series of the measured lunate megaripple orientations for Storm1 and Storm2. There is considerable time variability in the measured orientations during both storms. Mean lunate megaripple orientations ranged from +20° to -30° during Storm1 and +20° to -80° during Storm2 (Figure 5.2). There is no obvious correlation between the mean cross-shore flow shown earlier in Figure 4.7 and the measured lunate megaripple orientations shown in Figure 6.2. However, it is interesting to note that there are some similarities between the megaripple orientations and the direction of mean longshore velocity vector. For example the southward flow of mean longshore currents on Yeardays 277.3-277.9 during Storm1 can be correlated with the southward-oriented megaripples during that period (Figure 5.2 in Chapter 5). Similarly, the northward mean longshore currents on Yeardays 286.5-288 can be correlated with the northward-oriented megaripples during the same period (Figures 5.6 and 5.7 in Chapter 5).

Figure 6.3 shows the histograms of all the measured lunate megaripple orientations for Storm1 and Storm2. The histogram for Storm1 has a mode near 0° while that for Storm2 has a mode at about -20°. This is another demonstration that although lunate megaripples were mostly cross-shore oriented during the two storms, some megaripples during Storm2 had northward orientation due to northward longshore currents at that period.

It is interesting to note that there seems to be a symmetric distribution pattern for the orientations (Figure 6.3). The measured orientations were therefore compared with a normal distribution function given by the formula

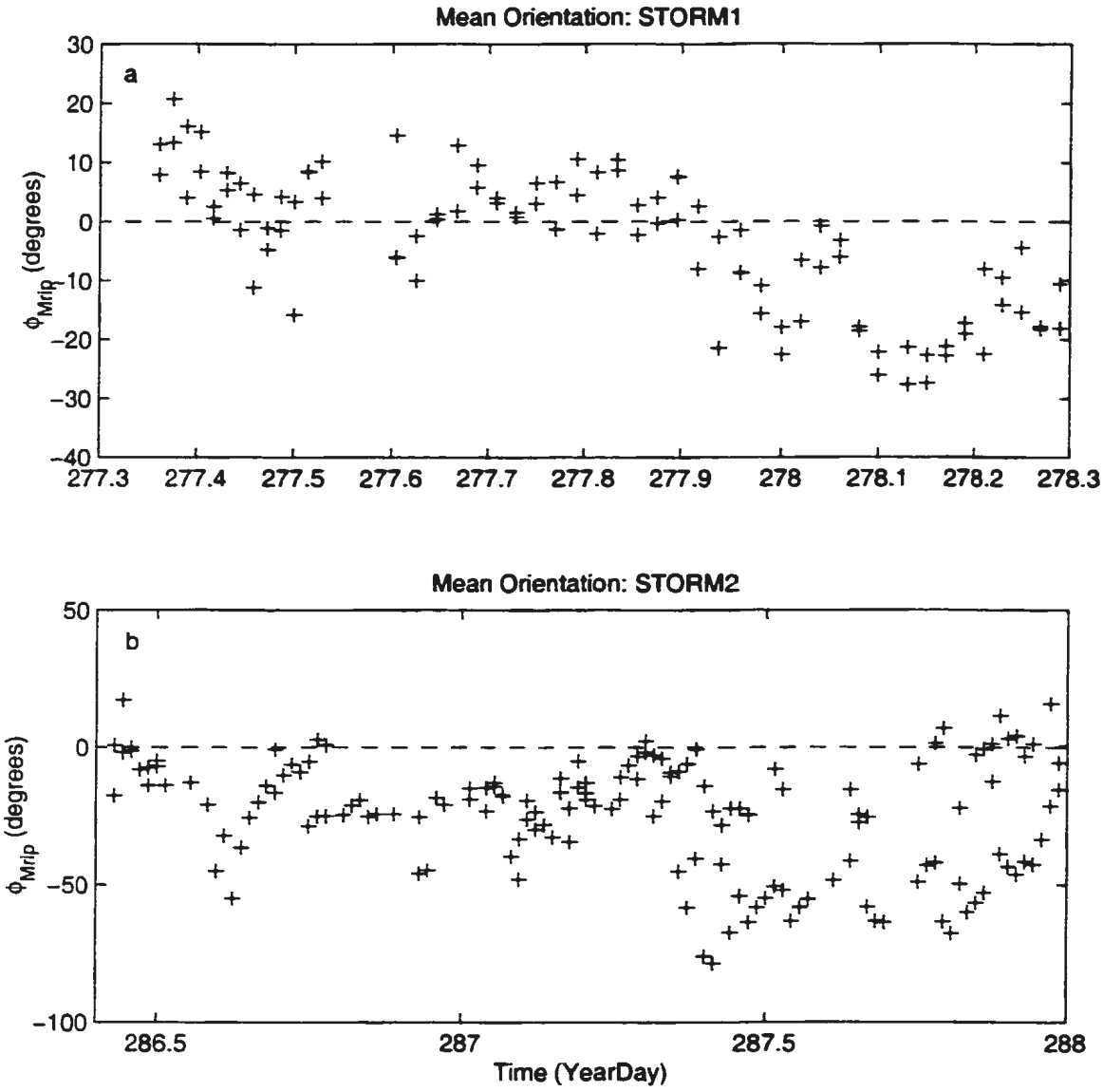

Figure 6.2: Measured mean megaripple orientations, ϕ_{Mrip}, for Storm1 (a) and Storm2 (b). The orientations were averaged every half-hour corresponding to the time interval between fan-beam images. Positive angles refers to southward oriented megaripples, while negative refers to northward oriented megaripples.

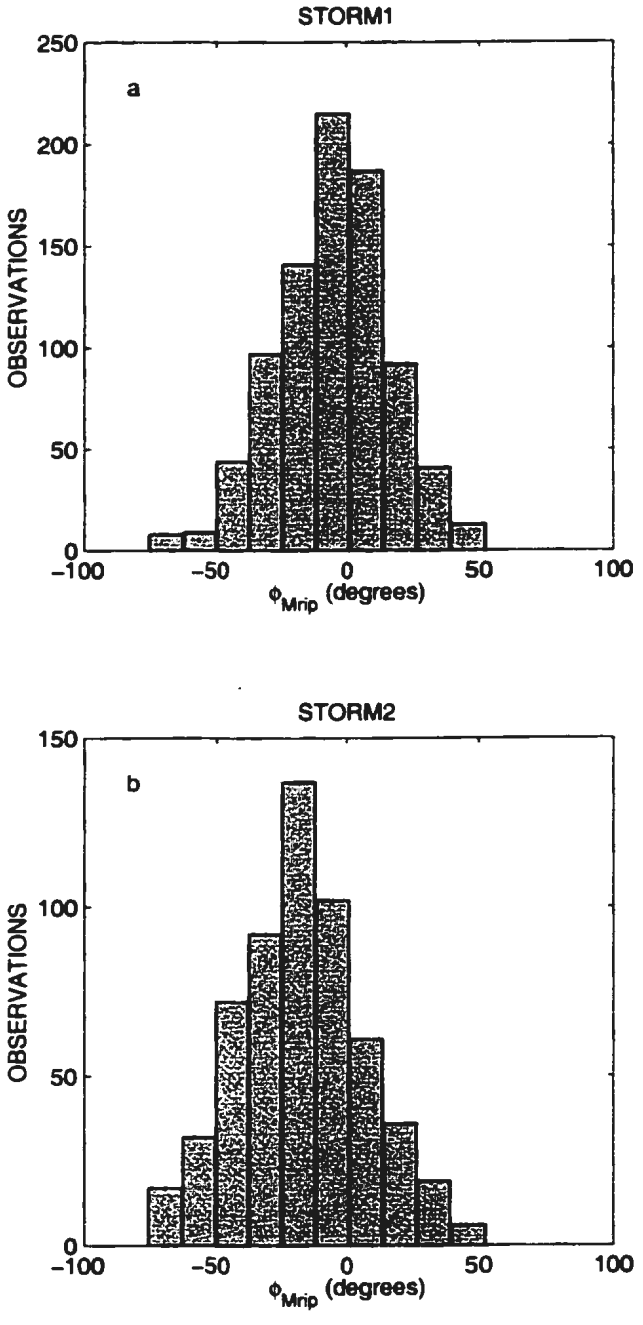

Figure 6.3: Histograms of all the measured lunate megaripple orientations (ϕ_{Mrip}) for Storm1 (a) and Storm2 (b).

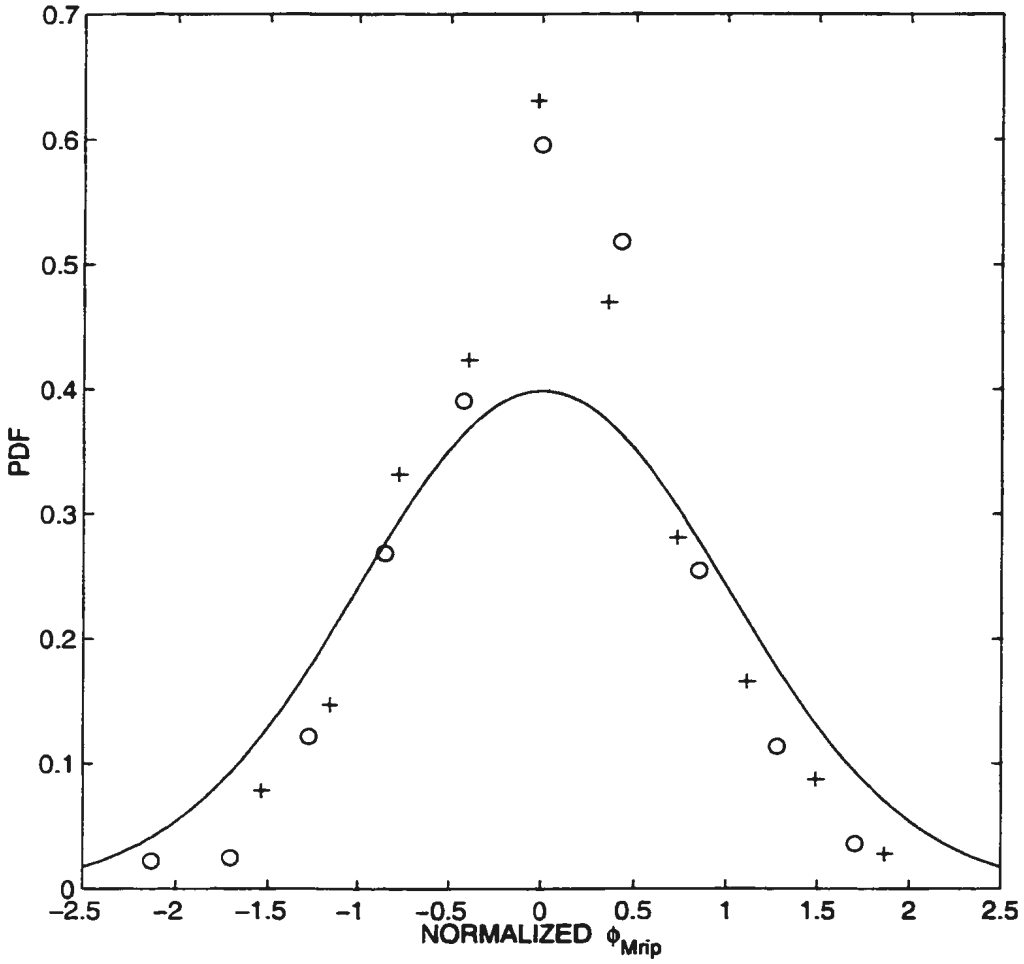

Figure 6.4: Fitting of a probability density function to normalized megaripple orientations, where (o)=Storm1 and (+)=Storm2 statistics. The solid line represents the fitted normal distribution function.

$$P_n = \frac{1}{\sqrt{2\pi}} e^{-\frac{(x-\bar{x})^2}{2\sigma^2}}, \tag{6.1}$$

where P_n is the probability density function for normal distribution, x represents the measurements and σ is the standard deviation of the measurements. The difference between orientations and the mean value were therefore normalized by $\sigma\sqrt{2}$. The computed histogram frequencies were then converted into probability densities to obtain the probability density functions for both storms. Figure 6.4 shows the distribution of the probability density of normalized megaripple orientations for both Storm1 and Storm2 as compared to the solid bell shaped curve which indicates the normal distribution function. The measured megaripple orientations show a distribution which tends to be more peaked than the normal distribution function. The normal distribution parameters were given by $\overline{\phi}_{Mrip} = -5.2^o$ and $\sigma_{Mrip} = 21.3^o$ for Storm1 and $\overline{\phi}_{Mrip} = -17.5^o$ and $\sigma_{Mrip} = 24.0^o$ for Storm2.

6.2 Direction of incident waves, mean and total currents

The direction of incident waves ϕ_{wave} is estimated from the measured cross-shore (u_w) and alongshore (v_w) components of the wave-orbital velocities, based on a method suggested by Fofonoff (1969):

$$\phi_{wave} = \frac{1}{2}\tan^{-1}\left[\frac{2\overline{u_w v_w}}{\overline{u_w}^2 - \overline{v_w}^2}\right]. \tag{6.2}$$

The directions of the half hourly averaged mean currents were calculated from

$$\phi_{mean} = \tan^{-1}\left[\frac{V}{U}\right]. \tag{6.3}$$

In addition, following Gallagher et al. (1998b), the directions of the vector sum of the mean and wave-orbital velocities were also calculated using

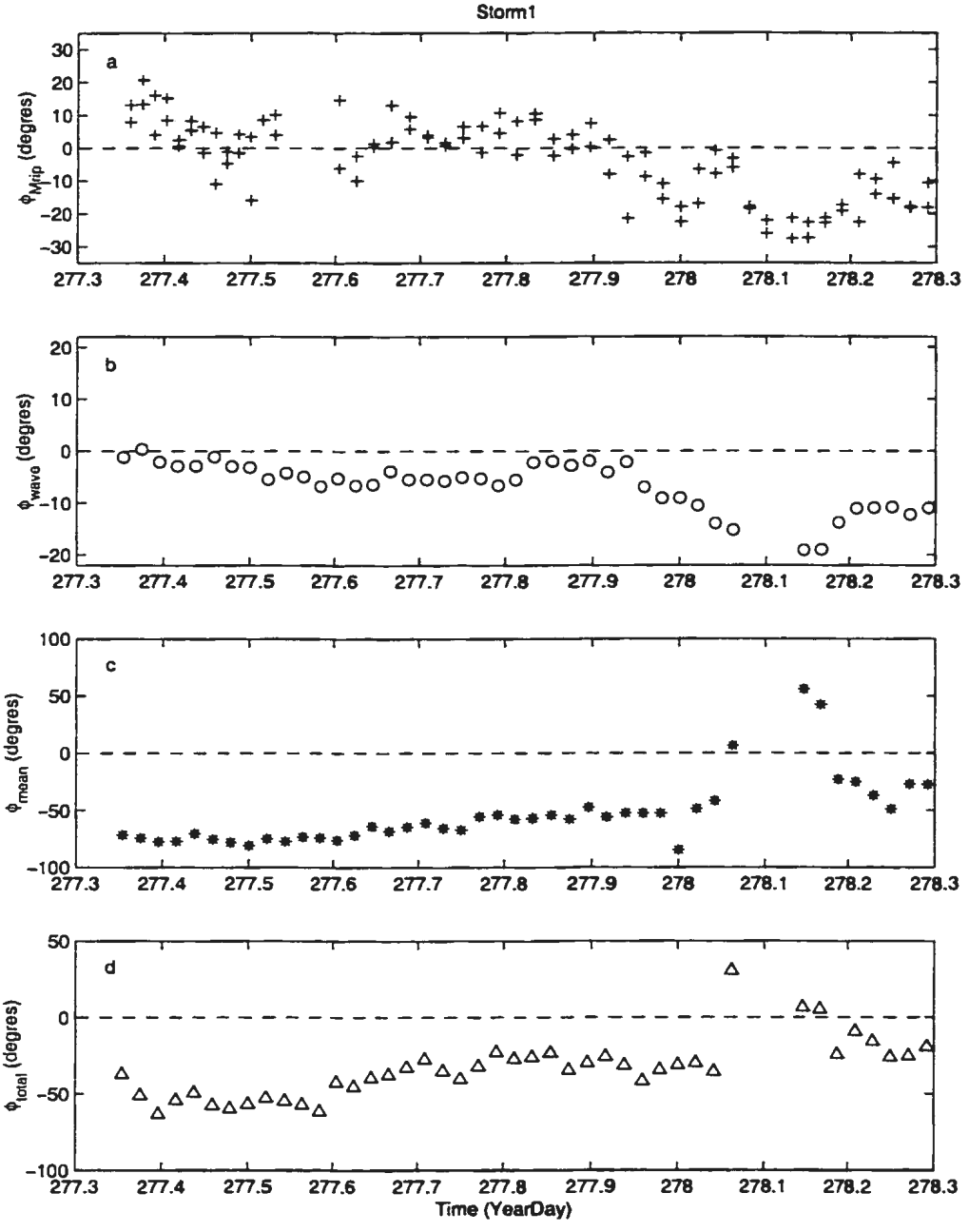

Figure 6.5: Time series of the measured mean lunate megaripple orientations (a), the calculated wave incident angles (b), direction of mean currents (c), and direction of total currents vector (d) for Storm1.

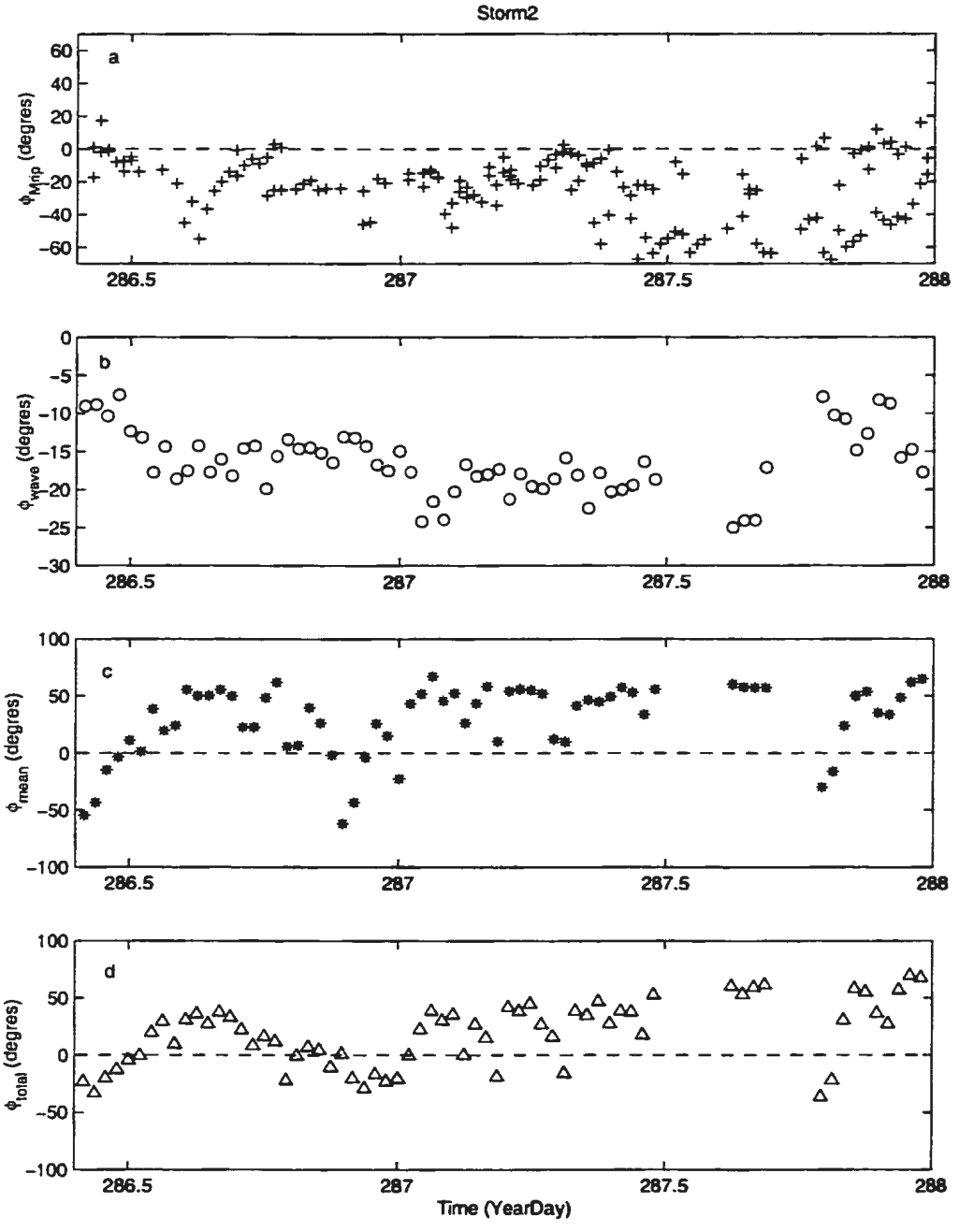

Figure 6.6: Time series of the measured mean lunate megaripple orientations (a), the calculated wave incident angles (b), direction of mean currents (c), and direction of total currents vector (d) for Storm2.

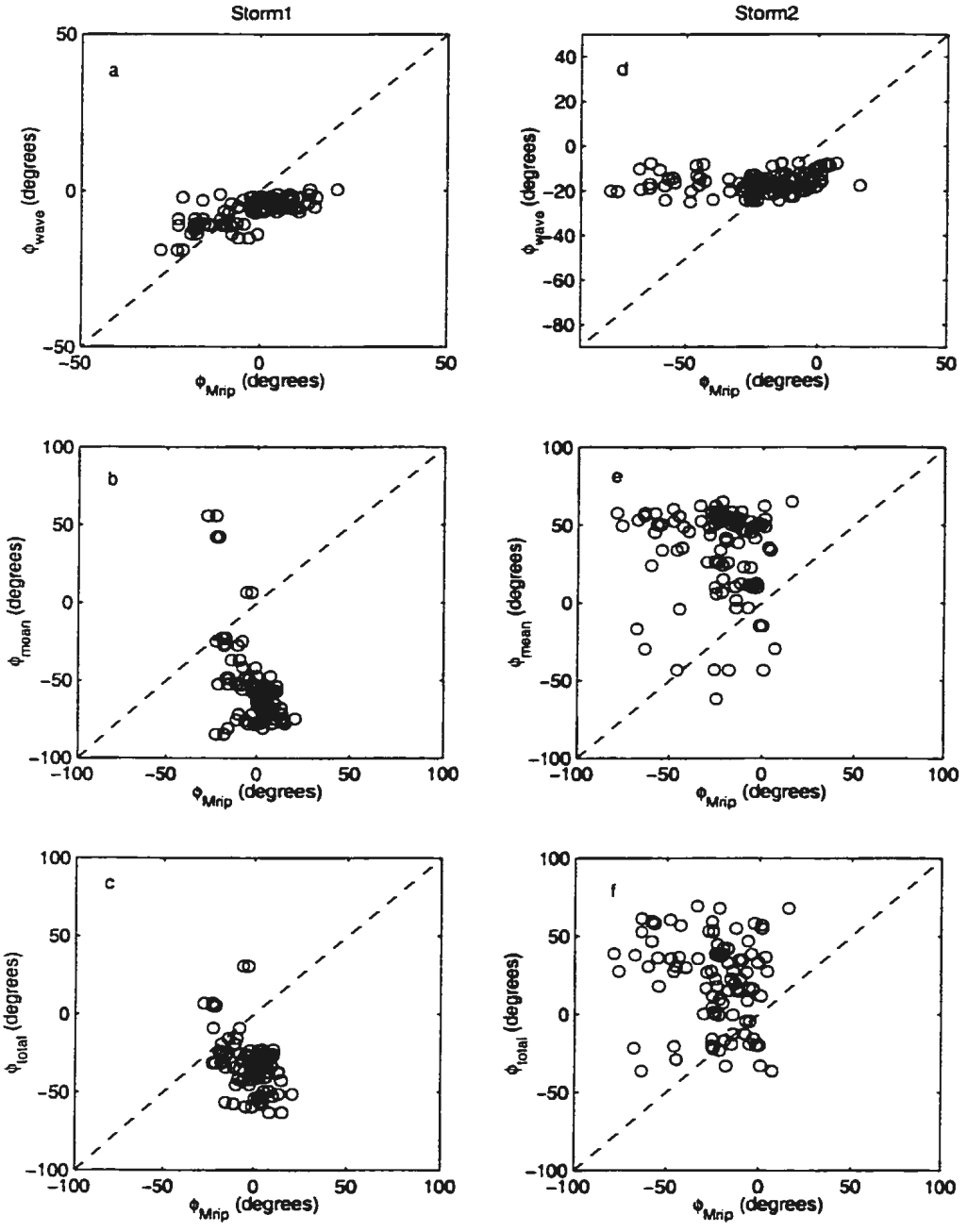

Figure 6.7: Scatter diagrams for the comparison between mean lunate megaripple orientations (ϕ_{Mrip}), with calculated directions of wave incident angles (a), mean currents (b), and total currents vector (c) for Storm1 and Storm2 (d, e and f). The dashed line represent 1:1.

$$\phi_{total} = \tan^{-1}\left[\frac{U + u_w}{V + v_w}\right]. \tag{6.4}$$

Figures 6.5 and 6.6 show the comparison between a time series of lunate megaripple orientations ϕ_{Mrip} with ϕ_{wave}, ϕ_{mean} and ϕ_{total} for Storm1 and Storm2 respectively. The comparison between measured orientations of lunate megaripples with local wave angles of incidence seems to be reasonably better than the direction of mean currents ϕ_{mean} or total currents vector ϕ_{total}. However, the scatter diagrams for the comparison between ϕ_{Mrip} and ϕ_{wave}, ϕ_{mean} and ϕ_{total} (Figures 6.7a-c and 6.7d-f) show a poor correlation. The results indicate that lunate megaripples are not aligned with the direction of ϕ_{wave}, ϕ_{mean} or ϕ_{total}. A similar lack of alignment was observed by Gallagher et al. (1998b) between 48-hour average migration direction and these quantities.

6.3 Rule of maximum gross bedform-normal transport

Rubin and Hunter (1987) suggested that bedform crests are aligned such that the gross transport normal to the ripple crest is maximal. Transport over any bedform can be resolved into two components, one normal and another parallel to the bedform crest. Gross bedform-normal transport G_B is therefore the sum of the absolute value of bedform-normal components (Rubin and Hunter, 1987): that is

$$G_B = D_B|\sin\varphi| + S_B|\sin(\gamma - \varphi)|, \tag{6.5}$$

where D_B and S_B are the amounts of transport represented by the dominant and subordinate transport vectors respectively in the two half cycles of a periodic forcing function (Figure 6.8); φ is the angle between the dominant transport vector and the bedform orientation; and γ is the angle between D_B and S_B. The bedform trend that yields the maximum value of G_B is then

$$\tan\varphi = \pm\frac{|D_B|/|S_B| + |\cos\gamma|}{|\sin\gamma|}. \tag{6.6}$$

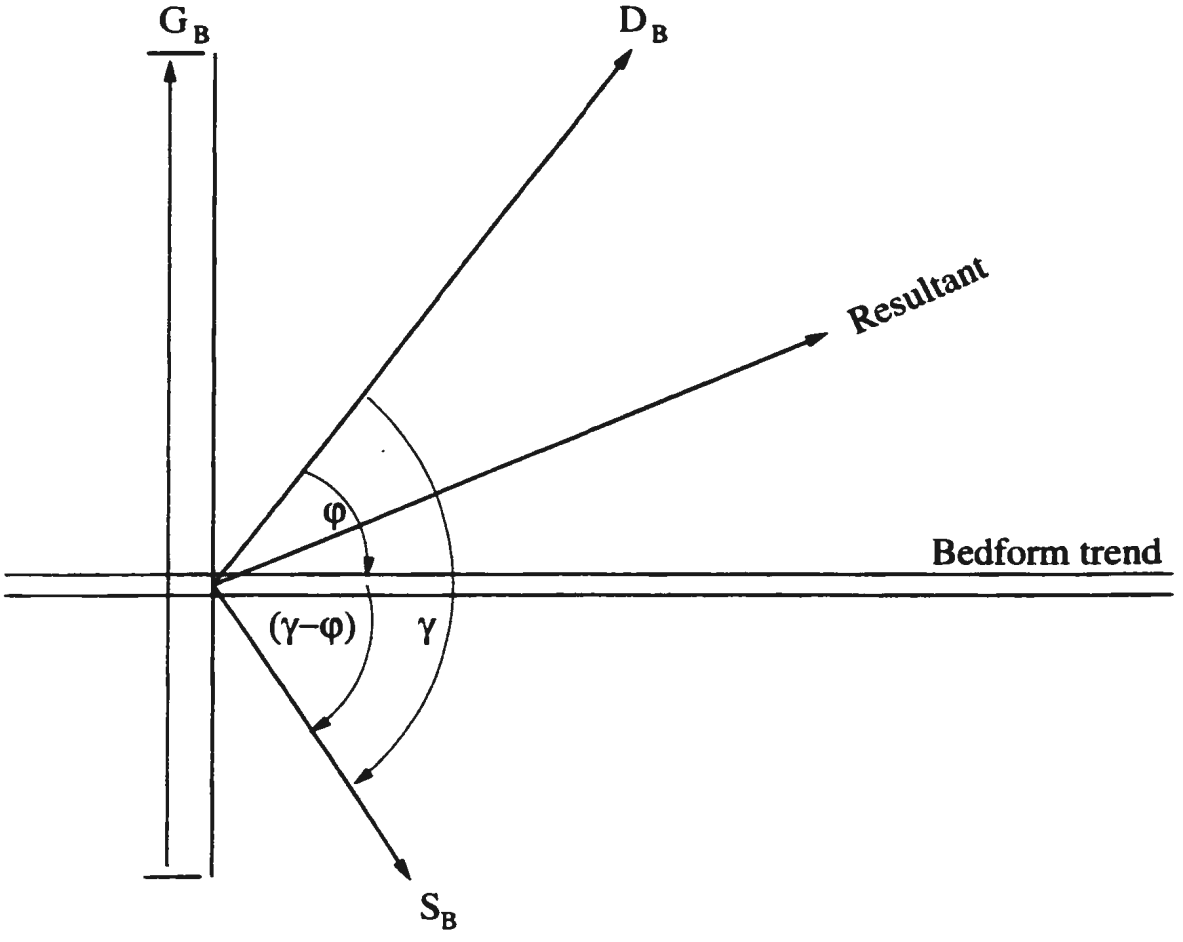

Figure 6.8: Schematic diagram showing the transport vectors and bedform orientation from Rubin and Hunter (1987). The angle between the dominant (D_B) and subordinate (S_B) transport vectors is γ, the angle between D_B and the bedform crest (double line) is φ, Resultant is the vector sum of D_B and S_B, and G_B is the gross bedform-normal transport.

The minus sign gives the correct value of φ for γ ranging from 0° to 90°, and the plus sign gives the correct value for γ ranging from 90° to 180°.

In natural flows there is a large range of magnitudes and directions for individual waves, so that sediment can be transported in any number of directions. In this case one must compute, for the given flow conditions, the gross bedform-normal transport for a variety of arbitrary bedform trends, and to select the trend that yields the maximum value (Rubin and Hunter, 1989; Gallagher et al., 1998b). For natural surf-zones, Equation (6.5) is therefore modified to include a sum over a continuum of instantaneous transport vectors. Thus,

$$G_{B_j} = \sum_{i=1}^{n} |Q_{By_i} \sin \beta_j + Q_{Bx_i} \sin(\pi/2 - \beta_j)|, \tag{6.7}$$

where the subscript i represent each data point, n is the total number of velocity data points in each half hour time series and j represents a given choice of the bedform trend β (Figure 6.9). Using the stress-based model described in Chapter 5, Q_{Bx} and Q_{By} (see Appendix B) are the along-shore and cross-shore components of bedload sediment transport respectively given by

$$Q_{Bx} = [\hat{A}(\rho\sqrt{f_c f_w})^{\xi-1}(\rho f_c)]\chi_x, \tag{6.8}$$

$$Q_{By} = [\hat{A}(\rho\sqrt{f_c f_w})^{\xi-1}(\rho f_c)]\chi_y. \tag{6.9}$$

The parameter inside the square brackets is the same in both Equations (6.8) and (6.9), and a constant. Therefore for the purposes of this analysis Q_{Bx} and Q_{By} were simply represented by the forcing terms χ_x and χ_y for both $\xi = 3/2$ and $\xi = 5/2$.

The gross bedform-normal transport G_B was therefore maximized numerically to give the lunate megaripple orientation during a particular run. The approach was to assign a variety of arbitrary values of angle β ranging from $-\pi/2 < \beta < \pi/2$ (1° increments) for each half hourly run, and to select the values of β that yields the maximum value of G_B.

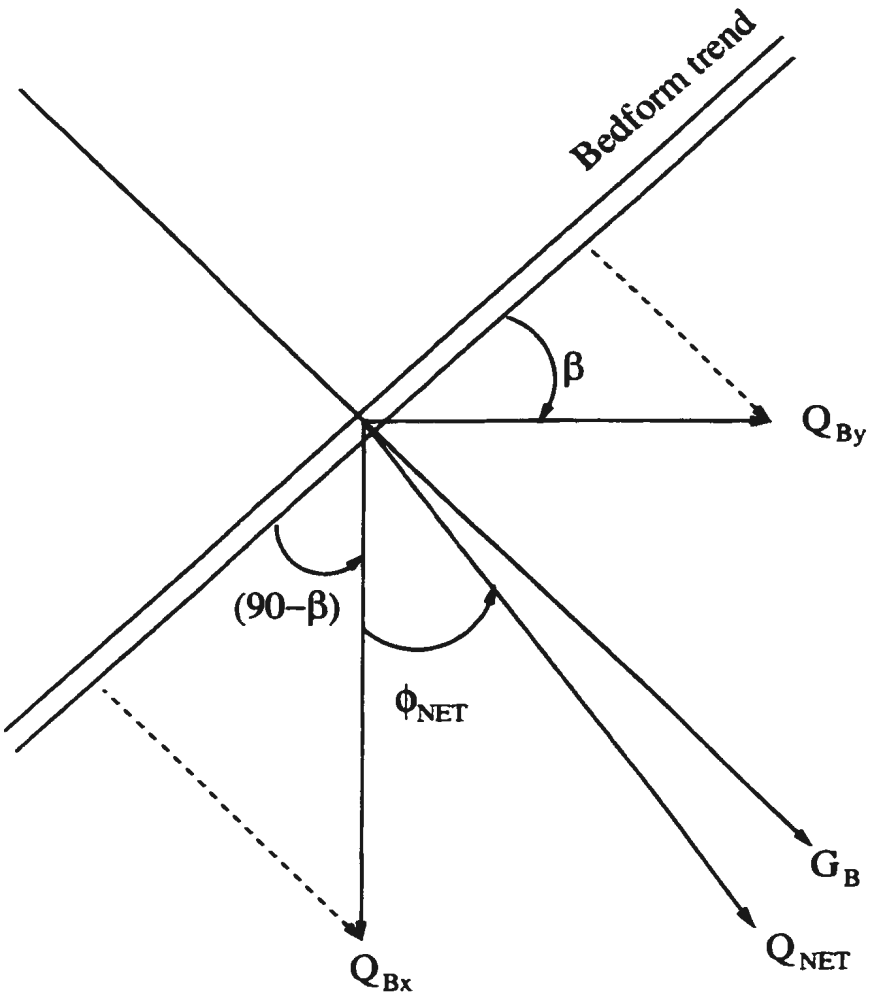

Figure 6.9: Schematic diagram showing the orientations of lunate megaripples with respect to the directions of sediment transport vectors, including the gross bedform-normal transport (G_B), alongshore (Q_{By}) and cross-shore (Q_{Bx}) bedload transport components. The angle ϕ_{NET} represent the direction of resultant bedload transport Q_{NET}. The angle β represent the orientation of lunate megaripple crest (double line) such that the gross bedform-normal transport is maximized.

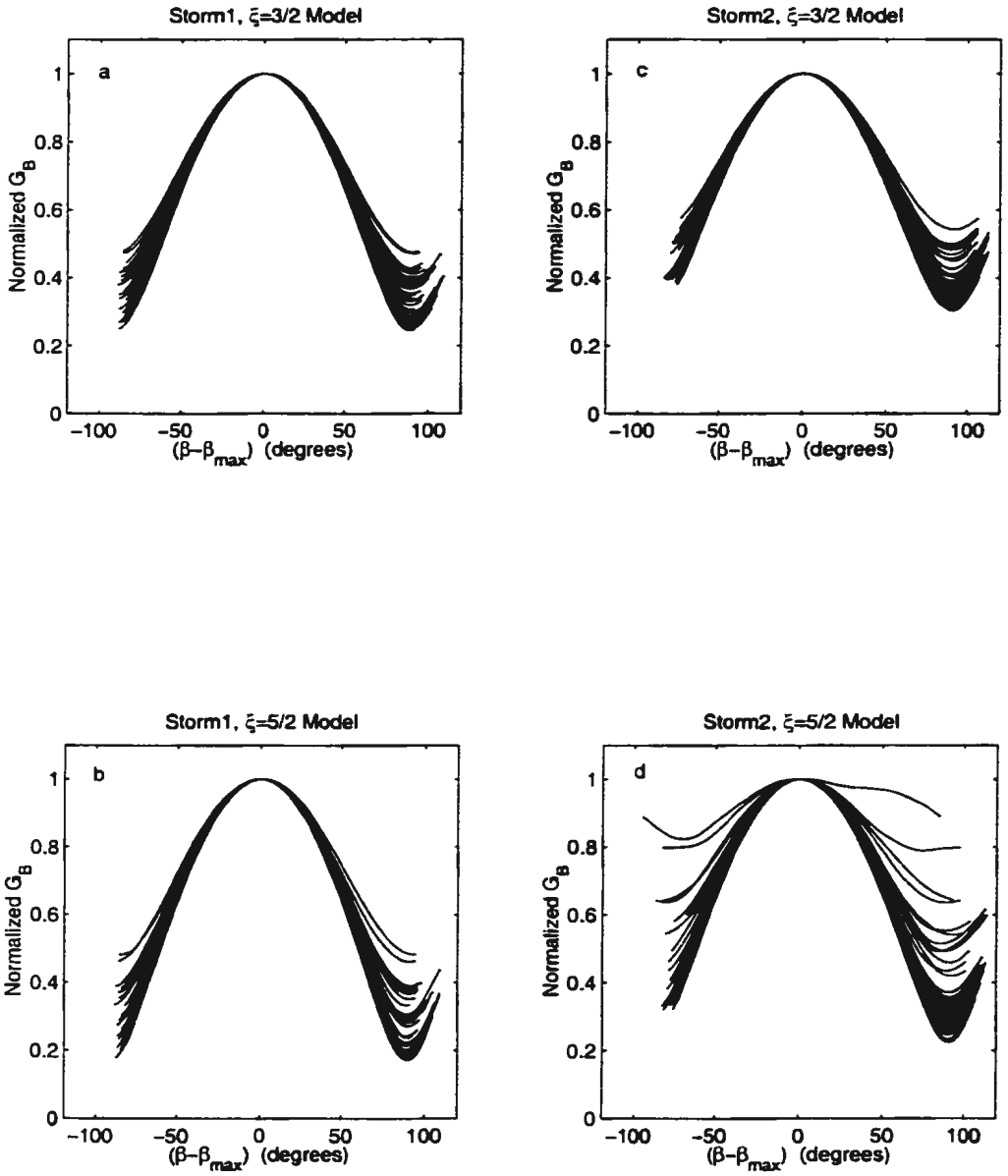

Figure 6.10: Normalized gross bedform-normal transport G_B used in the estimation of megaripple orientations based on Rubin and Hunter hypothesis (ϕ_{RH}). The peak G_B values at β_{max} angles are shown for Storm1 using $\xi = 3/2$ model (a), Storm1 using $\xi = 5/2$ model (b), Storm2 using $\xi = 3/2$ model (c) and Storm2 using $\xi = 5/2$ model (d).

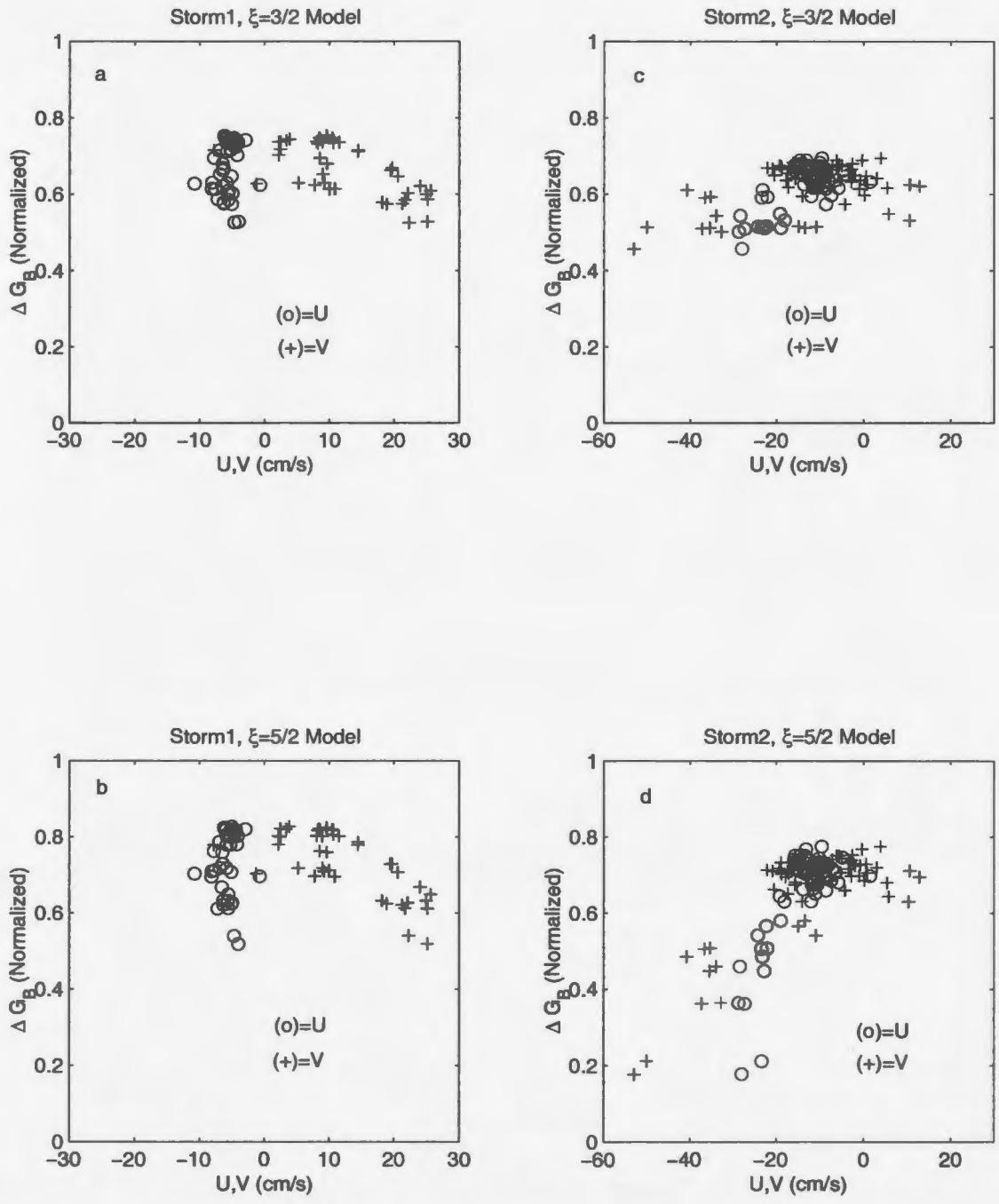

Figure 6.11: The difference between the maximum and minimum values of normalized gross bedform-normal transport (ΔG_B) compared with the mean cross-shore (o) and alongshore (+) velocities. The plots show the comparisons for Storm1 using $\xi = 3/2$ model (a), Storm1 using $\xi = 5/2$ model (b), Storm2 using $\xi = 3/2$ model (c) and Storm2 using $\xi = 5/2$ model (d).

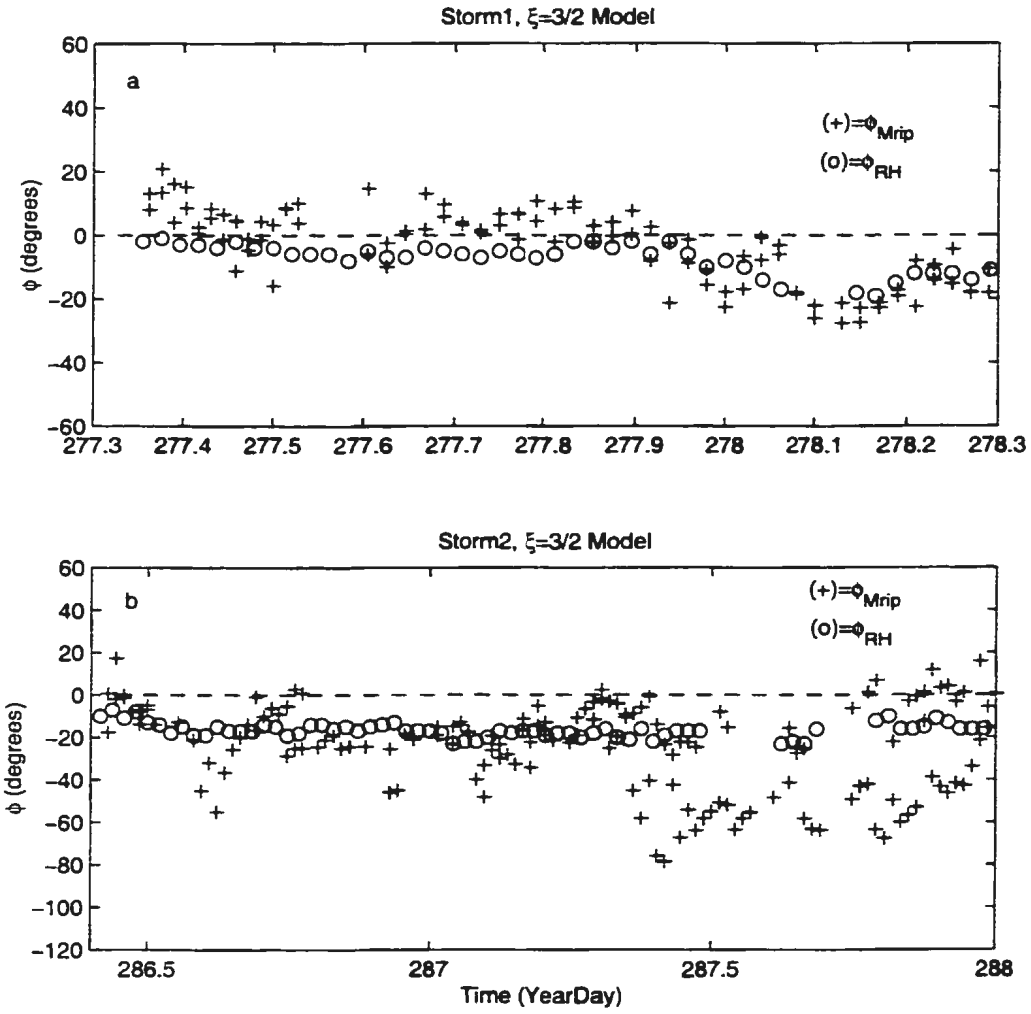

Figure 6.12: The time series of the measured lunate megaripple orientations (ϕ_{Mrip}) compared to the calculated directions of maximum gross bedform-normal bedload transport ϕ_{RH} for Storm1 (a) and Storm2 (b) using $\xi = 3/2$ model.

The value of β for which G_B is maximum gave the predicted lunate megaripple orientation according to Rubin and Hunter (1987) which is here referred to as ϕ_{RH}.

The calculated values of ϕ_{RH} can therefore be compared with the measured lunate megaripple orientations ϕ_{Mrip}. Both $\xi = 3/2$ and $\xi = 5/2$ bedload transport models were investigated. It is important to mention that the computed gross bedform-normal transport G_B for most runs used in this analysis showed an unambiguous maximum. This is demonstrated by the diagrams of normalized G_B against $(\beta - \beta_{max})$ during Storm1 using $\xi = 3/2$ model (Figure 6.10a), Storm1 using $\xi = 5/2$ model (Figure 6.10b), Storm2 using $\xi = 3/2$ model (Figure 6.10c) and Storm2 using $\xi = 5/2$ model (Figure 6.10d). The peaks of computed G_B were however slightly less distinct (Figure 6.10d) for the days which had strong mean flows. This is demonstrated by plotting the differences between the maximum and minimum values of normalized gross bedform-normal transport (ΔG_B) against the mean cross-shore and along-shore velocities (Figure 6.11). The computed ΔG_B values decreased with the increase in the strength of the mean flows. This result indicates that the selection of maximum values of G_B may be less accurate during durations with strong mean flows.

The time series of calculated ϕ_{RH} compared to ϕ_{Mrip} is shown in Figure 6.12 for Storm1 and Storm2 for the case of $\xi = 3/2$ model. The calculated values of ϕ_{RH} were consistently negative for both storms. This was contrary to the measured orientations, particularly for Yeardays 277.4-277.9 during Storm1. The calculated ϕ_{RH} angles were also noticeably smaller compared to the measurements for both storms.

The comparison of ϕ_{Mrip} with ϕ_{RH} for $\xi = 3/2$ (Figure 6.15a) and for $\xi = 5/2$ (Figure 6.15c) show no particular relationship between the two parameters. ϕ_{RH} exhibit a narrow range of values compared to the observations, and positive values of ϕ_{RH} are not predicted, whereas $\phi_{Mrip} > 0$ is observed. Figure 6.14 shows the details of the measured cross-shore and alongshore velocities during the days of interest. Both Storm1 and Yeardays 286.4-287.75 during Storm2 were characterized by quasisteady flow conditions. However, yeardays 287.75-288 during Storm2 were characterized by highly variable (0-50 cm/s) longshore currents, and strong (20-30 cm/s) cross-shore flows at the end of day

287. These complex flow conditions are reflected in the scatter of megaripple orientations close to the end of Storm2 (Figure 6.12b&6.13b) giving no preferred trends, most likely because the megaripples could not attain equillibrium with the higly changing flow conditions. It is therefore interesting to note that a poor relationship is obtained between ϕ_{Mrip} and ϕ_{RH} even after removing the measurements for Storm2 between Yeardays 287.35-287.75 (shown as triangles in Figures 6.15a and 6.15c) when northward longshore currents produced large observed angles for northward-oriented megaripples and Yeardays 287.75-288 (shown as squares in Figures 6.15a and 6.15c) when the flow field was highly variable. Therefore, there seems to be a poor agreement between the measured lunate megaripple orientations and the gross bedform-normal sediment transport direction.

6.4 Direction of resultant bedload sediment transport

The direction of resultant or net bedload transport was calculated every half hour using

$$\phi_{NET} = \tan^{-1} \frac{Q_{By}}{Q_{Bx}}. \tag{6.10}$$

The results were then compared with ϕ_{Mrip}. The time series of calculated ϕ_{NET} compared to ϕ_{Mrip} is shown in Figures 6.13 for Storm1 and Storm2 for $\xi = 3/2$. The results for $\xi = 5/2$ are similar and are not shown. There are variations in both measured orientations and calculated ϕ_{NET} (Yeardays 277.6-277.9) and magnitude (Yeardays 277.4-277.6) during Storm1 (Figure 6.13a). However, both the direction and magnitudes of calculated ϕ_{NET} angles for Storm2 (Yeardays 286.4-287.5) were consistent with the measured orientations (Figure 6.13b). Most of the calculated ϕ_{NET} angles were however significantly larger than the measurements near the end of Storm2 (Yeardays 287.7-288).

The comparison of ϕ_{Mrip} with ϕ_{NET} for $\xi = 3/2$ (Figure 6.15b) and for $\xi = 5/2$ (Figure 6.15d) show considerable scatter. However, if the measurements for Storm2 when megaripples had large angles of northward orientation are excluded (shown as triangles in Figures 6.15b and 6.15d) the comparisons between ϕ_{Mrip} with ϕ_{NET} improve somewhat. Still, many of these triangle points are consistent with the relationship between ϕ_{NET} and

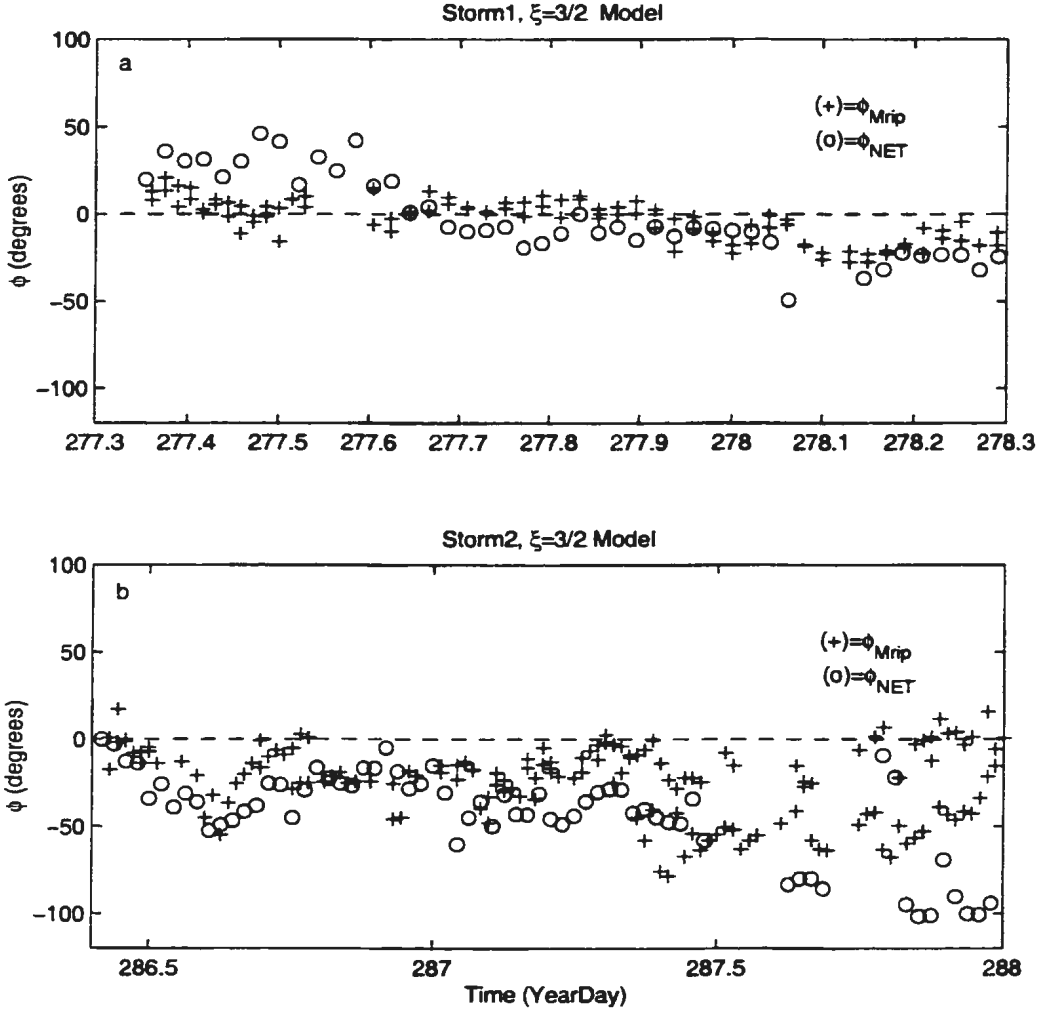

Figure 6.13: The time series of the measured lunate megaripple orientations (ϕ_{Mrip}) compared to the calculated direction of the resultant bedload transport (ϕ_{NET}) for Storm1 (a) and Storm2 (b) using $\xi = 3/2$ model.

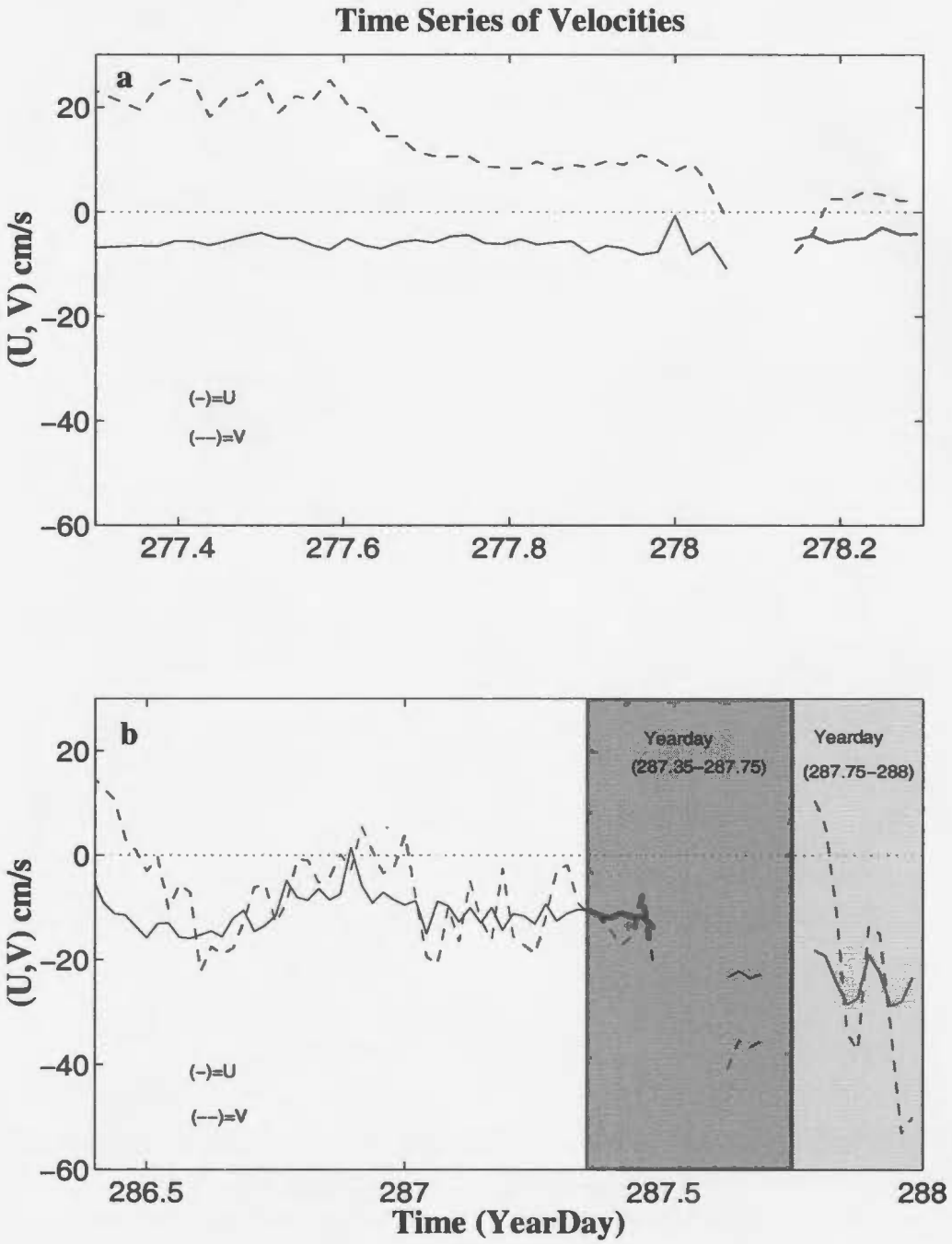

Figure 6.14: The time series of the measured cross-shore and alongshore velocities for Storm1 (a) and Storm2 (b) during the days of interest.

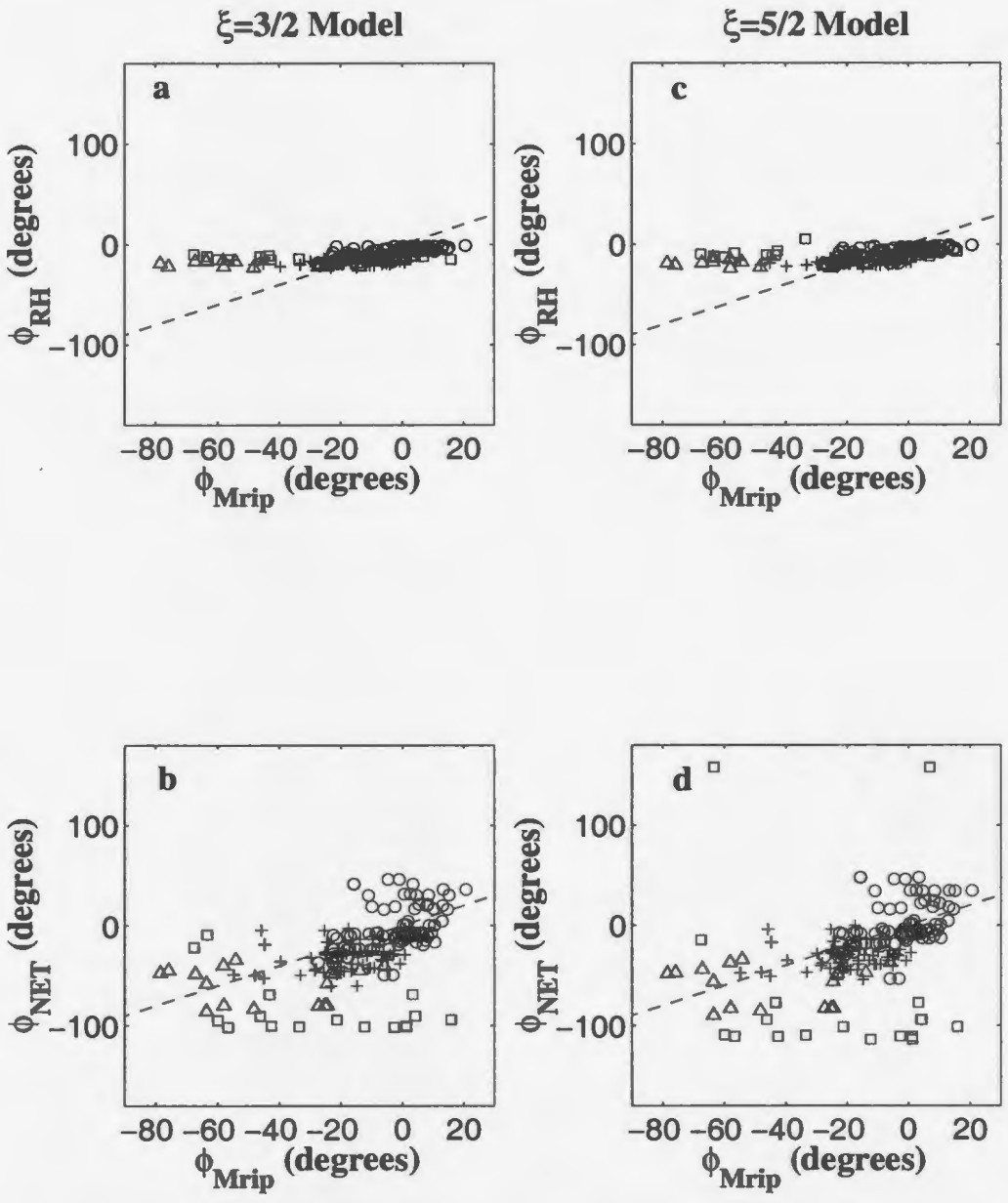

Figure 6.15: Scatter diagrams for the comparison between lunate megaripple orientations (ϕ_{Mrip}), with calculated directions of maximum gross bedform-normal bedload transport ϕ_{RH} (a), direction of the resultant bedload transport ϕ_{NET} (b) when using $\xi = 3/2$ and $\alpha = 6$. Also shown is a similar comparison for the case of $\xi = 5/2$ and $\alpha = 2$ (a&d). The symbols (o)=Storm1 measurements, (+)=measurements for Storm2 yeardays 286.4-287.35, (triangles)= measurements for Storm2 yeardays 287.35-287.75 and (squares)=measurements for Storm2 yeardays 287.75-288.

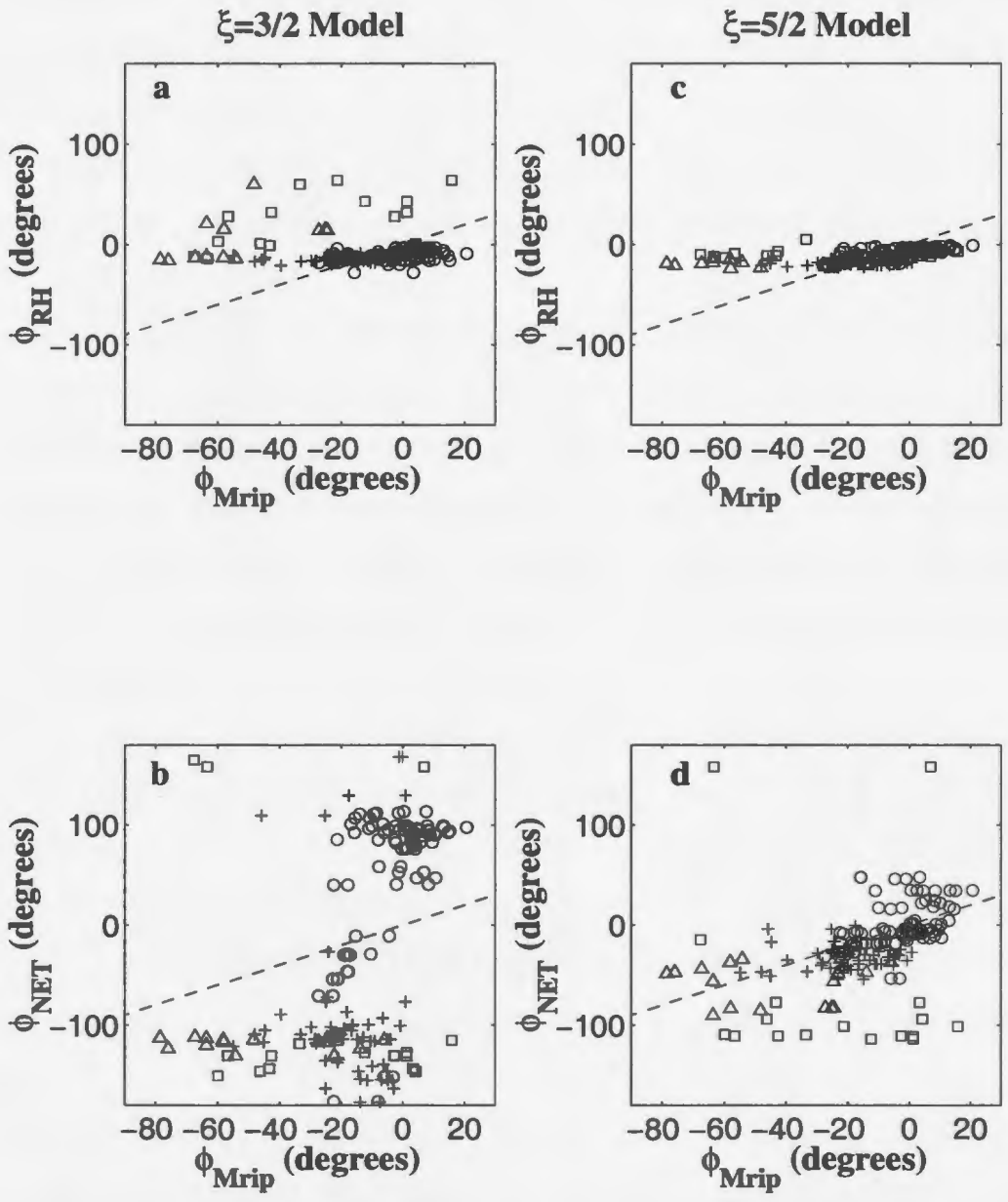

Figure 6.16: Scatter diagrams for the comparison between lunate megaripple orientations (ϕ_{Mrip}), with calculated directions of maximum gross bedform-normal bedload transport ϕ_{RH} (a), direction of the resultant bedload transport ϕ_{NET} (b) when using $\xi = 3/2$ and $\alpha = 1$. Also shown is a similar comparison for the case of $\xi = 5/2$ and $\alpha = 1$ (c&d). The symbols (o)=Storm1 measurements, (+)=measurements for Storm2 yeardays 286.4-287.35, (triangles)= measurements for Storm2 yeardays 287.35-287.75 and (squares)=measurements for Storm2 yeardays 287.75-288.

ϕ_{Mrip} indicated by the rest of the data. It is the triangles in the lower right quadrant which are most different. By comparing Figure 6.15b&d to Figure 6.14, it can be seen that these data points correspond to times of highly variable (0-50 cm/s) longshore currents, and strong (20-30 cm/s) cross-shore flows at the end of day 287. Thus there is a reasonable agreement between megaripple orientations and net bedload sediment transport directions during the periods of quasisteady flow conditions when megaripples appear to be in equilibrium with the flow.

Overall, the data indicate a better relationship between lunate megariple orientations and the direction of net sediment transport than gross normal transport. This is in marked contrast to the conclusion reached by Gallagher et al. (1998b). A possible reason for the different result is the different approaches used for sediment transport estimation. Gallagher et al. (1998b) estimated sediment transport as proportional to the instantaneous velocity cubed. In contrast, here bedload sediment transport is estimated using vector addition of the wave and current bed shear stresses.

In order to test the sensitivity to choice of wave and current friction factors we set $\alpha = 1$ which is approximately equivalent to Gallagher et al. (1998b). Figure 6.16 shows the resulting comparison. The obtained ϕ_{RH} and ϕ_{NET} computed using $\xi = 3/2$ model and $\alpha = 1$ were quite different from those obtained using $\alpha = 6$ (Figure 6.15). The obtained ϕ_{RH} and ϕ_{NET} computed using $\xi = 5/2$ model and $\alpha = 1$ were not very different from those obtained using $\alpha = 2$. The estimated values of ϕ_{RH} and ϕ_{NET} are sensitive to the choice of α.

The fact that the values of ϕ_{NET} which are comparable with the measured megaripple orientations are obtained when using the values of α which yielded a best fit to the migration velocities is encouraging, as orientation and migration rate are independent measurements. However, the sensitivity of the predicted orientations to the choice of α emphasizes the need for bottom stress measurements, as there are not yet reliable predictors for f_c and f_w for these flow conditions. Setting $\alpha = 1$ does not improve the comparison between ϕ_{RH} and ϕ_{Mrip}. Thus, the discrepancy between these results and those of Gallagher et al. (1998b) remains.

Chapter 7

Conclusions

Two storms occurred during the period of the Duck94 experiment. Cross-shore oriented lunate megaripples were the dominant bedform on Yeardays 277-279 during the first storm, and Yeardays 286-288 during the second storm. These time intervals are referred to in the thesis as Storm1 and Storm2 respectively.

Cross-shore oriented lunate megaripples during Storm1 and Storm2 occurred for grain roughness Shields parameter values in the range 0.5-1.4. The fan-beam sidescan sonar images show that lunate megaripple fields are complex and involve a mix of characteristic length scales and spacings. The results show that lunate megaripples over 1 m in horizontal scale persist for up to 3-6 hours.

The cross-shore lunate megaripples during the DUCK94 experiment ranged from 0.05 to 0.5 m in height. Lunate megaripple spans and spacings ranged from 0.25 to 2.75 m while the separation-length ranged from 0.5 to 4 m. These observations are comparable to those obtained by Clifton et al. (1971) by SCUBA observations on the southern coast of Oregon, Hay and Wilson (1994) along the southern shore of Lake Huron using rotary fan-beam side scan sonar, and those of Gallagher et al. (1998b) during DUCK94 using an array of downward-looking sonar altimeters.

There is a very good correlation between megaripple heights, η, and the horizontal separation-lengths, L. The ratio of η/L is about 1.2, which is comparable to the values for 2-D ripples. There is also a very good correlation between the spans and spacings. The

ratio of spans to spacings is close to unity. Megaripple scales correlate better with flow kinetic energy than with other flow variables. Best correlation ($r \sim 0.48$) was obtained between spacing and flow kinetic energy.

The measured slopes of the onshore megaripple "lee" faces for Storm1 were 30-33°, close to the angle of repose for natural sand. The measured slopes, together with the fact that megaripples were migrating in the direction of the "lee" faces, are consistent with the avalanche mechanism for bedform migration.

Both fan-beam and pencil-beam imagery were successfully used to provide quantitative estimates of cross-shore lunate megaripple migration velocities. The two methods yielded migration rates which are in close agreement. The megaripples migrated onshore at 10-20 cm/h during Storm1, opposite to the direction of the mean cross-shore fluid velocity which was 5-10 cm/s offshore. During Storm2 megaripples migrated onshore at 10-40 cm/h on Yeardays 286.4-287.5, when the mean cross-shore velocity was 5-20 cm/s offshore. Megaripples stalled and seemed to occasionally migrate offshore at 50 cm/h on Yeardays 287.6-288 during Storm2 when the mean cross-shore fluid velocity exceeded 20 cm/s offshore. This period was however characterized by northward mean longshore currents (20-50 cm/s) which produced northward-oriented lunate megaripples. Some of the apparent offshore migration may therefore have been associated with the development of these alongshore migrating lunate forms.

Wave-orbital velocity skewness, which is a velocity moment considered to be relevant to cross-shore bedload sediment transport, shows a reasonable correlation with the measured cross-shore migration velocities.

Thus, both mean cross-shore flows and waves appear to affect the observed megaripple migration velocities. Therefore the combined effect of waves and mean currents was investigated.

Stress-based bedload sediment transport models provide estimates of cross-shore bedload sediment transport which are reasonably consistent with the measured migration velocities. The Bagnold (1946) avalanche migration model seems to be successful in relating cross-shore bedload sediment transport rate with measured lunate megaripple heights and

cross-shore migration velocities. A similar conclusion was reached by Hay and Bowen (1999) who compared alongshore bedload transport computed using stress-based models similar to these presented here, to measured alongshore migration velocities. Therefore given accurate measurement of lunate megaripple heights, the observed lunate megaripple migration velocities can be modelled reasonably well using the measured local waves and currents.

Exponents of $\xi = 5/2$ and $\xi = 3/2$ in the stress-based bedload transport models produced similar results. However, the use of $\xi = 5/2$ appears to produce about 15% better agreement between the modelled and measured cross-shore migration velocities compared with the use of $\xi = 3/2$ exponent. Longshore stresses seem to be important, contributing about 15% to the predicted cross-shore megaripple migration velocities.

The infragravity band contributes to the offshore transport in these results. Treating infragravity velocities as waves increases the offshore transport, and gives about 10% better agreement between measured and computed migration velocities, in comparison to treating these motions as slowly varying currents.

The values of the current friction factor f_c giving the best fit to the migration velocities ranged from 6.0×10^{-3} to 8.0×10^{-3} for $\xi = 3/2$ and from 4.3×10^{-3} to 4.5×10^{-3} for $\xi = 5/2$. The best fit wave and current friction ratio α ranged from 6 to 15 for $\xi = 3/2$ and from 2 to 4 for $\xi = 5/2$. The best fit values of f_c are a factor of 2-5 larger than the expected values for flat-bed, fixed roughness, and no waves. This increase is consistent with the presence of mobile grains, and the combined effects of waves and currents, which are expected to produce larger values of f_c than the flat-bed, no wave, fixed roughness values. The best fit values of α are comparable to the expected value for flat-bed, fixed roughness case.

The observed megaripple orientations (ϕ_{Mrip}) ranged from -80° to 20°. There is a lack of alignment between lunate megaripple orientations and the direction of local waves, and mean and total currents. A similar lack of alignment was observed by Gallagher et al. (1998b) between 48-hour average migration direction and these quantities.

The calculated values of gross bedform-normal sediment transport (ϕ_{RH}) were consistently negative, implying positive orientation angles which is contrary to the measured

orientations, and exhibit a narrow range of values (ϕ_{RH} = -25° to 0°) compared to the observations. Comparison between the measured orientations and the direction of net bedload sediment transport (ϕ_{NET}) shows considerable scatter. However, the range of values of ϕ_{NET} (= -90° to 50°) during periods when the forcing is quasi-steady are comparable to the observations. ϕ_{RH} shows a poor comparison with ϕ_{Mrip} due to the dominance of wave effects, ϕ_{RH} is insensitive to small changes in longshore velocities. In contrast, ϕ_{NET} shows a better comparison with ϕ_{Mrip} because it is very sensitive to longshore velocities, while oscillatory flow produces little net sediment transport.

In summary, it has been shown that the observations of cross-shore migration of lunate megaripples during Duck94 can be reproduced in magnitude and direction (onshore and offshore) using stress-based transport models. The good agreement between the measured and modelled migration velocities depends upon the choice of friction coefficients. Although reasonable values of wave and current friction coefficients were obtained, there is a need for bottom stress measurements, as there are not yet reliable predictors of wave and current friction coefficients for combined wave and current flow conditions for different bedform types and mobile beds. Sleath's (1995) bedload transport model provides results that are consistent with the present measurements of lunate megaripple migration velocities and orientations. The fact that lunate megaripple migration velocities are consistent with bedload transport rates calculated using stress-based models suggests that lunate megaripples are useful for testing the predictive skill of bedload transport models, and in determining their coefficients, when applied to irregular wave conditions. The good comparison between the measured megaripple orientations and the computed net bedload sediment transport direction suggests that megaripple orientations reflect the direction of net transport, and may therefore be useful for inferring the direction of net bedload transport in the sedimentary record.

Appendix A

A.1 Marsh-McBirney electromagnetic current meters

The March-McBirney electromagnetic current meter has been known to have a complex response to varying hydrodynamic conditions. This has often lead to the suggestion that their measurements should be treated with care in cases demanding great accuracy. It is therefore natural to consider whether the measured mean cross-shore velocities during DUCK94 were actually in offshore direction or otherwise.

In order to examine this problem, the velocity measurement during the calm days, Year-days 280-283, were examined as shown in Figure A.1. Although some flowmeters showed a gain problem and a velocity offset, it is important to note that all 4 flowmeters measured a mean cross-shore flow of about 5 cm/s offshore (Figure A.1a). The mean cross-shore flow was clearly forced by tidal oscillations (Figure A.1c). Unfortunately the waves were not too small (Figure A.1d), where the significant wave height reached about 0.6m. The days with no waves at all would have offered a better opportunity for examining the flowmeters offset since the meters should all have registered a zero-mean velocity for a zero offset, if they worked properly. The results of flowmeter offset after calibrations indicated that EM849 was off by 2.7 cm/s, EM1320 by 6.1 cm/s, EM884 by 4.4 cm/s and EM1301 by 3.8 cm/s. Therefore, even if we assume that the measured mean cross-shore velocity of say 6 cm/s during these "relatively calm days" to be due to velocity offset of the flowmeters, our overall measurements during the days of interest which involved relatively larger mean cross-shore velocities, up to 10-50 cm/s, would still clearly confirm that the mean

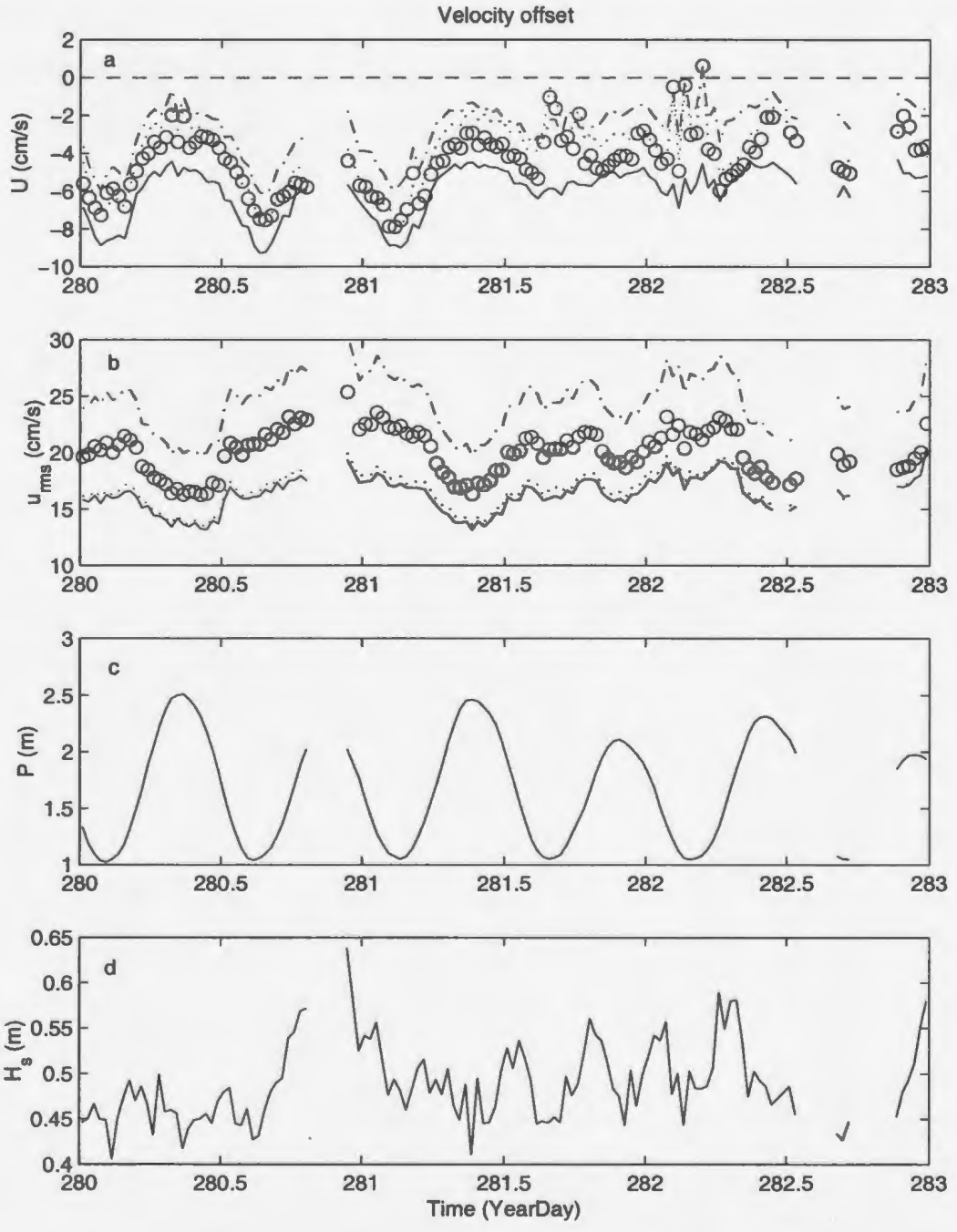

Figure A.1: Velocity measurements by all 4 flowmeters on the frame during calm days, including mean cross-shore velocity (a), rms cross-shore wave-orbital velocity (b), also shown is mean water level fluctuations measured by the bottom pressure gauge (c) and the significant wave height (d). The flowmeters and their location on the frame are given by (--)=EM1320 Top landward, (-.)=EM849 Bottom landward, (:)=EM1301 Top seaward and (o)=EM884 Bottom seaward.

cross-shore flow was surely in the offshore direction. Because of this, the fact that all 4 flowmeters registered offshore flow indicates that the offshore mean cross-shore flow measured here is genuine and the megaripples were in fact migrating opposite to the direction of the undertow during Storm1 and in the first half of Storm2.

Appendix B

B.1 Modelling the cross-shore migration velocities without including the longshore stresses

The cross-shore migration velocities were modelled in Chapter 5 for the case which included the effect of longshore stresses. The second case is considered here without the longshore stresses. The x-component of the time-averaged bedload transport (without longshore stresses) is given by

$$\overline{Q''_{Bx}} = \hat{A}\overline{|\tau_b|^{\xi-1}\tau_{bx}}, \tag{B.1}$$

where the bed-shear stress without longshore stresses is given by

$$\tau_b = [{\tau_{cx}}^2 + {\tau_{wx}}^2 + 2\tau_{cx}\tau_{wx}]^{1/2}, \tag{B.2}$$

hence

$$\tau_b = \tau_{cx} + \tau_{wx}. \tag{B.3}$$

Therefore Equation (B.1) can be written as

$$\overline{Q''_{Bx}} = \hat{A}\overline{|\tau_{cx} + \tau_{wx}|^{\xi-1}(\tau_{cx} + \tau_{wx})}. \tag{B.4}$$

Substituting $\tau_{cx} = 0.5\rho f_c''|U|U$ and $\tau_{wx} = 0.5\rho f_w''|U_{wo}|u_w$ into Equation (B.4) we obtain

$$\overline{Q''_{Bx}} = \hat{A}(\rho f_c'')^{\xi-1}(\rho f_c'')\overline{\left|\frac{|U|U}{2} + \frac{f_w''}{f_c''}U_{wo}u_w\right|^{\xi-1}(\frac{|U|U}{2} + \frac{f_w''}{f_c''}U_{wo}u_w)}, \tag{B.5}$$

where f_c'' and f_w'' are the current and wave friction coefficients without longshore stresses. The significant wave-orbital velocity amplitude without longshore velocities was estimated using the $2U_{rms}$ approach from $U_{wo} = 2u_{rms}$. Similarly, $0.5U_{pp}$ approach was also used to estimate wave-orbital velocity amplitude without longshore velocities by averaging the peak-to-peak amplitudes of u_w.

Thus after putting $\alpha'' = f_w''/f_c''$ and re-arranging Equation (B.5) we obtain

$$\overline{Q''_{Bx}} = \hat{A}(\rho f_c'')^{\xi}\overline{\chi''_x}, \tag{B.6}$$

where $\overline{\chi''_x}$ is given by

$$\overline{\chi''_x} = \overline{\left|\frac{1}{2} \mid U \mid U + (\frac{\alpha''}{2}U_{wo}u_w)\right|^{\xi-1}}\left(\frac{1}{2} \mid U \mid U\right) +$$

$$\overline{\left|\frac{1}{2} \mid U \mid U + (\frac{\alpha''}{2}U_{wo}u_w)\right|^{\xi-1}\left(\frac{\alpha''}{2}U_{wo}u_w\right)}. \tag{B.7}$$

Note that $\overline{\chi_x}$ (Equation 5.20) has slightly different α-dependence because of differences in the friction factor dependence of Equations (4.19 and B.5) Modelled cross-shore

megaripple migration velocities without longshore stresses can therefore be obtained from Equation (B.6). As in Chapter 4, the time-mean bedload sediment transport without longshore stresses is non-dimensionalized by $[(s-1)gD^3]^{1/2}$. Similarly, the bed shear stresses are also non-dimensionalized by $[\rho(s-1)gD]$. Thus the non-dimensional time-averaged bedload sediment transport without longshore stresses can be written as

$$\Phi''_{Bx} = \frac{Q''_{Bx}}{[(s-1)gD^3]^{1/2}} = \frac{A(\rho f''_c)^{\xi}}{[\rho(s-1)gD]^{\xi}}\overline{\chi''_x}.$$

Thus

$$Q''_{Bx} = \frac{A(f''_c)^{\xi}D}{[(s-1)gD]^{\xi-1/2}}\overline{\chi''_x}. \tag{B.8}$$

Equation (5.1) in Chapter 5 and Equation (B.8) are then combined to obtain

$$U''_m = A\left[\frac{(f''_c)^{\xi}D/\eta}{(1-\epsilon)[(s-1)gD]^{\xi-1/2}}\right]\overline{\chi''_x}. \tag{B.9}$$

Equation (B.9) is therefore used to model the cross-shore migration velocities without the effect of longshore stresses. Figure B.1 shows the correlation coefficients for the comparison between $\overline{\chi_x}$ and megaripple migration velocities, whereas Table A.1 gives the summary of the peak correlation coefficients. Table A.2 gives the summary of the obtained correlation coefficients and slopes of regression lines for the comparison between measured and modelled migration velocities without longshore stresses for both raw and interval-averaged data, using the values of α'' from results shown in Table A.1. Also listed are the f''_w/f''_c and f''_c constants used in the model. Figures B.2 and B.3 show the scatter diagrams for the comparisons between measured and modelled cross-shore migration velocities using the raw data. The solid lines indicates the regression lines while R and S represent the correlation coefficients and slope of the regression lines respectively. Similarly, Figures B.4 and B.5 show the scatter diagram for the comparison between measured and modelled migration velocities using the interval-averaged data.

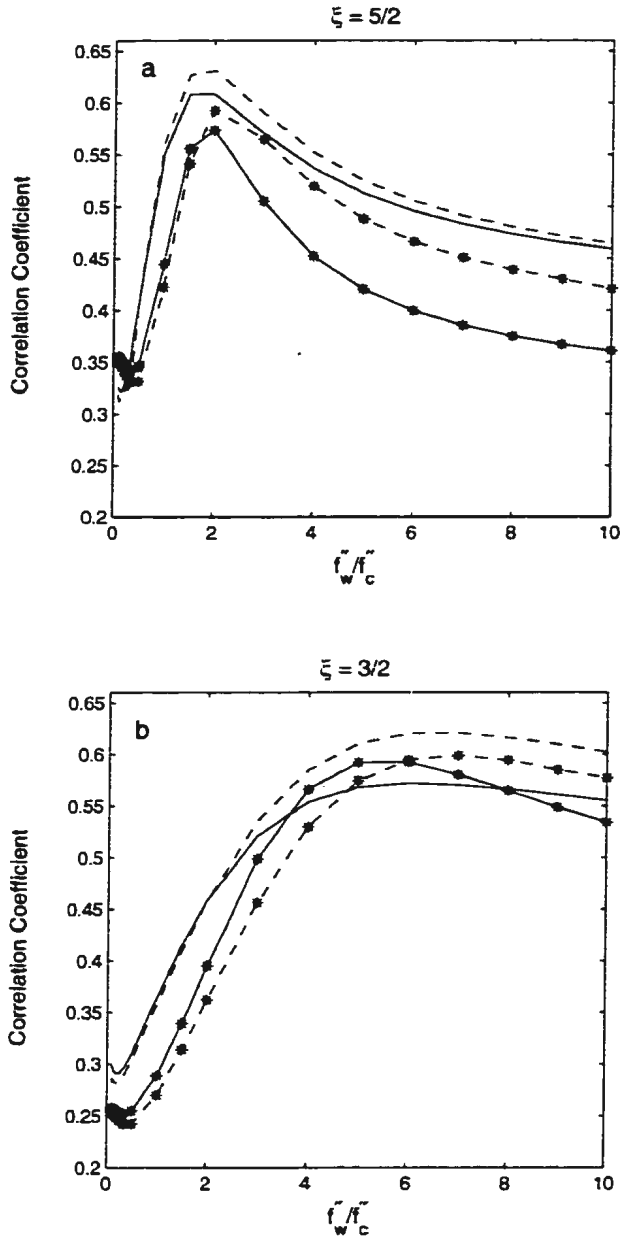

Figure B.1: Correlation coefficients between measured migration velocities and $\overline{\chi''_x}$ as a function of friction coefficient ratio, $\alpha'' = f''_w/f''_c$. The solid lines are the results for $U_{wo}(t_s) = 0.5U_{pp}(t)$; the dashed lines are the $U_{wo} = 2U_{rms}$. The symbol (*) is for infragravity velocities treated as currents and the lines with no symbols are for infragravity velocities treated as waves.

Table B.1: Maximum correlation coefficients (R) for the comparison of measured megaripple migration velocities with $\overline{\chi''_x}$ computed using various approaches of estimating wave-orbital velocity amplitudes, ξ values and f''_w/f''_c ratios without including longshore stresses.

U_{wo} Approach	ξ	$\frac{f''_w}{f''_c}$	R
$0.5U_{pp}$ & U_{ifg} as waves	3/2	6	0.57
$0.5U_{pp}$ & U_{ifg} as currents	3/2	6	0.59
$0.5U_{pp}$ & U_{ifg} as waves	5/2	2	0.61
$0.5U_{pp}$ & U_{ifg} as currents	5/2	2	0.57
$2U_{rms}$ & U_{ifg} as waves	3/2	6	0.62
$2U_{rms}$ & U_{ifg} as currents	3/2	6	0.60
$2U_{rms}$ & U_{ifg} as waves	5/2	2	0.63
$2U_{rms}$ & U_{ifg} as currents	5/2	2	0.59

Table B.2: Comparison between measured and computed megaripple migration velocities without longshore stresses where R and S are the correlation coefficients and slopes of linear regression lines using raw data, R_I and S_I are the correlation coefficients and slopes of linear regression lines using interval-averaged data, f''_w/f''_c and f''_c are the constants used in the model.

vspace0.05in

U_{wo} Approach	ξ	$\frac{f''_w}{f''_c}$	f''_c	R	S	R_I	S_I
$0.5U_{pp}$ & U_{ifg} as waves	3/2	6	$8.0\text{x}10^{-3}$	0.53	0.58	0.93	0.68
$0.5U_{pp}$ & U_{ifg} as currents	3/2	6	$8.0\text{x}10^{-3}$	0.48	0.49	0.90	0.29
$0.5U_{pp}$ & U_{ifg} as waves	5/2	2	$3.5\text{x}10^{-2}$	0.56	0.60	0.92	0.40
$0.5U_{pp}$ & U_{ifg} as currents	5/2	2	$3.5\text{x}10^{-2}$	0.51	0.52	0.92	0.34
$2U_{rms}$ & U_{ifg} as waves	3/2	6	$1.0\text{x}10^{-2}$	0.55	0.80	0.96	0.59
$2U_{rms}$ & U_{ifg} as currents	3/2	6	$1.0\text{x}10^{-2}$	0.53	0.81	0.99	0.67
$2U_{rms}$ & U_{ifg} as waves	5/2	2	$3.5\text{x}10^{-2}$	0.58	0.79	0.95	0.55
$2U_{rms}$ & U_{ifg} as currents	5/2	2	$3.5\text{x}10^{-2}$	0.55	0.69	0.98	0.56

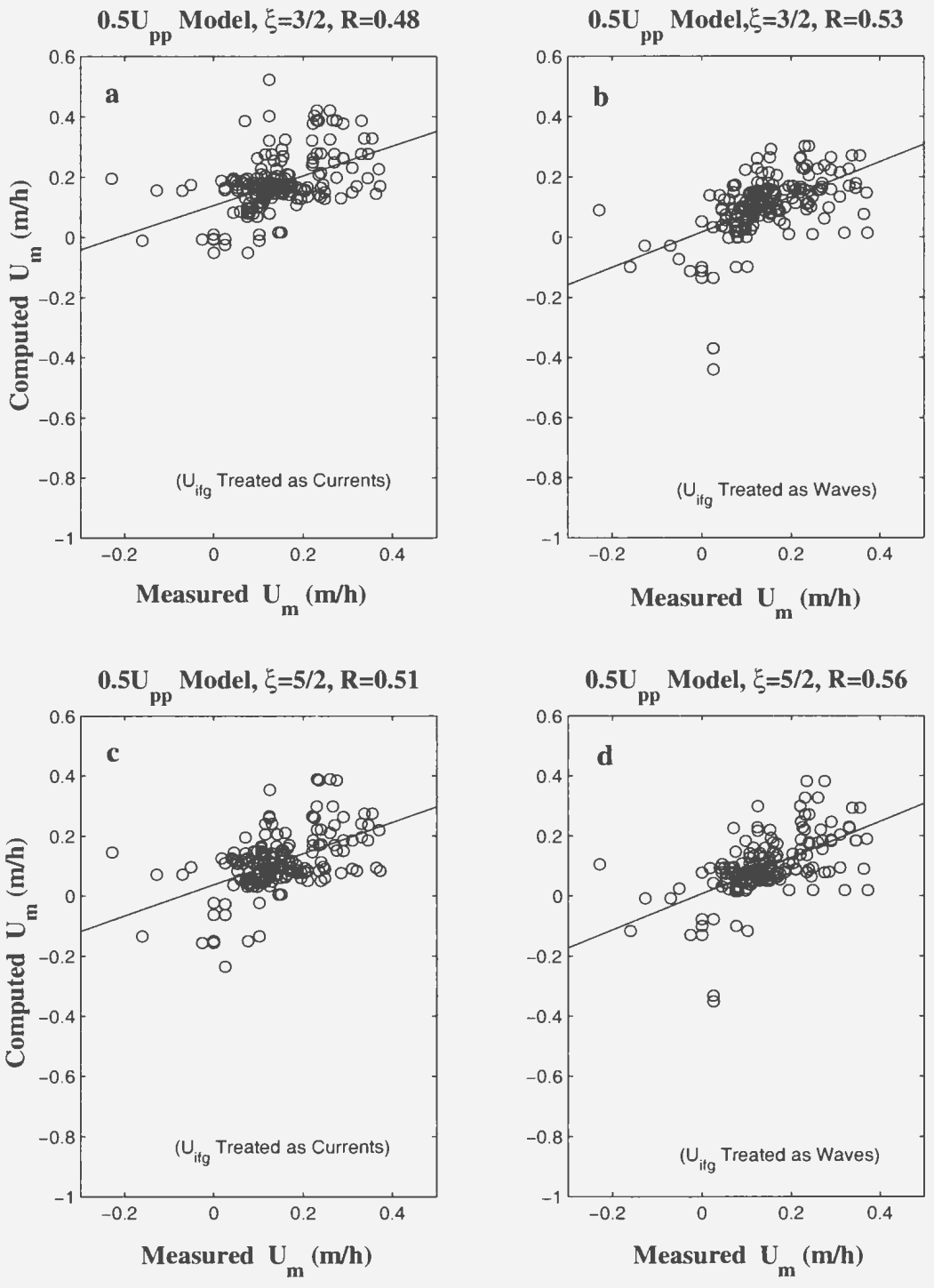

Figure B.2: Comparisons between the raw measured and computed cross-shore migration velocities using $0.5U_{pp}$ approach, without longshore stresses,with $U_{ifg}(t)$ treated as currents and $\xi = 3/2$ (a), with $U_{ifg}(t)$ treated as waves and $\xi = 3/2$ (b), with $U_{ifg}(t)$ treated as currents and $\xi = 5/2$ (c), with $U_{ifg}(t)$ treated as waves and $\xi = 5/2$ (d). The solid lines are the linear regression lines and R is the correlation coefficient.

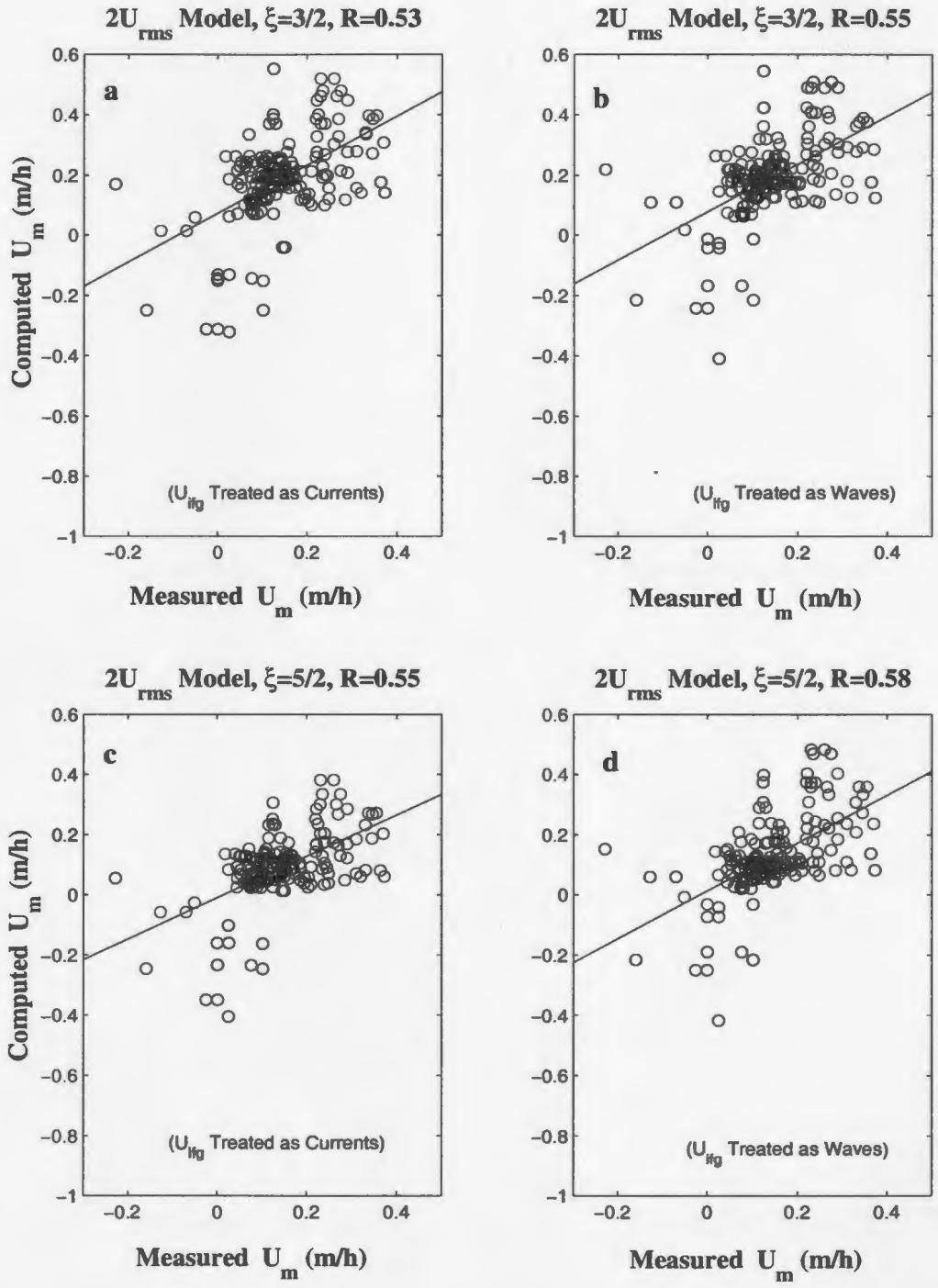

Figure B.3: Comparisons between the raw measured and computed cross-shore migration velocities using $2U_{rms}$ approach, without longshore stresses, with $U_{ifg}(t)$ treated as currents and $\xi = 3/2$ (a), with $U_{ifg}(t)$ treated as waves and $\xi = 3/2$ (b), with $U_{ifg}(t)$ treated as currents and $\xi = 5/2$ (c), with $U_{ifg}(t)$ treated as waves and $\xi = 5/2$ (d). The solid lines are the linear regression lines and R is the correlation coefficient.

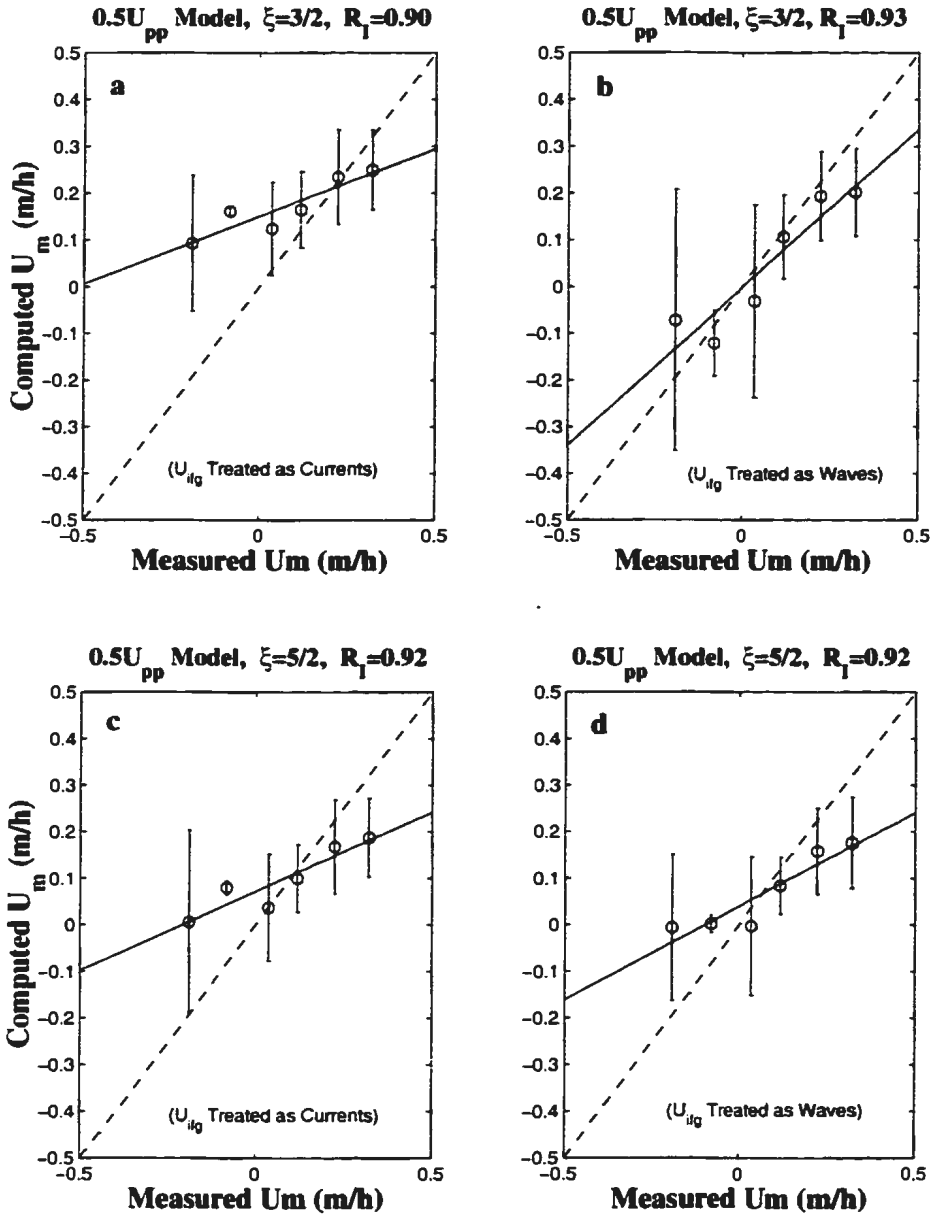

Figure B.4: Comparisons between interval averaged measured and computed cross-shore migration velocities using $0.5U_{pp}$ approach, without longshore stresses, with $U_{ifg}(t)$ and treated as currents and $\xi = 3/2$ (a), with $U_{ifg}(t)$ and treated as waves and $\xi = 3/2$ (b), with $U_{ifg}(t)$ and treated as currents and $\xi = 5/2$ (c), with $U_{ifg}(t)$ and treated as waves and $\xi = 5/2$ (d). The solid lines shows the regression lines, the dashed lines is the 1:1 fit and R_I is the correlation coefficient.

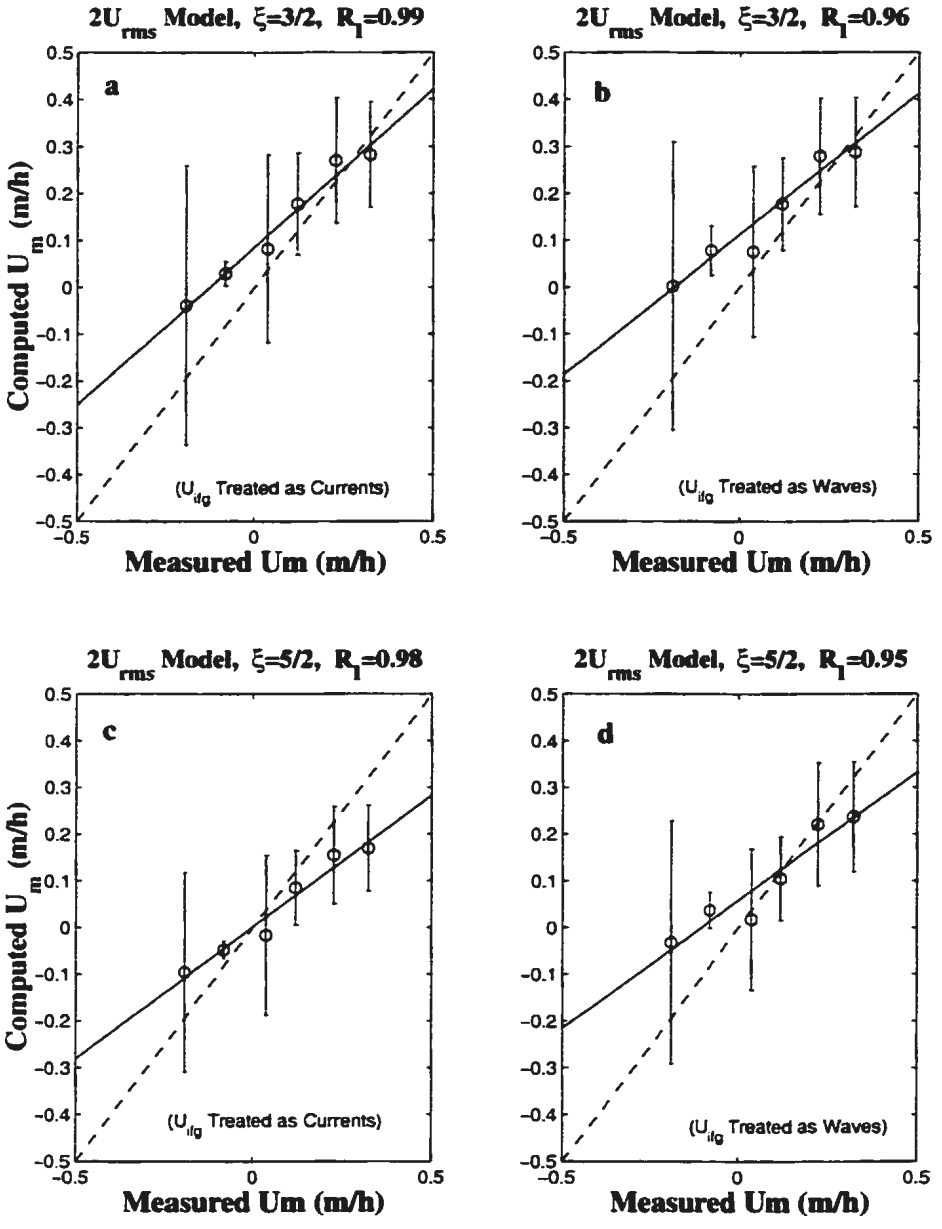

Figure B.5: Comparisons between interval averaged measured and computed cross-shore migration velocities using $2U_{rms}$ approach, without longshore stresses, with $U_{ifg}(t)$ treated as currents and $\xi = 3/2$ (a), with $U_{ifg}(t)$ treated as waves and $\xi = 3/2$ (b), with $U_{ifg}(t)$ treated as currents and $\xi = 5/2$ (c), with $U_{ifg}(t)$ treated as waves and $\xi = 5/2$ (d). The solid lines shows the regression lines, the dashed lines is the 1:1 fit and R_I is the correlation coefficient.

References

Abou-Seida, M.M., 1965. Bed-load function due to wave action. *Rep. HEL 2-11*, 78 pp., Hydraul. Eng. Lab., Univ. of Calif., Berkeley.

Allen, J.R.L., 1968. *Physical Processes of Sedimentation*. Earth Science Series 1. Allen and Unwin, London.

Allen, J.R.L., 1979. A model for the interpretation of wave ripple-marks using their wavelength, textural composition and shape. *J. Geol. Soc. London, 136*: 673-682.

Allen, J.R.L., 1984. *Sedimentary Structures. Their Character and Physical Basis*. Elsevier, Amsterdam, 593 pp.

Bagnold, R.A., 1946. *The Physics of Blown Sand and Desert Dunes*, 265 pp., Chapman and Hall, London.

Birkemeir, W.A., H.C. Miller, S.D. Wilheim, A.E. DeWall, and C.S. Gorbics, 1985. A User's Guide to the Coastal Engineering Research Center's (CERC's) Field Research Facility, *Instruction Report CERC-85-1*, Waterways Experiment Station, Corps of Engineers, Vicksburg, MI, 136 pp.

Birkemeir, W.A., A.E. DeWall, C.S. Gorbics and H.C. Miller, 1981. A user's guide to CERC's field research facility. U.S. Army Corps Eng., *Coastal Eng. Res. Cent. MR*

81-7.

Boyd, R., D.L. Forbes, and D.E. Heffler, 1988. Time-sequence observations of wave-formed sand ripples on an ocean shoreface. *Sedimentology, 35*: 449-464.

Bowen, A.J., 1980. Simple models of nearshore sedimentation; beach profiles and long-shore bias. In *Proc. of the Conf. on Coastline of Canada*, Halifax, 1978. Geol. Surv. of Canada.

Brown, C.B., 1950. *Sediment transportation*. In: H. Rouse (Ed.), Engineering Hydraulics, Wiley, N.Y., p.797.

Clifton, H.E.R., R.E. Hunter, and R.L. Phillips, 1971. Depositional structures and processes in the non-barred high-energy nearshore , *J. Sediment. Petrol., 41*, 651-670.

Clifton, H.E., 1976. Wave-formed sedimentary structures - A conceptual model. In: R.A Davis, Jr. and R.L Ethington (Editors), Beach and Nearshore Sedimentation. *SEPM Spec. Publ., 24*, 126-148.

Clifton, H.E.R. and J.R. Dingler, 1984. Wave-formed structures and paleoenvironmental reconstruction, *Mar. Geol., 60*: 165-198.

Christoffersen, J.B. and I.V. Johnsson, 1985. Bed friction and dissipation in a combined current and wave motion. *Ocean Engng., 12* 387-423.

Cornforth, D.H., 1973. Prediction of drained strength of sands from relative density measurements. *Am. Soc. Test. Mat. Spec. Tech. Pub.* 523; pp. 281-303.

Davidson-Arnott, R.G.D., and B. Greenwood, 1976. Facies relationships on a barred coast,

Kouchibouguac Bay, New Brunswick, Canada, In: Davis R.A. Jr., and R.L. Ethington (Eds.) Beach and Nearshore Sedimentation, *Spec. Publ. Soc. Econ. Paleontol. Mineral., 24*, 149-168.

Dalrymple, R.W., R.J. Knight and J.J. Lambiase, 1978. Bedforms and their hydraulic stability relationships in a tidal environment, Bay of Fundy, Canada. *Nature, 275*: 100-104.

Dingler, J.R., 1974. Wave-formed ripples in nearshore sands, Unpubl. Ph.D dissirtation, University of California, San Diego, 136 pp.

Dingler, J.R. and D.L. Inman, 1977. Wave-formed ripples in nearshore sands. *Proc. 15th Coastal Engineering Conference. Am. Soc. Civ. Engnrs.*, Honolulu, Hawaii, pp.2109-2126.

Dingler, J.R., J.C. Boylls and R.L. Lowe, 1977. A high-frequency sonar for profiling small-scale subaqueous bedforms. *Mar. Geol, 24*: 279-288.

Dyer, K.R. and R.L. Soulsby, 1988. Sand Transport on the continental shelf. *Annu. Rev. Fluid Mech., 20*, 295-324.

Fofonoff, N.P., 1969. Spectral characteristics of internal waves in the ocean. *Deep Sea Res. Suppl., 16*, 58-71, Appendix.

Fredsoe, J., and R. Deigaard, 1992. *Mechanics of Coastal Sediment Transport*, World Scientific, River Edge, New Jersey, 369 pp.

Frere, H.B.E., 1870. Notes on the Runn of Cutch. *J.R. Geogr. Soc., 40*: 181-207.

Gadd, P.E., J.W. Lavelle and D.J.P. Swift, 1978. Estimate of sand transport on the New York shelf using near-bottom current meter observations. *J. Sediment. Petrol. 48*, 239-252.

Gallagher E.L., S. Elger and R.T. Guza, 1998. Observations of sand bar evolution on a natural beach. *J. Geophys. Res. 103(C2)*, pp.3203-3315.

Gallagher E.L., S. Elger and E.D. Thornton, 1998b. Observations and predictions of mega-ripple migration in a natural surf-zone *Nature*. (Accepted).

Gilbert, G.K., 1914. The transportation of debris by running water.*U.S. Geol. Surv., Prof. Pap., 86*: 1-263.

Goud, M.R. and D.G. Aubrey, 1985. Theoretical and observational estimation of nearshore bedload transport rates. *Mar. Geol. 64*, 91-111.

Grant, W.D. and O.S. Madsen, 1979. Combined wave and current interaction with a rough bottom. *J. Geophys. Res. 84*, 1797-1808.

Greenwood, B. and P.B. Hale, 1980. Depth of activity, sediment flux and morphological change in a barred nearshore environment. In: McCann, S.B. (Ed), *The Coastline of Canada*, Pap. 80-10. Geol. Surv. Can., Halifax, pp. 89-109.

Greenwood, B., R.G. Richards and R. Brander, 1993. Acoustic imaging of seabed geometry: A High Resolution Remote Tracking Sonar (HRRTS II). *Mar. Geol., 112*: 207-218.

Guza R.T. and E.B. Thornton, 1985a. Velocity moments in the nearshore.*J. Waterw., Port Coastal Ocean Div., ASCE, III*, 235-256.

Guza R.T and E.B. Thornton, 1985b. Observations of surf beat. *J. Geophys. Res., 90*, 3161-3172.

Hay, A.E. and A.J. Bowen, 1993. Spatially correlated depth changes in the nearshore zone, during autumn storms. *J. Geophys. Res., 98(C7)*: 12,387-12,404.

Hay, A.E. and D.L. Wilson, 1994. Rotary sidescan images of nearshore bedform evolution during a storm. *Mar. Geol., 119*, 57-65.

Hay, A.E. and A.J. Bowen, 1999. Alongshore migration of lunate megaripple during DUCK94: Part I. *J. Geophys. Res.* (In press).

Heathershaw, A.D. and F.D.C. Hammond, 1979a. Swansea Bay (Sker) Project Topic Report, 6. Offshore sediment, movement and its relation to observed tidal current and wave data. *Inst. Oceanogr. Sci. Rep., 93*: 119 pp.

Heathershaw, A.D., 1981. Comparisons of measured and predicted sediment transport rates in tidal currents. In: Nittrouer, C.A. (Ed.), Sedimentary Dynamics of Continental Shelves. *Mar. Geol. 42*, 75-104.

Howd, P.A., and R.A. Holman, 1984. Beach foreshore response to long-period waves. *Proceedings 19th Coastal Engineering Conference*, American Society of Civil Engineers: 1968-1982.

Horikawa, K., 1988. (Ed.) *Nearshore Dynamics and Coastal Processes*, 522 pp. University of Tokyo Press, Tokyo.

Holman, R.A. and, A.J. Bowen, 1982. Bars, bumps and holes: models for the generation of complex beach topography. *J. Geophys. Res. 87*, 457-468.

Horn, D.P. and T. Mason, 1994. Swash zone sediment transport modes. *Mar. Geol. 20*: 309-325.

Huntley, D.A. and D. Hanes, 1987. Direct measurement of suspended sediment transport. Coastal Sediments '87, *Proc. Speciality Conf. Advances in understanding coastal sediment processes, ASCE*, New York, NY, p. 738-755.

Inman, D.L., 1957. Wave-generated Ripples in Nearshore Sands, *Tech. Memo. 100*, Beach Erosion Board, U.S. Army Corps of Engineers, 65 pp.

Jonsson, I.G., 1966. Wave boundary layers and friction factors. *Proceedings of the 10th Coastal Engineering Conference*, Tokyo, pp. 127-148.

Kachel, N.B. and R.W. Sternberg, 1971. Transport of bedload as ripples during an ebb current. *Mar. Geol. 10*, 229-244.

Kajima, R., K. Maruyama, T. Shimizu, T. Sakakiyama, and S. Saito, 1982a. Experimental study of waves on beaches with prototype wave flume. *Proc. 29th Japanese Conf. on Coastal Eng., JSCE*, pp. 213-217.

Kalkanis, G., 1964. Transportation of bed material due to wave action. *Technical Memorandum 2*, Coastal Engineering Research Center, 68 pp.

Komar, P.D. and D.L. Inman, 1970. Longshore sand transport on beaches. *J. Geophys. Res., 75*: 5914-5927.

Komar, P.D. and R.A. Holman, 1986. Coastal processes and the development of shoreline erosion. *Annual Review of Earth Planetary Science, 14*: 237-265.

Larson, M., and N.C. Kraus, 1995. Prediction of cross-shore sediment transport at different spartial and temporal scales. *Mar. Geol. 126*, 111-127.

Li, M.Z., C.L. Amos and D.E. Heffler, 1977. Boundary layer dynamics and sediment transport under storm and non-storm conditions on the Scotian Shelf. *Mar. Geol. 141*, 151-181.

Madsen, O.S., and W.D. Grant, 1976. Sediment transport in the coastal environment, *Rep. 209, Ralph M. Parsons Lab.*, Mass. Inst. of Technol., Cambridge.

Madsen, O.S., and W.D. Grant, 1977. Quantitative description of sediment transport by waves, in *Proc. of 15th Coastal Eng. Conf., ASCE*, New York, 1093-1112.

Meyer-Peter, E. and R. Müller, 1948. Formula for bed-load transport, *Rep, 2nd Meet. Int. Assoc. Hydraul. Struc. Res.*, Stockholm, 39-64.

McCave, I.N., 1971. Sand waves in the North Sea off the coast of Holland. *Mar. Geol. 10*: 199-255.

McLean, S.R., 1983. Turbulence and sediment transport measurements in a North Sea tidal inlet (The Jade). In: J. Sundermann and W. Lenz (Eds.), *North Sea Dynamics*. Springer, Berlin, pp. 436-452.

Miller, M.C., and P.D. Komar, 1980. A Field investigation of the relationship between oscillatory ripple spacing and the near-bottom water orbital motions. *J. Sedimentary Pet., 50*: 183-191.

Middleton, G.V and J.B. Southard, 1984. Mechanics of sediment movement. SEPM. Tulsa.

Nielsen, P., 1981. Dynamics and geometry of wave-generated ripples, *J. Geophy. Res., 86(C7)*, 6467-6472.

Ollerhead, J.W. and B. Greenwood, 1990. Bedform geometry and dynamics in the upper shoreface, Bluewater Beach, Ontario, Canada. *Proc. Canadian Coastal Conf., Kingston, Ont., ACOS*, Natl. Res. Counc. Canada, Ottawa, p. 337-348.

Osborne, P.D. and C.E. Vincent, 1992. Timescales of bed response in a low energy surf zone. *Proc. of the 23th Coastal Eng. Conference*, Venice, Italy, ASCE, pp. 2321-2331.

Pattiaratchi, C.B. and M.B. Collins, 1985. Sand transport under the combined influence of waves and tidal currents: An assessment of available formulae. *Mar. Geol. 67*, 83-100.

Rubin, D.M. and R.S Hunter, 1987. Bedform alignment in directionally varying flows. *Science, 237*, 276-278.

Rubin, D.M and H. Ikeda, 1990. Flume experiments on the alignment of transverse, oblique, and longitudinal dunes in directionally varying flows. *Sedimentology, 37*, 673-684.

Roelvink, J.A and M.J.F. Stive, 1989. Bar-generating cross-shore flow mechanisms on a beach. *J. Geophy. Res. 94(C4)*, pp. 4785-4800.

Salsman, G.G., W.H. Tolbert and R.G. Villars, 1966. Sand wave migration in St. Andrew Bay, FL.*Mar. Geol., 4*: 11-19.

Sallenger, A.H., Jr. and B.M. Richmond, 1984. High-frequency sediment-level oscillation in the swash zone.*Mar. Geol., 60*: 155-164.

Seymour, R.J., and D.B. King Jr, 1982. Field comparisons of cross-shore transport models, Journal of the Waterways, Port, Coastal and Ocean Division, *Proceedings of the American Society of Civil Engineers, 108(WW2)*, May, 1982: 163-179.

Simons, D.B. and E.V. Richardson, 1961. Forms of bed roughness in alluvial channels: *Am. Soc. Civil Engineers Proc.*, V. 87, no. HY3, p. 87-105.

Simons, D.B. and M.L. Albertson, 1960. Uniform water conveyance channels in alluvial material. *Proc. A.S.C.E. J. Hydrauli. Div. 86(HY5)*: 33-99. Am.

Simons, D.B., E.V. Richardson and C.F. Nordin, Jr. 1964. Sedimentary structures generated by flow in alluvial channels. *Report CER 64 DBS-EVR-CFN 15*, Colorado State Univ., Fort Collins, Colorado.

Sleath, J.F.A., 1978. Measurement of bed-load in oscillatory flow. Proc. A.S.C.E.J. Waterw.*Port Coastal Ocean Eng. Div. 104 (WW3)*: 291-307.

Sleath, J.F.A., 1984. *Sea Bed Mechanics*, 335 pp., John Wiley, New York.

Sleath, J.F.A., 1995. Sediment transport by waves and currents. *J. Geophy. Res. Vol. 100, C6*, pp. 10,977-10,986.

Southard, J.B., J.M. Lambie, D.C. Federico, H.T. Pile and C.R. Weidman, 1990. Experiments on bed configurations in fine sands under bidirectional purely oscillatory flow, and the origin of hummocky cross-stratification. *J. Sedim. Petrol., 60*: 1-17.

Sorby, H.C., 1859. On the structures produced by the currents present during the deposition of stratified rocks. *The Geologist*, v. 2, pp. 137-147.

Stive, M.J.F. and H.G. Wind, 1986. Cross-shore mean flow in the surf zone. *Proc. of 10th Coastal Eng. Conf.* pp. 325-340.

Thornton, E.B. and R.T. Guza, 1983. Transformation of wave height distribution. *J. Geophys Res., 88(C10), 5925-5938.* pp. 325-340.

Vincent, C.E., R.A. Young, and D.J.P. Swift, 1981. Bed-load transport under waves and currents, *Mar. Geol., 39*, 71-80.

Vincent, C.E and P.D. Osborne, 1993. Bedform dimensions and migration rates under shoaling and breaking waves. *Cont. Shelf Res., Vol.13(11)*, pp. 1267-1280.

Watanabe, A., Y. Riho and K. Horikawa, 1980. Beach profiles and on-offshore sediment transport, *Proc. 17th Coastal Eng. Conf., ASCE*, pp. 1106-1121.

Watanabe, A., 1981. Numerical simulation of nearshore current and beach transformation. In: *Proc. of 28th Conf. on Coastal Eng.*, pp. 285-289, Japan Society of Civil Engineering, Tokyo.

Watanabe, A., 1982. Numerical models of nearshore currents and beach deformation. *Coastal Eng. Jpn.*, 25, 147-161.

Wiberg, P.L. and C.K. Harris, 1994. Ripple geometry in wave-dominated environments. *J. Geophy. Res., 90(C1)*, 775-789.

Wilson, K.C., 1966. Bed-load transport at high shear stress. *J. Hydraul. Div., ASCE 92 (HY6)*, 49-59.

Wright, L.D., J.D. Boon, M.O. Green and J.H. List, 1986. Response of the mid-shoreface of the southern mid-Atlantic Bight to a "Northeaster". *Mar. Geol. Lett., 6*: 153-160.

Wright, L.D., J.D. Boon and J.J. List, 1991. Modes of cross-shore sediment transport on the shoreface of the middle Atlantic bight. *Mar. Geol. 96*, 19-51.

Yalin, M.S., 1977. *Mechanics of Sediment Transport*. Pergamon, Oxford, 298 pp.